Probing superfluid properties in strongly correlated Fermi gases with high spatial resolution

Dissertation zur Erlangung des Doktorgrades
an der Fakultät für Mathematik, Informatik und Naturwissenschaften
Fachbereich Physik
der Universität Hamburg
vorgelegt von Wolf Weimer
Hamburg, 2014

Zusammenfassung

In dieser Arbeit wird ein experimenteller Aufbau zur Erforschung von ultrakaltem fermionischem ^{6}Li mit einstellbarer Wechselwirkungsstärke und Dimensionalität vorgestellt. Der Aufbau wird zur Untersuchung der Schallgeschwindigkeit v_s und der suprafluiden kritischen Geschwindigkeit v_c im Übergang von Bose-Einstein Kondensation (BEC) zu Bardeen-Cooper-Schrieffer (BCS) Suprafluidität eingesetzt. Die Ergebnisse dienen als Richtwerte für Theorien zur Beschreibung stak korrelierter Systeme.

Um v_c zu messen wird eine Störung, welche durch einen stark fokussierten Laserstrahl erzeugt wird, mit konstanter Geschwindigkeit entlang einer Linie konstanter Dichte durch eine suprafluide Probe bewegt. Für Geschwindigkeiten größer als v_c wird eine Erwärmung des Gases beobachtet. Die kritische Geschwindigkeit wird für verschiedene Wechselwirkungsstärken gemessen, wobei der BEC-BCS Übergang abgedeckt wird.

Nach dem Landau Kriterium und der Bogoliubov Theorie sind v_c und v_s in einem Bose-Einstein-Kondensat eng miteinander verknüpft. Zur Messung von v_s wird ein Dichteüberschusses im Zentrum der Probe erzeugt und die sich daraufhin ausbreitende Dichtemodulation beobachtet. Die beiden Geschwindigkeiten v_c und v_s werden bei ähnlichen Wechselwirkungsstärken und in ähnlichen Proben gemessen, um die Vergleichbarkeit sicher zu stellen.

Der Aufbau, welcher die ultrakalten Proben zur Verfügung stellt, ist ein zwei Kammer Design mit einer magneto-optischen Falle welche mittels eines Zeeman-Slowers geladen wird. Die darauffolgenden Kühlschritte sind rein optisch und erzeugen schlussendlich eine ultrakalte oblate Atomwolke innerhalb einer flachen Vakuumkammer. Diese bietet optimalen optischen Zugang und befindet sich zwischen zwei Mikroskopobjektiven mit hoher numerischer Apertur. Diese Objektive werden dazu genutzt, um die Proben in-situ auf Längenskalen zu untersuchen, welche den intrinsischen Längenskalen der Gase entsprechen. Gleichermaßen werden optische Dipolpotentiale eingesetzt, um die Wolken auf diesen Längenskalen zu manipulieren. Die oblaten Proben sind so dünn, dass ihre Ausdehnung entlang der Mikroskop Achsen kleiner als die Tiefenschärfe der Objektive ist. Mittels eines zusätzlichen blau verstimmten optischem Gitters ist es möglich, einlagige zweidimensionale Gase zu erzeugen. An diesen werden zurzeit Experimente durchgeführt.

Abstract

In this thesis an apparatus to study ultracold fermionic ^{6}Li with tunable interaction strength and dimensionality is presented. The apparatus is applied to investigate the speed of sound v_s and the superfluid critical velocity v_c across the BEC-BCS crossover. The results set benchmarks for theories describing strongly correlated systems.

To measure v_c an obstacle, that is formed by a tightly focused laser beam, is moved through a superfluid sample with a constant velocity along a line of constant density. For velocities larger than v_c heating of the gas is observed. The critical velocity is mapped out for various different interaction strengths covering the transition from Bose-Einstein condensation to Bardeen-Cooper-Schrieffer superfluidity.

According to the Landau criterion and Bogoliubov theory, v_c should be closely related to v_s in a Bose-Einstein condensate. The measurement of v_s is conducted by creating a density modulation in the centre of the cloud and tracking the excited modulation. The velocities v_s and v_c are measured in a similar range of interaction strengths and in similar samples to ensure comparability.

The apparatus which provides the ultracold samples is a two chamber design with a magneto-optical trap that is loaded via a Zeeman slower. The subsequent cooling steps are all-optical and finally create an ultracold oblate atom cloud inside a flat vacuum cell. This cell provides optimal optical access and is placed between two high numerical aperture microscope objectives . These objectives are used to probe the samples in-situ on length scales which are comparable to the intrinsic length scales of the gases. Similarly, optical dipole potentials are employed to manipulate the clouds on the same small length scales. The oblate samples are sufficiently flat such that there spatial extent along the microscope axes is smaller than the depth of field of the objectives. With an additional blue-detuned optical lattice it is possible to create single-layer two-dimensional gases on which presently experiments are being performed.

Publikationen

Im Rahmen der vorliegenden Arbeit ist die folgende wissenschaftliche Veröffentlichung entstanden.

Publications

The following research article has been published in the course of this thesis.

[1] W. Weimer, K. Morgener, V. P. Singh, J. Siegl, K. Hueck, N. Luick, L. Mathey, and H. Moritz, *The critical velocity in the BEC-BCS crossover*, eprint arXiv:cond-mat/1408.5239v1 (2014). Under review for Physical Review Letters

Contents

1 Introduction

Superconductivity and superfluidity are two of the most striking macroscopic phenomena originating from microscopic quantum effects. They describe frictionless flow of either electrons, atoms or molecules in their surrounding medium. Of particular interest are strongly interacting systems where the superfluid state is most stable. Examples are superfluid ^{4}He and high temperature superconductors. The technological relevance especially of the latter is inestimable.

The remarkable property of superfluids is best illustrated by considering an obstacle which moves through a superfluid medium. No energy will be dissipated as long as the flow velocity is below a certain critical velocity v_c. A general expression for v_c was determined by Landau [1] by considering a object with infinite mass that moves through a superfluid under conservation of momentum and energy.

In this thesis, I present an experimental study of the superfluid critical velocity in ultracold ^{6}Li. The experiment realizes the idealized measurement scenario considered by Landau: a superfluid dilute atomic gas is probed by a moving obstacle as shown in the figure. It is the first time where the size of the obstacle is comparable to the intrinsic length scales of the cold gas, e.g. the inter-particle distance. In the BEC regime, the obstacle can excite phonons and the Landau criterion predicts that the critical velocity is given by the speed of sound. Consequently we also measure the speed of sound by exciting and monitoring density waves and compare the results with the critical velocity. Further, we validate our experiments with simulations performed by Vijay Singh and Ludwig Mathey.

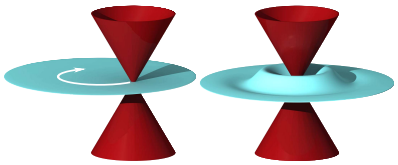

Illustration of the measurements to determine v_c (left) and v_s (right).

A particular feature of our physical system is that the interaction strength of the superfluid under study is tunable. The gas can therefore either resemble a Bose-Einstein condensate (BEC), a Bardeen Cooper Schrieffer (BCS) superfluid or a strongly interacting system. This tunable interaction strength is a distinct advantage of experiments with ultracold fermionic gases compared to studies of condensed matter systems.

The adjustability of the interaction strength is made possible by a Feshbach resonance [2] which can be addressed with a magnetic offset field. The corresponding Zeeman shift brings a molecular bound state into resonance with the kinetic energy of two colliding

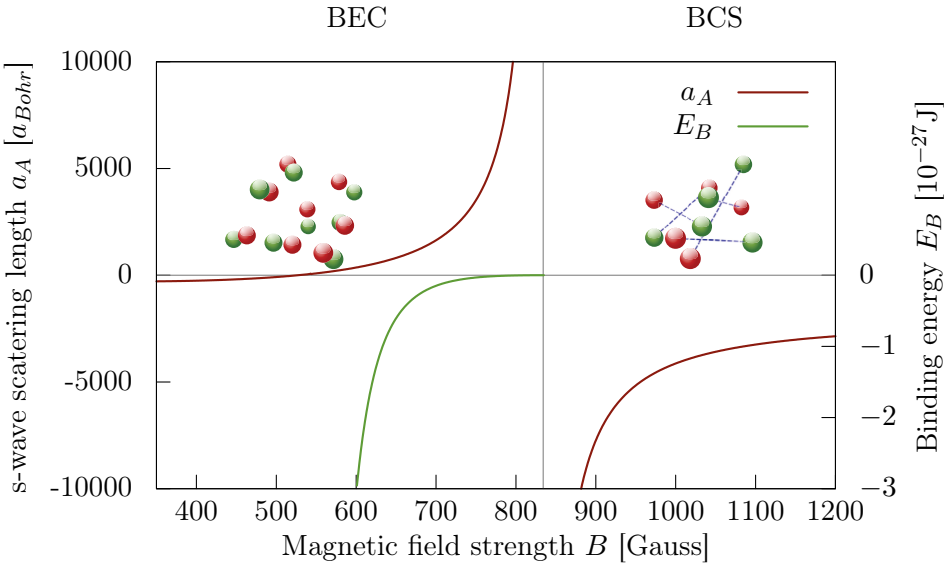

Figure 1.1: Illustration of the Feshbach resonance between the two lowest hyperfine states of ^{6}Li. The resonance is located at 834 Gauss and leads to a divergence of the s-wave scattering length a_A (red line). At high magnetic field strengths the scattering length is negative, corresponding to an attractive interaction between the atoms which are depicted as the green and red spheres. The atoms can form pairs similar to Cooper pairs and the gas is described by BCS theory. When the Feshbach resonance is approached from the right, the scattering length diverges and the system enters the so called unitary regime. Exactly on the resonance a molecular bound state becomes available (green line) and the atoms form bosonic dimers. Further on the left side of the resonance those dimers condense into a BEC which is described properly by Bogoliubov theory. The dimers themselves interact repulsively with a scattering length of $a_D = 0.6a_A$ [7].

distinguishable fermions. As a consequence, the s-wave scattering length diverges as depicted in Fig. 1.1. The resulting change of the interaction strength leads to the so called BEC-BCS crossover reviewed in [3, 4, 5, 6]. Far on the right side of the resonance, the scattering length is small and negative which corresponds to a weak attractive interaction between the fermions as described by BCS theory. On the left side, the constituents of the gas form bosonic dimers which Bose condense and feature a weak repulsive effective interaction. The regime in between is governed by strong interactions and a theoretical treatment is extremely challenging. No description in terms of quasi-particles has been found and perturbation theory is not applicable due to the lack of a small parameter. Consequently, neither BEC nor BCS approaches give accurate results. In this regime experiments such as the one described here can provide novel and valuable insights. As an example, we present data for the critical velocity and the speed of sound along the entire BEC-BCS crossover which serves as a benchmark for theories aiming towards a understanding of strongly correlated systems.

A system to investigate superfluid ^{6}Li

To perform the experimental studies on ultracold ^{6}Li a new apparatus was built, which shall be described briefly in the following. Fermionic ^{6}Li is initially cooled and trapped inside a magneto-optical trap that is loaded by a Zeeman slower. A sequence of dipole traps is employed to trap the atoms and to provide further cooling using forced evaporation. Finally, the cold gas cloud is transported to a separate vacuum cell which provides optimal optical access for experiments.

Around that vacuum cell two microscope objectives are placed in close proximity to the ultracold gas as shown in Fig. 1.2. The high resolution of the objectives has several advantages. Amongst them is the possibility to manipulate the gas locally on length scales down to approximately 700 nm, comparable to the Fermi wavelength of typical samples. Similarly, it is possible to image the gas in-situ. Therefore, not only the spatial density distribution but also to the density-density correlations in the sample are directly accessible. Especially for strongly interacting gases in-situ probing is superior to time-of-flight techniques as the cloud's expansion is not simply given by the momentum distribution but also by the interaction energy.

The high resolution of the microscopes can only be fully utilized if the thickness of the imaged atom cloud is less than the depth of field of the objectives. In our experiment the sample is therefore trapped in an optical dipole trap with a highly elliptical beam waist. By employing an additional optical lattice it is possible to compress the cloud even further such that the gas becomes effectively a two-dimensional system. In that situation the chemical potential and the temperature of the gas do not suffice to populate the first excited state of the potential in the strongly confined direction. With all atoms forced to reside in the ground state in that direction the kinematics of the gas are restricted to the remaining two dimensions. The altered dimensionality has major impact on the properties of the gas. For instance long-range order and therefore formation of true BECs is no longer possible in two-dimensional systems [8, 9]. It will be intriguing to see how the reduced dimensionality changes the many-body physics in the strongly correlated regime.

The work presented in this thesis was carried out in close collaboration with Kai Morgener, Jonas Siegl, Klaus Hueck and Niels Strohmaier.

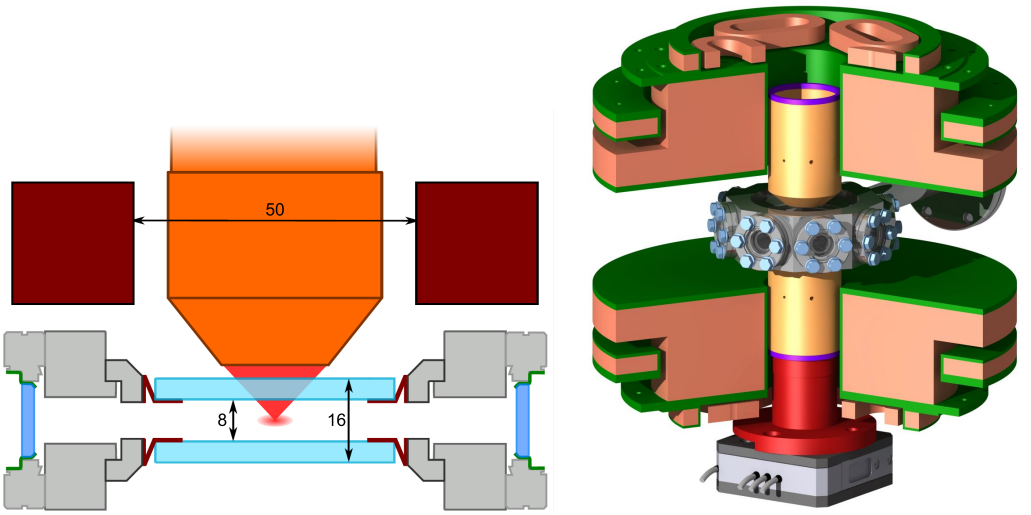

Figure 1.2: Sectional view and 3D rendering of the setup with which experiments on ultracold fermionic ^{6}Li are performed. The gas is confined by an optical dipole trap inside an ultra-high vacuum chamber. Multiple windows in the chamber provide optimal optical access to the atoms. Microscope objectives are placed above and below the chamber (only upper objective shown in the left panel) and allow highly resolved probing and manipulation of the degenerate gas. The Feshbach resonance is addressed via a magnetic field that is created by large coils placed around the vacuum chamber. The microscope objectives are placed inside the central bores of the coils. Dimensions are in mm. The graphic in the left panel is adopted from Ref. [10].

Outline of the thesis

This thesis is divided into the following chapters:

- **Chapter 2** describes how the apparatus produces a degenerate cloud of ^{6}Li with tunable interaction. It aims towards a reader who intends to learn how to operate the machine. It contains detailed descriptions of the individual components and a step by step walk-through of the experimental sequence.
- **Chapter 3** introduces the optical system capable of acquiring in-situ images of the cold atom clouds. The achieved resolution is on the order of typical intrinsic length scales of the ultracold gases. In addition, the chapter describes how the setup creates the flat samples required for such high resolution images.
- **Chapter 4** presents measurements of the speed of sound carried out with the apparatus. The measurement is performed at various different interaction strengths such that the whole BEC-BCS crossover is mapped out. The chapter includes a theoretical description of sound propagation which is in good agreement with the experimental data.
- **Chapter 5** presents measurements of the superfluid critical velocity across the BEC-BCS crossover. The measurements where performed on samples similar to those used in the speed of sound measurements. Therefore a direct comparison of the speed of sound and the critical velocity is possible. Further, the experimentally determined critical velocities are compared with simulation results.
- **Chapter 6** introduces our approach to create two-dimensional atom clouds. First, an overview of the theory of the physics in two dimensions is given focussing on ultracold gases featuring strong interactions. Next, the experimental realisation is presented as well as our method to verify the single-layer capability of the procedure. Further, the chapter explains advanced manipulation possibilities implemented in the setup.

2 An apparatus to create degenerate strongly interacting ^{6}Li

2.1 Setup I: From the oven to an ultracold gas

The art of cooling atom clouds to ever lower and lower temperatures is driven by the introduction of new technologies. One very notable development used by almost all cold atom machines nowadays is the magneto-optical trap (MOT). It was first implemented in 1987 [11] and paved the way for to the first observation of Bose-Einstein condensation in 1995 [12, 13]. Since that time many new techniques have become available which made it possible to turn the focus from just producing cold gases towards doing research on them or even use the clouds as environment for simulations of entirely different physical systems. Most new cold atom machines follow a fairly similar approach to produce cold gases. They start by either a Zeeman slower or a two-dimensional MOT to load a three-dimensional MOT where initial laser cooling is performed. This cooling process is ultimately limited by the recoil temperature. Further cooling is then accomplished via evaporation either in a magnetic trap or an optical dipole trap to reach the desired low temperatures. After the subsequent manipulation, to carry out the scientific experiment, an image is acquired, either by using an absorption or a fluorescence technique. In the following sections I describe the concept and the details of our approach to create an ultracold gas.

2.1.1 General considerations and cooling concept

The machine set up in the course of this thesis is very specialised in order to meet challenging requirements. These are to cool down a fermionic sample to degeneracy, confine it in a single two-dimensional trap to perform sophisticated manipulation of the sample and finally probe it with high spatial resolution. To enter the regime of strong interactions the interaction of the atoms with each other should be freely adjustable. This chapter is intended to describe how to produce a cold gas to work with and to realize the conditions suitable for further, more advanced manipulation and detection methods. The latter are described in chapters 3 and 6.

The choice of element

One of the first decisions we had to make during the early design phase of our machine concerned the selection of the chemical element. Alkali metals are the most commonly used elements in cold atom experiments as they have a rather simple level scheme. Furthermore, the necessary technology to cool those atoms is well developed since they have been used in cold gas experiments for many years. Amongst the alkali metals only two fermionic isotopes, ^{6}Li and ^{40}K, are radioactively stable. We chose ^{6}Li since it offers the following advantages: most importantly it has a very broad Feshbach resonance which can be used to conveniently tune the interaction across the BEC-BCS crossover with very low inelastic loss rates and hence long life times. Very low temperatures in units of the Fermi temperature can therefore be achieved which is crucial for observing quantum phenomena which otherwise can be easily obscured by thermal effects. The light mass of lithium compared to potassium can be advantageous as well. In experiments with optical lattices the tunnelling from one site to the next scales inversely with the mass of the used atoms. The low mass of ^{6}Li makes it easier to access quantum phase transitions. The lattice spacing in such experiments can then be chosen larger compared to ^{40}K which is advantageous for the development of an imaging system with single site resolution. The level scheme and especially the number of accessible hyperfine ground states of ^{40}K is richer as compared to ^{6}Li which makes potassium a predestined candidate for exploring spin physics [14]. There are also technological features which make it more convenient to work with lithium rather than with potassium. The natural abundance of ^{6}Li is $\sim 7\%$ whereas that of ^{40}K is only 0.012%. This has a large impact on the price and availability of the materials. Highly enriched ^{6}Li can be bought in rods several centimetres long whereas enriched potassium with a ^{40}K concentration of less than 15% is bought in sealed ampoules containing only a few milligrams of the material. Obviously this has an impact on how economical the setup has to deal with the initial resource of atoms. The existent experience within a certain research group plays a significant role in the selection process as well. In our case a large amount of expertise was available in the work with ^{6}Li expediting the development process of the machine significantly. Finally, we came to the decision to use ^{6}Li in our ultracold gas experiment.

Cooling strategy

The selection of the element is closely linked to the design of the cooling strategy. With the motive of saving time in setting up the machine we decided to implement a cooling procedure very similar to the lithium experiment set up in Zurich by Bruno Zimmemann, Torben Müller and Henning Moritz [15, 16, 17]. The knowledge obtained during the development of this machine could be utilized for our own apparatus. The part of the machine which deals with the ultracold gas after its initial production was then tailored to the needs of our scientific goals.

The experiment concept is based on cyclic operation which means that an ultracold sample of atoms is produced and a certain experiment is performed on it. Afterwards the

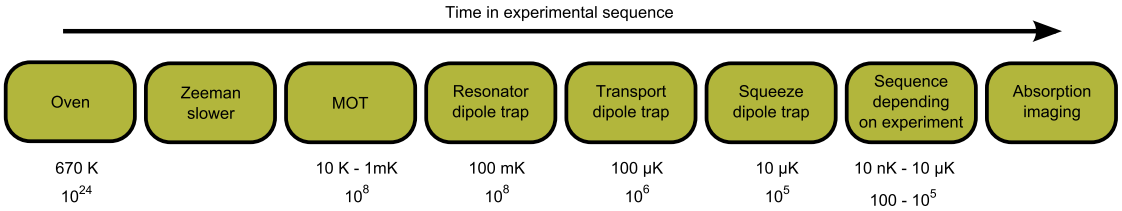

Figure 2.1: Overview over the cooling sequence. The numbers below the boxes indicate the approximate temperature scales which are relevant at the corresponding steps and the approximate number of particles. The atoms in the Zeeman slower are in a non thermalized state and no atoms are trapped in it so no atom number and no temperature can be given. The absorption imaging at the end of the cycle destroys the sample and the cycle is repeated.

sample is destroyed by the imaging procedure and a new sample is created. The cycle duration is ranging from 10 s to 15 s. Figure 2.1 gives an overview of the consecutive steps of one experimental cycle and Fig. 2.2 shows the basic layout of the setup.

The following list describes the basic experimental steps. For more details about the performance see chapter 2.2.

- The preparation starts with the oven where blocks of lithium are heated to obtain a sufficiently high vapour pressure. With the help of a set of apertures a fairly well collimated hot jet of atoms is created.

- This jet is slowed down by a Zeeman slower. It consists of a vacuum tube through which the atoms travel, a spatially varying magnetic field and a near resonant laser beam shone on the atoms opposite to their direction of travel. The laser beam slows down a certain velocity class of atoms in the atom jet due to the momentum of the absorbed photons (re-emission is spatially isotropic and has no net effect on the atoms). The magnetic field tunes the level scheme of the atoms due to the Zeeman effect to compensate for the velocity depended Doppler shift of the transition frequency. It is designed such that the laser beam is resonant on a fairly fast velocity class in the velocity distribution of the atom jet at the beginning of the vacuum tube and slower velocity classes at the end of the tube. This allows for a constant deceleration of the atoms along the Zeeman slower.

- The slowed atoms enter the main chamber and come nearly to a complete stop within the MOT where the atoms are cooled down initially. The MOT consists of a spatially varying magnetic field and six laser beams incident from all sides. The laser beams slows down the atoms, similar to the Zeeman slower by utilizing the Doppler effect, acting on all spatial directions. The combination of magnetic field and laser beams also creates a spatially dependent force that traps the atoms. Typical temperatures which can be reached with such a concept are on the order of the Doppler temperature caused by the finite linewidth of the transition frequency. Even lower temperatures, down to the recoil limit, can be in principle reached

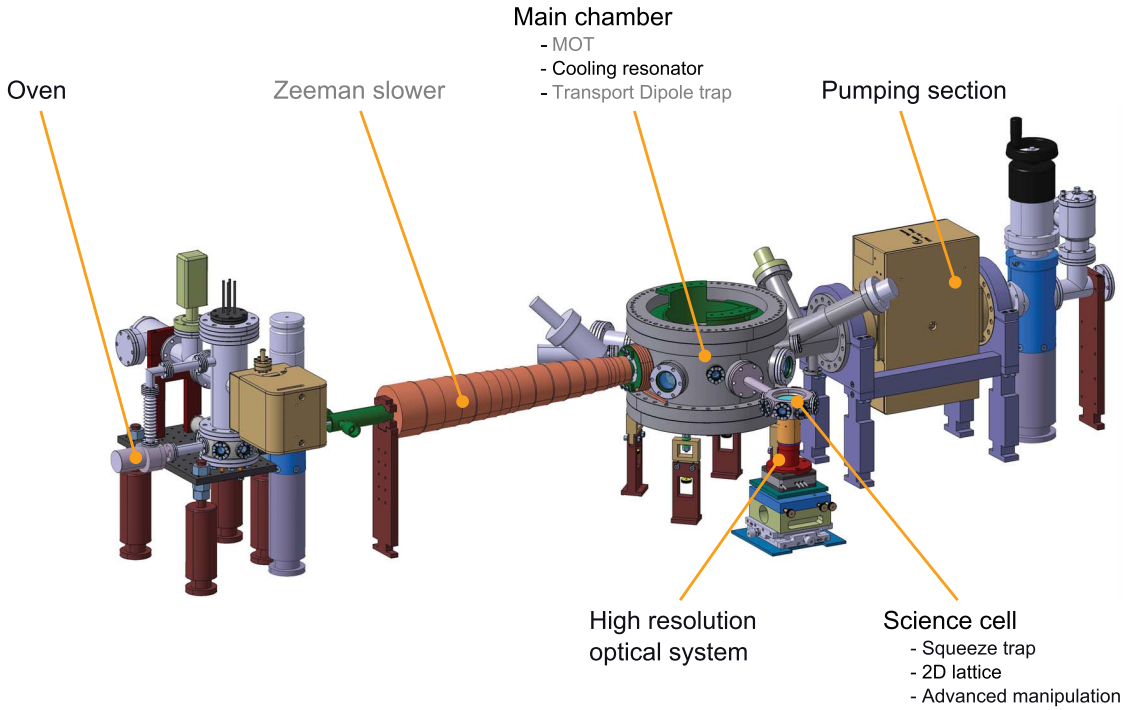

Figure 2.2: The basic layout of the apparatus. First, lithium is evaporated inside the oven. Second, the created atom beam is slowed down by a Zeeman slower and brought to a stop inside the main chamber. There, the atoms are trapped and cooled inside a MOT and transferred into a resonator enhanced optical dipole trap where further cooling is performed. Next, the atoms are transported into the science cell where the actual experiments on the atoms are performed. Finally a highly resolving optical system acquires an image of the atom cloud. Greyed out labels indicate that the description of the corresponding parts can be found in the doctoral thesis of my co-worker Kai Morgener [18].

by more sophisticated laser cooling methods which are not implemented at the moment.

- After having been cooled down in the MOT the atoms are transferred into a resonator enhanced dipole trap in which the cloud is cooled further by evaporation. This resonator is explained in detail in section 2.1.3. The main idea of the resonator enhancement is to combine a very deep dipole trap with a large capture volume to achieve high transfer ratios from the MOT into the dipole trap.

- To achieve a good optical access to the atoms we transport them out of the main chamber into a small science cell which is easily accessible with laser beams from multiple directions. Therefore, we transfer the atoms from the resonator enhanced dipole trap into a running wave dipole trap which features a movable trap centre. After completion of the transfer the trap centre is shifted from the main chamber into the science cell and further evaporative cooling is performed by lowering the laser light power.

- In the science cell the atoms are transferred into a third dipole trap. The equipotential surfaces of this trap are very oblate and the atomic cloud flattens out into a pancake shaped form. I will refer to this trap as the squeeze trap during the course of this thesis.

- The steps after the squeeze trap depend on the individual experiment to be performed with the cold atoms. They may include the confinement to two dimensions, manipulation with optical lattices or other custom procedures.

- After finishing the experimental steps the readout is performed via absorption imaging using the high resolution optics around the science cell. Fluorescence imaging might also be applied in the future.

The experiment is housed inside a modern laser laboratory equipped with two optical tables and with good air conditioning to ensure stable environmental conditions. The lab, and in fact the whole building, were designed to reduce vibrations from the outside to a minimum. Altogether, these external factors are very satisfactory and offer a good basis for building the machine.

In the next sections I will give a more detailed description of the parts in our setup that are concerned with creating an ultracold gas. I will start with the vacuum system and continue with the bow-tie resonator enhanced dipole trap. This concept was used for the first time in a cold gas machine and involves several interesting experimental aspects. Thereafter follow sections covering our transport dipole trap, the laser systems, the low resolution imaging system and the magnetic field system. I will cover certain components only very briefly since they will be treated with in more detail in Ref. [18], see also Fig. 2.2.

2.1.2 Vacuum design

Ultracold gases, like BECs or degenerate Fermi gases, are among the most delicate systems which are known to exist. One point is that almost every interaction with atoms from the environment increases the energy of the system such that the fragile state is destroyed or at least a fraction of the ultracold gas is removed. This is the reason why all ultracold atom experiments are performed within ultra-high vacuum environment. Typical pressures are on the order 1×10^{-11} mbar which corresponds to lifetimes on the order of 100 s. The mean free path of a gas particle under such conditions is several tens or hundreds of kilometres, much larger than the size of the vacuum chambers. The gas flow under these conditions is described by the molecular flow theory where the gas particles fly in a ballistic manner from one wall to the next without interacting with other particles. Such low pressures can only be achieved by using selected materials with low out-gassing rates for the vacuum chamber and any possible interiors. In our case we decided for stainless steel which has the additional advantage of being non-magnetic. This is particular important as we have to use strong magnetic fields to cool and manipulate the atomic clouds. The geometry of the chamber had to be designed such that it is possible to bring those magnetic field coils close to the position of the atoms without compromising the optical access. All the connections are made with the ConFlat (CF) flange system, which uses copper gaskets to achieve a tight seal with minimal leakage rates. The pumps used to maintain the low pressure, once it is established, are two ion pumps and two titanium sublimators. The main residual gas is expected to be molecular hydrogen as it is the most likely gas to diffuse through chamber walls or seals. Hydrogen also diffused into the steel of the chamber in large quantities during the time it was exposed to normal atmosphere after being machined. These embedded molecules will gas out over a long time after the chamber is evacuated. To artificially accelerate the outgassing a bake-out of the chamber was performed during the creation of the vacuum.

As shown in Fig. 2.2 the vacuum chamber can be divided into several sections. These are the oven chamber, the Zeeman slower, the main chamber, the science cell and the main pumping section. These and further parts of the vacuum system are described in the following sections.

Oven chamber

The sequence of our experiment starts by vaporizing solid lithium in an oven to create a beam of hot atoms which is then slowed down with a Zeeman slower. The other possible method to create such an atom beam would be to use a 2D MOT which is loaded via background pressure. Such a 2D MOT makes more economical use of the available lithium resource but is technologically far more demanding in terms of the required optics and laser system. As lithium is cheap we decided to use the oven/ Zeeman slower combination

At room temperature, the vapour pressure of lithium is far too low for our purposes but it increases approximately by a factor of 10 for each 60 K that the temperature is increased [19]. To achieve sufficient vapour pressure temperatures of around 400 °C are

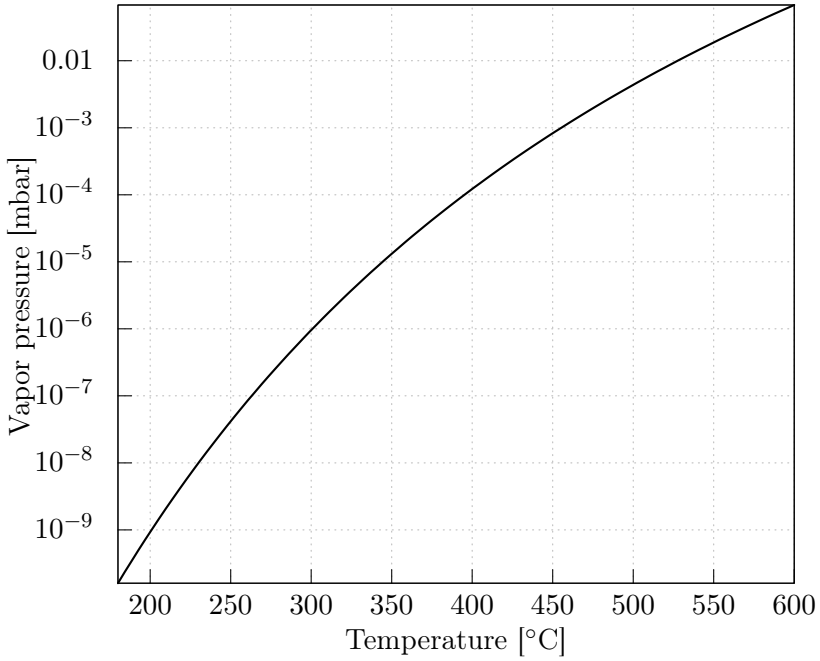

Figure 2.3: Vapour pressure curve for liquid lithium. We operate our oven at temperatures of around 400 °C where the pressure increase is approximately a factor of 10 for each 60 K in temperature increase. The formula to plot the curve can be found in Ref. [19]. Lithium melts at 180 °C and boils at 1340 °C.

needed. Figure 2.3 shows the vapour pressure as a function of the temperature. Lithium is liquid at our operational temperatures and chemically very reactive which imposes certain constraints on the design of the oven and the used materials.

The design of the oven chamber was largely adopted from the experiment in Zurich and details about the oven can be found in the thesis of Bruno Zimmermann [15]. The oven itself is a can-like stainless steel container containing several blocks of lithium. It has two ports for pumping to maintain the vacuum. On the axis where the atom jet leaves the oven, several apertures collimate the beam, see Fig. 2.4. One aperture is placed directly in front of the first flange after the oven to ensure that no liquid lithium can reach the gasket. This is crucial since liquid lithium can damage the copper seals. For this reason all the gaskets close to the oven are made from nickel rather than copper. A short distance behind the oven a shield is placed which can be turned via a rotation feed-through[1] from the outside to stop the flow of atoms when the experimental cycle does not demand it. The opposite side of this shield is angled and polished such that it is possible to use it as a mirror to inspect the inside of the oven or the Zeeman slower tube by looking through one of the viewports at the side of the oven chamber. It has to be

[1] Vacom, MagiDrive MD16

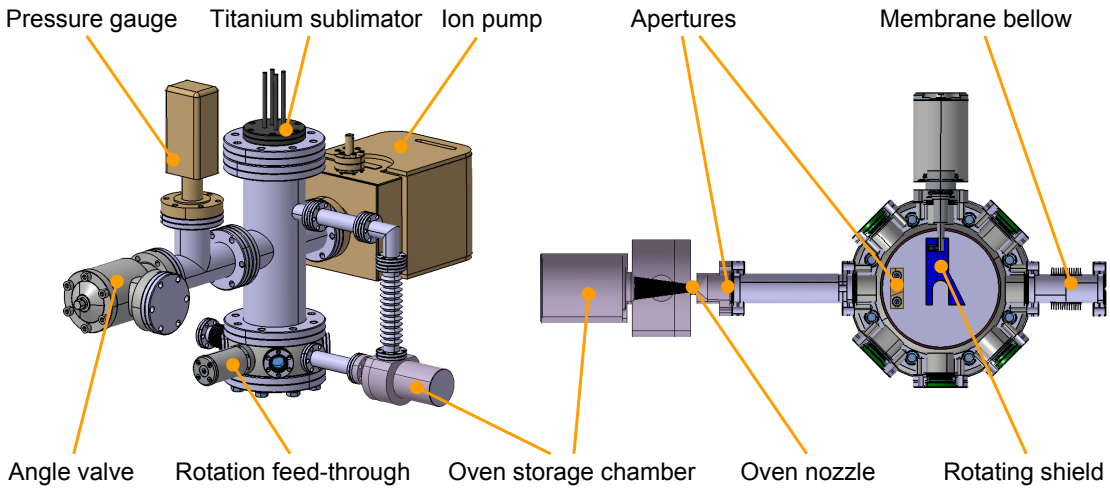

Figure 2.4: A CAD picture of the oven chamber. The right part of the figure shows a sectional view in which the atom beam is directed to the right side and leaves the oven chamber via the membrane bellow.

mentioned that a bearing of the rotational feed-trough was damaged after three years of operation and for the moment we do not shut off the atom beam during the experimental cycle. We could not observe any negative effect on the experiments performance caused by the continuous atom beam. As the design of the feed-through relies only on magnetic transfer of force the integrity of the vacuum is not affected.

To ensure a good vacuum a 25 l ion pump with titanium and tantalum electrodes[2] as well as a titanium sublimator[3] are placed inside the oven chamber. The pressure is measured with a hot cathode ionisation gauge[4]. In the case of a leak, an empty oven or an upgrade which would require to break the vacuum the oven chamber can be sealed off from the rest of the vacuum system with a CF16 gate valve[5]. For separate pumping of the oven chamber a CF40 angle valve[6] is installed. The connection between the oven chamber and the gate valve is realised with a CF16 membrane bellow. The valve is then connected directly to the differential pumping stage described below.

The oven is divided into two heating sections, the nozzle and the storage chamber. Both have their own heating element, temperature sensor and PID controller. Each controller operates a solid state relay in pulse-width modulation with a pulse length of 2 s. Those relays directly control the current through the heating elements. Normal operating temperatures are 400 °C for the storage chamber and 390 °C for the nozzle. When set on standby overnight, both temperatures are reduced to 250 °C to save lithium

[2] Gamma vacuum, 25S-DI-2V-SC-N-N
[3] Vacom, Titansublimationspumpe DN40CF
[4] Pfeiffer, PBR260
[5] VAT, Ganzmetall-Schieber DN16
[6] VAT, “Easy-Close” Ganzmetall-Eckventil DN40

Description	Value
Temperature sensors maximum temperature	1200 °C
Nozzle heating band maximum temperature	450 °C
Storage chamber heating band maximum temperature	900 °C
Insulation material maximum temperature	1000 °C
Pressure gauge range	5×10^{-10} mbar to 1000 mbar
Pressure nominal at standby temperature 250 °C	under range
Pressure nominal at 390 °C/ 400 °C	1.4×10^{-9} mbar
Temperature, maximum operation	450 °C/ 470 °C, causes visible deposit on shield after 10 min

Table 2.1: Typical values and limitations for the oven chamber.

while keeping it above its melting point of ∼180 °C. Special care has to be taken when filling or refilling the oven with fresh lithium. Lithium is typically sold in kerosene which has to be completely removed before placing it into the oven. When brought into contact with air the lithium quickly develops a lithium hydroxide layer. This layer is highly temperature stable (melting point ∼450 °C [20]) and can compromise the function of the oven. Other compounds which can develop as well are even more temperature stable. Examples are Lithium nitride (melting point 813 °C [21]) or Lithium oxide (melting point 1438 °C [22]). The surface layer can be easily cut off from the lithium with a knife. To prevent a new layer from growing the oven and the lithium were placed inside an argon bath for filling.

Differential pumping stage

With the oven operating at temperatures of approximately 400 °C, the gas release processes limiting the pressure of the vacuum are much more significant than at room temperature. The pressure in the oven chamber is therefore about a factor 100 higher than the desired pressure in the main chamber. To maintain this pressure difference a differential pumping stage is employed. It separates the two vacuum sections effectively from each other (up to a certain pressure ratio) and each section can be evacuated separately without affecting the pressure in the other section. However, it is still possible for the atom beam coming from the oven to enter the main chamber. The physical realisation of the differential pumping stage is a thin and long pipe. The longer and thinner the pipe the less likely it is for a gas particle to fly through and to affect the pressure on the other side. In our case we connect the oven chamber with the rest of the vacuum apparatus via a pipe with an inner diameter of 4 mm and a length of 280 mm. The physical quantity which determines how efficiently a gas particle can pass the tube is called conduction and its unit is m^3/s. The lower the conductance the fewer particles will pass the pipe. However, the diameter of the pipe must not be chosen too small as the atom beam created by the oven should still be able to fly through unaffected. For a thin pipe

the conductance is given by [23]

$$C(\mathrm{m}^3/\mathrm{s}) = \frac{\pi}{12}\nu\frac{d^3}{l}. \tag{2.1}$$

Here l is the length and d the diameter of the pipe, both given in metres. The arithmetic mean average velocity ν of the particles with mass m at a absolute temperature T is

$$\nu = \sqrt{\frac{8k_BT}{\pi m}}, \tag{2.2}$$

with the Boltzmann constant k_B. For normal ambient air and molecular hydrogen at 22 °C this yields

$$\begin{aligned} C_{Air}(\mathrm{m}^3/\mathrm{s}) &= 121\tfrac{d^3}{l} \\ C_{H_2}(\mathrm{m}^3/\mathrm{s}) &= 463\tfrac{d^3}{l}. \end{aligned} \tag{2.3}$$

These formulas show that the effectiveness of the differential pumping stage is limited by the lightest gas particle present in the residual gas. In our case this is molecular hydrogen. With our design values for the differential pumping stage we end up with a conductance of

$$C_{H_2} = 1.06 \times 10^{-4}\,\mathrm{m}^3/\mathrm{s}. \tag{2.4}$$

The oven chamber and the differential pumping stage act as an effective leak for the vacuum in the main chamber. The amount of gas that passes into the main chamber in a given time is called throughput Q

$$Q = C\left(p_{oven} - p_{main}\right). \tag{2.5}$$

The unit of Q is m^3 Pa/s. Assuming the main chamber has no leaks, the equilibrium pressure in the main chamber is given by

$$p_{main} = \frac{Q}{S} \tag{2.6}$$

with the pump rate S (unit m^3/s) characterizing all pumps in the main chamber. The maximum pressure ratio between the oven chamber and the main chamber, which can be maintained by the pumps in the main chamber, is then given by

$$\frac{p_{oven}}{p_{main}} \approx \frac{p_{oven} - p_{main}}{p_{main}} = \frac{S}{C} \tag{2.7}$$

since $p_{oven} \gg p_{main}$. For our apparatus the maximum pressure ratio for molecular hydrogen is thus

$$\frac{p_{oven}}{p_{main}} \approx 950. \tag{2.8}$$

The value given in Eq. 2.8 is valid under the assumption of no leaks in the main chamber and a pumping rate of $0.1\,\mathrm{m}^3/\mathrm{s}$ for molecular hydrogen at a temperature of 22 °C. If the above ratio is exceeded the pressure in the oven chamber will affect the pressure in the main chamber. Normally we operate at a pressure ratio of approximately 100. As a consequence, the differential pumping tube separates the main chamber from the oven chamber such that their corresponding pressures are independent from each other. This could be confirmed by monitoring the pressure gauges during heating up the oven. We conclude that the pressure in the main chamber is not limited by the effective leak caused by the differential pumping stage and the oven chamber but rather by other sources of gas entry.

Zeeman slower

From a vacuum point of view the Zeeman slower is just a stainless steel tube, roughly 700 mm long. Its first part is the differential pumping pipe described in the previous section. It is important to place the differential pumping stage close to the oven as the atom beam diverges with travelling distance. After the differential pumping section the inner tube diameter increases to 22 mm. More details about the Zeeman slower can be found in the thesis of my co-worker Kai Morgener [18].

Main chamber

The main chamber was designed in the framework of the diploma thesis of our former student Florian Wittkötter and many details about it can be found in his thesis [24]. A picture of the chamber is shown in Fig. 2.5. It plays a particularly important role in the cooling sequence of the atoms as several steps are performed in it. The atoms arrive from the Zeeman slower and are captured and cooled by the MOT. After this initial cooling, the atoms are transferred into a resonator enhanced dipole trap in which further cooling is performed. The main chamber contains this resonator as it needs to be placed completely inside the vacuum. To continue the sequence, the atoms are transferred into the transport dipole trap and transported out of the main chamber into the science cell. This imposes a couple of constraints on the design of the main chamber which were only possible to meet with a custom made chamber rather than with off the shelf components. The main features are:

- The chamber has following ports:
  - a port to accept the Zeeman slower (CF25)
  - a port to accept the main pumping section (CF100)
  - 6 viewports for the MOT (4 x CF40; 2x CF100)
  - 2 viewports for the cooling resonator, 1 for incident light (CF40), 1 for monitoring (CF16)
  - an electrical feed-trough to control the piezo of the cooling resonator

  - a port to accept the science cell (CF40)
  - a viewport for the transport dipole trap (CF40)
  - a port for a potassium 2D MOT as part of a potential future upgrade (CF16)
  - a viewport opposite to the potential 2D MOT (CF16)
  - multiple pairs of diametrically placed viewports for imaging (CF16)

- It houses the cooling resonator, see section 2.1.3.
- It accepts the magnetic field coils for the Feshbach field and the MOT field.

After the MOT phase our cooling strategy involves a transport of the cloud for ∼2 cm performed by the cooling resonator before the atoms are transferred into the transport dipole trap. As a consequence the ports for the MOT and the Zeeman slower have to be aligned on a different point than the ports for the science cell and the transport dipole trap. This and the sheer density of ports makes it impossible to use a ready-made, commercially available cell. We decided to use the same magnetic field coils to create the Feshbach field for evaporation and the MOT-gradient field. As the two corresponding spatial locations are at different positions, we centred the coils around the evaporation spot and use additional coils to the side of the main chamber to shift the magnetic centre of the MOT field to its designated position. To reduce thermalisation effects of the magnetic field coils on the vacuum chamber, the coils are mounted on a separate frame which has no mechanical contact to the vacuum chamber. The aforementioned port for a potassium 2D MOT contains a gate valve[7] but there are no plans at the moment to realize this possibility. The material we chose for the main chamber is the steel 1.4301 (V2A) which is well machinable, non magnetic and well suited for ultra-high vacuum applications.

Main pumping section

To maintain the vacuum, after it is established in the first place, it is necessary to continue pumping due to gas release from the walls, potential small leaks and possibly even diffusion of hydrogen through the chamber walls and seals. In our setup this pumping is provided by the main pumping section which is attached to the main chamber opposite to the Zeeman slower as shown in Fig. 2.2. It contains a $100\,\mathrm{l\,s^{-1}}$ ion getter pump with titanium and tantalum electrodes[8] connected to the main chamber with a large diameter tube ensuring a good conductance. The pump itself provides a free optical path for a laser beam entering from the other side of the pump via a sapphire viewport required to operate the Zeeman slower. Sapphire was chosen since it has a better resistance against the chemical aggressive lithium than quartz glass. The tube connecting the ion pump with the main chamber contains a titanium sublimator[9] which can coat a large area of

[7] MDC Vacuum, Similar to MIV-150-T / 316000 with CF-16 on the right side
[8] Gamma vacuum, 100L-DI-6D-SC-N-N
[9] Varian, Mini Ti-Ball

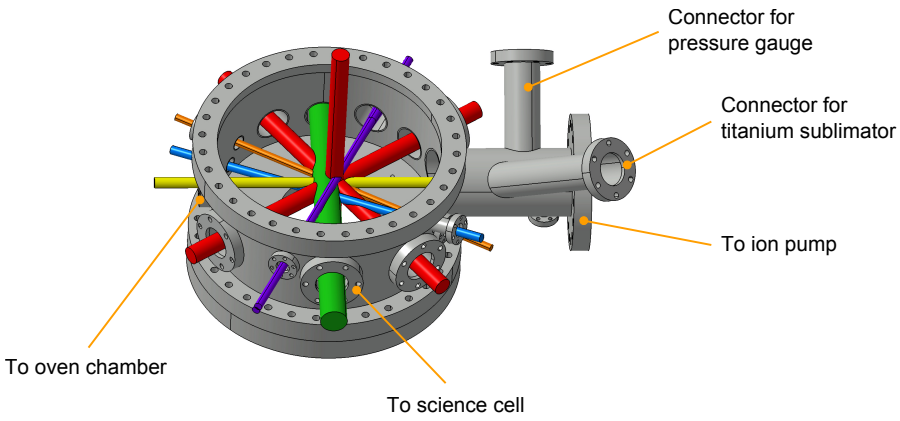

Figure 2.5: A CAD picture of the main chamber with the top window not shown. The indicated laser beams are determining the positioning of the ports. They are colour coded as follows: yellow - Zeeman slower, red - MOT, purple - cooling resonator, green - transport dipole trap, blue - imaging, orange - possibility for 2D MOT upgrade.

Description	Value
Pressure gauge maximum operating pressure at 10 mA emission current	1.4×10^{-4} mbar
Titanium sublimator recommended maximum current	50 A
Pumping section nominal pressure	1.8×10^{-11} mbar

Table 2.2: Typical values and limitations for the pumping section.

the tube as well as a part of the main chamber with titanium. Both, the ion pump and the chemical pumping with the titanium coating work without any moving parts and thus without causing vibrations. This ensures minimal impact on the performance of the rest of the apparatus. The large diameter connection tube houses also an ionization pressure gauge[10]. A CF40 angle valve[11] is located on the far side of the pumping station, close to the Zeeman slower viewport which was used for initial evacuation of the whole vacuum chamber. In case the Zeeman slower viewport becomes opaque by lithium deposit on its inner surfaces a replacement without breaking the vacuum in the main chamber is possible by closing a CF40 gate valve[12].

[10] Varian, UHV-24p Nude Bayard-Alpert gauge; According to the data sheet, the indicated pressure for an actual pressure of 1×10^{-11} mbar is about a factor 2 too high.
[11] VAT, "Easy-Close" Ganzmetall-Eckventil DN40
[12] VAT, Ganzmetall-Schieber DN40

The science cell

The science cell can be regarded as the main component of the experiment's vacuum system even if its size and appearance might not be very impressive. In it all the actual "physics" experiments are performed whereas the rest of the vacuum setup is only required to provide the samples. There are several design requirements to this cell in our experiment. Most importantly we want to perform high resolution imaging on the atomic samples. This requires the optical quality of the windows of the science cell to be as good as possible. The distance between the atom cloud and the necessary microscope objective has to be as small as possible (see chapter 3 for more details). This inevitably leads to a very flat design as we placed two such objectives on both sides of the cell. Further, we need to maximise the optical access to install optics around the cell needed for manipulating or probing of the atomic clouds. Finally, the cell has to provide ultra-high vacuum environment in order to obtain long lifetimes of the ultracold gases. As we use strong magnetic fields to manipulate the cloud which are potentially quickly changing in time, the cell has to be non magnetic and ideally does not support eddy currents.

To make everything as perfect as possible we opted for a glass cell to avoid eddy currents completely. To make a long story short: this attempt failed and we now use a more conventional metal cell. Basically the usage of ultra-high vacuum glass cells is an established technology and one can order custom made cells. However, anti-reflection coated glass cells remain difficult to manufacture. The procedure of joining the different parts of a glass cell by fusing or bonding requires high temperatures which destroys any coating previously deposited on the components. Hence, a glass cell can only be coated after assembly which is simple from the outside but almost impossible from the inside. When designing the machine we had the idea to realize an optical resonator around the glass cell. To achieve a reasonable performance of such a resonator the cell must be anti-reflection coated well to reduce losses. We found a company[13] which claimed to be able to produce glass cell coated inside and outside with UHV capability. Unfortunately, the result did not match our specifications. After spending valuable time in design work, ordering three cells from that company and waiting for nearly a year we received three cells with inadequate properties. The broadband-coated windows showed a reflectivity of around 1.5 % per surface at the design wavelengths, see Tab. 2.3 for details. A single pass of a light beam through such a cell passes four of those surfaces and a resonator around the cell would have a very low finesse. After realizing that we switched back to a more conservative design and ordered a custom made metal cell.

This metal cell[14] is made from the non-magnetic steel 316LN which is well suited for vacuum applications. Its shape is a flat octagon with seven CF16 viewports on the sides as shown in Fig. 2.6. Those ports are angled by 2° to avoid undesired back reflections of laser beams which pass the cell diametrical. The eighth port is used to connect the cell via a tube to the main chamber. The top and bottom windows are 4.00 ± 0.05 mm

[13] Precision Glassblowing, Centennial, USA
[14] UKAEA CCFE Special Techniques, Abingdon, Oxfordshire, United Kingdom

Wavelength	Reflectivity of the large windows	Reflectivity of the small windows
532 nm	2.6 %	2.8 %
671 nm	1.4 %	1.1 %
1064 nm	1.1 %	1.4 %

Table 2.3: Performance of the anti-reflection coating of the glass cell. The values correspond to the reflected light intensity compared to the intensity of the incident beam. The light inside the resonator we planned to realize around the glass cell would have to pass four surfaces which would lead to intensity losses of 4.4 % to 11.2 % per round trip.

thick and separated by only 8 mm. The surface quality of the main windows is specified to be better than $\lambda/8$ and anti-reflection coated for 532 nm, 590 nm, 670 nm, 780 nm and 1064 nm for incident angles between 0° and 30°. To reduce the pressure in the science cell, a non-evaporable getter[15] was placed inside the connection tube. The getter material was activated during the bake-out. Compared to a glass cell the coating of the windows is much easier to realize as the assembly of the cell does not require high temperatures. However, there are also certain drawbacks of the metal cell design compared to the glass cell:

- Magnetic influence: The employed steel is not completely non-magnetic which might cause undesired vibrations when magnetic fields are switched rapidly. The material is also conductive which limits the switching times of magnetic fields due to eddy currents.

- Optical access: Due to spatial restrictions the optical access is not as good as that of the original glass cell design. With the glass cell there was the possibility for three additional in plane beams crossing under a 120° angle.

- Surface quality of the two main windows: The main windows of the metal cell design are connected to a metal frame prior to coating. Afterwards this metal frame is electron beam welded to the main body of the cell. This welding might induce stress in the windows which potentially could cause bending affecting the microscope resolution. A spherical curvature of a window can be mostly compensated by adjusting the focal position of the microscope objective whereas a cylindrical curvature cannot be compensated and imposes direct influence on the imaging resolution. To assess this potential issue, the curvature of the main windows of the assembled cell was measured with a interferometric technique. Indeed, one of the windows showed a curvature which was twice has high in one direction as in the other. This ratio might change under the influence of the vacuum but it seems very unlikely that the cylindrical component will disappear. The other window only showed a spherical curvature. We mounted the cell such that the window with

[15] SAES Getters, ST122/NCF/50-150/130X180/D

only spherical distortion faces downwards as the imaging microscope is positioned on this side.

- After the delivery of the cell, an angle between the top and bottom main windows of the cell was discovered. This angle is 0.5° and has to be taken into account when aligning the high resolution imaging system as elaborated in chapter 3.
- Vacuum connection: The tube connecting the cell with the main chamber is 126 mm long and has a diameter of 16 mm. This results in a conductance of $4 \times 10^{-3}\,\mathrm{m}^3/\mathrm{s}$. Assuming a pumping speed of $0.1\,\mathrm{m}^3/\mathrm{s}$ in the main chamber this gives an effective pumping speed at the science cell of $3.8 \times 10^{-3}\,\mathrm{m}^3/\mathrm{s}$. This value is rather low and might cause a relatively poor vacuum in the science cell which potentially limits the achievable lifetimes for the atom clouds in the experiments. Due to the lack of a possibility to measure the pressure in the science cell directly, it is not certain if this poses an issue. Nevertheless, a new connecting tube was designed and manufactured which maximizes the cross section as much as possible. It is not integrated into the apparatus yet, but if the vacuum of the machine is ever opened one should think of the possibility to replace the tube.
- Vacuum gas emission: A further possible issue limiting the base pressure is hydrogen outgassing from the metal. It is expected that glass has a lower emission rate than metal.
- Size: Due to the usage of standard CF16 viewports on the side, the height of the cell is increased to the size of a CF16 connector. The diameter of the cell is increased as well, since those viewports are large compared to glass cell windows and require screws increasing the size even further. This overall increase of the size had to be taken into account for all magnetic field coils and optical elements placed around the cell.

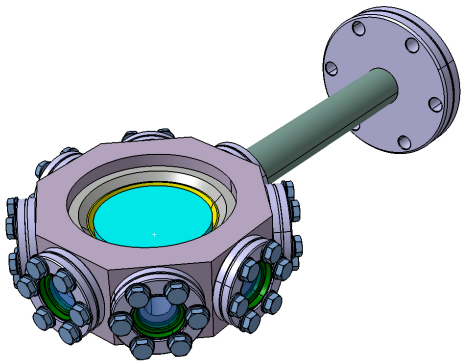

Figure 2.6: A CAD picture of the science cell. The drawing shows that the main windows are sunk into the cell to allow for a positioning of the microscope objectives close to the atoms.

Creating an ultra-high vacuum

After assembly of the vacuum system the next step is the evacuation. The apparatus provides the possibility to separate the oven chamber from the rest of the vacuum setup with a gate valve. The two sections were evacuated separately and connected after the vacuum was established.

The basic approach to achieve the ultra-high vacuum is to first pump the chamber and reduce the pressure to a value where it is limited by gas release from the walls and outgasing of potential contaminations inside the chamber. This pressure is on the order of 10^{-7} mbar. A further pressure reduction can then be achieved by heating the whole setup which increases this gas release rate significantly. After a few days of baking the temperature can be lowered again after the majority of the embedded gas has been pumped away. After this baking of the chamber, pressures on the order of 10^{-9} mbar can be reached. Further reduction is possible by using ion getter pumps and in particular titanium sublimation pumps. The latter coat the inside of the vacuum chamber with titanium. Titanium is chemically quite reactive and forms chemical compounds with many of the residual gas particles binding them to the chamber surface. Pressures of approximately 10^{-11} mbar can be achieved with this method. Even lower pressures can be reached by using cryogenic pumps. However, there is no necessity for such low pressures in the apparatus presented in this thesis and the additional effort would not be justified.

The pumps used for initial evacuation are a turbo molecular pump (TMP)[16] backed by an oil-free scroll pump[17]. The procedure is listed below in more detail:

- We evacuated only the main chamber with all ports closed by blind flanges with the TMP and baked it at 300 °C for 5 days. The final pressure, measured with a cold cathode gauge, was 3×10^{-9} mbar. This step served as a test for leak tightness of the custom produced chamber.

- We evacuated the complete system except the oven chamber and baked it at 190 °C for 5 days. The connecting tube between the main chamber and the science cell was heated to 450 °C to activate the non-evaporable getter inside. To keep the temperature from exceeding the limits of the window coatings of the science cell we attached a heat sink to the connection tube close to the science cell. Due to the high temperatures we did not use aluminium foil for insulation but a special insulation material which can withstand higher temperatures. During the bake-out we operated the titanium sublimator at a current of 30 A to release contamination therein. The pressure final obtained, was 1.2×10^{-9} mbar measured with the hot cathode gauge after the bake-out was completed.

- Next, we switched on the ion pump. After 5 days the final pressure dropped to 5×10^{-10} mbar measured with the hot cathode gauge. The start-up process of this

[16] Pfeiffer, HiPace 80 Turbo-Drag-Pump
[17] Varian, SH110

particular ion pump is known to fail occasionally. It helps to increase the voltage in small steps starting from 3000 V to the final 7000 V.

- Finally, the titanium was sublimated with the ion pump switched off. This has to be done at least twice as the first sublimation emits a large amount of undesired gas embedded in the titanium ball and the pressure might even increase. We operated the sublimator at 53 A (8.7 V) for 10 min which is well above the recommended maximum value of 50 A. The colour of the source should be white during sublimation. Higher currents should not be used as we destroyed one sublimator when operating it at 56 A. After 50 s the electrical connection was lost and we had to break the vacuum for replacement. Leaks can also result from temperature induced stress in the main chamber walls during titanium sublimation. We had to replace one of the large CF250 gaskets on the lower port of the main chamber after a sublimation.

- We removed the TMP. A couple of days after the titanium sublimation the pressure in the main chamber reduced to 4.5×10^{-11} mbar and has continued to decrease since then. Now, approximately 3 years later, we reached an indicated pressure of 1.7×10^{-11} mbar if the apparatus is cold. If it is running and thermalized, the pressure rises to approximately 2.1×10^{-11} mbar.

The oven chamber was evacuated using a similar procedure:

- We assembled the oven chamber and filled the oven with lithium.

- We baked the oven chamber at 190 °C. The storage chamber of the oven itself was heated to 600 °C and the nozzle to 450 °C using the heating elements later used for normal operation. The bake-out duration was 4 days. At high temperatures the oven emits large quantities of lithium and special care was taken that the polished surface of the rotating shield was facing away from the oven.

- After cooling down (oven kept at 300 °C) and activating the ion pump the pressure in the oven chamber dropped below the lower measurement limit of the installed cold cathode gauge of 5×10^{-10} mbar.

- We started the titanium sublimation with the ion pump switched off. The installed titanium sublimator has three filaments which can be operated separately. All three filaments were heated at a current of 40 A for 20 s followed by 50 A for 15 s for cleaning. The final titanium sublimation was then performed with filament number 1 at a current of 42 A until the pressure stabilized followed by 49 A at 5.21 V for a duration of 2 min.

- We switched on the ion pump and removed the TMP. With the oven on a standby temperature of 250 °C the indicated pressure was under range and with the oven operating at 390 °C/ 400 °C (nozzle/ storage chamber) the indicated pressure rose to 1.4×10^{-9} mbar.

After both sections were successfully evacuated, the CF16 gate valve connecting them was opened. There was no indication that the pressure in the one section influenced the pressure in the other section. This indicates that the differential pumping stage is working as intended.

2.1.3 Cooling inside a resonator

The cooling scheme of most ultracold atom experiments starts with a MOT and continues with an evaporation in either a magnetic or an optical dipole trap. Both approaches have their advantages and disadvantages. The magnetic trap has a very large capture volume, larger than the MOT size, and thus can capture a large fraction of the atoms which are previously trapped and laser cooled by the MOT. However, the trap frequencies are relatively low, which leads to small atom densities. This causes the evaporation to be less efficient, as thermalisation takes a long time. Furthermore, as the magnetic field is used for trapping it is impossible to create high offset fields to address a magnetic Feshbach resonance at the same time.

An optical trap does not depend on any magnetic fields and a Feshbach resonance can be used without affecting the trap. The trap frequencies which can be realized with optical traps are high compared to magnetic traps which improves evaporative cooling. Moreover, the trapping mechanism works independently of the hyperfine state of the trapped atoms and even largely independent from the chemical element used as long as the light is red-detuned with respect to the atomic transition. On the downside, the trapping volume of a typical optical dipole trap is small compared to the size of a MOT which means that a significant portion of the atoms in the MOT cannot be transferred into the trap. Besides, building far detuned optical dipole traps which are deep compared to the temperature of a MOT requires high laser powers which is cost intensive and potentially dangerous to work with.

To combine the benefits of both methods we implemented an optical cooling concept using a resonator inside the vacuum which was originally conceived by Tilman Esslinger [25, 26]. The basic working principle is shown in Fig. 2.7. Its function relies on the fact that a ring resonator supports both running wave and standing wave operation. If only one beam is coupled into the resonator, a running wave mode is excited. If two beams are coupled in, travelling in opposite directions, a standing wave pattern emerges which is similar to the pattern in a two-mirror linear resonator.

As shown in the Fig. 2.7, the resonator is designed such that its eigenmode has a beam waist a certain distance away from the MOT position. Due to beam divergence the mode profile has a relatively large cross section where it passes through the location of the MOT. This means that if the atoms are transferred from the MOT into the cooling resonator the spatial overlap is good, and high transfer ratios can be achieved. As a standing wave forms the dipole trap at that point, the atoms are not accelerated towards the beam waist. When detuning one of the incident beam frequencies with respect to the other, the standing wave pattern starts to shift and can be used to transport, the atoms

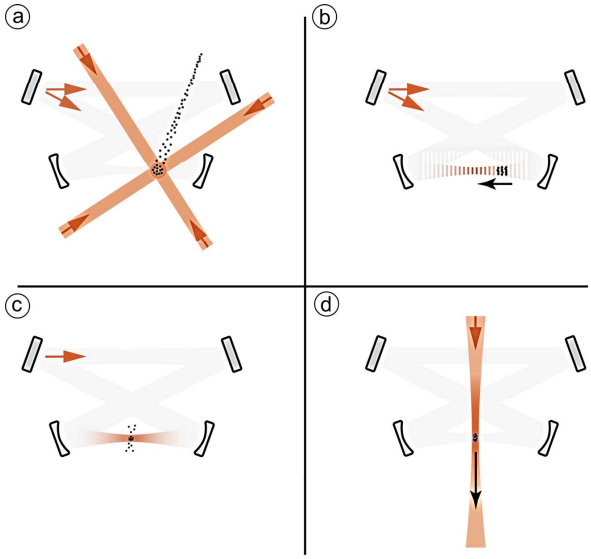

Figure 2.7: Working principle of the cooling resonator.(a) After the Zeeman slower and MOT phase the atoms are loaded into the standing wave pattern inside the resonator. (b) A frequency detuning between the two incident trapping beams causes the standing wave pattern to shift and transports the atom into the beam waist. (c) One beam is switched off and evaporative cooling is performed in the remaining running wave dipole trap by lowering the beam power. (d) Afterwards the atoms are transferred into the transport dipole trap which moves the cloud into the science cell. The graphic is adopted from Ref. [24].

to the beam waist. During the transport the cloud is adiabatically compressed which increases the thermalisation rate for later evaporation. When the atoms reach their final position, one of the resonator beams can be switched off as longitudinal confinement is now provided by the beam divergence. At this stage, evaporative cooling can be performed efficiently and the atoms are ready to be used for further steps. The frequency detuning between the two incident beams must not be larger then the linewidth of the resonator, as otherwise one of the beams will no longer be coupled into the resonator. The expression for the shift speed v is

$$v = \lambda \cdot \delta\nu \tag{2.9}$$

with the laser frequency difference $\delta\nu$ and the laser wavelength λ.

A further advantage of using a resonator is that the light intensity inside the resonator is enhanced compared to the incident beams. This effect permits the use of far detuned wavelengths and moderate laser powers to create a very deep dipole trap.

Realisation

The realisation and testing of the cooling resonator was one of the topics in the diploma thesis of our former student Florian Witkötter and details about the design can be found in his thesis [24]. One design goal was to realize a resonator with a high finesse to have sufficient enhancement of the light power. This can only be realized when placing the resonator inside the vacuum chamber to avoid losses at the viewports. Therefore, only vacuum compatible materials can be used and any potential virtual leaks have to be avoided. Once adjusted, the setup also has to be stable enough to operate without readjustment for several years. The result of the design work can be seen in Fig. 2.8. The resonator is mounted on a baseplate which enabled us to align it in a test setup outside the vacuum and afterwards to integrate the fully adjusted assembly into the main vacuum chamber as a whole. The design is a four mirror bow-tie configuration with two curved mirrors, creating the desired beam waist of the eigenmode. The bow-tie configuration leads to an almost perpendicular incident angle of the beams on the curved mirrors which causes the resulting beam waist to be almost circular. One of the mirrors is mounted on a piezo actuated mirror holder which was intended to be used for frequency stabilisation of the resonator on the laser light frequency. We do not use this option at the moment as it is more convenient to stabilize the laser on the resonator than the other way around. The most important parameters of the cooling resonator are collected in Tab. 2.4 on page 38.

The optical layout to couple light into the resonator is shown in Fig. 2.9. The two beams which excite eigenmodes in the two different propagation directions of the resonator are guided towards the resonator through one of the CF40 viewports of the main chamber. On the opposite side of the chamber the power of the light transmitted by the resonator is measured. A fraction of the reflected light of one of the beams (the primary beam) is separated with a beam sampler from the incident light of the secondary

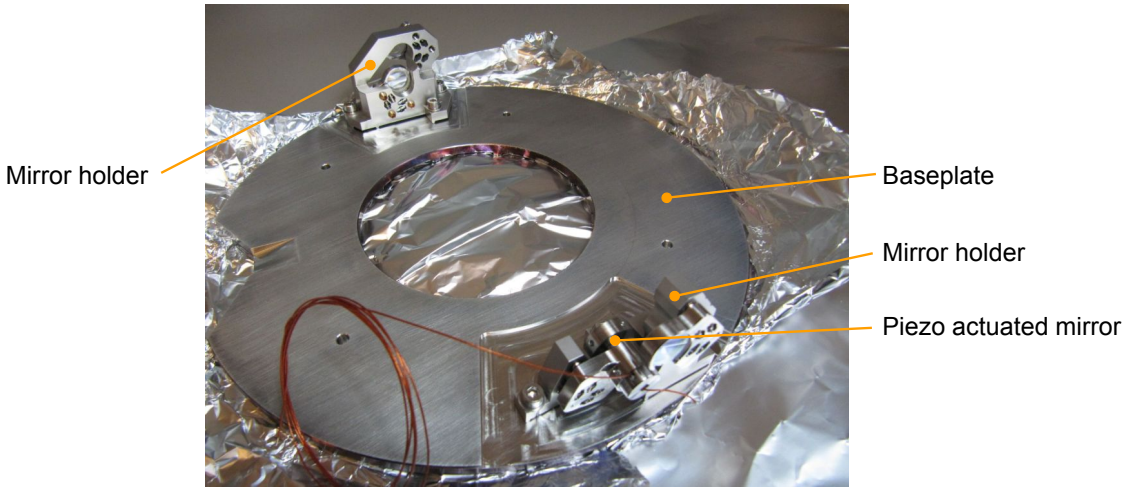

Figure 2.8: A photograph of the cooling resonator assembly before integration into the vacuum chamber. Each mirror holder supports two mirrors. The capton insulated wire visible in the picture was intended to supply the piezo on which one of the four mirrors is mounted. This option to stabilize the resonator length was not pursued and the wire was removed.

beam travelling on exactly the same axis (although in opposite direction). This light is used for the Pound-Drever-Hall (PDH) frequency stabilisation (see below). As the four mirrors of the bow-tie resonator define a plane in space it brakes rotational symmetry along the axis of the incident light. This leads to a polarisation dependence of the coupling efficiency, which would not occur for a simple, rotationally symmetric, linear resonator. Therefore, we placed quarter-waveplates and half-waveplates in the paths of the two incident beams and carefully adjusted the polarisation to maximize the coupling efficiency. The coupling efficiency also depends on the quality of the transversal mode matching of the incident beams with the eigenmodes of the resonator. As the two curved mirrors of the resonator are hit by light under a certain angle the effective radius of curvature is different for the two transversal directions. As a result, the created beam waist is elliptical and not circular. This results in differing divergence angles in the two transverse directions and the incident light beams should have an elliptical beam profile. We use a combination of spherical lenses and anamorphic prism pairs to shape the incident beams for optimal mode matching.

The above mentioned cooling scheme requires a high level of control over the light field inside the resonator. An overview is shown in Fig. 2.10. As the resonator accepts only light with certain frequencies it is necessary to stabilize the laser output frequency onto the resonator. Furthermore, a mechanism is required to introduce a controlled frequency difference between the two incident beams to perform the transport of the atoms inside the resonator. At the same time, the two beam frequencies have to be phase stable with respect to each other to prevent any oscillations of the standing wave pattern. To perform evaporative cooling the beam powers have to be stabilized and controllable. This

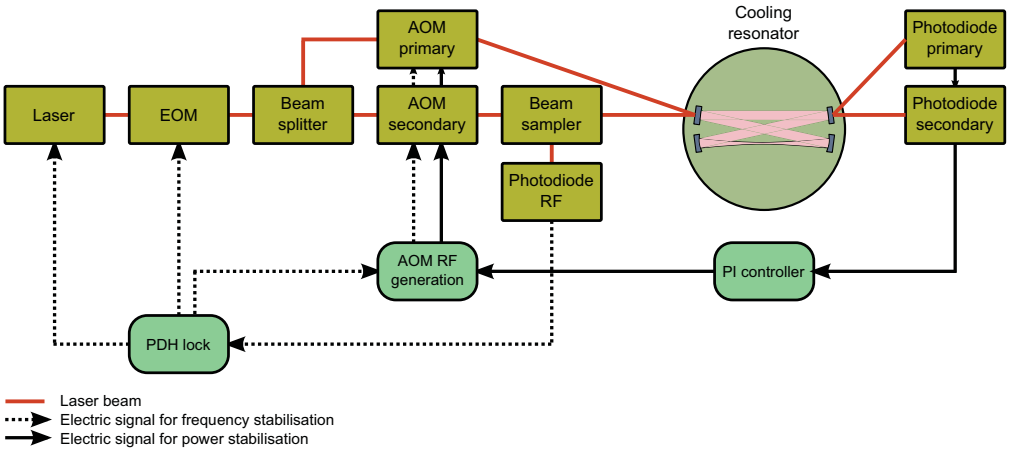

Figure 2.9: The beam delivery concept for the cooling resonator. The electro-optical modulator (EOM) creates frequency sidebands on the laser beam which is necessary for the Pound Drever Hall (PDH) stabilisation of the laser output to the length of the resonator. Two AOMs allow for separate control of the power and the frequency of the two beams coupled into the resonator. A beam sampler in the incident path of the secondary beam picks up a small percentage of the reflected light of the primary beam (which travels along the same path as the incident secondary beam) and guides it to an RF photodiode for the PDH lock. The feedback elements are the AOM frequencies and the laser itself. Two photodiodes, one for the primary and the other for the secondary beam, behind the resonator monitor the power which is coupled into the resonator. Their output is used for power stabilisation using the AOMs as control element.

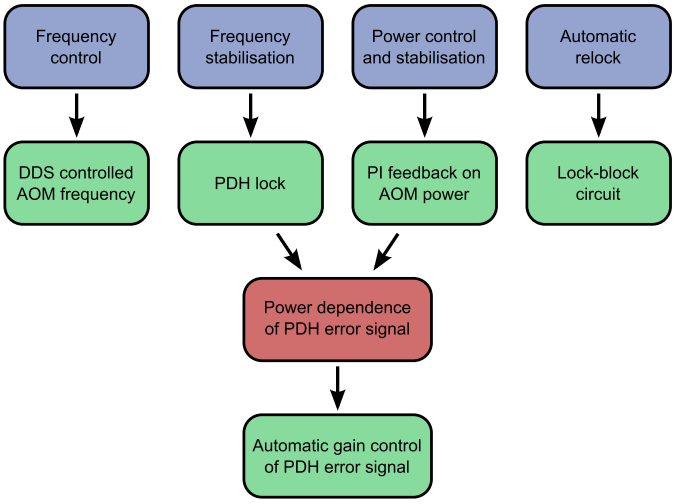

Figure 2.10: Overview of the different control systems of the cooling resonator. The blue boxes are the requirements and the green boxes describe the corresponding system to meet those requirements. As the beam power is varied during the experimental sequence and the error signal of the frequency stabilisation depends on that power we implemented an additional automatic gain control of this error signal. This guaranties a good performance of the frequency stabilisation over a wide range of input power.

has implications on the frequency stabilisation as it has to work independently from the beam power incident on the resonator. A further requirement is automatic relocking. In each experimental cycle the resonator is switched off once and the frequency stabilisation has to perform an automatic relock in each cycle. The relock has to work reliably such that it always captures the correct transversal mode of the resonator. The components which provide all this control are described in the following sections.

Power control and stabilisation

For a stable operation and especially for evaporative cooling we accurately control the beam powers inside the resonator. The regulating elements are the two AOMs placed in the beam paths of the two incident beams. We positioned two low noise photodiodes behind the resonator, outside the vacuum chamber. They monitor the light that is transmitted by the resonator as soon as an eigenmode is excited. These measured powers are compared with set values given by the computer-based experiment control and handed to two PI controllers. Their output signals are then controlling the deflection of the AOMs and thus stabilize the beam powers to the given set values. The achieved regulation speed is 10 kHz (3 dB point).

Frequency stabilisation

An optical resonator only accepts light with certain wavelengths to excite longitudinal eigenmodes. Only when the wavelength of the incident laser beam matches the round trip length of the resonator it is possible to couple light into it. Therefore, it is necessary to actively stabilize the length of the resonator with respect to the frequency of the incident laser light. For our application of optical dipole trapping we are not interested in a certain absolute frequency so it is sufficient to stabilize the system to an arbitrary longitudinal mode of the resonator. For the case of our cooling resonator this stabilisation was a challenging task as the linewidth of the eigenmodes is only 80 MHz. Hence, it is necessary to stabilize the length of the resonator with a precision on the order of 0.3 nm or to adjust the wavelength of the laser light correspondingly. The basic stabilization technique is the PDH lock. Its details are explained for example in Ref. [27]. We modulate frequency sidebands onto the laser light with the help of an electro-optical modulator. The reflected light of the primary beam which is not coupled into the resonator, including the side bands, is monitored by an RF photodiode and the phase of the beat signal is processed to obtain an error signal according to the PDH scheme. For feedback we use multiple elements to control the laser output frequency. The secondary beam does not have to be frequency stabilized independently as the two beams are emitted by the same laser and the eigenfrequencies of the two possible travel directions inside the ring resonator are identical. We do not control the length of the resonator as we observed problems with the electrical connection of the piezo inside the vacuum. The different feedback mechanisms are:

- AOM frequency: For fast feedback we change the modulation frequency of the two AOMs by directly using the PDH error signal to change the frequency of the RF source. Details about the RF generation are explained in the next section about frequency control. The achieved bandwith is 100 kHz.

- Piezo of the laser: The laser generating the light for the cooling resonator contains a piezo crystal changing the output wavelength. We use this option as feedback element with intermediate speed. The corresponding control signal is created by an integral controller with the PDH error signal as input. The control bandwith is 42 kHz. The maximum stroke is limited by the specified maximum voltage of the piezo in the laser. The tuning range is thereby limited to approximately 200 MHz which is less than the free spectral range of the optical resonator (345 kHz). As a consequence, there is sometimes no resonator line within reach and another feedback loop is required to keep always one resonator line within the tuning range of the piezo feedback loop.

- Temperature of the laser crystal: The temperature of the laser crystal can be controlled and thus utilized to tune the laser wavelength over a wide range. We use the (not yet amplified) control voltage of the laser piezo to control the laser temperature via a very slow PID controller. If the resonator line drifts, the feedback

loop with the laser piezo will change the laser's output wavelength to follow that drift by changing the piezo control voltage. This causes the temperature of the laser crystal to change as well. Hence, the piezo voltage is kept low and there is always one resonator line in the centre of the tuning range of the piezo feedback loop. Temperature feedback is naturally slow and the bandwith is on the order of 1 Hz.

As the resonator dipole trap is switched off once per experimental cycle, an automatic relock mechanism had to be implemented. A relock is only possible if there is a resonator line within the tuning range of the piezo feedback loop. This is not always the case as the length of the cooling resonator changes due to thermalisation effects during machine warm up or even due to cycle periodic temperature fluctuations. Occasionally there is no longitudinal resonator mode available for the piezo feedback to lock on after the light is switched back on. In that case the aforementioned temperature PID controller automatically resets its integral part. The sudden change in laser crystal temperature then changes the laser wavelength quickly and new lines become available for locking.

Frequency control

To create a stable, non fluctuating standing wave pattern inside the resonator it is necessary to stabilize the driving frequency of the two AOMs which the two incident laser beams pass. A schematic of the AOM frequency generation is shown in Fig. 2.11. The phase stability is ensured by creating the radio frequency with two direct digital synthesizers (DDS) which share the same clock signal. Their output signals are mixed with the signal from a single voltage controlled oscillator (VCO). The capability of the VCO to quickly change its output frequency is used for the fast feedback loop of the frequency stabilisation (see previous section). The signal strengths are then adjusted by two voltage controlled attenuators which therefore control the power of the laser beams incident onto the resonator. Electronic switches are installed to completely switch off of the RF frequencies. Eventually the signals are amplified to supply the AOMs.

The cooling procedure requires a small frequency detuning (less than a linewidth of the resonator) as described above to transport the atoms inside the cooling resonator by shifting the standing wave pattern. This is realized by a frequency change of the DDS supplying the primary beam. By using the DDS for this purpose phase stability between the two output signals is ensured even for differing frequencies.

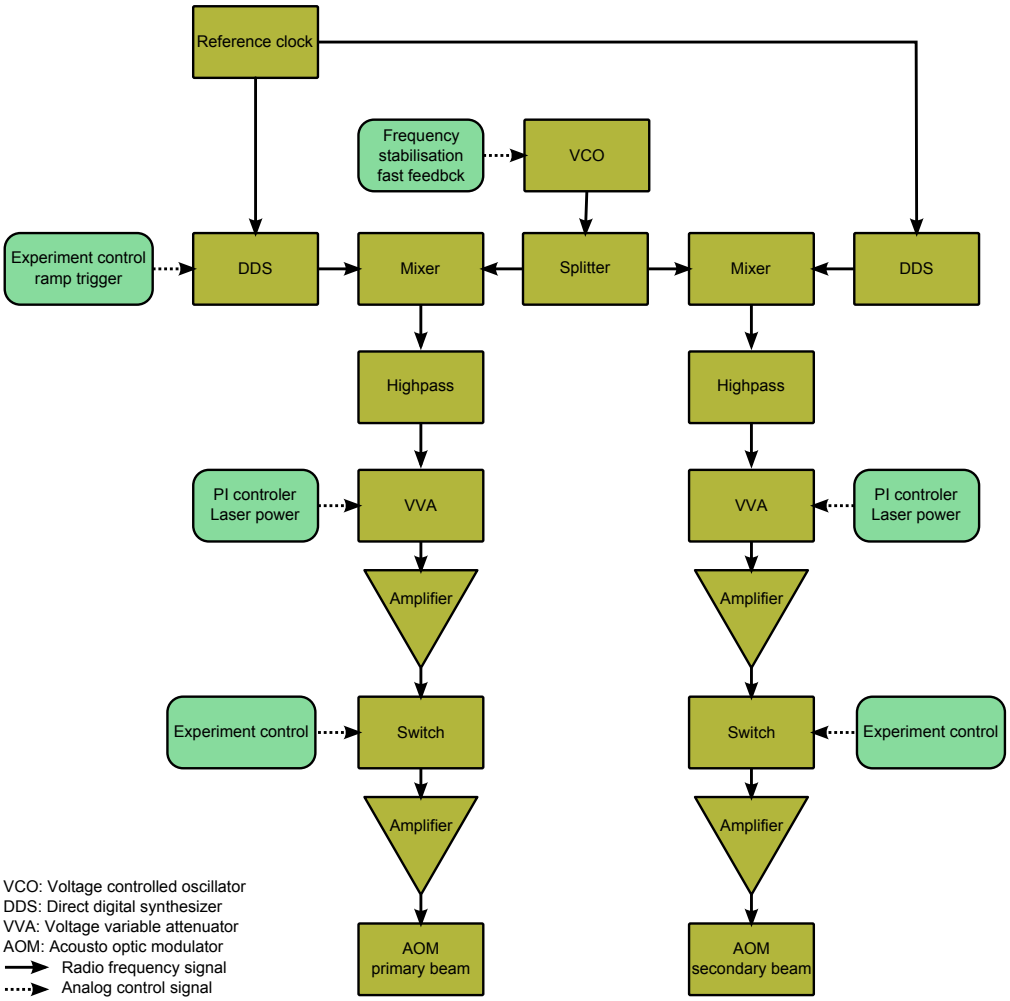

Figure 2.11: A scheme for the radio frequency generation needed to supply the AOMs of the cooling resonator laser beams. The frequency and power of the signal driving the AOMs determine the frequency and power of the light beams. The power can be controlled with a pair of voltage variable attenuators. The frequency is the sum of the frequency of a voltage variable oscillator (VCO, which is the same oscillator for both AOMs) and that of two direct digital synthesizers (DDS) sharing the same clock. The VCO is used for stabilisation of the frequency as it acts equally on both beams and the two DDS are used to create a small frequency difference between the beams to perform the transportation of the atom cloud inside the cooling resonator.

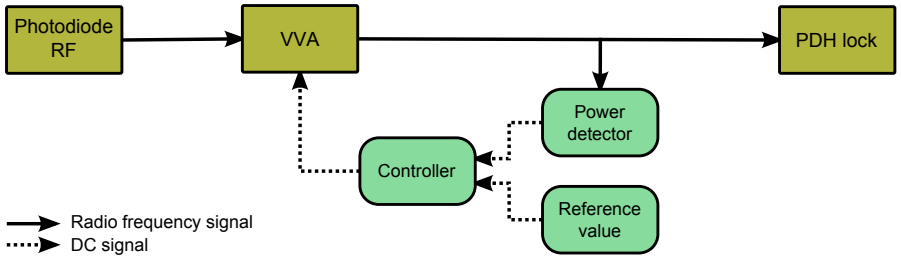

Figure 2.12: A scheme of the automatic gain correction circuit to ensure constant lock performance over a wide range of incident beam power. A power detector measures the RF power coming from the fast photodiode, used for the PDH lock, and controls a voltage controlled attenuator (VVA) to keep this power constant. By this the amplitude of the PDH error signal becomes almost independent of the beam power incident onto the resonator.

Power independent frequency stabilisation: Lock-tight

For evaporative cooling the beam power inside the cooling resonator is reduced. This reduces the amplitude of the PDH lock error signal which is proportional to the incident beam power. Therefore, evaporative cooling would result in a reduced stability and performance of the frequency lock. To encounter this problem we use an automatic gain correction circuit. It was developed by Alexander Frank and Robert Jördens and details can be found in Ref. [26]. A schematic explaining its function is shown in Fig. 2.12.

Automatic relocking: Lock-block

After we set up the hardware for the resonator we observed a serious problem. Although the lock was quite stable and the frequency and power control worked as intended the automatic relocking was not working properly. Due to the complicated transversal mode profile and polarisation dependence of the resonator eigenmode, we were not able to perfectly match the modes of the incident light and the resonator TEM_{00} eigenmode. We always excited higher transversal modes at different frequencies as well. As a result, the PDH error signal showed various features which belong to those higher modes. The automatic relock randomly locked onto those features and in many cases the laser was stabilized onto one of the higher transversal modes. To distinguish between the different modes, it is possible to monitor the beam power transmitted by the resonator. The coupling efficiency of the higher transversal modes is low and the transmitted beam power will be low as well if the lock captures such a mode. We made use of this behaviour to develop an electronic circuit we call "lock-block". A schematic is shown in Fig. 2.13. It compares the measured power of the monitoring photodiode behind the cooling resonator with a constant value set by a potentiometer. Only when this measured power is higher than the threshold, the lock function of the piezo feedback loop described above is enabled. If the power is below the threshold, the piezo controller switches into a "dither" mode where the piezo constantly scans the laser's output wavelength searching for a cap-

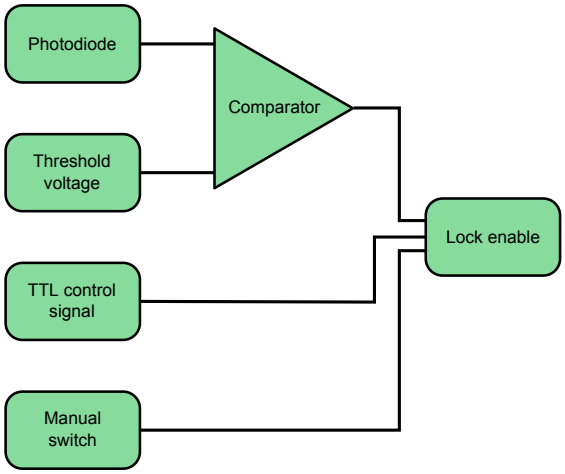

Figure 2.13: The basic working principle of the lock-block circuit. A photodiode monitors the light power transmitted by the cooling resonator. If the adjustable threshold power is exceeded, the PDH lock is enabled. For evaporative cooling in the resonator, the beam power is reduced deliberately and the circuit can be bypassed with a TTL signal. A manual bypass is possible as well for adjustment purposes.

ture point in the PDH error signal. If the coupling efficiency of all higher (undesired) transversal modes of the cooling resonator is low enough, there exists a certain setting of the threshold value such that the lock is only able to capture the correct mode. If the beam power in the resonator is lowered for evaporative cooling the circuit can be bypassed with a digital signal sent by the experiment control computer. A manual bypass for adjustment purposes is possible as well. The challenge in designing the circuit was to make it fast. The scan of the laser wavelength over 200 MHz needs approximately 50 ms. The linewidth of the resonator is 80 kHz which implies that the circuit needs to establish the lock within less than 20 µs.

Identifying the waist via the light shift

It is rather straightforward to transfer atoms from the MOT into the cooling resonator due to the large depth of the dipole trap. But it is far more demanding to locate the waist of the beam in the resonator. The waist's position needs to be known to determine the duration of the transport inside the resonator trap to move the atoms from the MOT location to the intended position for evaporation and unloading. We cannot examine the spatial extend of the trapped cloud directly inside the resonator as there is no high resolution imaging available in the main chamber. However, it is possible to measure the light shift of the trapped atoms. If absorption imaging is performed on trapped atoms, their transition frequency will change depending on the locally present laser intensity [28]. The modification of the transition frequency reaches a clear maximum at the position of highest intensity which is inside the laser beam waist as shown in Fig. 2.14. It turned

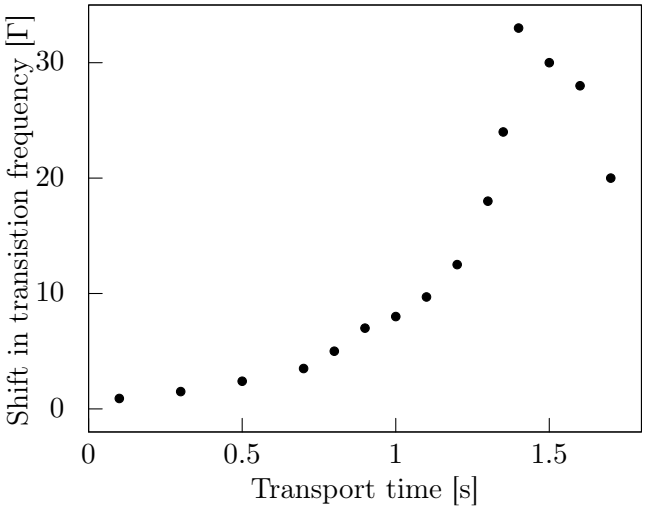

Figure 2.14: Measurement of the imaging transition frequency due to the light shift inside the cooling resonator. The detuning is given in units of the transition linewidth of ^{6}Li ($1\Gamma \approx 6\,\mathrm{MHz}$) and the zero detuning point is set to the loading position. The optimal transport time in this example is approximately 1.4 s, which corresponds to a spatial distance of 29 mm. The frequency detuning between the two resonator beams was 20 kHz.

out to be advantageous for this measurement to switch off the secondary beam just prior to imaging.

Performance and parametric heating

After we implemented stabilisation and control for the beam power and frequency as well as the automatic gain control and the lock-block circuit, the resonator operation became stable. If the apparatus is thermalized and properly adjusted, the automatic relocking works in a very satisfactory manner and we observe a failed relock attempt only every couple of hundred shots. The lock itself is stable and the laser frequency remains stabilized on the resonator reliably during the evaporation process. However, the adjustment of the feedback loops is a delicate process and requires a certain amount of exercise. Fortunately, readjustment is typically not necessary on a daily basis.

Nevertheless, there was a major problem with the cooling sequence and thus we use the resonator in a different fashion as initially intended and described above. During the transport, the trap frequencies are position-dependent as the beam diameter, and thus the local intensity is changing as well during the movement from the MOT position (loading) to the beam's waist (evaporation and unloading). If the local trap frequency becomes resonant with another oscillation frequency present in the system, e.g. a fluctuation of the laser power, parametric heating occurs which leads to atom loss [29]. Due to the continuous sweep of the trap frequency during the transport, we encountered such a

resonance. On absorption images it was possible to observe a region of high loss rate at a certain spatial position. The exact location of this region is changing slightly with time, probably due to changes in the exciting frequency leading to the parametric heating. To avoid this atom loss, we decided not to use the transport feature of the resonator dipole trap. Instead, we perform the evaporation in the standing wave pattern at the loading position. During the evaporation the power of the secondary resonator beam is ramped down faster than that of the primary beam. Therefore, the last part of the evaporation is performed in a running wave trap. The longitudinal confinement along the resonator mode is provided by the transport dipole trap which is already switched on at that moment and the trap has the character of a crossed beam dipole trap.

To increase the cooling performance it should be possible to change the way the cooling resonator is used and to overcome the problem with parametric heating. A more sophisticated transport scheme, like switching the secondary beam off for a certain time and letting the atoms "fall" to the waist position before switching it back on, might be a possible solution.

Description	Value
Roundtrip length	0.87 ± 0.01 m
Incident angle of beams on resonator mirrors	2°
Material	Stainless Steel
Linewidth	83 ± 9 kHz
Finesse	3880 ± 40
Free spectral range	345 ± 4 MHz
Design wavelength	1064 nm
Power enhancement	1300 ± 100
Typical coupling efficiency (primary beam)	85%
Waist size ($1/e^2$ radius, intensity)	17.5 µm x 30 µm
Waist tilt angle with respect to the baseplate	$\sim 45°$
Diameter of the baseplate	238 mm
Regulation speed of the PI power control	10 kHz
Lock sideband modulation frequency with EOM	68 MHz
Lock bandwith AOM feedback	100 kHz
Lock bandwith piezo feedback (on laser)	20 kHz
Tuning range of piezo feedback (on laser)	±100 MHz
Lock bandwith temperature feedback	∼1 Hz
Incident beam powers for loading (per beam)	105 mW
Incident beam power at end of evaporation (primary beam only)	8 mW
Trap depth for ^{6}Li during loading	40 mK
Trap frequencies for ^{6}Li during loading	10 MHz × 135 kHz × 80 kHz
Transport distance in resonator, design value	20 mm
Transport frequency detuning	up to 40 kHz
Transport frequency detuning ramp time	200 µs
Transport time	∼1.4 s
AOM design frequency	110 MHz

Table 2.4: Properties of the cooling resonator. All resonator specific data are adopted from Ref. [24]. The trap frequencies and depths were calculated with measured beam powers.

Description	Value
Wavelength	1064 nm
Waist size ($1/e^2$ radius, intensity)	23 µm
Focal length of focusing lens	1000 mm
Trap frequencies for ^{6}Li and 4 W beam power	8800 Hz × 8800 Hz × 90 Hz
Trap depth for ^{6}Li and 4 W beam power	290 µK
Power regulation	AOM and PID controller with logarithmic photodiode
Regulation speed of the PI power control	5 kHz
Lateral position stabilisation	Active control loop with piezo actuated mirror and quadrant photodiode
Translation stage maximum travel range	−1.5 mm to 351.0 mm
Translation stage nominal travel	16.85 mm to 343.2 mm
Translation stage maximum current motor	4.5 A continuous, 14.2 A (RMS) peak
Translation stage maximum current controller	10 A

Table 2.5: Properties and limitations of the transport dipole trap.

2.1.4 Transfer into the science cell

After evaporative cooling in the cooling resonator, the atoms are transported from inside the main chamber into the science cell. The transport is performed by a focused running wave dipole trap which uses the same laser as the cooling resonator. As the atoms at this point are already pre-cooled, the power enhancement of a resonator is not necessary for trapping. The lens which focuses the beam for this dipole trap is mounted on an air bearing translation stage[18] and a movement of this lens shifts the focal position of the beam from the main chamber into the science cell. There, further evaporation is performed by lowering the beam power of the transport dipole trap. To ensure optimal stability the traps pointing is actively stabilized with a control loop. The pointing is monitored by a quadrant photodiode and regulated with a piezo actuated mirror. More properties of the transport trap are collected in Tab. 2.5. Details of it can be found in Ref. [18].

There is one potential issue which I would like to mention here. We observed strong atom losses under certain (unknown) conditions during the initial phase of the transport with this trap. We assume that back reflections of the trap beam, caused by optical elements behind the science cell are responsible for the losses. Solutions are to use an optimized acceleration scheme of the translation stage (the current limits of the controller must be observed) and to block all optics behind the science cell with a shutter which opens shortly before the translation stage reaches its final position.

[18] Stage: Heason AirGlide, Ultra Precice Air Bearing System, 350 mm; Controller: Aerotech, Ensemble ML10-40 digital controller and linear amplifier

2.1.5 Laser system at 671 nm

The MOT, the Zeeman slower and the imaging require a reliable and stable laser system to drive the ^{6}Li transition at a wavelength of approximately 671 nm. The level scheme of ^{6}Li together with the used transitions is shown in Fig. 2.15. We use the D_2 line which connects the $^2S_{1/2}$ and the $^2P_{3/2}$ electronic states. The lower state is split into two levels F=1/2 and F=3/2 by an energy corresponding to 228 MHz. The splitting of the upper state is less than the transition linewidth of 6 MHz and thus negligible in most cases. Exposed to a magnetic field, the two lower states split into a total of 6 states as shown in Fig. 2.16. The $^2P_{3/2}$ state shows a magnetic field dependence as well, which has to be taken into account for imaging at high magnetic fields. The requirements on the laser light used for cooling and imaging are as follows:

- MOT cooler: Drives the transition from $^2S_{1/2}$, F=3/2 to the $^2P_{3/2}$ state. Tuning of the beam's frequency is only required within ∼100 MHz for adjustment purposes and the MOT compression phase.
- MOT repumper: Drives the transition from $^2S_{1/2}$, F=1/2 to the $^2P_{3/2}$ state. The light has fixed frequency offset of 228 MHz with respect to the cooler light.
- Zeeman slower light: Drives the same transition as the cooler. But its frequency detuning has to be adjustable independently.
- Imaging light: Drives the same transition as the repumper, but requires a far larger frequency tuning range. To image the cold atoms at varying magnetic field strength, across the Feshbach resonance, a frequency tuning range of ∼1 GHz is required. Only low powers are necessary.

The lasers which produce the light for the MOT, the Zeeman slower and the imaging as well as the required optics are located on a separate optical table. The light is coupled into single mode, polarization maintaining optical fibres to guide it to the experiment table. A picture of the optical table with the laser system is shown in Fig. 2.17.

Concept and layout

The basic idea of the laser system is a reference laser which is stabilized onto the ^{6}Li transition line with the help of a lithium vapour cell. Two further lasers are then stabilized with respect to the reference laser with a frequency lock-in technique described in Ref. [30]. These offset locks offer a tunable frequency offset and thus the possibility to control and change the output frequencies of the lasers during the experimental cycle. A scheme of the laser system is depicted in Fig. 2.18. We use external cavity diode lasers in Littrow configuration[19] as they are easy to operate, affordable and compact. In addition they

[19] The reference laser and the MOT laser are homebuilt. The imaging laser is a Toptica DL 100 pro.

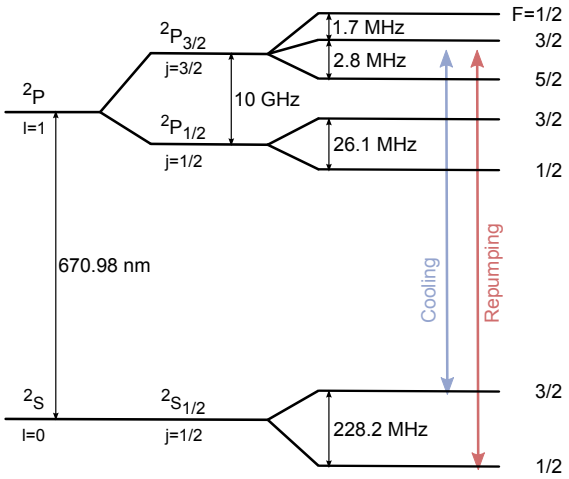

Figure 2.15: The level scheme of ^{6}Li showing the fine structure and hyperfine structure together with the transitions used in the experiment. The corresponding wavelength is approximately 671 nm. As the natural linewidth of this transition (6 MHz) is larger than the hyperfine splitting of the $^2P_{3/2}$ state no specific F state can be addressed. The hyperfine states themselves are degenerate due to different possibilities for the m_F quantum number. The frequency values are adopted from Ref. [19].

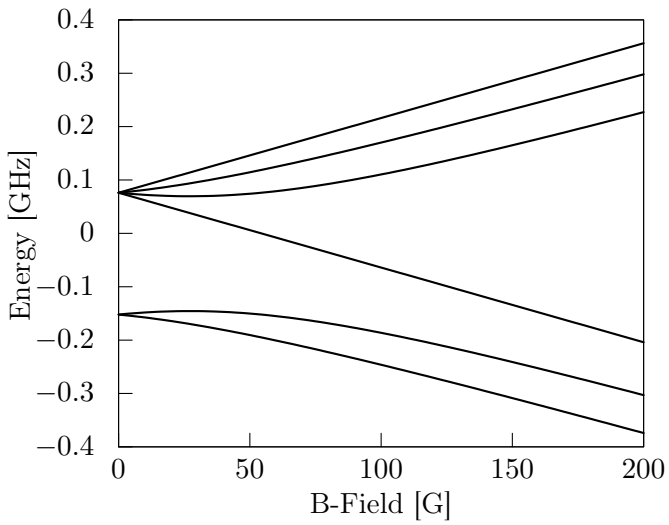

Figure 2.16: Magnetic field dependence of the $^2S_{1/2}$ groundstate of ^{6}Li calculated with the Breit-Rabi formula. The lower two lines correspond to $F = 1/2$ state ($m_F = \pm 1/2$), the upper four to the $F = 3/2$ state ($m_F = \pm 3/2, \pm 1/2$). We prepare the cold gases in the lower two states at the end of the MOT phase. If required for the experiment, radio frequency pulses can be used to transfer atoms into the other states.

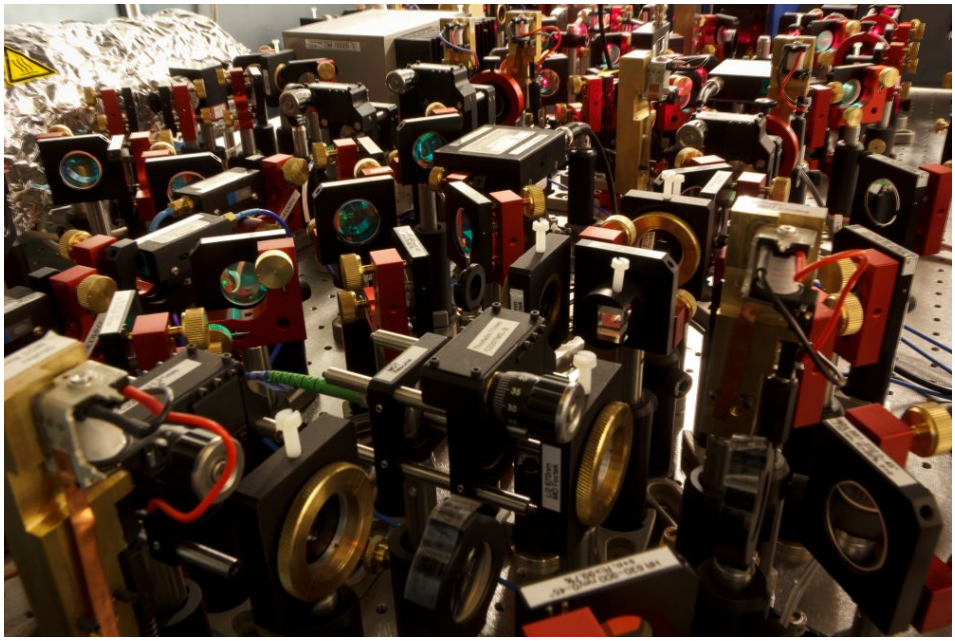

Figure 2.17: A picture of the 670 nm laser system. It creates the light needed for optical cooling in the MOT, the Zeeman slower and the beams necessary for imaging.

offer the convenient possibility to tune the output frequency by changing the angle of the laser grating with a piezo.

With minor modifications, the laser system can be used to cool bosonic ^{7}Li as well. The hyperfine splitting of the ^{7}Li groundstate is ∼800 MHz and thus the two 114 MHz AOMs have to be replaced by 400 MHz AOMs (see Fig. 2.18). The reference laser then has to be locked onto a ^{7}Li transition. Our vapour cell also contains the bosonic isotope of lithium for this purpose. Performance data of the laser system is presented in Tab. 2.6. In the following sections the individual lasers are described in more detail.

Reference laser

The reference laser is locked using the PDH locking scheme onto the atomic transition of ^{6}Li which causes absorption in a lithium vapour cell. More precisely, it is locked to the crossover of the D_2 line which is the mean of the cooling and repumping transition. Feedback is provided by the piezo which changes the angle of the laser grating. The sidebands needed for the PDH lock are created by modulating the current of the laser diode. The layout of the absorption cell is described in Ref. [31]. The cell is filled with nuggets of ^{6}Li and ^{7}Li and provides a vacuum to avoid undesired absorption lines. To obtain a sufficiently large lithium vapour pressure, the cell is heated to 340 °C. It is important to note that the vapour pressure increases by a factor of 10 for each 60 K in temperature, see also Fig. 2.3. Only a slight increase in heating power can cause the

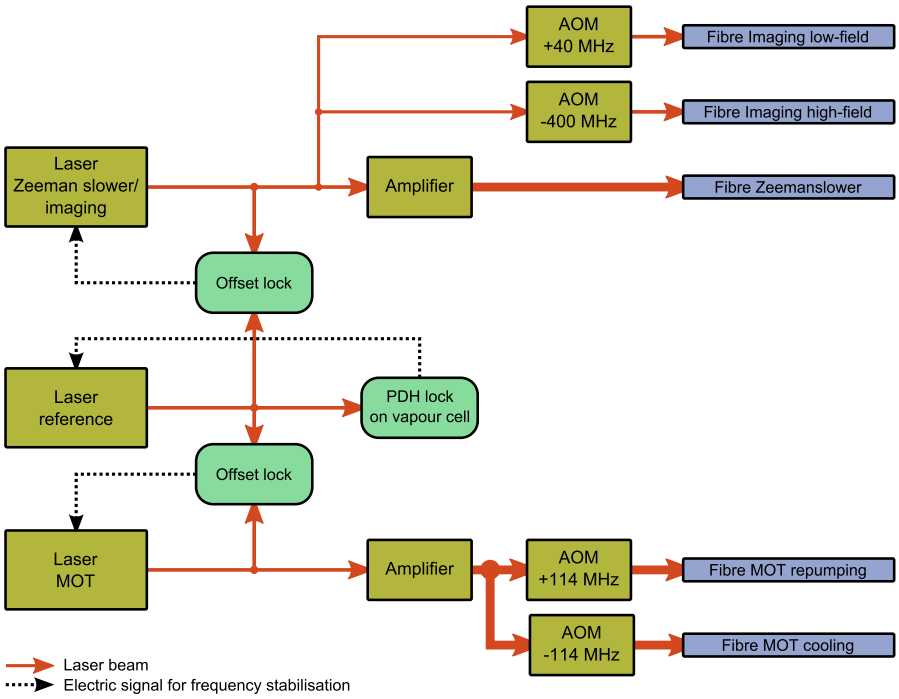

Figure 2.18: The basic concept of the laser system to cool ^{6}Li. The reference laser is stabilized onto the atomic transition using the PDH locking technique on the absorption signal of a vapour cell. The other lasers are stabilized using offset locks with respect to the reference laser which offers the possibility to tune the output frequency over a wide range during the experimental cycle. The light for the MOT and the Zeeman slower is amplified by tapered amplifiers. The AOMs are performing slight frequency adjustments of the light as well as rapid switching and regulation of the beam powers. Additional mechanical shutters, not shown in the figure, can be used to switch off individual beams completely.

vapour pressure to rise such that the windows of the cell become coated. As a measure of prevention, an independent temperature guard monitors the temperature and shuts down the heating if the set limit is exceeded.

MOT laser

The laser for the MOT cooling and repumping beam uses an offset lock to stabilize the output frequency relative to the reference laser. The light is amplified with a tapered amplifier and split into two beams. The beams' frequencies are shifted with the help of an AOM by 114 MHz for the repump beam and −114 MHz for the cooler beam which takes into account the hyperfine splitting of the groundstate of 228 MHz. Both beams can be separately switched off by mechanical shutters located in front of the single mode, polarisation maintaining fibres guiding the beams to the experiment. The powers of the beams are measured behind those fibres and stabilized with PI controllers acting back onto the AOMs previously mentioned.

Image and Zeeman slower laser

The laser used for the Zeeman slower and imaging is stabilized to the reference laser with an offset lock as well. Here, the photodiode monitoring the beat signals between the two lasers has been optimized for high speed up to approximately 3 GHz. This ensures a large tuning range of the output frequency required for imaging at high magnetic fields. The tuning range finally achieved in the experiment is approximately 1 GHz, limited by other electronic elements in the offset lock circuit. The light is split behind the offset lock into two beams, one for the Zeeman slower and the other for imaging. The beam path for the Zeeman slower contains a tapered amplifier to create sufficient light power. The imaging beam is further split into two beams both controlled by AOMs. One of the AOMs shifts the light's frequency by +40 MHz and the other by −400 MHz. In combination with the tuning range provided by the offset lock, the latter allows for a frequency shift sufficiently large to image atoms at a magnetic field strength of more than 1000 G, whereas the beam passing the +40 MHz AOM is used for low field imaging. Fast switching of the beams is also performed with those AOMs followed by mechanical shutters to prevent any light from leaking through.

2.1.6 Dipole trap lasers

Manipulation laser at 780 nm

To manipulate the ultracold clouds, we set up an external cavity diode laser with an output wavelength of 780 nm. A tapered amplifier increases the beam power which is then regulated and stabilized with the help of an AOM. The light of this laser can be used to create an attractive potential which was for example used in our measurements of the superfluid critical velocity of strongly correlated atoms. More details on those measurements can be found in 5.

Description	Value
Reference laser, locking point	D_2 line of ^{6}Li
Vapour cell, temperature set point	341 °C
Reference laser, output power	10 mW
Reference laser, power available for lock on ^{6}Li transition	0.5 mW
Reference laser, power available for offset locks	4.5 mW
MOT laser, output power behind laser	28 mW
MOT laser, output power in front of tapered amplifier	15 mW
MOT laser, output power behind tapered amplifier (operated at 710 mA)	240 mW
MOT laser, output power in front of the AOMs	121 mW(Cooler), 44 mW(Repumper)
MOT laser, output power behind the AOMs	61 mW(Cooler), 29 mW(Repumper)
MOT laser, output power in front of fibres	53 mW(Cooler), 28 mW(Repumper)
MOT laser, output power behind fibres	20 mW(Cooler), 13 mW(Repumper)
Imaging laser, output power behind laser	22 mW
Imaging laser, output power in front of tapered amplifier	15 mW
Imaging laser, output power behind tapered amplifier (operated at 810 mA)	330 mW
Imaging laser, output power in front of Zeeman slower fibre	255 mW
Imaging laser, output power behind Zeeman slower fibre	80 mW
Imaging laser, output power available for imaging	3 mW
Imaging laser, offset lock tuning range (locking on the first rising edge)	130 MHz to 830 MHz
Imaging laser, offset lock tuning range (locking on the second rising edge)	350 MHz to 1000 MHz

Table 2.6: Typical performance values of the 670 nm laser system. The power values are meant as reference and the actual values reached in the experiment may differ.

Pinning laser at 672 nm

A further diode laser works at 672 nm and is intended to create near detuned optical dipole potentials. Due to the small detuning with respect to the atomic transition, the resulting traps can be very deep. In a lattice configuration very efficient spatial pinning of the atoms can be achieved. Such pinning might be required for future single atom detection experiments using fluorescence imaging.

Laser system 1064/532 nm

Apart from the diode lasers we also use solid state lasers with an output wavelength of 1064 nm[20]. A part of this light is frequency doubled to obtain the wavelength of 532 nm[21]. Both wavelengths are used to create dipole traps which are either attractive (1064 nm) or repulsive (532 nm). Due to the far detuning with respect to the atomic transition wavelength of lithium high laser powers of several tens of watts are required. It is very difficult to couple beams with such high powers into single mode fibres. Therefore, we placed the corresponding light sources directly on the experiment table and used only free space optics. More details about the solid state laser system can be found in Ref. [18].

2.1.7 Low resolution imaging system for monitoring purposes

Several low resolution optics with simple small CCD cameras[22] are placed around the experiment to perform absorption imaging. The absorption images acquired by those cameras provide valuable information for the adjustment and optimization of the apparatus. The imaging optics are designed as confocal microscopes with two achromatic lenses to minimize aberrations. A list of the installed imaging options is shown in Tab. 2.7.

2.1.8 Magnetic field creation

The design and the setup of the magnetic coil system were subject of the doctoral work of my co-worker Kai Morgener and details can be found in Ref. [18]. A sketch of the locations of the coils around the vacuum chamber is shown in Fig. 2.19. The coils are able to produce offset fields with a strength of more than 1500 G as well as anti-Helmholtz fields required for the MOT.

[20] Innolight, Mephisto MOPA and Nufern, Sub-1174-22 Fibre laser
[21] Evans & Sutherland, doubling cavity
[22] Point Grey, 1.3MP B&W Chameleon

Name of the camera	Position of camera	View direction	Magnification
Flea	Above main chamber	$-z$	-
BEC-X	2D board	$-x$	5
BEC+Y	2D board	$+y$	0.905
BEC-X+Y	2D board	$-x+y$	1
MOT-Z	MOT board	$-z$	0.31

Table 2.7: A List of the installed imaging systems for low resolution imaging. The axes are defined as follows. x: along Zeeman slower away from the oven, y: from science cell to MOT chamber, z: vertical direction facing upwards. The "2D board" is the breadboard around the science cell and the "MOT board" is the breadboard for the MOT optics. The magnification of the camera named Flea was not determined as it is only used to monitor the fluorescence light of the MOT in real time during the experimental cycle and is not used for data acquisition. The other cameras are used for absorption imaging.

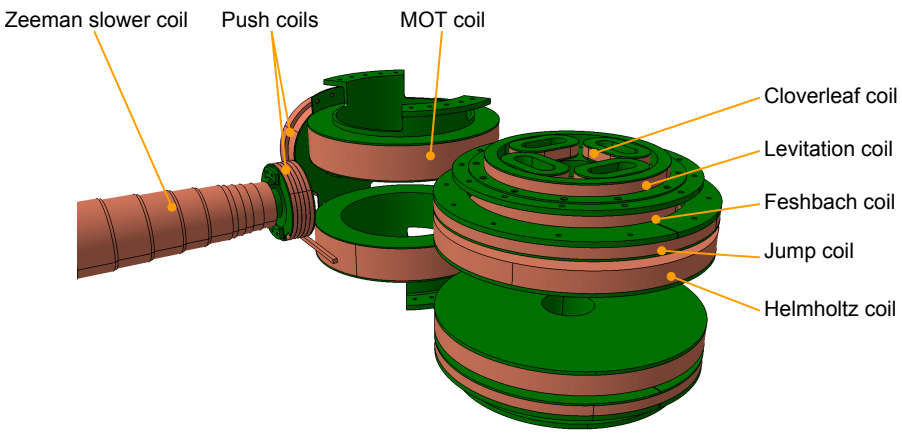

Figure 2.19: The placement of the magnetic field coils in the experiment. The vacuum chambers are not shown for simplicity. The coils themselves are shown in brown and the support frames in green. The push coils and the MOT coils are located around the main chamber, whereas the stacked coils in the foreground are placed around the science cell.

2.2 Sequence and performance

This section describes the cooling sequence in detail, starting from solid lithium blocks in the oven and ending with an ultracold gas with tunable interaction located in the science cell. I would like to refer the reader who is particularly interested in the creation of a single-layer, two dimensional sample to chapters 3 and 6. A list of reference values for atom numbers and sequence times is presented in Tab. 2.8.

1. The sequence starts with loading the MOT with atoms emitted by the oven and slowed down by the Zeeman slower. During the loading phase the cooler and repumper beams are red-detuned with respect to their corresponding atomic transitions by approximately 5.5 linewidths. After typically 5 s, we trap approximately 30×10^6 atoms inside the MOT.

2. After the MOT is loaded we switch off the Zeeman slower and compress the MOT by ramping the detunings of the cooler and repumper laser closer to their respective resonances. Simultaneously the powers of the two lasers are reduced to a fraction of the initial values. The reduction of the repump beam power is faster than that of the cooling beam. This leads to a transfer of atoms from the $F = 3/2$ ground state to the $F = 1/2$ state as shown in Fig. 2.15. During the compression, the location of the MOT is shifted to the loading position of the cooling resonator with the push coils .

3. Already during the MOT loading phase, the cooling resonator beams are running at their maximum power values. After the MOT is compressed, the lasers for optical cooling can be switched off completely and the atoms are trapped solely by the resonator dipole trap. When the transfer is completed, the magnetic field configuration is changed from an anti-Helmholtz (needed for the MOT) to a Helmholtz configuration. This creates an offset field with a strength of approximately 210 G[23] which increases the scattering length between atoms in the two hyperfine states $F = 1/2$, $m_F = \pm 1/2$ due to the Feshbach resonance. The achieved interaction is strong enough to perform forced evaporative cooling in the resonator by linearly lowering the light intensity of the dipole trap. The secondary beam is ramped down slightly faster than the primary beam, changing the trap continuously from a standing wave trap into a running wave trap. Before the secondary beam is switched off entirely, the beam of the transport dipole trap is switched on to provide longitudinal confinement. After the evaporation is finished, the beams of the cooling resonator are switched off completely and the atoms are confined by the transport trap.

4. The transportation from the main chamber into the science cell is then performed by moving the lens focusing the beam of the transport dipole trap. This process takes approximately 1.5 s and induces almost no atom loss.

[23] This corresponds to an s-wave scattering length of $a \approx -750\,a_{\mathrm{Bohr}}$.

5. When the atom cloud arrives at its final position inside the science cell, the magnetic field strength is increased to address the Feshbach resonance. The ramp of the magnetic field is performed as fast as the power supplies allow to cross lower lying p-wave Feshbach resonances as quickly as possible. Those very narrow resonances cause strong atom loss rates. After the magnetic field is ramped up, the next evaporative cooling step is performed by lowering the laser intensity of the transport dipole trap. The beam power is ramped down exponentially to optimize the cooling efficiency. Before reaching its final value, the ramp is interrupted for a short time to perform the active position stabilisation of the transport trap with the help of a quadrant photodiode and a piezo actuated mirror. The stabilisation is always performed at a laser power of 100 mW to be independent of the final evaporation depth. The evaporation continues after the stabilization is completed.

6. After the last evaporation step, an image of the cloud can be taken. Either by the high resolution microscope system or by one of the low resolution optics. To compensate the Zeeman shift, the frequency of the imaging laser has to be adjusted according to the magnetic field strength during the image acquisition. At very low magnetic fields the atomic transition is not closed. To obtain a picture of the atoms at no or at low magnetic fields it is required to shine in the cooling beam of the MOT to constantly clear the F=3/2 state during the imaging process.

If the last evaporation step ends with a sufficiently shallow trap, an ultracold, elongated gas is produced. The magnetic field can then be adiabatically ramped to a value which corresponds to the desired interaction between the atoms. It is possible to create either a molecular BEC or a superfluid with fermionic constituents described by BCS theory. Density profiles of one of the first BECs we created with the apparatus are shown in Fig. 2.20. When lowering the final evaporation beam power, a bimodal shape of the density distribution becomes visible which is a distinguishing feature of a BEC. Almost pure condensates with 100×10^3 Atoms (per hyperfine state) can be produced. Atoms in the two hyperfine states are present in equal numbers as the evaporation tends to minimize any population difference. For the experiments presented in chapters 4 and 5 as well as for the creation of two dimensional atom clouds (chapter 6), the final evaporation depth is chosen higher such that the gas is just cold enough to transfer the cloud into the squeeze dipole trap which is explained in chapter 3.

Compared to similar machines of other research groups, the atom number trapped in our MOT is fairly small (approximately 30×10^6 compared to $\sim 10 \times 10^9$ in the Lithium experiment in Zurich [15]). The reason is unknown at the moment. Possible issues are insufficient laser power or insufficient atom flux emitted by the oven. The magnetic field design might be responsible as well. It is rather complicated as the MOT centre is pushed away from the geometric centre of the main MOT coils. Nevertheless, we still obtain decent atom numbers at the end of the evaporation which implies that our cooling scheme is quite efficient.

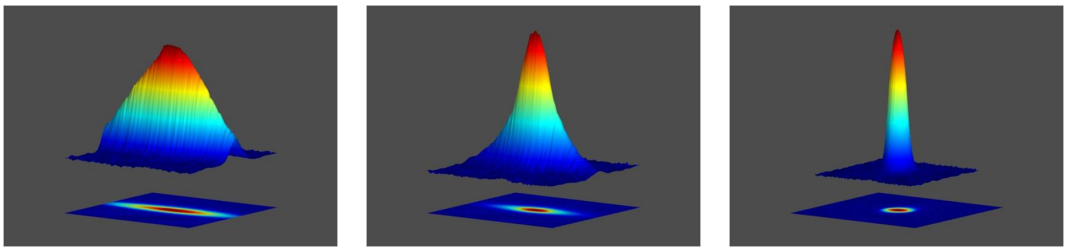

(a) Final trap power 40 mW (b) Final trap power 15 mW (c) Final trap power 2.5 mW

Figure 2.20: Density distributions of a cold gas in the transport dipole trap. With decreasing final evaporation depth the gas becomes colder and a bimodal density distribution appears. This is evidence that we produced a molecular BEC of ultracold ^{6}Li.

Sequence time	Point in sequence	Atom number (per spin state)
0 s	Start	-
5.5 s	MOT, loaded	30×10^6
5.5 s	Cooling resonator, loaded	20×10^6
7.1 s	Transport trap, loaded	1×10^6
8.5 s	Transport trap, transport completed	1×10^6
10.9 s	Transport trap, evaporated to stabilisation	230×10^3
11.3 s	Transport trap, end of evaporation	100×10^3
13 s	Experiment ready for next cycle	-

Table 2.8: The table presents reference values for atom numbers which can be reached for a experimental sequence that aims for the creation of an almost pure BEC trapped by the transport trap inside the science cell. The atom numbers correspond to a final evaporation power of 5 mW.

3 From a cold gas to a flat gas

One particularly fascinating property of the science with ultracold gases is the readout of the experiments. Although the investigated samples are extremely fragile, it is possible to simply take pictures of them. The underlying microscopic physics, which governs the behaviour of the gas cloud, is influencing its macroscopic shape. Thus the acquired images can reveal quantum mechanical effects in a striking fashion. It was possible to show remarkable quantum mechanical effects on ultracold atom clouds which could be made visible without complicated data analysis. Examples are the matter wave interference of two BECs [32] or the direct observation of quantised vortex patterns present in superfluid gases [33].

The two possible techniques used for acquiring those pictures, are fluorescence and absorption imaging. For the latter the atoms are illuminated with resonant light and the resulting absorption pattern is imaged on a camera. In fluorescence imaging, the spontaneously re-emitted photons are detected. Due to very low background, very small atom numbers can be detected with fluorescence imaging. However, it is also more challenging to implement. Due to the typically small signals, care has to be taken that stray light does not reach the camera. In the experiments presented in this thesis absorption imaging is used.

Although applied very successfully, the imaging of cold atom clouds is always confronted with two particular difficulties. Firstly, the clouds are typically fairly small, only a couple to tens of µm in diameter. Optics which achieve spatial resolutions on this length scale are quite complex, work-intensive in design and require large numerical apertures. Secondly, the atom clouds can be fairly dense which leads to an insensitive density retrieval in absorption imaging as simply all light is absorbed. Thus, the strategy which was followed by many cold atom experimentalists was to let the cloud expand prior to the image acquisition by switching off the confining traps. After a short time-of-flight (TOF), during which the cloud expands, the picture is acquired. At the same time, this expansion reduces the optical density to more feasible values. For a non-interacting gas TOF imaging maps the momentum distribution prior to the release of the atoms into their real space positions during the image acquisition (for a TOF sufficiently long). This approach has been, and still is, very successful and numerous interesting results could be obtained with it. Furthermore, TOF imaging was developed into more sophisticated techniques like band-mapping in optical lattice experiments [34] or Stern Gerlach type experiments and also applied to interacting gases where the understanding of the expansion processes

is more challenging [35, 36, 37].

During the last years a change in the image acquisition strategy can be observed within the cold atom community. More and more experiments are performed which are able to spatially resolve the cold gas clouds confined in the trap without using the TOF imaging technique. Such in-situ imaging promises interesting possibilities for new studies on ultracold gases. The real space information acquired in such experiments avoids difficulties of deducing properties from TOF pictures. This is particularly interesting in systems featuring strong interactions as they can complicate the dynamics during TOF significantly such that the expansion is not entirely understood yet. In-situ imaging can reveal non-trivial distributions of the atoms in the trap. An example would be the plateau, or "wedding-cake" structure of Mott-insulators [38]. In-situ imaging with a high resolution opens the door to investigate spatial fluctuations of the gas properties. For example, the correlations of density fluctuations can be used to derive other quantities of the gas such as the temperature [39]. In combination with optical lattices even single site and thus single atom resolution comes within reach, which would allow the study of models developed for solid state physics on a microscopic level. Such experiments do already exist for bosons [40, 41], but not yet for fermions.

Another property of high resolution experiments is that if it is possible to resolve certain length scales, it is also possible to shine light onto the atoms with the same resolution. As a consequence, such experiments offer the possibility for high resolution manipulation (via the dipole force). This can range from shining in single small obstacles into the atom cloud (see chapter 5 for an example) to complicated, arbitrary potential landscapes. The latter brings mesoscopic physics into the scope of quantum gas experiments.

Thus, the idea of building a cold fermion machine capable of in-situ high resolution imaging seems to be a promising endeavour. But it is quite challenging as well, as I will show in this chapter. There are basically two reasons. One is the need for exceptionally good optical access to the atoms and a microscope objective which is placed in close proximity to the sample. The other is the necessity of a very flat, ideally two-dimensional, atom cloud to fully utilize the potential offered by the highly resolving optics as the depth of field of such optics with high numerical aperture is inevitably quite short. Additionally, unwanted integration along the imaging axes should be avoided.

The wide range of research possibilities which become accessible in such "2D-quantum gas microscope experiments" and the increasing level of skill in tackling the involved technical challenges recently triggered construction efforts of such machines in many quantum gas research groups all over the world. An incomplete list of examples are the machines in the Chin group in Chicago [38], the Dalibard group in Paris [42], the Jochim group in Heidelberg [43], the Bloch group in Munich [40], the Greiner group in Boston [41] and the setup described in this thesis. The combined efforts of all those groups promise a huge variety of interesting physics to be discovered in the coming years.

The following two sections describe our own microscope system and the creation of flat, but still three-dimensional, samples. Our approach to confine ultracold atom clouds into two dimensions is presented in chapter 6.

3.1 Imaging and manipulation with high resolution

The following pages elaborate the technical realisation of our high resolution microscope system. A section about the theoretical background of imaging optics is included as well as information about the testing of the components, the integration of the assembly into the machine and the verification of its proper function. The section covering the alignment procedure of the microscope assembly is meant to serve as a manual for future re-alignment. If the reader is in the situation to adjust this part of the machine it is strongly recommended to read these instructions carefully.

3.1.1 Imaging theory

This section is intended to give a short theoretical introduction to the topic of imaging. It closely follows the master's thesis of our former student Jan-Henning Drewes [10]. The properties of an ideal lens will be discussed to define a criterion for resolution. The point spread function (PSF), which determines the resolution, will be introduced and its connection to the numerical aperture (NA) of the system will be explained. As real lens assemblies are non-ideal, they cause several types of optical aberrations. Therefore, the major aberrations of our high resolution optical system will be discussed as well.

Ideal lenses, diffraction limit

Consider an ideal lens, fully characterized by its focal length f and its aperture diameter a, which is used to image a point-like light source located at a distance d_1 from the lens and at a position (ξ, η) (in Cartesian coordinates) in the object plane perpendicular to the optical axis. A sketch is shown in Fig. 3.1. The resulting field distribution in the image plane, at a distance d_2 from the lens, is called the point spread function $h(u, v, \xi, \eta)$, where (u, v) are the coordinates on the imaging plane. Furthermore we will assume $\frac{1}{d_1} + \frac{1}{d_2} = \frac{1}{f}$ which is the condition for a focused image.

For an extended object $U_O(\xi, \eta)$ the convolution of the object with the PSF yields the field at the imaging plane:

$$U_I(u, v) = \int_{-\infty}^{\infty} \int_{-\infty}^{\infty} h(u, v, \xi, \eta) U_O(\xi, \eta) \, \mathrm{d}\xi \, \mathrm{d}\eta. \tag{3.1}$$

In this sense, the PSF can be regarded as the transfer function of the optical system.

For the ideal case, one could assume that the PSF is a delta distribution and the system would be fully characterized by its magnification $M = d_2/d_1$. The above equation then simplifies to

$$U_I(u, v) = \frac{1}{M^2} U_O\left(\frac{u}{M}, \frac{v}{M}\right). \tag{3.2}$$

This assumption of a delta-type PSF is not realistic even for the ideal lens sketched above due to diffraction of the light at the lens' aperture. A more realistic PSF can be obtained by considering the electric field emitted by the light source and then calculating

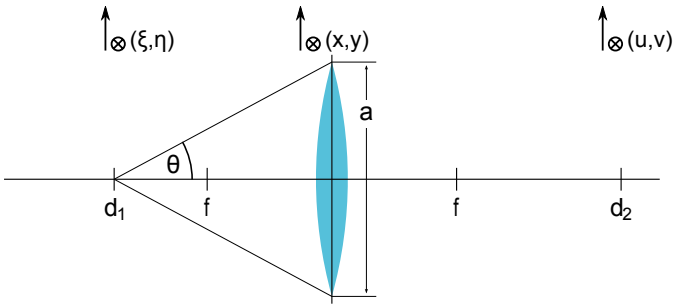

Figure 3.1: Sketch of a perfect lens with focal length f which images a point like light source. The source is located at a distance d_1 to the left of the lens and its image is at a distance d_2 to the right of the lens. The angle θ and the diameter a of the open aperture are determining the resolution of the lens. The coordinate labels given in the illustration correspond to those used in the calculations in the text.

its propagation through the lens to the imaging plane. The lens introduces a position dependent phase shift of the electric field [44]. The obtained expression for the PSF is

$$\begin{aligned} h(u,v,\xi,\eta) \quad = \quad & \frac{1}{\mathrm{i}\lambda^2 d_1 d_2} \underbrace{\exp\left(\frac{\mathrm{i}k}{2d_2}\left(u^2+v^2\right)\right)}_{1} \cdot \underbrace{\exp\left(\frac{\mathrm{i}k}{2d_1}\left(\xi^2+\eta^2\right)\right)}_{2} \\ & \cdot \int_{-\infty}^{\infty}\int_{-\infty}^{\infty} P(x,y) \underbrace{\exp\left(\frac{\mathrm{i}k}{2}\left(\frac{1}{d_1}+\frac{1}{d_2}-\frac{1}{f}\right)\left(x^2+y^2\right)\right)}_{3} \\ & \cdot \underbrace{\exp\left(-\mathrm{i}k\left(\left(\frac{\xi}{d_1}+\frac{u}{d_2}\right)x+\left(\frac{\eta}{d_1}+\frac{v}{d_2}\right)y\right)\right)}_{4} \mathrm{d}x\,\mathrm{d}y. \end{aligned} \tag{3.3}$$

Here, λ is the wavelength of the light and $k = 2\pi/\lambda$ the corresponding wavenumber. The pupil function $P(x,y)$ accounts for the finite size of the lens. It is 1 for (x,y) inside the lens' free aperture and 0 elsewhere. Equation 3.3 can be simplified significantly.

- Term 1 can be neglected as we are only interested in the intensity distribution in the image plane and therefore the amplitude information of the field .
- Term 2 could potentially affect the imaging process due to the convolution given in Eq. 3.1. However, for a good imaging system the PSF should be close to a delta distribution which implies that only a small region in the object plane affects the field at a given point in the image plane. Using the magnification M yields:

$$\exp\left(\frac{\mathrm{i}k}{2d_1}\left(\xi^2+\eta^2\right)\right) \approx \exp\left(\frac{\mathrm{i}k}{2d_1}\frac{u^2+v^2}{M^2}\right). \tag{3.4}$$

  Therefore, term 2 can be neglected similar to term 1.

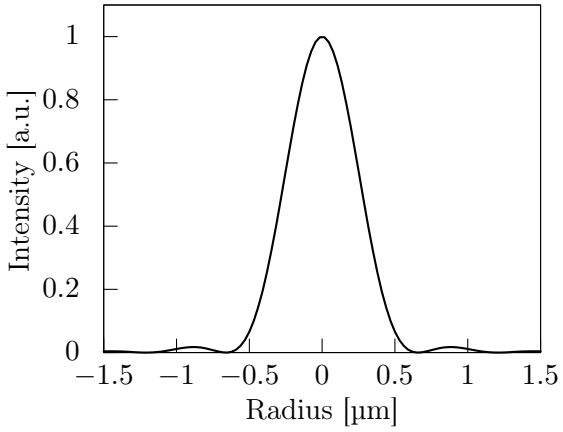

Figure 3.2: The squared PSF for a perfect lens with the optical parameters of our microscope objectives. The position of the first minimum determines the resolution according to the Rayleigh criterion.

- Term 3 can be neglected if d_2 is chosen such that $\frac{1}{d_1} + \frac{1}{d_2} = \frac{1}{f}$. This is exactly the classical lens law for geometrical optics.
- Rescale the coordinates in the object plane $\tilde{\xi} = M\xi$ and $\tilde{\nu} = M\nu$.

Hence,

$$h(u, v, \xi, \eta) \approx \frac{1}{\mathrm{i}\lambda^2 d_1 d_2} \cdot \int_{-\infty}^{\infty} \int_{-\infty}^{\infty} P(x, y) \cdot \exp\left(-\mathrm{i}k\left(\left(u - \tilde{\xi}\right)x + (v - \tilde{\eta})\, y\right)\right) \mathrm{d}x\, \mathrm{d}y. \quad (3.5)$$

This is the Fourier transform of the pupil function $P(x, y)$ of the lens. A circular ideal lens with diameter a and $(\xi, \eta) = (0, 0)$ results in

$$h(r) \propto \frac{\mathrm{J}_1\left(kar/d_1\right)}{kar/d_2}, \quad (3.6)$$

where J_1 is the Bessel function of the first kind and first order and $r = \sqrt{u^2 + v^2}$. The intensity distribution of a point like light source is the square of this result and is shown in Fig. 3.2.

The shape of the PSF can be used to define the resolution of an optical system. According to Lord Rayleigh [45] the resolution is given by the position of the first zero crossing of the PSF given in Eq. 3.6 which is also illustrated in Fig. 3.3:

$$r_R = 0.61 \frac{\lambda}{\mathrm{NA}}. \quad (3.7)$$

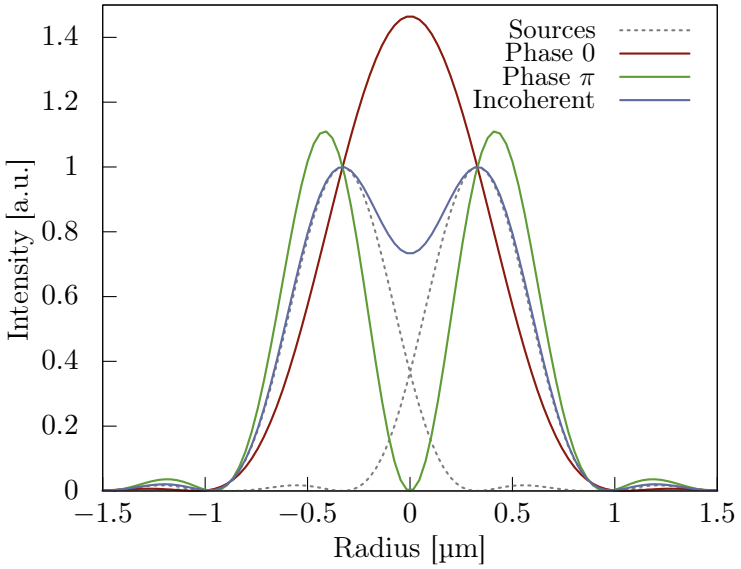

Figure 3.3: Illustration of the intensity distribution of two overlapping PSFs separated by the distance given by the Rayleigh resolution of our microscope objectives. It depends on the relative phase relation of the light emitted by the two sources if they can be separated after they have been imaged. In the case of absorption imaging, the light is typically coherent and the phase difference between neighbouring regions is small, which reduces the resolution of the optical system.

Here the numerical aperture is defined as $\mathrm{NA} = a/(2d_1) = \sin\theta$, where θ is the angle between the optical axis of the lens and the ray which passes the lens at the maximal distance to its centre as shown in Fig. 3.1.

This resolution is solely limited by the finite size of the lens, it is also referred to as the diffraction limit. The microscopes in our quantum gas experiment feature a numerical aperture of $NA = 0.62$ which corresponds to a resolution of $r_R = 660\,\mathrm{nm}$ for the imaging wavelength of 671 nm. Another possibility to define the resolution is to claim that two points in the object plane can be separated as long as their overlapping PSFs in the imaging plane have a minimum in between. This is the so called Sparrow criterion. The corresponding expression in terms of the numerical aperture is:

$$r_S = 0.47\frac{\lambda}{\mathrm{NA}}. \tag{3.8}$$

The above considerations for the resolution assume an incoherent light field. For two overlapping PSFs the total intensity consequently is the sum of the two individual intensities. For coherent light the amplitudes of the fields have to be added and the phase difference of the light emitted by the two sources has to be taken into account as shown in Fig. 3.3. In the case of absorption imaging, the light is strongly coherent and the resolution is reduced if the imaging light travels along the optical axis (due to Babinet's

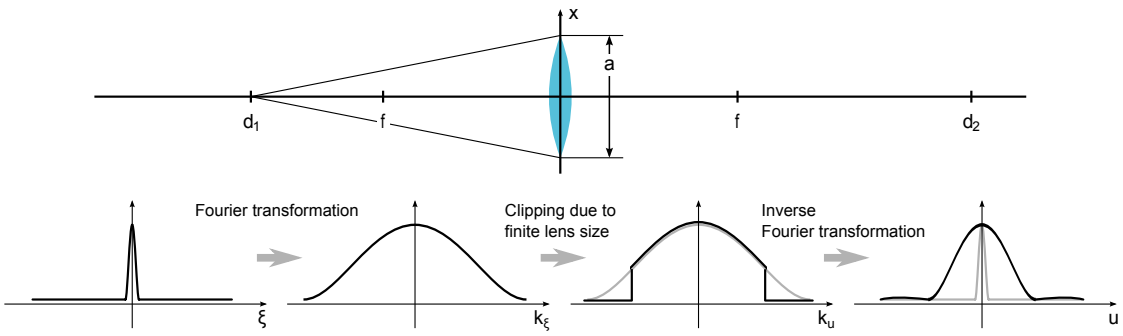

Figure 3.4: Illustration of how a finite aperture of an otherwise ideal lens limits the resolution. The small object corresponds to a broad distribution in momentum space ((k_ξ, k_η)-space). Each momentum corresponds to a certain angle. The lens can only accept angles up to a certain value and therefore clips the momentum distribution. The inverse Fourier transformation then yields a broadened image on the imaging plane.

principle). For fluorescence imaging, a certain degree of incoherence can be achieved which improves the resolution. A detailed analysis about the degree of incoherence for the example of fluorescence imaging of a 2D MOT insulator can be found in Ref. [46].

Another way to look at the phenomenon that even an ideal lens has only a finite resolution is as follows, see also Fig. 3.4. The spatial Fourier transform of the object in the ξ and η directions corresponds to a certain distribution of wave-vectors k_ξ and k_η. The total length of the wavevector is fixed by the wavelength of the light $k = 2\pi/\lambda$. Therefore, a given (k_ξ, k_η) determines a certain angle with respect to the imaging axis under which the corresponding ray propagates through space. If this ray cannot pass the pupil defined by the lens the momentum information is lost. Therefore, the finite size of the lens acts is a rectangular filter in k-space. The propagation from the lens to the imaging plane corresponds to the inverse Fourier transformation. As the high momenta components are clipped by the pupil the resulting PSF must have a finite width. For a shorter wavelength (larger k) the same (k_ξ, k_η) corresponds to a smaller angle. Consequently, smaller features can be resolved by using shorter wavelengths.

Real lenses, aberrations

Real lenses or lens assemblies often do not reach the limit of diffraction-limited resolution, due to aberrations caused by imperfections of the lenses themselves and inaccurate alignment of the system. Both result in a broadening of the PSF and thus in a reduced resolution. The higher the numerical aperture of an optical system, the more effort has to be put into the design of the system such that it operates close to the diffraction limit. Aberrations can be classified as monochromatic or chromatic. The latter are caused by wavelength dependent effects of the optical system on the transmitted light. An example would be chromatic focal shift where the focal length of a lens varies with the wavelength of the light. Monochromatic aberrations, in contrast, appear even when using a single

wavelength. In the case of imaging an ultracold gas cloud the light used is monochromatic and the corresponding aberrations have to be considered.

Lord Rayleigh showed that for a spherical aberration of 0.25 λ (absolute) the resolution is close to the diffraction limit with a Strehl ratio of $S = 0.8$. The Strehl ratio is defined as the peak intensity of the image compared to the maximum attainable value achieved with an ideal, diffraction-limited lens. For arbitrary aberrations, the situation is more complex and the actual resolution depends on the specific type of the aberration. An analytical study for several types of aberrations can be found in Ref. [47]. An approximate formula to calculate the Strehl ratio for a given aberration is derived in Ref. [48]:

$$S = \exp\left(-\left(\frac{2\pi\sigma}{\lambda}\right)^2\right). \tag{3.9}$$

Here σ is the root-mean-square deviation of the wavefront of the light with wavelength λ. According to this expression an aberrated wavefront with $\sigma/\lambda < 0.07$ results in a resolution close to the diffraction limit ($S < 0.8$).

The monochromatic aberrations can be further classified by the Zernike polynomials which can be used to fit the aberrated wavefront. According to this classification the lowest order, and typically most influential, aberrations are defocus, astigmatism and coma which are illustrated in Fig. 3.5:

- **Defocus:** Defocus results in a parabolic wavefront at the imaging plane. In our experiment it can be easily corrected for by adjusting the distance between the microscope and the atoms. The distance on the object side over which the lens can image a source with diffraction-limited resolution is called the depth of field. A lens with a high numerical aperture has a short depth of field which then requires precise focal adjustment of the objective and a flat sample.

- **Astigmatism:** Astigmatism is described by a Zernike polynomial of the same order as defocus but with additional azimuthal contribution. The optical system has two different focal lengths in the sagittal and tangential direction. As a result, a point-like light source can only be focused to the diffraction limit in one of the two directions. Astigmatism is the major aberration observed if our microscope objective is not well aligned with respect to the glass window of the science cell.

- **Coma:** If defocus and astigmatism could be eliminated by design and alignment, coma will become significant as next-order effect. It affects objects located away from the optical axis and the resulting image appears wedge shaped. If the microscopes are misaligned with respect to the science cell windows in our experiment, coma is observed in addition to astigmatism.

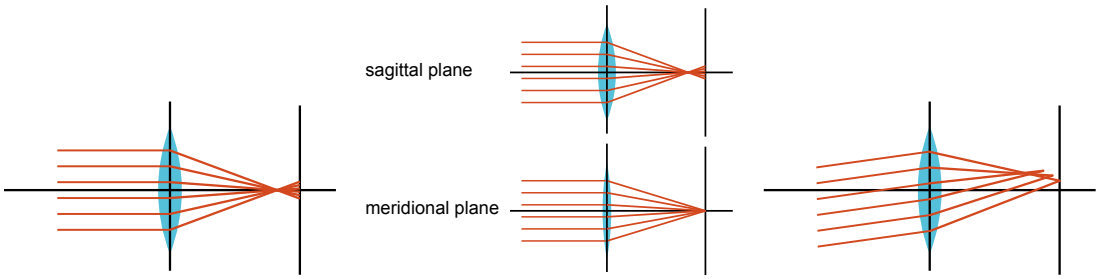

(a) Defocus (b) Astigmatism (c) Coma

Figure 3.5: The three main types of aberrations encountered in our high resolution microscope system: defocus, astigmatism and coma. Defocus is the aberration where the focal point is positioned in front of or behind the imaging plane. This results in a circular blurring of the image. Astigmatism occurs if the lens has different focal lengths in the sagittal and meridional planes. This might arise from design (e.g. cylindrical lens), manufacturing or alignment errors. As a result, only one of the two directions can be in focus at a time. Coma affects only off-axis light sources. The position of the focal point depends on the distance between the corresponding ray and the optical axis of the lens. Lenses which are corrected for coma are called aplanatic.

Correction strategies to reduce aberrations

A simple spherically curved lens shows strong aberration and diffraction-limited resolution can only be achieved for small numerical apertures. If higher resolutions are required, lens combinations can be used, where different aberrations of the single lenses cancel each other. The higher the required resolution, the more complex the design and the smaller the manufacturing and alignment margins. If chromatic aberrations have to be reduced as well, different glass types can be used in combination. Lenses that are corrected for chromatic aberrations are called achromats (same focal plane for two wavelengths) or apochromats (same focal plane for three wavelengths).

3.1.2 Concept of the system

The basic concept of our high resolution imaging optics is the infinity corrected microscope. The system consists of an objective with a high numerical aperture placed close to the atom cloud which is imaged. The light emitted by an imaginary light source at the position of the atom cloud exits the objective as a collimated beam and is guided to a telephoto lens assembly which focuses the light onto a CCD detector. A sketch of the setup is shown in Fig. 3.6. A symmetric arrangement of two objectives was chosen, where one is used for imaging in connection with the telephoto lens and the other to guide highly focussed beams onto the ultracold sample. Those beams can affect the atoms via the dipole force and can thus be used for manipulation with high resolution. The testing and development of the microscope system was part of the master's project

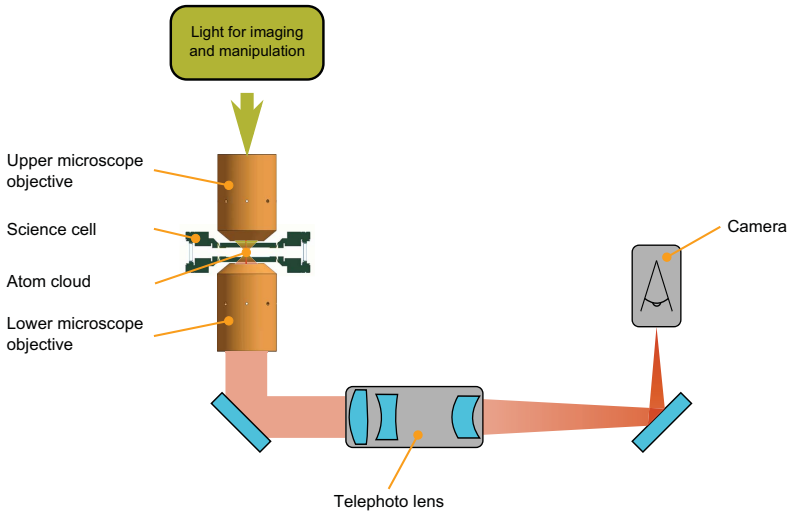

Figure 3.6: A sketch of the high resolution optics arrangement in our experiment. The lower microscope objective and the telephoto lens are primarily used for imaging. The upper microscope objective is used for high resolution manipulation of the cold gas with focussed laser beams. The imaging beam for absorption imaging enters via the upper objective as well.

of Jan-Henning Drewes [10].

Microscope objectives and telephoto lens

The main components of the imaging system are the two microscope objectives. Together with the telephoto lens they form an optical system of high performance and they are a key component of the machine. The experimental apparatus is designed specifically to allow the placement of those objectives and to provide the conditions for them to perform well. The general properties of the optics are:

- Numerical aperture of 0.62 which corresponds to a spatial resolution of 660 nm for light with a wavelength of 671 nm (Rayleigh criterion). This is on the order of several intrinsic length scales of the gas which can be expected for the experiments we plan like the healing length, inter atom distance or lattice constants for experiments with optical lattices.

- Diffraction-limited performance for the imaging wavelength of 671 nm. This corresponds to a wavefront deviation of less than 0.07 root mean square or 0.25 absolute as described above.

- Diffraction-limited performance for other wavelengths which are possibly used in the experiments ranging from 532 nm to 780 nm.

- Correction for the science cell windows. To achieve the required resolution it is crucial to correct for the effects of the windows of the science cell. For the same reason the manufacturing requirements for wedge-angle and accurate thickness of the window are strict as well.

- Non-metallic materials. The objectives are placed in the central bore of the large magnetic field coils around the science cell. Any response of the microscopes to varying magnetic fields would have a negative influence on their performance.

- The diameter of the housing of the objectives is 44 mm. If the objectives would be larger, there would be not sufficient adjustment range inside the central bore of the magnetic field coils.

- Field of view of 150 µm in diameter. This reflects the estimated size the our atom clouds.

- No cemented surfaces. This is a particularly exotic requirement for such microscope objectives. It is planned to guide a red-detuned dipole trap through the upper microscope objective with a wavelength of 1064 nm. As the detuning with respect to the transition wavelength is quite large, high beam powers are necessary to create a deep trap. The approximate radius of the laser beam[1] is 370 µm in the plane of the atoms. A beam with such a spot size at the place of the atoms is only slightly affected by the microscopes lenses, which means it does not change its diameter significantly when passing through the optics. The intensity of the beam is estimated to reach values up to 10 kW/cm^2 inside the microscope objective to create a dipole trap of sufficient depth. According to the manufacturer of the objective, optical cement would not be able to withstand such intensities. As a consequence, an air spaced lens design is chosen for which imposes no intensity limitations.

- Low chromatic focal shift for the specified wavelengths (532 nm to 780 nm).

- The telephoto lens is compatible with the full the numerical aperture of 0.62 offered by the microscope objective.

The requirements for the optics were challenging to meet, so the design and manufacturing work was assigned to a company specialised on precision optical components[2]. The final design for the microscope is an eight-lens objective shown in Fig. 3.7. It reaches the requested numerical aperture of 0.62 and operates diffraction-limited for wavelengths ranging from 532 nm to 780 nm. It has an effective focal length of 26.2 mm which results in a beam diameter of 32.5 mm behind the objective if a point-like light source is located in the focal plane. Further properties are collected in Tab. 3.1 on page 67.

[1] $1/e^2$ intensity
[2] Special Optics, New Jersey, USA

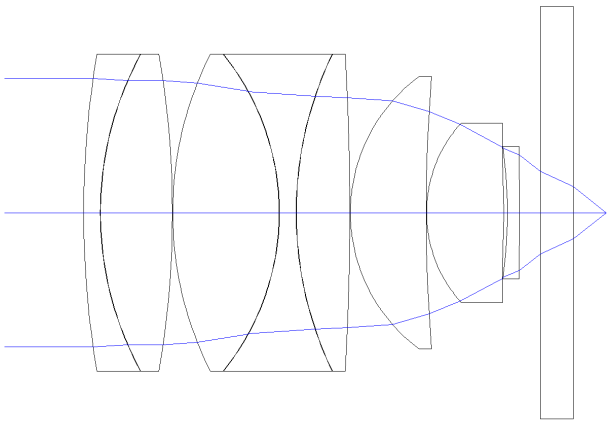

Figure 3.7: The lens design of the microscope for the high resolution imaging and manipulation system. All the lenses are air spaced to avoid the usage of optical cement which would limit the maximally allowed light intensity. The two planar surfaces at the right side of the drawing symbolize the window of the science cell. The diameter of the largest lens in the drawing is 19.2 mm. The numerical aperture achieved by the objective is 0.62.

Polarisation management

There is an issue caused by the possibility of shining in a far detuned dipole trap via the upper microscope. The beam creating such a trap will also pass through the lower microscope objective and the telephoto lens and will finally reach the camera. As the camera contains a highly sensitive CCD sensor it must be protected from such high-intensity beams. Filters can only be a solution if the powers and intensities involved are not too high due to typically low damage thresholds. A more elaborated solution is to make use of the polarisation of the light. In front of the upper microscope objective and behind the lower one large multi-order waveplates[3] are placed (diameter of free aperture 34 mm), which act as quarter waveplates for the imaging wavelength of 671 nm. In addition a polarising beam splitter cube[4] (edge length 40 mm) is installed in front of the telephoto lens as shown in Fig. 3.8.

The concept is as follows: the imaging light is linearly polarised before it passes through the first quarter waveplate. This waveplate is oriented such that the light exits circularly polarised to drive the imaging transition of the atoms. After the light passes the two microscope objectives and the atom cloud, which does not change the polarisation, the second waveplate changes the polarisation back into a linear one. The following polarising beam splitter cube is oriented such that the light can pass and continue to the camera via the telephoto lens. The two waveplates are compensating each other and in combination they act as an effective zero-waveplate. This holds for all wavelengths. The

[3] LENS-Optics, W4M36-671
[4] LASEROPTIK, custom made with optical contact bond

high-intensity dipole trap beam with a wavelength of 1064 nm has a linear polarisation perpendicular to that of the imaging light before reaching the first waveplate. After exiting the second waveplate it is still linearly polarised perpendicular to the polarisation of the imaging light. The beam splitter cube thus efficiently separates the high-intensity beam from the imaging light and guides it to a beam dump. As the waveplates are not designed for the wavelength of 1064 nm their effect on this light is difficult to predict. Most likely the polarisation of the dipole trap beam is elliptical between the two waveplates. As the dipole force is polarisation independent this has no negative effect on the performance of the trap.

The proper function of this concept to protect the camera depends on the purity of the polarisation in front of the first waveplate, the precise adjustment of the waveplates with respect to each other and the optical quality of the components used. A complete suppression of the dipole trap beam power which reaches the camera can thus not be anticipated. A high quality band-pass filter[5] is placed in front of the camera to block any remaining light which could damage the CCD sensor or distort the acquired images. The filter also blocks any low intensity light of other wavelengths which potentially are used for manipulation of the ultracold gas cloud.

Camera

The high resolution imaging employs an Andor Ixon EMCCD camera which contains a back-illuminated 512×512 pixel CCD sensor. Its entrance window is anti-reflection coated for several wavelengths including 671 nm. In addition the window is wedged by 0.5° to avoid undesired interference effects. The effective pixel size at the position of the atoms is 400 nm × 400 nm and the field of view of the camera is 200 µm × 200 µm, matching the field of view of the microscope objective. This camera was selected since it offers optimal performance for low photon numbers which we expect for fluorescence imaging and it already has proven itself to be a reliable component in other ultracold atom experiments, e.g. in the lithium experiment in Zurich [49].

Mechanical design

To hold the microscope objectives in their position, it was necessary to design and build a stable and precisely adjustable mounting system. Imaging in the sub-µm regime requires optics which are stable on at least a similar length scale over a long time. It is important to design the mounts such that they are adjustable, since precise alignment of the microscope objectives is necessary to achieve diffraction-limited resolution. An independent requirement is the insensitivity to magnetic field influence as the microscopes operate in a high magnetic field environment. The concept is based on the design which is used in the experiment in Zurich [15], Fig. 3.9 shows a sketch. It is a stacked assembly with multiple stages that offers different degrees of freedom for coarse and fine adjustment.

[5] Semrock, single-band bandpass filter 661/20-25

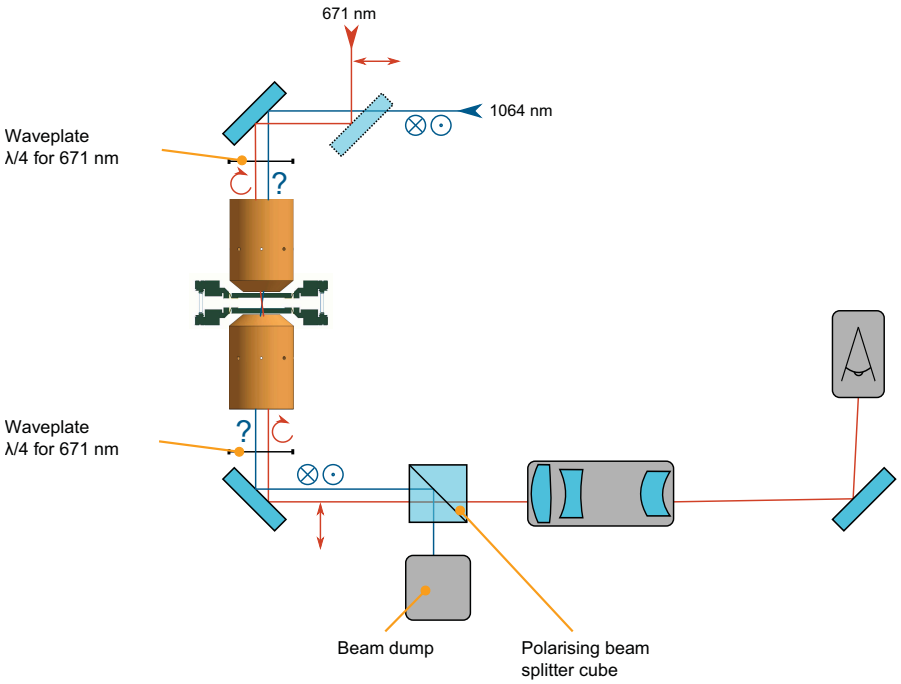

Figure 3.8: The polarisation concept of the imaging system. Two waveplates are placed in the setup such that their net effect is that of a zero-waveplate. Hence, the polarisation of a beam is maintained after passing both waveplates, independent of the wavelength. Therefore, a polarising beam splitter cube can be used to separate two beams which are linearly polarised perpendicular to each other before entering the optical system. The two waveplates are designed as quarter-waveplates for the wavelength of 671 nm to create the desired circular polarization for absorption imaging. The concept allows the efficient separation of high-intensity beams from the imaging light to protect the camera.

The stack for the lower microscope is described in the following. The upper stack is very similar apart from that the spacer block and the turning mirror are missing.

1. **Base plate:** The base plate is mounted onto the optical table. It holds a 90° turning mirror to guide the light from the atoms towards the telephoto lens. A metallic mirror with minimal surface curvature is used for this purpose which also ensures that the polarisation of the light is not affected. The mirror does not change its position if any of the following adjustment stages moves. This is important for the alignment process described later in this chapter.

2. **Translation stage:** The manual translation stage[6] offers coarse adjustment in the two linear directions parallel to the optical table.

3. **Spacer block:** The spacer block offers the space required to place the mirror mounted on the base plate.

4. **Tilting stage:** The tilting stage offers the possibility to adjust the two tilt angles which are crucial for the correct operation of the microscope objectives. It is also used to adjust the position of the microscope along the imaging axis. The travel range offered in this direction exceeds 20 mm. This is particularly important to assemble the system as explained in section 3.1.4. It is a custom design, since no commercial system is available that meets the requirements.

5. **Piezo stage:** For precise adjustment of the microscope objective in the three linear directions, a three-axes piezo stage[7] is used. It offers a travel range of 100 µm in all directions. Strain gauges allow an active stabilization of the stage to suppress any long-term drifts and piezo hysteresis. The stage can be used to quickly change the microscope position from one experimental cycle to the next without the need to open the shielding of the apparatus.

6. **Connector tube:** The connector tube connects the microscope objective with the piezo stage. It is manufactured from the same material as the microscope housing[8] and hence is absolutely insensitive to magnetic fields. Its thermal expansion coefficient is similar to aluminium which reduces thermally induced stress and even compensates certain expansion effects as the table on which the upper microscope mechanics are mounted is made from aluminium. The large waveplate for the polarisation management is kept in place by the connector tube as shown in Fig. 3.9.

7. **Microscope objective:** The microscope objective itself is mounted on top of the connector tube.

[6] OWIS, KT 90-D56-EP
[7] piezosystem jena, Tritor 102 SG
[8] Material: Ultem® 2300, PEI-GF30

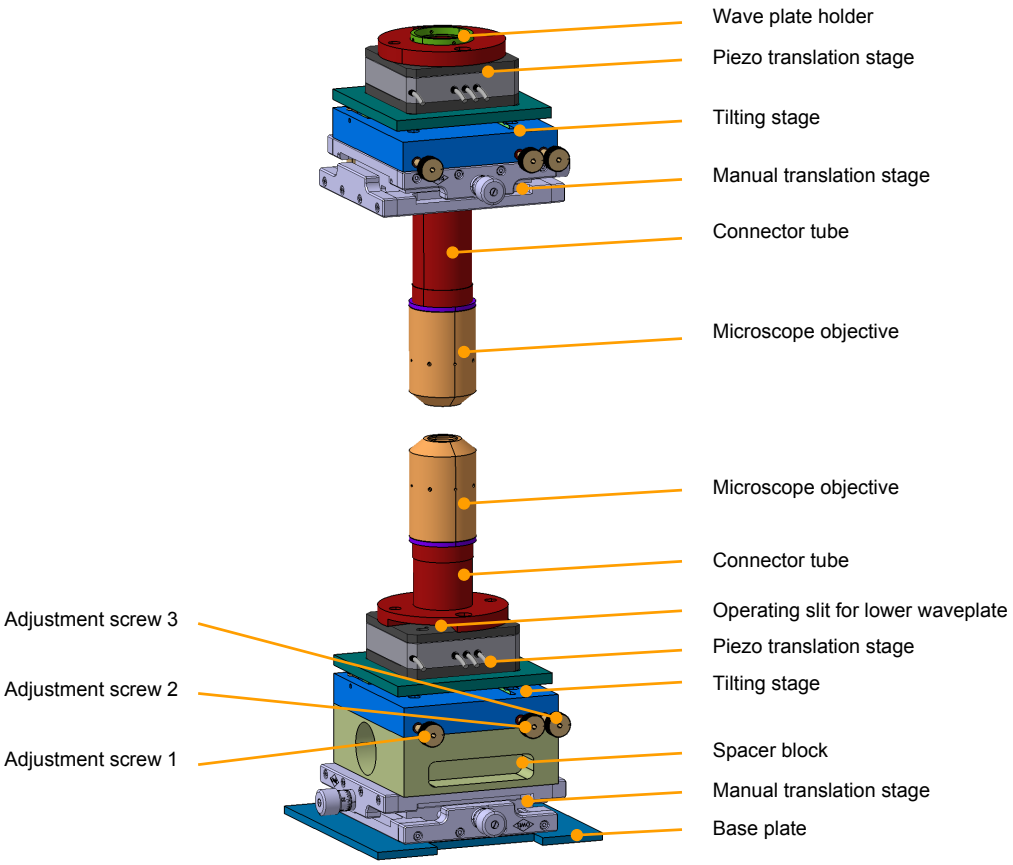

Figure 3.9: A sketch of the mount assembly for the microscope objectives. It offers precise and accurate positioning of the objectives in all three linear directions and for the two relevant angles. The labelling of the adjustment screws is important for the alignment process.

Description	Value
Objective, Numerical aperture	0.62
Objective, Effective focal length	26.2 mm
Objective, Design wavelengths	532 nm to 780 nm
Objective, Field of view	150 µm in diameter
Objective, Working distance Last lens - Atoms	10.5 mm
Objective, Working distance Last lens - Window surface	2.5 mm
Objective, Working distance Housing - Window surface	1.3 mm
Objective, Number of lenses	8
Objective, Chromatic focal shift	$<$ 2 µm for λ between 580 nm and 1064 nm
Objective, Transmission losses	532 nm: 16.7 %; 671 nm: 7.9 %; 1064 nm: 21.9 %;
Objective, Housing material	Ultem® 2300, PEI-GF30
Objective, Housing outer diameter	44 mm
Objective, Maximum tilt angle with respect to window for a wavefront deviation $<$ 0.25(absolute)	0.06°
Telephoto lens, Effective focal length	1000 mm
Telephoto lens, Number of lenses	3
Telephoto lens, Maximum tilt angle with respect to the imaging axis for a wavefront deviation $<$ 0.25(absolute)	0.25°
Telephoto lens, Maximum position shift with respect to the imaging axis	3 mm
Objective and telephoto lens, Anti reflection coating	Broadband 500 nm to 1050 nm
Objective and telephoto lens, Manufacturer	Special Optics, New Jersey
Objective and telephoto lens, Magnification	40
Camera, type and manufacturer	Andor Ixon back-illuminated EMCCD
Camera, pixel number	512 × 512
Camera, pixel size	16 µm × 16 µm

Table 3.1: Properties of the high resolution imaging and manipulation system

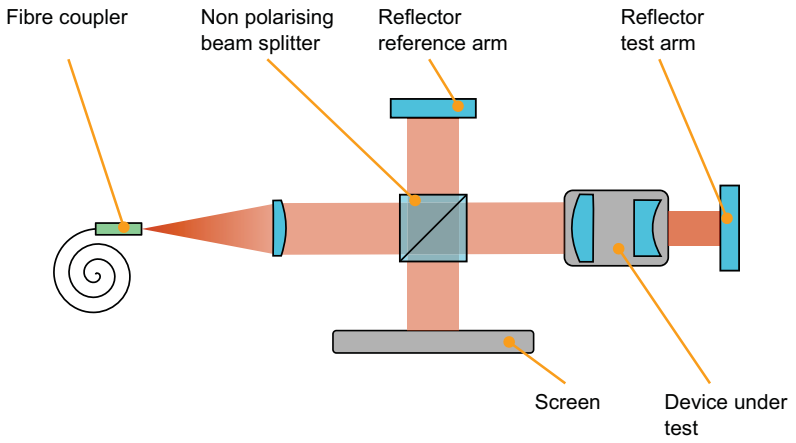

Figure 3.10: A sketch of the Twyman-Green interferometer to test optical components. It is a Michelson interferometer where one arm with a mirror of good quality acts as reference and the other arm contains the DUT as well as a back reflector with similar quality to that of the reference arm. Any wavefront deviation introduced to the beam by the DUT changes the interference pattern visible on the screen. If the DUT is focussing or defocussing the reflector of the test arm has to be chosen accordingly, as shown in Fig. 3.11. The screen can be replaced by a simple imaging system and a CCD camera.

3.1.3 Testing of the components

Due to the high complexity, it was necessary to test the performance of all components used for the high resolution optical system individually. After these individual tests a test setup was built to verify the performance of the whole system and to develop an alignment strategy. A proper alignment strategy is crucial due to the tight tolerances of the optical design of the microscope objectives. Diffraction-limited resolution can only be reached if the objectives are oriented perpendicular to the science cell windows with an accuracy better than 0.06°.

An Twyman-Green interferometer was used for the individual testing of single components [50]. A sketch is shown in Figure 3.10. The reference arm contains a good quality mirror which causes minimal wavefront deviation. The test arm contains the device under test (DUT) and a back reflector of good quality. The back reflector is chosen according to the properties of the DUT, either a plane mirror or a high quality spherical reflector[9]. Fig. 3.11 gives an overview over the different configurations. Spherical aberrations of mirrors can be difficult to measure with this setup as it is difficult to find back reflectors for the two interferometer arms which are not curved themselves. Figure 3.11(a) shows a solution to the problem.

Each type of optical aberration causes unique features in the interference pattern visible on the screen. A collection is shown in Fig. 3.12.

During the tests of several components used in the high resolution test setup, we ob-

[9]The group of Selim Jochim kindly lent us a reference sphere for that purpose

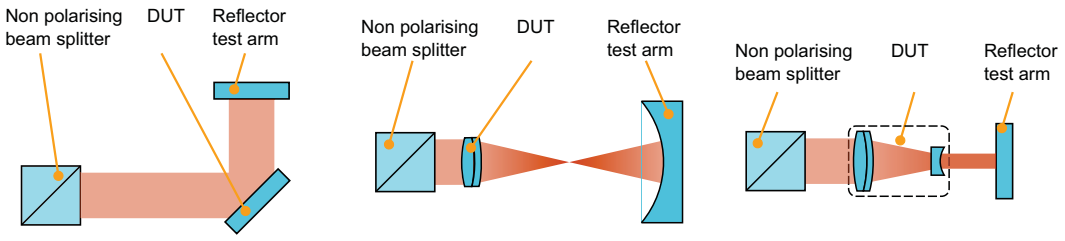

(a) Mirror (b) Focussing element (c) Non focussing element

Figure 3.11: Different configurations of the test arm of the Twyman-Green interferometer. If the spherical curvature of a plane mirror is under investigation configuration (a) is suitable. Due to the non-perpendicular incident beam, the mirror under test shows different effective curvatures in the sagittal and tangential beam direction. This results in an elliptical interference pattern and the curvature of the DUT can be separated from the curvature of the back reflectors. If a focussing elements is under test, configuration (b) is used. Care should be taken that the spherical back reflector is of high surface quality. Configuration (c) is suitable to test a non-focussing optical element. The reference arm and the light source are not shown in the figures for simplicity.

served that the Bragg mirrors used in our experiment show significant surface curvatures which causes wavefront deviations of up to 2 λ (absolute). We assume that the reason is mechanical stress induced by the coating but also the way how the mirrors are mounted in their mirror holders. It turned out that the common way of mirror mounting by using a locking screw which presses on the side of the mirror can cause the mirrors to bend significantly. As the mirrors are mostly used in a 45° configuration the resulting wavefront deviation is elliptical. This makes it impossible to compensate for the aberration with simple focus adjustment of lenses in the beam path. Mirrors with metal coating perform significantly better. If the usage of Bragg mirrors is unavoidable, tilted lenses in the beam path can be used to compensate the deviation to a certain degree. Spherical curvature of an even higher degree was measured for dichroic mirrors. Those aberrations have to be considered if high quality beams with several different wavelengths shall be combined by using such dichroic mirrors. For focussing a beam to a diffraction-limited spot with the microscope objectives it is absolutely necessary to correct the aberrations which are caused by the curved mirrors.

After verifying that each optical element which is part of the high resolution optical system performs within the specifications, the system as a whole was analysed in a dedicated test setup. It contained a mock-up of the science cell to simulate the real cell of the experiment. Details about this test setup can be found in Ref. [10]. An alignment strategy was developed by using this setup which is described in the next section. To

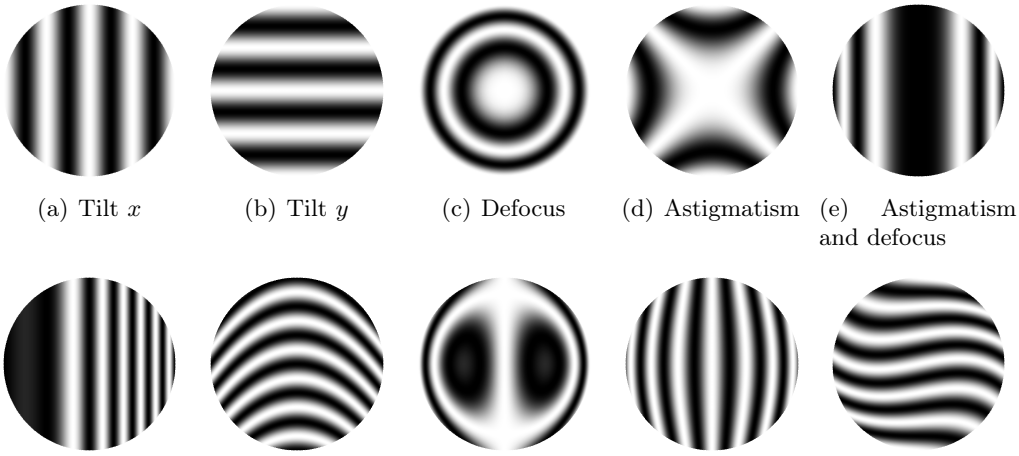

(a) Tilt x (b) Tilt y (c) Defocus (d) Astigmatism (e) Astigmatism and defocus

(f) Astigmatism, defocus and tilt x (g) Astigmatism, defocus and tilt y (h) Coma (i) Coma and tilt x (j) Coma and tilt y

Figure 3.12: Simulated interference patterns which could be obtained with the Twyman-Green interferometer. Tilt can be obtained by tilting the mirror in the reference arm and should not be considered as aberration (a), (b). Defocus can be a result of a curved reflector in the reference arm or a wrong distance between a focussing DUT and the spherical reflector in the test arm (c). For focussing elements (e.g. a microscope objective) defocus can be corrected by refocusing. Astigmatism and coma can be caused by misalignment or manufacturing errors of the optical elements (d), (h). Depending on the presence of additional defocus and tilt the resulting interference patterns change significantly (f), (g), (i), (j).

measure the resolution of the adjusted imaging system, small scale targets[10] which were placed inside the mock-up cell were imaged. This and other testing methods are presented in section 3.1.5 including an interferometric approach which offers several advantages to the imaging of known targets.

[10] 1951 USAF resolution test chart, group 9 with smallest element 3; and a pinhole target with hole diameter $< 1\,\mu m$ manufactured by Lenox Laser

3.1.4 Integration and alignment

To build a high numerical aperture optical system which reaches the diffraction-limited resolution, high precision and accuracy are required in the manufacturing and in the alignment process. Any misalignment of the lenses used will cause aberrations and distort the final performance. As a logical consequence the microscope objectives used in our machine have to be aligned with high accuracy with respect to the windows of the science cell. The allowed angular tolerance is 0.06°. To reach this accuracy an alignment procedure was developed by using the test setup. In this section I will present this procedure in a step by step manner in detail such that it can be used as an instruction manual for future alignment. A reader of general interest may skip this section. The strategy is first to set up guidance beams which are well aligned with respect to the windows of the science cell and then use those beams to align the microscopes and the telephoto lens. An overview of the used components is given in Fig. 3.13.

Before starting the alignment the machine has to be able to produce a cold atom cloud which is trapped within the magnetic field centre of the coils around the science cell (e.g. by using the transport dipole trap). These trapped atoms will serve as a position reference for the alignment process.

1. **Set the upper guidance beam angle:** The upper guidance beam should be collimated and have a small diameter. Collimation can be checked with a shearing interferometer. After adjustment it should be precisely perpendicular to the upper window of the science cell. The adjustment is carried out by guiding the beam which is reflected from the upper window back into the fibre coupler of the upper guidance beam. A beam splitter can be placed in front of the fibre coupler on the laser table combined with a photodiode or CCD camera to observe that light was coupled back into the fibre. There is an angle of 0.5° between the upper and lower window of the science cell which is larger than the required accuracy for the microscope objective angle. A piece of paper with a small hole can be placed on the science cell to distinguish the reflection from the upper window from that of the lower window. The guidance beam is shone through the hole with a certain angle with respect to the windows. Only the back reflection of the upper window can be observed as the paper blocks the reflection from the lower one. Remove the piece of paper and memorize which reflection belongs to which window.

2. **Set the upper guidance beam position:** Prepare an atom cloud in the transport trap at the location of the magnetic centre of the coils around the science cell. The centre can be found by TOF imaging and minimizing the position shift during TOF. Set up a low resolution absorption imaging system and use the upper guidance beam as imaging beam to image the atom cloud. Move the guidance beam until it is centred with the atom cloud. The smaller the diameter of the guidance beam, the higher the accuracy that can be achieved.

3. Repeat steps 1 and 2 until angle and position of the upper guidance beam are

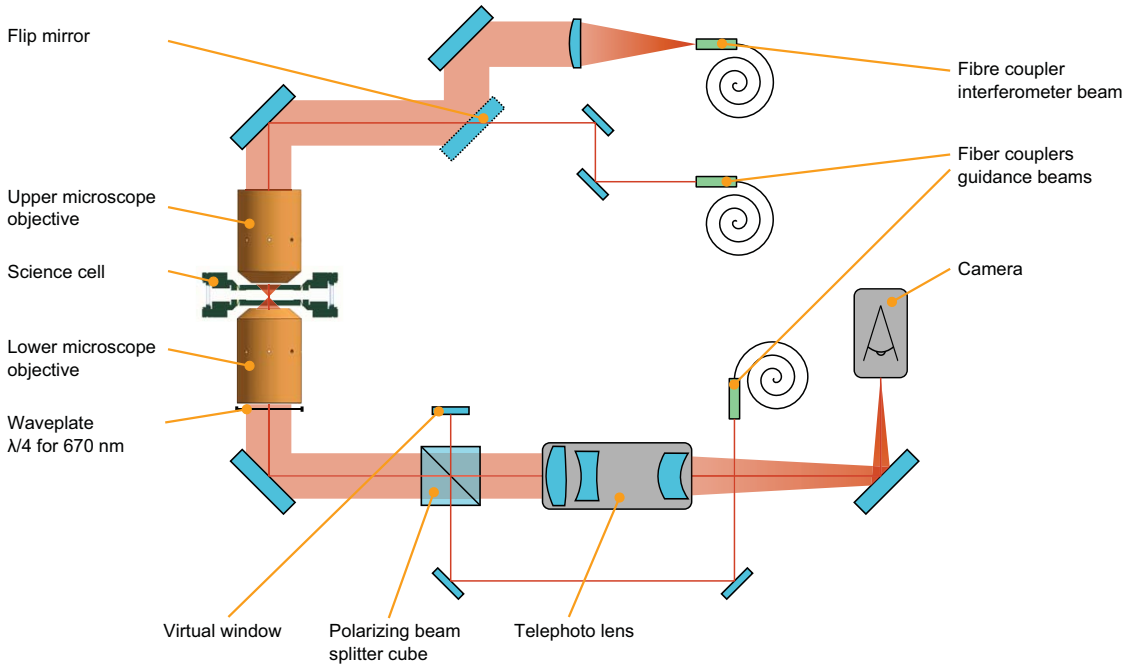

Figure 3.13: The adjustment setup for the high resolution optics. The two guidance beams are perpendicular to the science cell windows and serve as reference for angular alignment of the microscope objectives and the telephoto lens. The large-diameter interferometer beam is used for lateral positioning of the objectives as described in the text. It can be used for an interferometer in Twynman-Green configuration to test the quality of the alignment as shown in Fig. 3.15.

satisfactory and stable. Make sure that the guidance beam passes through all optical elements centred. Lock all adjustment screws of the mirror mounts and mark the fibre which is used for the guidance beam. If the guidance beam should be used again in future, it is important to use exactly the same fibre as each one has a slightly different connector.

4. **Set up the lower guidance beam:** Repeat the procedure described above in a similar way for the lower guidance beam. Use the reflection of the lower window as reference this time. Install the large polarizing beam splitter cube and the metallic turning mirror of the lower microscope mount for the guidance beam. Only use the baseplate with the mirror mount at this stage without all the other parts of the microscope mount assembly. Take care that this last mirror in front of the science cell is targeted at the centre by the adjusted lower guidance beam.

5. **Set up the virtual window:** Later in the process, after the microscope objectives are installed, the reflections of the guidance beams from the science cell windows cannot be used any more for alignment purposes as they are strongly divergent after passing through the microscope objectives. Therefore, a mirror is placed at one of the ports of the large polarising beam splitter which reflects the light of the lower guidance beam back into the fibre, as shown in Fig. 3.13. This creates a collimated reference beam on the path where the telephoto lens is placed after the lower microscope is installed and the back reflection of the window cannot be used any more. This step concludes the guidance beam setup. When working with the polarising beam splitter cube it might be necessary to install additional quarter-waveplates in the beam paths to obtain similar beam powers in all paths.

6. **Install the upper microscope objective:** It is necessary to temporarily remove the mirror holder which holds the last turning mirror in front of the science cell to install the upper microscope objective. It is required to re-mount it at exactly the same position after the upper microscope assembly is installed. For this purpose, several kinematic stops are placed on the vertical breadboard defining a reference edge. If the same person mounts the mirror several times in a row a reproducibility of the angle below 0.01° for the reflected laser beam can be achieved after practising. When screwing the microscope objective to its support tube, strong tightening should be avoided as this could cause the internal lens alignment to deteriorate. During the installation, extend the three plungers of the tilting stage to their maximum to ensure that the microscope objective does not crash into the science cell window. Lower the microscope by retracting the plungers of the tilt stage. A lens cleaning tissue can be placed on the cell to ensure sufficient spacing between the objective and the science cell window. Everything is safe as long as it is possible to move the tissue back and forth.

7. **Align the upper microscope objective angle:** Place the alignment glass plate (the one with two strings attached to it) into the rectangular holes cut into the

connector tube and make sure it rests stable on the edge of the microscope housing. Use the upper guidance beam to adjust the angle of the microscope assembly. The back reflections from the alignment glass plate should return to the fibre coupler. The alignment glass plate has a small wedge angle and two back reflections can be seen. The alignment should be performed such that the two reflections are symmetrically placed around the fibre coupler. The placement of the glass plate inside the connector tube is a delicate task with the risk of damaging the microscope objective. Prior practice is recommended.

8. **Set up the large-diameter interferometer beam:** Create a collimated laser beam with a diameter of approximately 33 mm. This beam will later be used to check the proper performance of the whole system but it is also utilized for the alignment procedure. It enters the upper microscope objective along the same path as the upper guidance beam via flip mirror mounts. Make sure the beam is well aligned with respect to the upper microscope using the alignment glass plate. Check for proper collimation in front of the last mirror with a shearing interferometer.

9. **Align the upper microscope objective position:** The (low resolution) imaging, which previously served to determine the correct position of the upper guidance beam, is used to place the upper microscope objective at the correct spatial position. The interferometer beam is focused by the upper microscope to a diffraction-limited spot which can be imaged with the imaging system below the cell. Use the tilt stage and the manual translation stage to move the microscope objective until the imaged beam is at the same place where the atoms where previously imaged and the spot size is minimal. Make sure that during the procedure the piezo stage is in a neutral position in all three directions to provide sufficient adjustment range for later corrections.

10. Repeat steps 8 and 9 until angle and position of the upper objective are satisfactory and stable. Remove the alignment glass plate. Remove the lower low resolution optics.

11. **Install the lower microscope:** The installation of the lower microscope and the positioning stages works in multiple steps. During the process, do not move the base plate of the positioning stages and the large polarizing beam spitter. Install each individual part of the mount assembly separately, starting with the manual translation stage. The last item to install is the lower microscope objective mounted on its connector tube. Do not separate them! It is necessary to lower the tilt stage to its minimum[11] to install the mounting tube on the piezo stage. Install the lower large-diameter waveplate. After the complete assembly is installed, raise the microscope by extending the plungers of the tilt stage. Again take care not to crash into the science cell window.

[11] Caution: The minimum distance is 2 mm before the platform touches the base.

12. **Align the lower microscope angle:** Use the lower guidance beam to align the angle of the lower microscope objective. Several back reflections of the lower guidance beam can be seen in front of the port of the polarizing beam splitter which faces the camera. One originates from the virtual window and another from the waveplate installed in the lower microscope connector tube. When the waveplate holder is turned, the corresponding back reflection will trace out a circular pattern. The centre of this circle should be aligned with the back reflection originating from the virtual window. It is easier to achieve this if the reflections are guided to a screen or wall a few metres away from the cube. The lower microscope objective is not mounted perfectly perpendicular to the waveplate as the mount tube is slightly bended. Screw 1 has to be turned 225° clockwise and screw 2 180° clockwise to compensate this bend. The screw labelling is shown in Fig. 3.9. Mark the position of the centre of the circle which is now traced out by the reflection originating from the waveplate on the screen.

13. **Align the telephoto lens:** The lower guidance beam and the camera are used to align the telephoto lens. Mark the pixel number where the reflection of the virtual window hits the CCD sensor. Install the telephoto lens. Place a mirror on the exit side of the lens housing and position the lens such that the back reflection from that mirror and the one from the virtual window overlap. Remove the mirror and position the telephoto lens until the beam hits the camera at the same spot as without the lens. Iterate until the angle and the position are correct.

14. **Align the lower microscope position:** Image the focused beam created by the upper microscope and the interferometer beam with the lower microscope and the camera. Position the lower microscope objective until the spot has minimal diameter and is centred on the CCD sensor. Recheck the angular alignment with the help of the back reflection of the guidance beam from the waveplate.

If it is impossible to position the microscopes without touching one of the windows of the science cell, the magnetic centre has to be adjusted. This can be achieved by using one of the extra magnetic field coils which are placed around the science cell. The alignment of the transport dipole trap has than to be changed to the new centre and the microscope alignment can be repeated.

A general issue to consider is that if any component is screwed onto a breadboard or the optical table it takes a certain time until the system stabilizes. Drifts can be observed over several days. This should be kept in mind when doing any changes to the machine close to the high resolution optics.

3.1.5 Final testing and verification

As the proper alignment is crucial for the high resolution optics to perform as specified it is necessary to verify it. In our experiment several methods can be used to test the

quality of the alignment. They differ in which components are tested and if they just provide a quality measurement or also indications of what can be done to improve the performance. A combination of the methods listed below has to be employed to obtain a complete picture of the performance of the entire optical system.

- **Target:** The most straight forward method to check the imaging quality is to image a known, small-scale target placed in the object plane. The approach is very reliable and requires only very limited interpretation of the results. It can be easily used to extract information on astigmatism by comparing the optimal focal settings of the microscope for minimal spotsize in two perpendicular directions when imaging a small pinhole. This method measures the combined performance of the whole imaging system, including the telephoto lens and all other involved components. It is not possible to differentiate which element is misaligned if the performance does not meet the expectations. However, as the required accuracy for the objective is much higher than that for the other elements, it can be assumed that the major aberrations are caused by incorrect alignment of the objective. The main disadvantage of this approach is that it cannot be used in the real machine but only in the test setup. There is no possibility to place a target inside the vacuum cell. For future machine designs, it might be a helpful feature to allow the placement of a target inside the science cell. In addition this would simplify the alignment of the microscopes. As the method requires a complete imaging system, including a telephoto lens and a camera, the alignment of the upper microscope objective has to be tested separately.

- **Focused beam:** One method to test the performance of the whole imaging and manipulation system is to use a high quality beam with large diameter, focus it with the upper microscope and image the focus with the lower microscope objective and the telephoto lens. A measurement of the spotsize on the camera serves as a measure of the alignment quality. Figure 3.14 shows an example. This method is useful to verify the alignment. However, if the spot on the camera shows aberrations, it is difficult to find the reason. It might be misalignment of one of the two microscope objectives, the telephoto lens, the incident beam itself or any combination of those. The quality of the imaged spot on the camera depends significantly on the quality of the large-diameter collimated beam that enters the system from the top. The creation of such a beam is time consuming, see for e.g. Ref. [51]. Especially, the usage of dichroic mirrors in the beam path make a proper collimation of the beam rather complex. These dichroic mirrors show a strong spherical curvature which has to be corrected for, if they are used in reflection. The focussed beam method should thus be used only if a high quality beam with a large diameter is already available. Nevertheless, the method offers the possibility to check the relative alignment of the entire optical system. The method does not verify if the system is well aligned with respect to the position of the atoms.

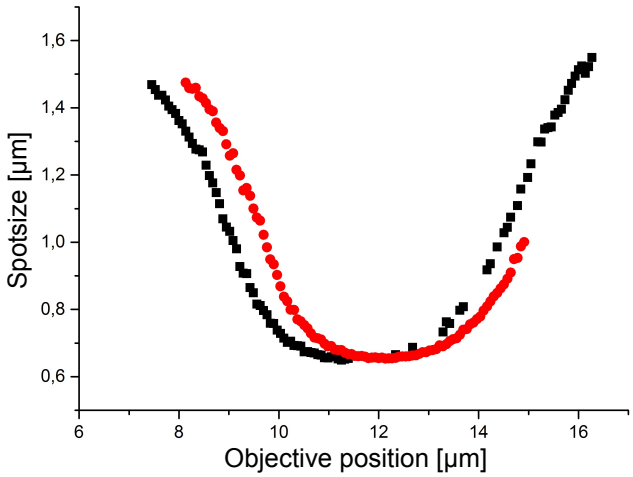

Figure 3.14: Measured spotsize ($1/e^2$ radius of a Gaussian fit to the intensity distribution) on the camera for imaging a highly focused beam for different focal settings of the microscope. The two curves correspond to the spotsize in two perpendicular directions. The imaging wavelength was 780 nm. The two curves are slightly shifted with respect to each other which is an indication for astigmatism. The measurement for this plot was performed by our former Bachelor student Martin Schlederer [51].

- **Interferometer:** The most feasible way to check the alignment of the microscope objectives is the Twyman-Green interferometer in the configuration shown in Fig. 3.15. The setup is very similar to the one described in section 3.1.3. A large non-polarizing beam splitter cube (NPBS) is placed on the upper optical breadboard right in front of the last mirror before the microscope to set up the interferometer. Two additional mirrors are used as back reflectors, one right behind the lower microscope mount assembly and the other behind one of the open ports of the NPBS. In combination with the large diameter interferometer beam, which was previously used to align the microscope objectives, and a screen on the remaining port of the NPBS the setup is complete. The working principle is the same as explained in section 3.1.3 with both microscope objectives and the science cell serving as DUT. The main advantage of the interferometric approach is that it not only provides precise information about the wavefront quality, but also shows the type of the aberration which causes any possible wavefront distortion. Figure 3.16 shows examples of interference patterns. Another advantage of this method is that only the optical system itself is tested. The actual beam quality of the laser beam used does not influence the interference pattern. The time required to set up this interferometer and check the alignment of the objectives is much less compared to the focused beam method. A complete check can be done in approximately one hour which makes this method also suitable for more frequent tests of the performance of the imaging and manipulation system. Note that this

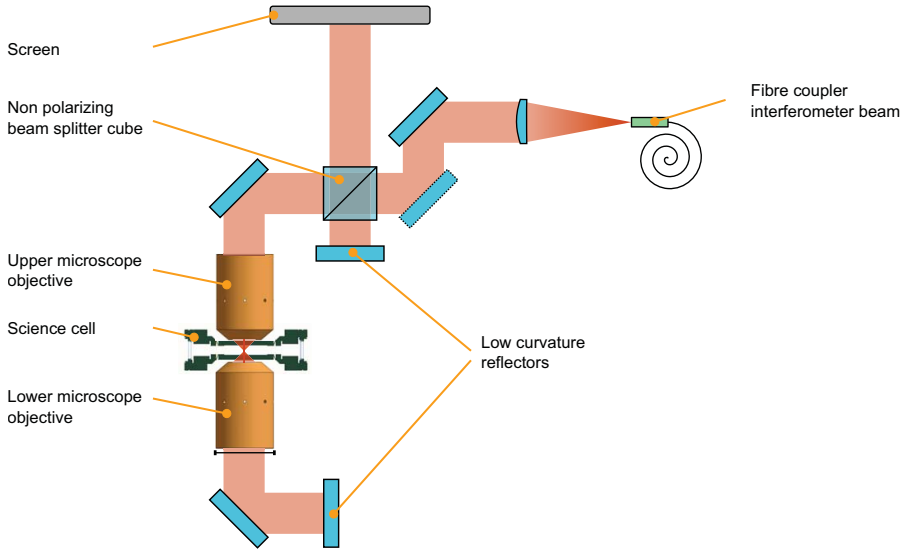

Figure 3.15: Setup for testing the alignment of the microscope objectives by using the interferometric approach. The additional elements compared to the configuration for image acquisition are the non-polarizing beam splitter cube, the screen and the reflectors for the two arms of the interferometer. As the interference pattern on the screen is determined by the difference of the two interferometer arms, the properties of the incident laser beam play only a minor role.

method only checks for relative alignment of the system and correct positioning with respect to the atoms has to be verified separately. If the back reflectors of the interferometer arms have different spherical surface curvatures, the optimal focal setting obtained with this approach is inaccurate and should be confirmed independently. The possibility to test the alignment of the microscope objectives with a Twyman-Green interferometer is quite unique to our experiment, as almost all other quantum gas microscope machines use only one microscope objective.

- **Atom noise:** A completely different approach to test the imaging quality is to look at spatial density fluctuations of the atom cloud [52]. The higher the resolution, the more spatial density fluctuations will be visible on the imaged clouds. This method tests the alignment of the lower microscope objective and the telephoto lens by directly measuring the resolution on the object which is supposed to be imaged. A possible approach would be to prepare a warm gas of atoms with very small intrinsic length scales (e.g. de Broglie wavelength) which are smaller than the diffraction-limited resolution of the microscope. The spatial density fluctuations in the sample are then present on the small intrinsic length scale. The autocorrelation matrix of an acquired image of the atom cloud will show a central peak. This peak is broadened by the PSF of the imaging system and can be used to determine the resolution. Care has to be taken that no density correlations in the atom cloud itself are responsible for the broadening of the central peak of the autocorrelation

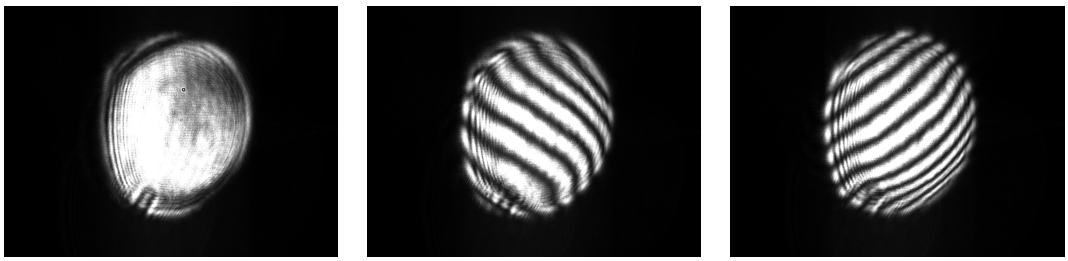

(a) (b) (c)

Figure 3.16: Interference patterns obtained with the properly aligned optical system by using the Twyman-Green interferometer (a) with incident light with a wavelength of 671 nm. A tilted reflector of the reference arm creates a characteristic stripe pattern (b,c). The total wavefront deviation is approximately 1 λ (absolute) after passing each microscope objective twice. This indicates that the system will operate close to diffraction-limited resolution if used for imaging. The remaining wavefront deviation seems to be mainly due to coma and higher order aberrations.

matrix. This method has not been applied to our experiment yet.

- **Single-atom light source:** The resolution of an imaging system is determined by its PSF. Thus the most direct way to determine the resolution is to look at the image of a point-like light source. Basically our machine is designed such that single-site resolution experiments in optical lattices can be performed. In such an experiment, a low filling of the lattice and strong spatial pinning of the atoms would ideally be suited to look at the PSF directly. This has not been done yet in our machine. If the machine should be used to perform optical lattice experiments in the future this method will probably be the most convenient technique to determine the performance of our high resolution imaging system.

For given experimental settings in our machine also other measuring and optimization methods become available. For example, if the upper microscope is used to create a highly focused beam which serves as an attractive dipole trap, it is possible to monitor the effect of that trap on a flat cloud of atoms from the side. The observed "suction"-effect can then be used to adjust the focus of the upper microscope objective as shown in Fig. 3.17.

3.1.6 Image acquisition and density retrieval

The absorption images which are acquired by the camera have to be processed to retrieve the density distribution of the atom cloud. A typical image of an atom cloud acquired in our experiment is dominated by features which are caused by the beam that is used to illuminate the atoms. One of such pictures is shown in Fig. 3.18 (a). Four pictures are acquired in total to retrieve the actual density distribution.

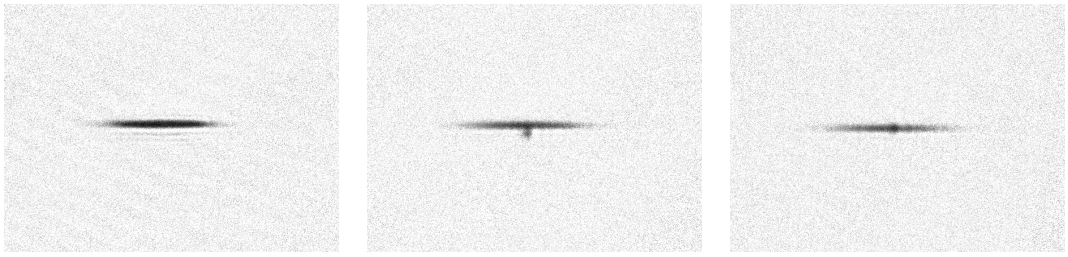

(a) (b) (c)

Figure 3.17: Images of atom clouds imaged from the side inside the science cell. A focussed red-detuned laser beam is shone onto the cloud via the upper microscope objective and pulls a fraction of the atoms out of the initial cloud. In Fig. (b) the beam's waist is located 0.8 µm below the atom plane. In Fig. (c) the waist is inside the atom cloud. Fig. (a) shows an undisturbed cloud. The images are adopted from Ref. [51].

1. One picture of the atoms. This picture contains the absorption information and all the features of the imaging beam.

2. One picture of the imaging beam. This picture is acquired a few milliseconds after the first picture. It only shows the imaging beam. The ratio between the first two pictures yields the optical density of the atom cloud. The kinetic mode of the camera[12] is used to take the two pictures in fast succession. Thus it is unlikely that optical elements drift during the time between the two acquisitions. Therefore, any fringes caused by interference effects can be reliably identified and removed by the analysis.

3. Two pictures without atoms and imaging light. These two "dark" pictures are acquired in the same way as the previous ones and are used to account for any pixel and stray light effects.

The pictures can be converted into "real" column-density information by using the modified Beer-Lambert law presented in Ref. [53]:

$$\tilde{n} = \frac{1}{\sigma}\left(-\alpha \log\left(\frac{I_{Atom}}{I_{Bright}}\right) + \frac{I_{Bright} - I_{Atom}}{s}\right). \tag{3.10}$$

Here I_{Atom} is the light intensity of the picture which contains the shadow image of the atoms. The intensity can be calculated from the corresponding CCD counts, known magnification of the system, absorption of the optical elements, quantum efficiency, pixel size,

[12] In this mode, the excitations created in the CCD segments by taking the first picture are shifted to a covered area of the sensor instead of being read out. This shift is performed fast and the second picture can be acquired quickly after the first one. Afterwards, both pictures, which are now stored on the sensor, are read out.

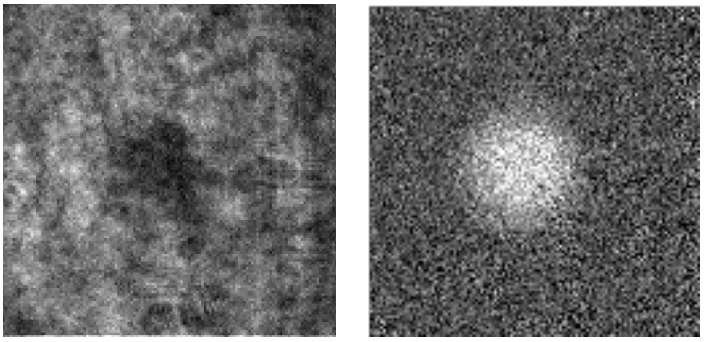

(a) (b)

Figure 3.18: Illustration of the density retrieval process. Figure (a) is an absorption picture as it is captured by the camera. It is dominated by the features of the imaging beam which illuminates the sample. Figure (b) shows the retrieved line-of-sight integrated density distribution.

CCD sensitivity of the camera and the illumination time. I_{Bright} is the corresponding intensity of the second picture which is acquired without the atom cloud. The photon-atom scattering cross section $\sigma = 3\lambda^2/(2\pi)$ is determined by the wavelength λ of the resonant imaging light. The saturation intensity of the imaging transition used is $s = 25.4\,\mathrm{W/m^2}$ (^{6}Li, D_2 line) [19]. The dimensionless parameter α accounts for any imperfections of the imaging process, like imperfect polarisation or not entirely closed atomic transitions. We estimate it to be $\alpha \approx 1.1$ in our experiments. If the saturation is low, the second term in Eq. 3.10 can be neglected. In the remaining part, the constants which connect the intensities I_{Atom} and I_{Bright} with the corresponding CCD counts cancel each other which significantly simplifies the calibration.

Equation 3.10 thus might suggest that the best way of imaging would be to use long duration, low intensity light pulses for absorption imaging in order to keep the saturation low. This is not entirely true, as long pulses cause blurring of the retrieved density distribution [49, 54]. The reason is that the atoms acquire a certain momentum for every absorbed imaging photon. Therefore, they are ejected out of the depth of field, if the illumination time is too long. This is particular significant in case of lithium, as it is a rather light atom. A suitable compromise between reduction of this blurring and saturation of the imaging transition is to work with approximately unity saturation.

Due to the low mass of lithium, the acceleration experienced by the atoms during illumination is significant. After approximately 40 absorption and re-emission events, the Doppler shift becomes larger than the transition linewidth and the atoms turn dark[13]. This is particularly important for fluorescence imaging with low atom numbers, e.g. in an optical lattice experiment. Here a strong pinning lattice combined with simultaneous

[13]The Doppler shift equals 3 MHz for a velocity of $2\,\mathrm{m\,s^{-1}}$ which is half the linewidth of the imaging transition. The recoil velocity for a wavelength of 671 nm is $\sim 0.1\,\mathrm{m\,s^{-1}}$.

cooling, e.g. optical molasses or Raman side-band cooling, during the imaging process seems to be the only available solution, see e.g. Ref. [41].

The image acquisition process always integrates along the line-of-sight of the optics and thus only the column density can be retrieved. To obtain information about the three dimensional density distribution additional knowledge about the trap geometry and further processing is necessary, e.g. an inverse Abel transformation. For a two-dimensional sample, which is a design goal of our machine, local density retrieval is obviously not an issue.

3.2 Setup II: Realisation of a flat sample

The high resolution imaging system can only develop its full potential if the imaged object is flat. The two reasons are a short depth of field and the (optical) integration along the imaging axis. This section describes our approach to create a flat cloud suitable for the highly resolving optics presented in the previous section. The preparation of a flat cloud is also an essential prerequisite for the realisation of single-layer, two-dimensional ultracold clouds which is presented in chapter 6. The corresponding optical system which is shown here was largely developed in the course of the master's thesis of Klaus Hueck [55].

3.2.1 Squeeze trap

The shape of an ultracold gas cloud is primarily determined by the parameters of its confining trap and the atom number. Internal properties like interaction or temperature are in most cases only a small correction to the shape determined by the trap. Hence, the realisation of a flat atom cloud is favourably approached by creating a suitable trapping potential. We use an optical dipole trap, called the squeeze trap, for this purpose. A highly asymmetric beam waist is realized by shining in a red-detuned laser beam which is tightly focused in the vertical direction and wide in the horizontal one. The aspect ratio of the two radii of the elliptical waist[14] is $w_z/w_x \approx 400\,\mu\text{m}/10\,\mu\text{m} = 40$. The laser which creates the beam for the trap is the same as the one used for the transport dipole trap. It operates at a wavelength of 1064 nm. The extend of clouds confined within this squeeze trap is comparable to the depth of field of our high resolution imaging system. However, the confinement is not strong enough to create a 2D gas for typical atom numbers. The main features of the squeeze trap are the following:

- High aspect ratio of the beam waist.
- Similar trap frequencies in the two radial directions.
- Shone into the science cell via one of the CF16 viewports on the side of the cell.
- High stability with respect to the microscope objective used for the high resolution imaging.
- Possibility to conveniently adjust the beam waist position.
- Stability of the beam power and the possibility of rapid power ramps, e.g. for evaporation.

A photograph of the trap setup can be seen in Fig. 3.19.

The achievable aspect ratio of the beam waist depends primarily on how tightly the beam can be focussed in the vertical direction. The waist size is limited by the

[14] $1/e^2$ radius, intensity

numerical aperture of the optical system and by aberrations introduced by misalignment and lens quality. The manufacturing quality of spherical lenses is typically better than that of cylindrical ones especially in the direction where the cylindrical lenses are curved. Therefore, the idea behind the design is to create a high-quality symmetric beam waist by using only spherical lenses and then introduce one cylindrical lens to horizontally widen the spot in the focal plane[15]. Aberrations are thus reduced in the more sensitive direction. A beam waist[16] of 8 µm could be confirmed by measuring the beam divergence in a test setup [55]. After the integration into the experiment, the waist deteriorated slightly and the vertical size is now approximately 10 µm in radius.

The divergence of the trapping beam in the highly focused direction is responsible for the trap exerting reasonable longitudinal confinement forces as well. The corresponding length scale is the Rayleigh length which is approximately 200 µm for a beam waist radius of 8 µm. To fulfil the requirement of radially symmetric trapping in the two weakly confined directions, the beam width in the weakly focused direction has to be adjusted to match the Rayleigh length of the strongly diverging direction of the trapping beam. The horizontal spotsize[17] of 370 µm which is created in our setup leads to a circular trapping region in the horizontal plane. A perfectly symmetrical trapping potential cannot be created, as the beam has a Gaussian intensity profile in one direction and a $1/(1+x^2)$ dependence along the propagation axis due to the beam divergence.

The whole optical setup for the squeeze trap has to be very stable with respect to the high resolution imaging system and it has to tolerate rapid magnetic field changes. This is particularly important for our approach to create single-layer two-dimensional gases as described in chapter 6. Therefore, all optical components are mounted on a non-conductive breadboard[18] which is placed around the science cell. The breadboard has no direct physical connection to either the vacuum chamber or the magnetic field coil support structure. The quadrant photodiode which is used to stabilize the position of the transport dipole trap is mounted on that breadboard as well, which ensures a good stability of the transport dipole trap with respect to the squeeze trap. This is particularly important for an efficient transfer of atoms from the transport trap into the squeeze trap during the experimental sequence. All the components used in the vicinity of the magnetic field coils have been selected for minimal magnetic response. The used materials are polymers or aluminium and minimal amounts of high-quality stainless steel, where it could not be avoided.

The installation space available for the optics around the science cell and in between the large magnetic field coils is quite limited. In fact, many of the mounts for the optical components had to be custom built to be able to place them on the breadboard. The limited space makes it almost impossible to adjust any of the components by hand. They were aligned on the breadboard prior to its integration into the machine and afterwards

[15] Thanks to Christoph Becker for the idea
[16] $1/e^2$ radius, intensity
[17] $1/e^2$ radius, intensity
[18] Erhard Hippe, EP GC 201

not moved any more. To obtain a certain degree of adjustability two piezo controlled elements where introduced into the setup as shown in Fig. 3.19. The last spherical lens is mounted on a remote controllable translation stage. Motion of this stage shifts the position of the squeeze trap centre along the beam direction without changing its waist dimensions. Additionally, one of the turning mirrors is mounted on a two-axes piezo controllable mirror holder. This allows to move the beam waist in the plane perpendicular to the beam propagation.

It is possible to image trapped atoms or the beam of the squeeze trap itself to monitor the position of the trap centre. The latter is advantageous to check the trap position perpendicular to the beam's propagation direction, as it is independent of any magnetic forces trapped atoms might experience in addition to the dipole force. The focal shift of the imaging system at different wavelengths has to be taken into consideration when observing the beam waist position.

As during a typical experimental sequence evaporative cooling is performed within the squeeze trap, a mechanism is needed to control the beam power. A photodiode measures the actual beam power and feeds a proportional-integral (PI) controller. The created control signal acts on an AOM which regulates the beam power. The reference signal for the PI controller is created by our experiment control computer. Regulation speeds of 17 kHz (90° point) are reached with this control loop.

3.2.2 Performance

Sequence and typical parameters

A typical experimental sequence which employs the squeeze trap works as follows. First, an atom cloud is prepared in the transport dipole trap inside the science cell as described in chapter 2. The shape of the trapping potentials of the two traps differ significantly from each other. Therefore, it is expected that the transfer process from the transport trap into the squeeze trap induces considerable heating. Hence, the optimal way to cool the gas is to delay the evaporation as long as possible. The final evaporation of the transport dipole trap is chosen just deep enough to ensure that the squeeze trap can accept the cloud with a good transfer efficiency. After the transfer is completed, the transport dipole trap is switched off and the subsequent evaporative cooling is performed by lowering the beam power of the squeeze trap. The power is ramped down exponentially to achieve optimal cooling performance. It is easy to reach degeneracy in this trap and create ultracold gases with adjustable interaction by utilizing the Feshbach resonance. Exemplary power values and other parameters related to the squeeze trap are listed in Tab. 3.2 on page 90.

To understand the cloud's shape an additional magnetic confinement has to be considered. The magnetic coils which create the field to address the Feshbach resonance are not in an exact Helmholtz configuration which results in trapping of the atoms in the radial direction and anti-trapping in the vertical direction. The anti-confinement is negligible in most cases, as the trap frequency of the squeeze trap clearly dominates in

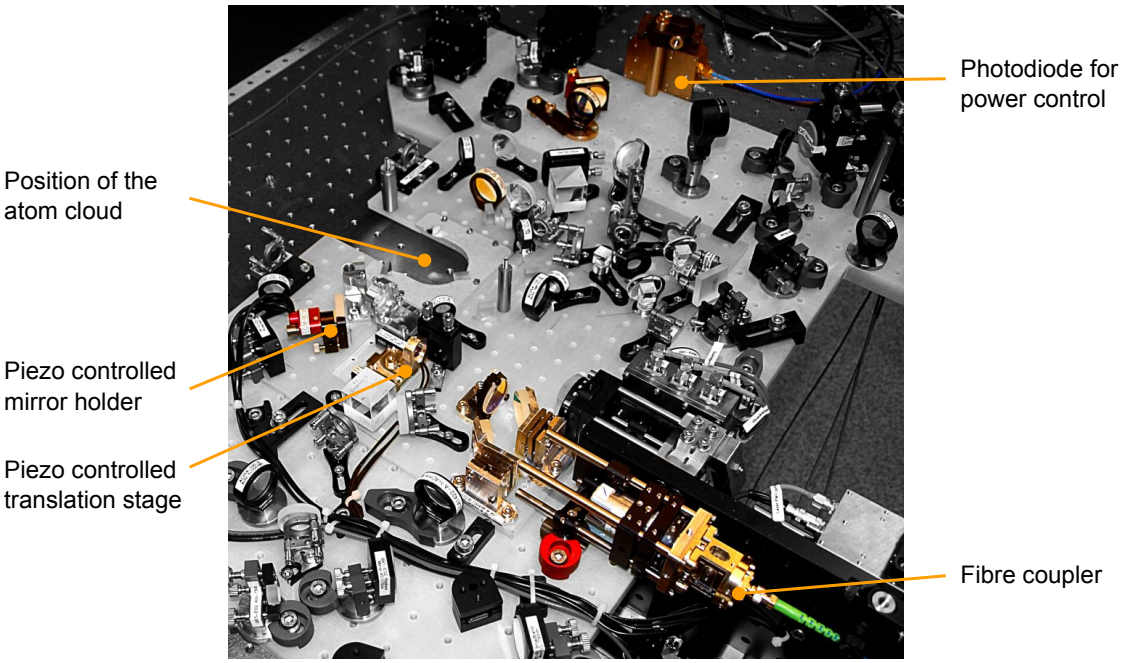

Figure 3.19: A photograph of the squeeze trap setup before integration to the experiment. All components of the squeeze trap are highlighted. The piezo controlled elements allow for convenient adjustment of the beam focus after the breadboard is integrated to the experiment. The photodiode used for power monitoring can be seen in the background. The picture is adopted from Ref. [55].

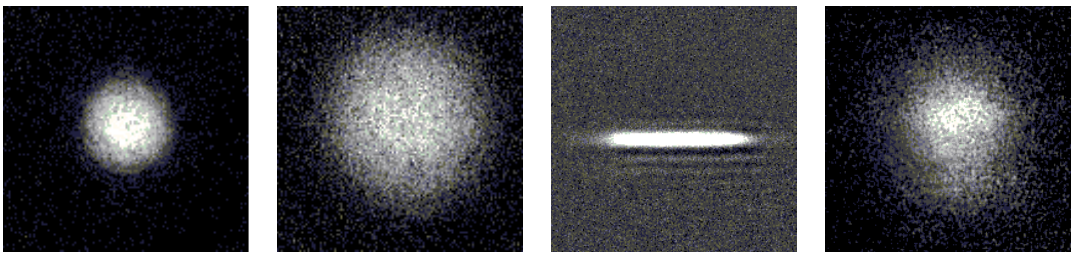

(a) 685 Gauss (b) 835 Gauss (c) 541 Gauss (d) 685 Gauss

Figure 3.20: Examples of density distributions in the squeeze trap as they can be seen by our high resolution imaging system (a), (b), (d). The different applied magnetic fields clearly influence the shape of the cloud due to the change of interaction strength between the atoms (a), (b). The power of the squeeze beam is 32 mW for both images. Sub-figure (c) shows a cloud which is imaged from the side at a squeeze beam power of 20 mW. Here, the spatial extend in the vertical direction, which is visible in the picture, is determined by the imaging resolution. The additional stripes which can be seen above and below the atom cloud are due to diffraction of the imaging light caused by the cloud. Sub-figure (d) is an illustration how imperfections in the beam profile of the squeeze trap affect the cloud's shape. To obtain the image the squeeze power was first lowered to 20 mW and afterwards increased to 200 mW. The colour scale has been adjusted separately for each of the figures.

the vertical direction, but the radial confinement becomes significant for low powers of the squeeze trapping beam. Thus, the shape of the atom cloud becomes more spherical for deep evaporation.

After the gas is prepared in the squeeze trap, the further manipulation depends on the particular experiment which is planned to be performed on the atoms. It is possible to experiment with the atoms directly in the squeeze trap (see for example chapters 4 and 5) or to continue the preparation and create a two-dimensional confinement (see chapter 6). In any case, the experimental cycle will end with an imaging sequence and the squeeze trap is suitable to make use of the high resolution imaging system. Examples of acquired density distributions can be seen in Fig. 3.20. Especially for high beam powers the cloud shape becomes non-circular and shows more complicated features. This is due to imperfections of the squeeze beam and has to be considered when performing experiments on the cloud. Typical atom numbers that can be achieved are 25000 per spin state for a molecular BEC, with a condensate fraction of approximately 90% or an ultracold Fermi gas at a temperature of $T/T_F \approx 0.07$ where T_F is the Fermi temperature of a non interacting Fermi gas [56]. The achieved lifetime of an ultracold gas on the Feshbach resonance is approximately 5 s. For a molecular BEC these lifetimes decrease significantly, most probably due to de-excitation processes of the Feshbach molecules, see Fig. 3.21.

A considerable drift of the position of the squeeze trap centre was observed after the machine is switched on in the morning. The time scale of this drift was several hours. The

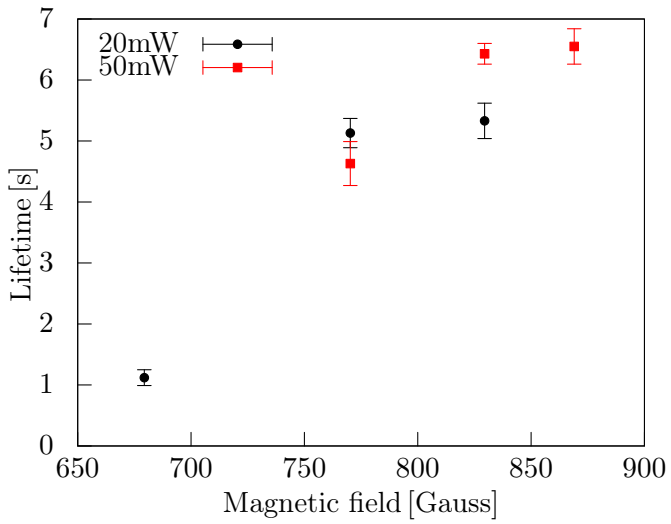

Figure 3.21: Lifetime of an ultracold gas cloud confined in the squeeze trap depending on the magnetic field strength. At low magnetic fields, the gas forms a molecular BEC and the lifetime decreases as the formed molecules start to de-excite into lower vibrational and rotational states. The released energy leads to the observed atom loss. The lifetimes where recorded at two different final evaporation depths in the squeeze trap: at 20 mW (black dots) and at 50 mW (red squares).

cause could be identified to be a thermalisation effect of the whole optical table, mainly caused by dissipated heat of power supplies and high current electric devices placed below the table. The heat dissipated by the magnetic field coils around the vacuum chamber has a certain influence on thermalisation as well. This demonstrates the sensitivity of the machine even though it is designed and constructed as rigid and stable as possible. The thermalisation problem could be solved by an active insulation layer below the table and an auxiliary heating system for the coils which pre-heats the apparatus a couple of hours before the machine is switched on.

Trap frequencies

As mentioned above, the trap frequencies of the squeeze trap are the result of a combination of optical and magnetic trapping. Due to the configuration of the coils the magnetic trap is confining in the radial direction and anti-confining in the vertical direction. The magnetic radial trapping frequency at a field strength of 835 Gauss is $\omega_{r,mag} \approx 2\pi \cdot 29\,\mathrm{Hz}$. Due to the Gauss law for magnetic fields $\vec{\nabla} \cdot \vec{B} = 0$ the frequency in the vertical direction is $\omega_{z,mag} \approx 2\pi\mathrm{i} \cdot 58\,\mathrm{Hz}$. The maximal achievable optical trap frequencies are approximately $\omega_{r,opt} = 80\,\mathrm{Hz}$ and $\omega_{z,opt} = 3800\,\mathrm{Hz}$ at a beam power of 1 W in the squeeze trap. The trapping frequencies caused by the magnetic field and the dipole trap have to be added to obtain the characteristics of the complete confining potential.

Trap frequencies add quadratically, i.e. $\omega = \sqrt{\omega_{mag}^2 + \omega_{opt}^2}$, which means that the magnetic trap can be neglected as long as the beam power in the squeeze trap is high. However, after the evaporative cooling is performed by lowering the optical trap depth the magnetic trap becomes more influential and can even dominate the radial trapping direction. This has considerable impact on the flatness of the trapped cloud. A typical example is a cloud with 10000 atoms per spin state at a magnetic field of 684 Gauss confined in the squeeze trap operating at 20 mW. The extent (radius) of the cloud in this configuration is 2.3 µm in the vertical and 38 µm in the radial direction. The ratio of these two radii is 16.5, which is significantly less than the aspect ratio of the squeeze trapping beam waist (~ 40), reflecting the influence of the magnetic field.

For many applications it is important to have precise information of the actual trapping frequencies. In the following, I present two methods to measure the trapping frequencies in the radial and in the vertical direction.

The vertical trapping frequency of the squeeze trap can be measured via parametric heating [29]. A typical measurement curve can be seen in Fig. 3.22. For this measurement, the power of the squeeze beam is slightly modulated for a certain time and afterwards the atom number is recorded. Due to the power modulation, a breathing mode is excited and finally leads to atom loss which can be observed. For a non-interacting gas the frequency of this mode is exactly twice the trap frequency $\omega_{breath} = 2 \cdot \omega_{trap}$. In the case of an interacting gas the dynamics become more complicated which affects the oscillation frequency of the breathing mode. Directly on the resonance the value is known for a very oblate gas [57] and can be used to deduce the underlying trap frequency: $\omega_{breath,resonace} = \sqrt{3} \cdot \omega_{trap}$[19].

The radial trap frequency has to be determined by another approach. The parametric heating rate is proportional to the fourth power of the resonance frequency rendering it non-detectable for the small trap frequency in the radial direction. However, it is possible to excite centre-of-mass oscillations by pushing the cloud and to observe its position after a certain waiting time. This measurement directly yields the trapping frequency and is independent of the interaction and other internal parameters of the atom cloud. A good method to execute the initial push of the cloud is to quickly switch on the 2D lattice which should be well misaligned with respect to the squeeze trap for this purpose. An example of a measurement performed with this approach is shown in Fig. 3.23.

[19] One might expect that the breathing mode frequency on resonance depends on the Bertsch parameter. However, it can be shown that the collective mode frequencies in a harmonic trap depend only on the power of the exponent γ in the polytropic equation of state $\mu \propto n^\gamma$ [57]. A general analysis (see section 4.3.4) shows that $\gamma = 2/3$ independent of the details of the equation of state.

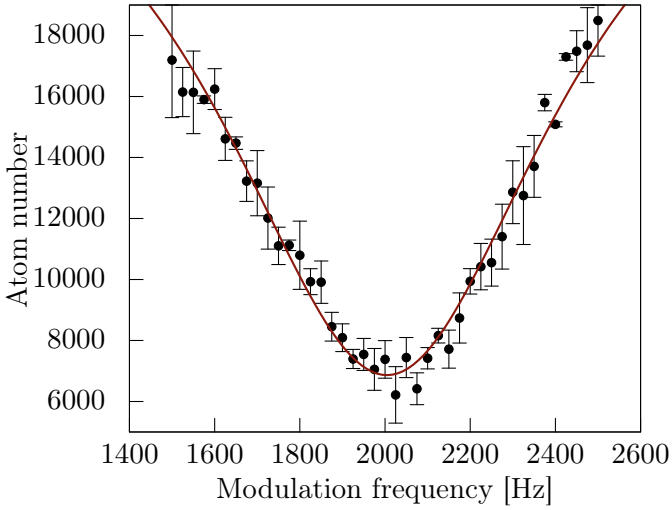

Figure 3.22: Atom loss in the squeeze trap due to parametric heating. The trap power is slightly modulated and atom loss sets in as soon as the breathing mode is excited. The data is obtained by averaging three measurements for each modulation frequency. The error bars are the standard deviation of the averaging. The red curve is a Lorentzian fit to the data yielding a maximum atom loss for a modulation frequency of 2004 Hz. The measurement is performed at a magnetic field of 835 Gauss, close to the Feshbach resonance. The beam power in the squeeze trap is 100 mW and it is modulated with an amplitude of 2 mW for 3 s.

Description	Value
Squeeze trap, wavelength	1064 nm
Squeeze trap, spotsize at beam waist ($1/e^2$ radius, intensity)	10 µm × 370 µm
Squeeze trap, typical beam power for loading	400 mW
Squeeze trap, trap frequencies for loading	68 Hz × 68 Hz × 2300 Hz
Squeeze trap, trap frequencies (optical) at 20 mW	15 Hz × 15 Hz × 500 Hz
Magnetic trap, trap frequencies on Feshbach resonance	29 Hz × 29 Hz × 58 Hz · i
Squeeze and magnetic trap, trap frequencies at 20 mW on Feshbach resonance	32 Hz × 32 Hz × 500 Hz
Squeeze trap, trap depth for loading	4 µK
Squeeze trap, Regulation speed of the PI power control (90° point)	17 kHz

Table 3.2: Parameters and reference values for the squeeze trap.

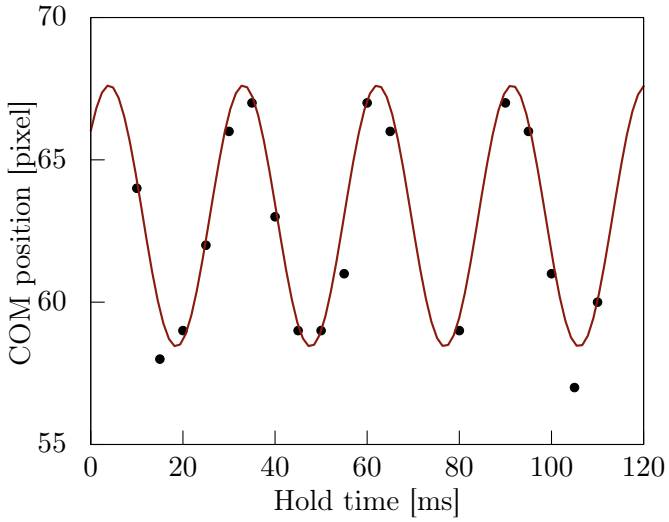

Figure 3.23: Radial centre of mass oscillations of the atom cloud in the squeeze trap. The (misaligned) 2D lattice is switched on rapidly to initiate the oscillations. The data is acquired at a magnetic field of 835 Gauss, a beam power of 20 mW in the squeeze trap and 700 mW in the 2D lattice. The solid line is a sine fit to the data and yields an oscillation frequency of 34.2 Hz which directly corresponds to the radial trap frequency.

4 The speed of sound across the BEC-BCS crossover

4.1 Introduction

When the interaction between the constituents of an ultracold fermionic gas is tuned from attractive to repulsive the behaviour of the gas changes dramatically. Even the quantum statistic is altered from fermionic to bosonic accompanied by such intriguing consequences as the formation of a molecular BEC. In the course of this fundamental change many properties of the gas are modified. Amongst those is the speed of sound which is essentially zero in the non-interacting BEC limit and on the order of the Fermi velocity in a Fermi gas. The exact behaviour close to the resonance is unknown as there is no precise knowledge of the equation of state in this regime[1]. The properties of sound propagation are determined by the type of the possible excitations in the gas. This makes a speed of sound measurement in the BEC-BCS crossover particularly interesting as the nature of the excitations in the strongly interacting regime is still unknown. It is even unclear if the gas can be described by quasi-particles at all. Thus the measurement of the speed of sound can serve as a benchmark for theories which describe the ultracold gas in the crossover.

Moreover the propagation of sound modes is strongly connected to the presence of superfluidity in the system. At low temperatures, an interacting Fermi gas is superfluid and in the case of a molecular BEC the speed of sound marks an upper limit to the superfluid critical velocity. The first direct measurement of the speed of sound in an ultracold gas was done in the Ketterle group [59] and it was mapped out over the whole crossover in a fermionic system in Ref. [60]. There have been also measurements of the critical velocity for superfluidity, e.g in Ref. [61], but so far there is no experimental investigation of the speed of sound and the critical velocity in the same system. Such a measurement, which compares the two velocities, is well suited to give new insights into strongly interacting Fermi gases.

In this chapter I present our measurements of the speed of sound in a strongly interacting gas including a theoretical description. The measurements of the superfluid critical velocity can then be found in chapter 5.

[1] There is an exception directly on the resonance where the s-wave scattering length diverges. For this particular point there exists a measurement of the equation of state published in Ref. [58].

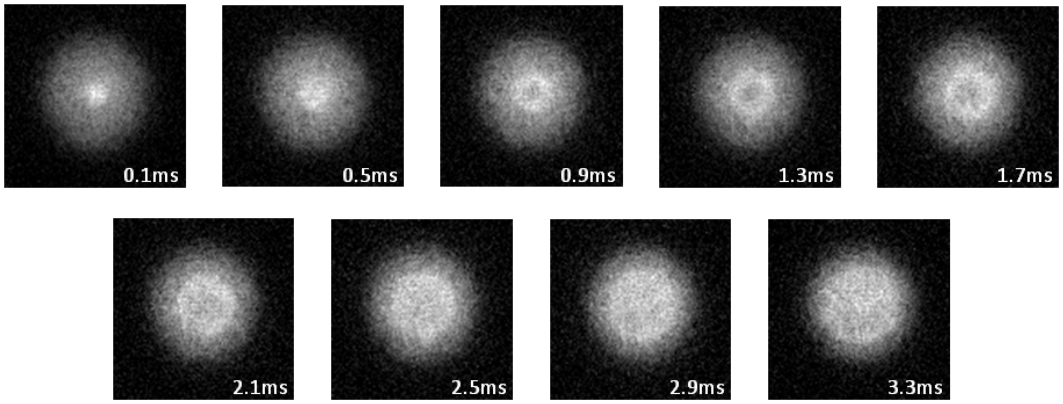

Figure 4.1: A density wave propagating in an ultracold atom cloud after its excitation by a laser pulse in the cloud centre. Its radial propagation speed is the speed of first sound. The measurement was performed at a magnetic field strength of 695 Gauss on the BEC side of the Feshbach resonance.

4.2 Experiment

Measurements of the speed of sound have been published in references [59] and [60]. In both experiments the medium for the sound waves is an elongated ultracold gas. A blue detuned laser beam is utilized to introduce a local density variation in the central region of the trap. After the laser is switched of a density wave starts to propagate through the cloud which can be observed at different times. The extracted propagation speed is the speed of sound. Our measurements are performed in a very oblate cloud of ultracold fermions which are prepared as described in chapter 3. The excitation is performed with a red-detuned laser and the sound wave spreads radially from the centre of the cloud. To measure the speed of sound at different interaction strengths we tune the magnetic field to the desired value before the excitation of the sound wave.

4.2.1 Our measurement

To excite a sound wave we focus a red-detuned laser beam with a wavelength of 780 nm into the centre of the cloud and linearly ramp up its power within 100 ms before holding it for 100 ms and then quickly switching it off. The maximum power of the beam is chosen between 7 µW and 40 µW depending on the interaction strength. The power was chosen higher on the BCS side of the Feshbach resonance compared to the BEC side to create a density wave of similar relative amplitude after the atoms are released from the excitation beam. The procedure creates a radial symmetric density modulation with a relative amplitude of approximately 30 % that moves outwards (see Fig. 4.1). We take pictures after a certain time τ after the modulation was created and subtract the

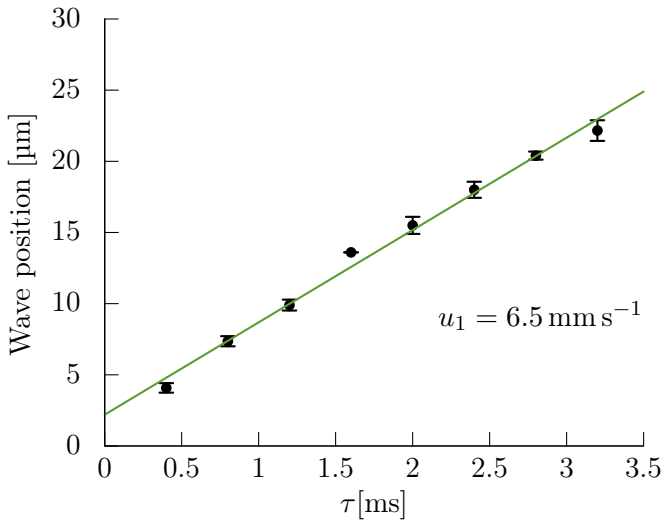

Figure 4.2: Analysis of the absorption images 4.1. The radial position of the wave maximum is plotted versus the time after the wave was excited. In this example the extracted speed of sound is $6.5\,\mathrm{mm\,s^{-1}}$.

density distribution of an undisturbed cloud. After radial averaging the positions of the maxima and minima of the density wave are identified and can be used to extract the speed at which the modulation is moving as shown in 4.2. Similar to Ref. [60] this velocity is identified with the speed of first sound u_1. Its propagation speed depends on the interaction strength $1/k_N a_A$ where a_A is the atom-atom s-wave scattering length and k_N the Fermi wave vector of a non-interacting Fermi gas[2]. The latter is defined via

$$\frac{\hbar^2 k_N^2}{2m} = \hbar\bar{\omega}\,(6N)^{1/3} \tag{4.1}$$

where m is the mass of a ^{6}Li atom, $\bar{\omega} = (\omega_x\omega_y\omega_z)^{1/3}$ is the mean trap frequency and $N = N_\uparrow = N_\downarrow$ the total atom number in a single hyperfine state. We only include measurements in the central region of the cloud where the column density is almost identical to the column density in the trap centre. Therefore, the reduced density in the outer regions of the cloud does not influence the measured speed of sound. The results of the experiment are shown in Fig. 4.3. In the figure the speed of sound is plotted in units of the Fermi velocity $v_N = \hbar k_N/m$. In general the propagation speed of the sound wave depends on the local density. However, if the oblate cloud is flat compared to the wavelength of the sound wave and in a entirely hydrodynamic regime it is the

[2]The sub-index N indicates that the Fermi wavenumber k_N is defined via the total atom number rather then via the density $\left(k_n^3/6\pi^2 = n\right)$. We use k_N to plot our data as we have direct experimental access to the particle number but not to the density. In the limit of a non-interacting Fermi gas the two definitions are identical $k_n = k_N$. See chapter 4.3.4 for further details.

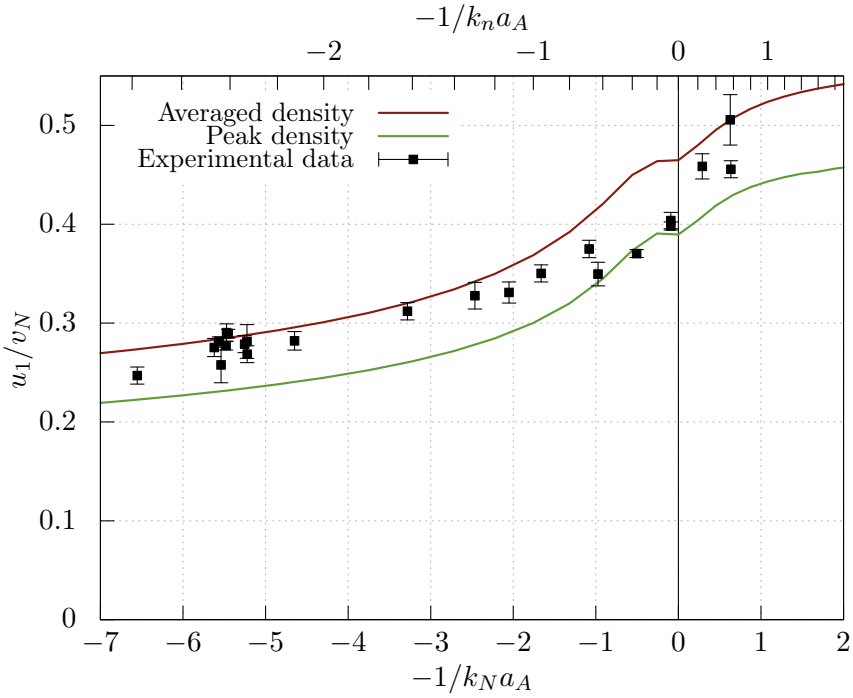

Figure 4.3: The speed of sound as a function of the interaction strength across the BEC-BCS crossover. The points are our measured data and the lines are theory curves which are explained in section 4.3. The two x axis use two different definitions for the Fermi wavenumber. For more details see section 4.3.4

average density along the strongly confined direction which determines the propagation speed [62, 63]. In the case that the cloud is not hydrodynamic in the strongly confined direction, i.e. the mean free path of the particles is longer than the cloud thickness, the observed speed of sound is determined by the density in the central layer. The two curves in the figure represent the theoretical prediction for the speed of sound in the two situations and are in good agreement with our measurement.

4.2.2 Dependence on excitation strength

The theory curves in Fig 4.3 assume that the amplitude of the density wave is small. For large amplitudes the speed of sound can be expected to change. To make sure that we work in the small amplitude limit, we performed measurements of the speed of sound with varying beam powers of the excitation laser while all other experimental parameters where held constant. The results can be seen in Fig. 4.4. The plot suggests that the speed of sound for an arbitrarily small perturbation is within the error bars of our observations at low excitation beam powers. The data points in Fig. 4.3 where all recorded in this low power regime which is described by the theory presented in section 4.3.

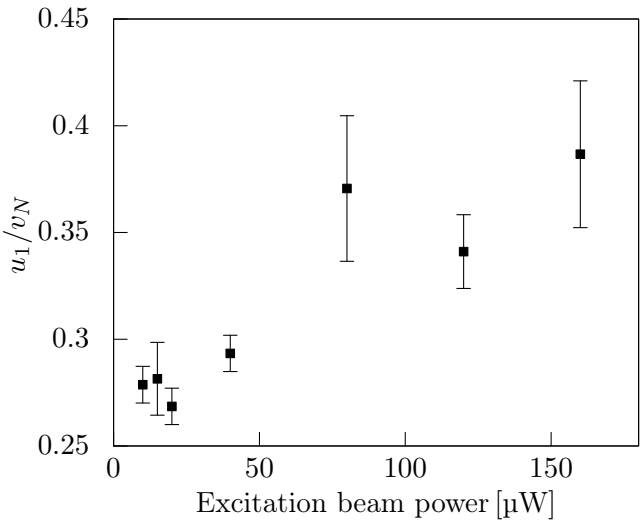

Figure 4.4: Measured speed of sound as a function of the beam power of the excitation laser. The measurements have been performed at an interaction strength of $-1/k_N a_A = -5.2$.

4.2.3 Dependence on the excitation beam diameter

To exclude the possibility that the measured sound velocities depend on the beam diameter of the excitation beam we performed measurements with different beam sizes, ranging from 1.5 µm to 7.1 µm[3], and otherwise constant experimental parameters. We observed no influence of the beam diameter on the measured propagation speed of the density wave.

[3] $1/e^2$ radius, intensity

4.3 Theory

This section is intended to give a theoretical overview on the speed of sound in superfluid ultracold Fermi gases in the crossover from the BEC to the BCS regime. Main results are the curves for the speed of sound shown in Fig. 4.3. As sound waves are a thermodynamic phenomenon we approach the theoretical description from a thermodynamic point of view. For simplicity we consider sound modes with frequency ω in a homogeneous gas and in the hydrodynamic limit $\tau\omega \ll 1$. Here τ is the collision time of the constituents of the gas. The presence of a superfluid density in the system is an additional degree of freedom and has the remarkable consequence that two different sound modes arise named first and second sound. A non-superfluid gas only supports first sound. At very low temperatures first sound describes a density wave whereas second sound is a pure temperature wave. However, for finite temperatures and interaction strengths the nature of first and second sound is a mixture of both density and temperature waves.

To derive the speed of sound we proceed along the lines of the paper of H. Heiselberg on sound modes in the BCS-BEC crossover [64]. We first derive a general formula for the speed of sound in a homogeneous system based on mass conservation and the acceleration of a superfluid due to a gradient in the chemical potential. We continue in giving explicit expressions for the speed of sound in the BEC, BCS and in the crossover regime. In the weakly interacting limits analytical expressions are available whereas quantum Monte Carlo data are the basis for our calculations in the strongly correlated regime. First the zero temperature situation is discussed and thereafter we consider the influence of finite temperatures. An important result is that the modification of the speed of sound due to finite temperature is small in the experiments presented in this thesis. The last part of this section then deals with additional effects which are present in a trapped system.

4.3.1 First and second sound

We follow the lines of references [64, 65] to derive a general expression for the speed of sound. The cold gas has to conserve its mass which leads to the continuity equation

$$\frac{\partial \rho}{\partial t} + \vec{\nabla} \cdot \vec{j} = 0 \tag{4.2}$$

with the mass density $\rho = \rho_{SF} + \rho_N$ and the mass current density $\vec{j} = \rho_{SF}\vec{v}_{SF} + \rho_N\vec{v}_N$. The superfluid (normal) mass density is given by ρ_{SF} (ρ_N) and the velocity of the superfluid (normal) part by $\vec{v}_{SF}$ ($\vec{v}_N$). If we neglect friction and non-linear effects the time derivative of the mass current is

$$\frac{\partial \vec{j}}{\partial t} = -\vec{\nabla} p \tag{4.3}$$

and thus

$$\frac{\partial^2 \rho}{\partial t^2} - \nabla^2 p = 0. \tag{4.4}$$

Here p is the pressure. Equation 4.4 is the first relation required to determine the speed of the sound waves. The second relation is derived by considering the acceleration of the superfluid fraction of the gas due to a gradient of the chemical potential:

$$m\frac{\partial \vec{v}_{SF}}{\partial t} = -\vec{\nabla}\mu. \tag{4.5}$$

Here we again neglect non-linear effects which restricts the calculations to small amplitudes of the sound modes. Under consideration of the Gibbs-Duhem relation Eq. 4.5 can be rewritten as (see Ref. [65] for details):

$$\frac{\partial^2 s}{\partial t^2} = \frac{\rho_{SF}}{\rho_N} s^2 \nabla^2 T \tag{4.6}$$

with the entropy per unit mass $s = S/(Nm)$, the total entropy S, the total particle number N and the temperature T.

To obtain the sound modes we consider small variations in density, temperature, pressure and entropy of the form $e^{\mathrm{i}(\vec{k}\vec{r}-\omega t)}$. We choose the fluctuations in density $\delta\rho$ and in temperature δT as independent variables. Whereas the changes of pressure and entropy are determined by equations 4.4 and 4.6. This procedure yields a condition for the phase velocity of the fluctuations $u = \frac{\omega}{k}$ which is the speed of sound. With the ansatz of plane wave fluctuations we obtain from Eq. 4.4

$$\omega^2 \delta\rho - k^2 \left[\left(\frac{\partial p}{\partial \rho}\right)_T \delta\rho + \left(\frac{\partial p}{\partial T}\right)_\rho \delta T \right] = 0 \tag{4.7}$$

and from Eq. 4.6

$$\omega^2 \left[\left(\frac{\partial s}{\partial \rho}\right)_T \delta\rho + \left(\frac{\partial s}{\partial T}\right)_\rho \delta T \right] - \frac{\rho_{SF}}{\rho_N} s^2 k^2 \delta T = 0. \tag{4.8}$$

To simplify the last two equations we introduce $c_S^2 = \left(\frac{\partial p}{\partial \rho}\right)_s$, $c_T^2 = \left(\frac{\partial p}{\partial \rho}\right)_T$, $c_2^2 = \frac{\rho_{SF} s^2 T}{\rho_N c_V}$ and $c_V = T\left(\frac{\partial s}{\partial T}\right)_\rho$. The quantity c_S is the adiabatic speed of sound, c_T is isothermal speed of sound, c_2 the "thermal" speed of sound and c_V is the specific heat per unit mass.

Furthermore, we need to derive the following relation between the adiabatic and the isothermal speed of sound:

$$c_S^2 - c_T^2 = \left(\frac{\partial s}{\partial \rho}\right)_T^2 \frac{\rho^2 T}{c_V}. \tag{4.9}$$

Equation 4.9 follows from the Maxwell relations:

$$\begin{aligned}
-\left(\frac{\partial p}{\partial V}\right)_S &= \left(\frac{\partial p}{\partial S}\right)_V \left(\frac{\partial S}{\partial V}\right)_p \\
&= \left(\frac{\partial p}{\partial S}\right)_V \left[\left(\frac{\partial T}{\partial V}\right)_p \left(\frac{\partial S}{\partial T}\right)_V + \left(\frac{\partial p}{\partial T}\right)_V\right] \\
&= \left(\frac{\partial p}{\partial S}\right)_V \left(\frac{\partial T}{\partial V}\right)_p \left(\frac{\partial S}{\partial T}\right)_V + \left(\frac{\partial p}{\partial S}\right)_V \left(\frac{\partial p}{\partial T}\right)_V \\
&= \left(\frac{\partial p}{\partial T}\right)_V \left(\frac{\partial T}{\partial V}\right)_p + \left(\frac{\partial T}{\partial S}\right)_V \left(\frac{\partial p}{\partial T}\right)_V^2 \\
&= -\left(\frac{\partial p}{\partial V}\right)_T + \left(\frac{\partial T}{\partial S}\right)_V \left(\frac{\partial S}{\partial V}\right)_T^2
\end{aligned} \tag{4.10}$$

where V is the Volume of the system. The first and the last expression in Eq. 4.10 written in terms of $\rho = \frac{Nm}{V}$ ($\frac{\partial}{\partial \rho} = -\frac{Nm}{\rho^2}\frac{\partial}{\partial V}$) and $s = \frac{S}{Nm}$ yield Eq. 4.9.

Equations 4.7 and 4.8 can now be rewritten as:

$$\begin{aligned}
\left(u^2 - c_T^2\right)\delta\rho - \left(\frac{\partial p}{\partial T}\right)_\rho \delta T &= 0 \\
u^2\left(c_T^2 - c_S^2\right)\left(\frac{\partial p}{\partial T}\right)_\rho^{-1}\delta\rho + \left(u^2 - c_2^2\right)\delta T &= 0.
\end{aligned} \tag{4.11}$$

The linear system of equations 4.11 has non-trivial solutions for $\delta\rho$ and δT only if the determinant of the coefficient matrix vanishes. Hence, we demand

$$\left(u^2 - c_T^2\right)\left(u^2 - c_2^2\right) + u^2\left(c_T^2 - c_S^2\right) = 0. \tag{4.12}$$

The two solutions of Eq. 4.12 are called first sound (u_1) and second sound (u_2) and are given by

$$u_{1/2}^2 = \frac{c_S^2 + c_2^2}{2} \pm \sqrt{\left(\frac{c_S^2 + c_2^2}{2}\right)^2 - c_T^2 c_2^2} \tag{4.13}$$

$$c_S^2 = \left(\frac{\partial p}{\partial \rho}\right)_s, \quad c_T^2 = \left(\frac{\partial p}{\partial \rho}\right)_T, \quad c_2^2 = \frac{\rho_{SF} s^2 T}{\rho_N c_V}, \quad c_V = T\left(\frac{\partial s}{\partial T}\right)_\rho \tag{4.14}$$

where u_1 corresponds to the positive sign and u_2 to the negative sign. The quantities c_S, c_T, c_2 and c_V are given again for convenience[4]. Equation 4.13 expresses the speed of sound as a function of thermodynamic quantities. Thus, we concentrate our attention on the energy and entropy of the cold gas in the following sections. We derive expressions

[4] At zero temperature the isothermal speed of sound is often written as $c_{T=0}^2 = \sqrt{\frac{n}{m}\left(\frac{\partial \mu}{\partial n}\right)_T}$. The expression can be derived with the Gibbs-Duhem equation.

for the speed of sound as a function of the interaction strength and the temperature of the gas. Already at this point we can deduce that a gas above the critical temperature for superfluidity features only first sound as the coefficient c_2 vanishes and therefore $u_2 = 0$. In the following we focus on the first sound as this is the quantity we measured in the experiment, however the speed of second sound is discussed as well wherever it is convenient.

4.3.2 Speed of sound at zero temperature

The experiments described in this thesis are performed on fermionic lithium with atoms of mass m present in two different hyperfine spin configurations. A molecular BEC of dimers with mass $m_D = 2m$ can be formed if the scattering length a_A is positive. The scattering length between two dimers a_D is different from the scattering length between the atoms. In this thesis I use the result $a_D = 0.6a_A$ which was obtained from quantum Monte Carlo [66] and four-body calculations [7]. The interaction is characterised by the dimensionless quantity $x = 1/k_F a_A$. The BEC regime is characterised by $x > 1$ and a dimer density n_D, the BCS regime by $x < 1$ and the atom densities $n_\uparrow$ and $n_\downarrow$ of the two hyperfine states. For $|x| < 1$ the gas features strong interactions and its description is difficult. The Fermi wavenumber is defined by[5] $n_\uparrow = n_\downarrow = n_D = \frac{k_F^3}{6\pi^2}$.

There is a general statement we can make which greatly simplifies the treatment of the speed of sound at zero temperature. If the dispersion relation of the excitations of the gas is described by a power law it implies $u_1 = c_T$ and $u_2 = c_2$. According to Ref. [64] a dispersion relation $E(k) \propto k^\alpha$ leads to an entropy and a heat capacity which follow a power law as well: $S \propto c_V \propto T^{3/\alpha}$ and the non-superfluid fraction is $\rho_N/\rho \propto (T/T_C)^{(5/\alpha)-1}$. Equation 4.9 then implies $c_S^2 - c_T^2 \propto T^{(3/\alpha)+1}$ and $c_2 \propto (\rho_S/\rho)\, T^{2-(2/\alpha)}$. In the limit $T \to 0$ it follows from Eq. 4.13 that $u_1 = c_T$ and $u_2 = c_2$. Furthermore, if the dispersion relation is linear ($\alpha = 1$), which corresponds to phonons as they are present in the BEC regime, u_2 might have a finite value at zero temperature. However, for excitations with the character of free particles ($\alpha = 2$) we can conclude $u_2(T = 0) = 0$.

Weakly interacting BEC

The limiting case of a non-interacting BEC ($1/k_F a_A \to \infty$) at zero temperature is trivial and leads to $u_{1/2} = 0$. Therefore, the first case we consider is an interacting Bose condensed gas with interaction parameter $x = 1/k_F a_A \gg 1$. The energy of the gas is given by [65]:

$$E = \frac{N_D^2 U_0}{2V}. \tag{4.15}$$

with the interaction between two dimers of the superfluid $U_0 = 4\pi\hbar^2 a_D/m_D$ and the total dimer number N_D. Here we assumed that the total energy is dominated by the interaction energy and the kinetic contribution can be neglected. This approximation

[5] Note, that k_F equals k_n in Fig. 4.3. For more details see section 4.3.4.

is well justified for the experiments described in this thesis and becomes exact in a homogeneous sample with infinite system size at $T = 0$ and $x \to +\infty$. However, Eq. 4.15 neglects the contribution which originates from the binding energy of the dimers as it does not contribute to the dynamics of the cold gas. We obtain for the pressure of the gas:

$$p = -\frac{\partial E}{\partial V} = \frac{N_D^2 U_0}{2V^2} = \frac{n_D^2 U_0}{2} = \frac{\rho^2 U_0}{2m_D^2} \tag{4.16}$$

and thus for the isothermal speed of sound:

$$c_T^2 = \left(\frac{\partial p}{\partial \rho}\right)_T = \frac{\rho U_0}{m_D^2}. \tag{4.17}$$

The values for c_S and c_2 are deduced from the entropy of the gas which vanishes at zero temperature. Therefore, we consider the entropy of a gas at low but non-zero temperature and take the limit $T \to 0$ at the end of the calculation. For low temperatures the entropy per unit mass is given by [65]

$$s = \frac{1}{T}\frac{\rho_N}{\rho}\frac{\rho U_0}{m_D^2} \tag{4.18}$$

which varies as T^3 as the normal density is

$$\rho_N = \frac{2\pi^2}{45}\frac{(k_B T)^4}{\hbar^3}\left(\frac{\rho U_0}{m_D^2}\right)^{5/2}. \tag{4.19}$$

From the expressions 4.9 and 4.14 we obtain:

$$\begin{aligned} c_S^2 - c_T^2 &= \frac{25}{12} sT \\ c_2^2 &= \frac{1}{3}\frac{\rho_{SF}}{\rho}\frac{\rho U_0}{m_D^2}. \end{aligned} \tag{4.20}$$

In the limit $T \to 0$, the superfluid density equals the normal density which implies $c_S = c_T$ and $c_2 = c_T/\sqrt{3}$. Finally, Eq. 4.13 yields the expression for the speed of the first and second sound of a weakly interacting BEC at zero temperature:

$$\begin{aligned} u_1 &= c_T = \sqrt{\frac{n_D U_0}{m_D}} \\ u_2 &= c_2 = \frac{c_T}{\sqrt{3}} = \sqrt{\frac{n_D U_0}{3m_D}}. \end{aligned} \tag{4.21}$$

In the case of the weakly interacting BEC in the limit $T \to 0$ we see from the system of linear equations 4.11 that $c_S = c_T$ and $u \neq c_2$ implies $\delta T = 0$ whereas $\delta\rho$ is arbitrary. Therefore, we conclude that under these conditions first sound is a pure density modulation without any temperature variation. In a similar fashion one can see that second sound is a pure temperature modulation with the density kept constant. As u_1, given

by Eq. 4.21, is identical to the propagation speed of Bogoliubov excitations we see that first sound corresponds to phonons. As thermal energy in the BEC is carried by those excitations, second sound can be identified with oscillations of the phonon density.

Later it will prove useful to write the speed of sound given in Eq. 4.21 in units of the Fermi velocity $v_F = \hbar k_F/m$ and as a function of $k_F a_A$. Note, that we use the atom mass $m = m_D/2$ instead of the dimer mass and the atom-atom scattering length $a_D = 0.6 a_A$ [7] instead of the dimer-dimer scattering length to allow a comparison of the results to those obtained in the BCS regime.

$$\begin{aligned} u_1 &= v_F \sqrt{\frac{1}{6\pi}\frac{a_D}{a_A}}\sqrt{k_F a_A} \approx 0.178 v_F \sqrt{k_F a_A} \\ u_2 &= v_F \sqrt{\frac{1}{18\pi}\frac{a_D}{a_A}}\sqrt{k_F a_A} \approx 0.103 v_F \sqrt{k_F a_A} \end{aligned} \tag{4.22}$$

See Fig. 4.6 on page 108 for a plot of the speed of first sound given by Eq. 4.22.

BEC extension towards the resonance

If the interactions become stronger, higher order effects in the description of the gas become more important. The next order correction to the energy given in Eq. 4.15 is [67]:

$$E = \frac{N_D^2 U_0}{2V^2}\left(1 + \frac{128 a_D^3}{15\sqrt{\pi}}\left(\frac{N_D}{V}\right)^{1/2} + \dots\right). \tag{4.23}$$

For the corresponding pressure we obtain:

$$p = -\frac{\partial E}{\partial V} = \frac{\rho^2 U_0}{2m_D^2}\left(1 + \frac{64}{5\sqrt{\pi}}\left(\rho a_D^3\right)^{1/2}\right) \tag{4.24}$$

and for the isothermal speed of sound:

$$\begin{aligned} c_T^2 = \left(\frac{\partial p}{\partial \rho}\right)_T &= \frac{\rho U_0}{m_D^2}\left(1 + \frac{32}{\sqrt{\pi}}\left(\rho a_D^3\right)^{1/2}\right) \\ &= \frac{\rho U_0}{m_D^2}\left(1 + \frac{32}{\sqrt{6\pi^3}}\left(k_F a_D\right)^3\right) \end{aligned} \tag{4.25}$$

In the zero temperature limit Eq. 4.9 yields $c_S = c_T$ and Eq. 4.13, for the first speed of sound, simplifies to

$$\begin{aligned} u_1 = c_T &= \left[\frac{n_D U_0}{m_D}\left(1 + \frac{32}{\sqrt{6\pi^3}}\left(k_F a_D\right)^3\right)\right]^{1/2} \\ &= v_F \sqrt{\frac{1}{6\pi}\frac{a_D}{a_A}}\sqrt{k_F a_A}\left[1 + \frac{32}{\sqrt{6\pi^3}}\left(\frac{a_D}{a_A}\right)^3 \left(k_F a_A\right)^3\right]^{1/2} \\ &\approx 0.178 v_F \left[k_F a_A + 0.507\left(k_F a_A\right)^4\right]^{1/2}. \end{aligned} \tag{4.26}$$

The speed of first sound given in Eq. 4.26 is plotted as a function of $1/k_F a_A$ in Fig. 4.6.

Non-interacting Fermi gas

In contrast to a non-interacting BEC at $T = 0$, a non-interacting Fermi gas at zero temperature is not trivial as the energy of the Fermi gas is finite due to Pauli blocking. The energy of the gas is given by [68]:

$$E = N\frac{3}{5}E_F. \tag{4.27}$$

Here N is the number of atoms in a single hyperfine state. If the gas consists of atoms in several spin states the corresponding populations can be treated separately since there is no interaction between them. In the experiments presented in this thesis two hyperfine states are populated in equal numbers $N = N_\uparrow = N_\downarrow$. The Fermi energy is $E_F = \hbar^2 k_F^2/(2m)$ with the atom mass m and the Fermi wave number defined by $n = n_\uparrow = n_\downarrow = k_F^3/(6\pi^2)$. For the pressure of the gas we obtain

$$p = -\frac{\partial E}{\partial V} = n\frac{2}{5}E_F. \tag{4.28}$$

As in the case of a BEC it can be argued that $u_1 = c_T$ which yields for the speed of first sound:

$$u_1 = c_T = \sqrt{\left(\frac{\partial p}{\partial \rho}\right)_T} = v_F\frac{1}{\sqrt{3}}. \tag{4.29}$$

See Fig. 4.6 for a plot of the result given in Eq. 4.29. As a non-interacting Fermi gas has no superfluid density there is no second sound, $u_2 = c_2 = 0$. As in the zero temperature BEC first sound is a pure density wave whereas second sound would be a thermal wave corresponding to variations in the density of excitations. The excitations in the Fermi gas at low temperature are free particles which do not interact and do not obey any Pauli principle. Therefore, any local excess of excitations does not cause a restoring force and the time scale of the corresponding oscillation diverges.

BCS extension towards the resonance

The two component Fermi gases, which we create in our experimental apparatus, experience a finite interaction. Two atoms in the same hyperfine state do not scatter due to the Pauli principle whereas two atoms in different hyperfine states can undergo scattering events characterised by the s-wave scattering length a_A. Lee and Yang calculated how the interactions change the energy of the gas [69]:

$$E = N\frac{3}{5}E_F\left(1 + \frac{10}{9\pi}(k_F a_A) + \frac{4(11-2\ln 2)}{21\pi^2}(k_F a_A)^2 + \dots\right). \tag{4.30}$$

The pressure which follows from Eq. 4.30 is

$$p = -\frac{\partial E}{\partial V} = \frac{2}{5} n E_F + \frac{2}{3\pi} n E_F k_F a_A + \frac{16\,(11 - 2\ln 2)}{105\pi^2} n E_F \left(k_F a_A\right)^2 . \tag{4.31}$$

The isothermal speed of sound which corresponds to this pressure is given by the following expression:

$$\begin{aligned} c_T^2 &= v_F^2 \frac{1}{3} \left(1 + \frac{2}{\pi} k_F a_A + \frac{8\,(11 - 2\ln 2)}{15\pi^2} \left(k_F a_A\right)^2\right) \\ &\approx v_F^2 \frac{1}{3} \left(1 + 0.637 k_F a_A + 0.520 \left(k_F a_A\right)^2\right) . \end{aligned} \tag{4.32}$$

As before, $u_1 = c_T$ and $u_2 = c_2$ in the limit $T \to 0$ and therefore

$$u_1 = v_F \frac{1}{\sqrt{3}} \left[1 + \frac{2}{\pi} k_F a_A + \frac{8\,(11 - 2\ln 2)}{15\pi^2} \left(k_F a_A\right)^2\right]^{1/2} . \tag{4.33}$$

See Fig. 4.6 for a plot of the speed of first sound given by Eq. 4.33. The speed of second sound is much smaller than the speed of first sound but non-zero, $0 < u_2 \ll u_1$. This allows for a smooth transition from the BCS to the BEC limit without any discontinuities in the speed of second sound. The physical mechanism is most likely based on the small interaction which supports the formation of weakly bound pairs. Those pairs should have a linear dispersion relation at low momenta similar to the dispersion relation in a BEC where $c_2 = u_2$ is non-zero.

Crossover

The calculation of the speed of sound in the crossover from the BEC to the BCS regime is difficult. Especially in the strongly correlated regime $|1/k_F a_A| < 1$ much is unknown. However, there are zero temperature quantum Monte Carlo simulations [66, 70, 71] and the known limits at $|1/k_F a_A| \gg 1$. In general the energy per atom at zero temperature, after subtracting the binding energy E_B, can be written as

$$\frac{E}{N} - \frac{E_B}{2} = \frac{3}{5} E_F \epsilon(x) \tag{4.34}$$

with $x = 1/k_F a_A$. The binding energy is a function of the scattering length a_A and has no contribution to the speed of sound so we can neglect it in our considerations. Equations 4.23 and 4.30 are defining $\epsilon(x)$ in the limiting cases of a BEC and a BCS superfluid. In the BEC case $x \gg 1$ one obtains

$$\epsilon(x) = \frac{5}{18\pi} \frac{1}{x} \frac{a_D}{a_A} \left(1 + \frac{128}{15\sqrt{6\pi^3}} \frac{1}{x^{3/2}} + \dots\right) . \tag{4.35}$$

And for the BCS superfluid $x \ll -1$:

$$\epsilon(x) = 1 + \frac{10}{9\pi} \frac{1}{x} + \frac{4\,(11 - 2\ln 2)}{21\pi^2} \frac{1}{x^2} + \dots . \tag{4.36}$$

Parameter	BEC value ($x > 0$)	BCS value ($x < 0$)
α_1	0.4200	0.4200
α_2	0.2674	0.3692
α_3	5.0400	1.0440
β_1	0.1126	1.4328
β_2	0.4552	0.5523

Table 4.1: Parameters of the equation of state 4.37 [72].

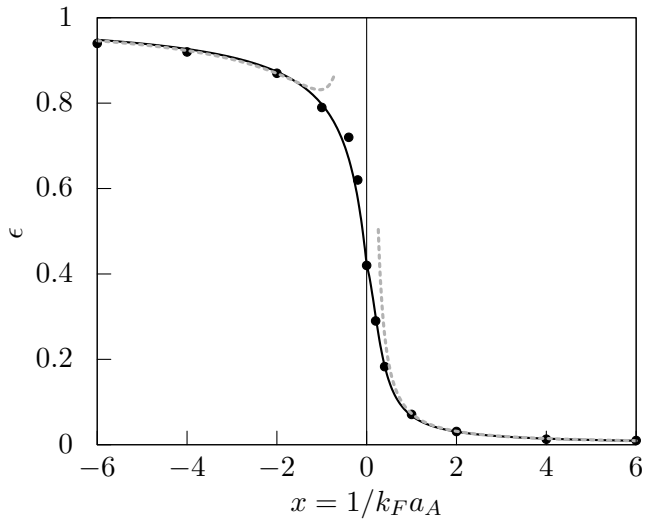

Figure 4.5: The energy per particle $\epsilon(x)$ as defined in Eq. 4.34, with $x = 1/k_F a_A$. The dots are the fixed-node Monte Carlo data of Ref. [66] and the solid line is the function 4.37 as proposed in Ref. [72]. The dashed lines are the expansions 4.35 and 4.36 with $a_D = 0.6 a_A$.

Equations 4.35 and 4.36 are only valid in their respective limits and become inaccurate as the interaction parameter x approaches zero, see Fig. 4.5.

The data for $\epsilon(x)$, which could be obtained by the Monte Carlo calculations [66], is be well fitted with an analytical formula proposed by Manini and Salasnich [72] (see also Fig. 4.5):

$$\epsilon(x) = \alpha_1 - \alpha_2 \arctan\left(\alpha_3 x \frac{\beta_1 + |x|}{\beta_2 + |x|}\right). \tag{4.37}$$

There are two sets of parameters for Eq. 4.37, one for $x < 0$ and a different one for $x > 0$. The values are given in Tab. 4.1 and chosen such that equations 4.35 and 4.36 are recovered in the limiting cases $|x| \gg 1$.

For our purposes, the main advantage of an analytic fit function to the QMC data across the Feshbach resonance is that it allows us to calculate an analytic expression for

the speed of first sound. As before we can argue that $u_1 = c_T$ in the zero temperature limit. If we use the general expression 4.34 for the energy, we can derive the pressure of the gas

$$p = -\frac{\partial E}{\partial V} = \frac{2}{5} n E_F \epsilon(x) - \frac{1}{5} n E_F x \epsilon'(x) \tag{4.38}$$

with $\epsilon'(x) = \frac{\partial \epsilon(x)}{\partial x}$ and $\frac{\partial}{\partial V} = \frac{x}{3V}\frac{\partial}{\partial x}$. By using $\left(\frac{\partial}{\partial \rho}\right)_T = -\frac{1}{3\rho} x \left(\frac{\partial}{\partial x}\right)_T$ one obtains for the speed of first sound:

$$u_1 = c_T = \left(\frac{\partial p}{\partial \rho}\right)_T^{1/2} = v_F \left(\frac{1}{3}\epsilon(x) - \frac{1}{5} x \epsilon'(x) + \frac{1}{30} x^2 \epsilon''(x)\right)^{1/2}. \tag{4.39}$$

The result given by Eq. 4.39 is shown in Fig. 4.6. The curve shows a noticeable kink directly on resonance. This is an artefact of the equation of state 4.37 which uses different sets parameters for $x \leq 0$ and $x \geq 0$. In reality there should be no discontinuities in the derivatives of the equation of state as it is known that the BEC-BCS crossover does not have the character of a phase transition.

There is also another crossover model which describes a smooth crossover from the BEC to the BCS superfluid proposed by Eagles [73] and Leggett [74] which yields similar results for the speed of sound as those shown in Fig. 4.6. However, the model predicts the dimer-dimer scattering length to be $a_{D,Leggett} = 2a_A$ which is not correct. As an extension of the BCS theory it naturally is accurate for $1/k_F a_A \ll -1$ and it also reproduces the known BEC limit correctly if the scattering length and mass are set to $a_D = 0.6 a_A$ and $m_D = 2m$. However, it remains unclear how the changing scattering length and the changing mass have to be treated in the strongly interacting regime $|1/k_F a_A| < 1$. More details on this approach are elaborated in the master's thesis of Klaus Hueck [55].

Directly on resonance

Directly on the Feshbach resonance the scattering length a_A diverges and thus cannot be a relevant quantity for determining the behaviour of the gas. If the scattering length is no longer part of the description the only parameters which are still available are those of the non-interacting gas. This implies that the speed of sound has to be proportional to the Fermi velocity, similar to the case of a non-interacting BCS superfluid (Eq. 4.29). However, this argumentation does not give any indication about the proportionality constants, which can be different from the non-interacting situation. The speed of sound directly on resonance ($x = 1/k_F a_A = 0$) is given by Eq. 4.39:

$$u_1 = v_F \sqrt{\frac{\epsilon(0)}{3}}. \tag{4.40}$$

The quantity $\epsilon(0)$ is referred to as Bertsch parameter and sometimes also written as $\beta(0) = \epsilon(0) - 1$. The Bertsch parameter is an important quantity which correlates many properties of the gas on the Feshbach resonance at zero temperature to those of

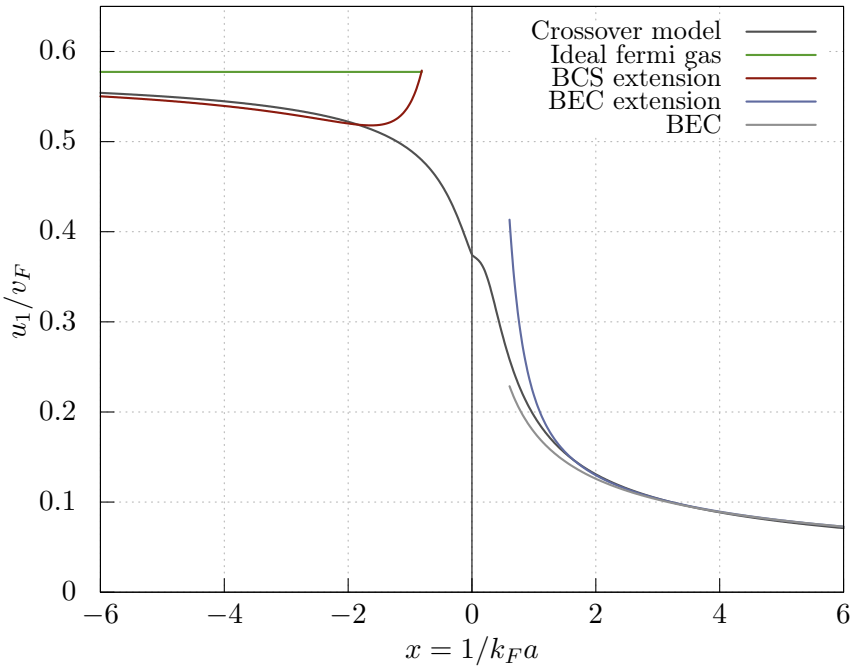

Figure 4.6: The speed of first sound in units of the Fermi velocity across the BEC-BCS crossover for zero temperature. The black curve is the result of Eq. 4.39 with the energy given by Eq. 4.37. In green is the result of the non-interacting Fermi gas, Eq. 4.29 and in red the BCS result including weak interaction, Eq. 4.33. The results for the weakly interacting BEC are shown in grey (Eq. 4.22) and blue (Eq. 4.26). The figure illustrates that the BCS extension is accurate for $1/k_F a_A \lesssim -1.5$ and the BEC extension for $1/k_F a_A \gtrsim 1$ which corresponds to $1/k_F a_D \gtrsim 0.6$.

a non-interacting gas. Different theoretical approaches calculate different values for the Bertsch parameter ranging from $\epsilon(0) = 0.358$ to $\epsilon(0) = 0.42$ [70, 71, 75, 76, 77, 78, 79]. Experimental measurements were e.g. performed in references [80] ($\epsilon(0) = 0.27$), [58] ($\epsilon(0) = 0.376$), [81] ($\epsilon(0) = 0.51$) and [82] ($\epsilon(0) = 0.74$). The experimental determination is difficult since it requires an extrapolation to zero temperature. In this thesis I use $\epsilon(0) = 0.42$ since it is in agreement with the equation of state given by Eq. 4.37 and Tab. 4.1 which can be applied in the whole crossover region.

4.3.3 Speed of sound at finite temperature

In the previous section we considered a superfluid gas at zero temperature which simplified the derivation of the speed of sound significantly. In this section the influence of a finite temperature is presented. We find that the relevant scale at which temperature effects become significant is the mean field temperature $k_B T^* = nU_0$ on the BEC side and the Fermi temperature $k_B T_F = E_F$ on the BCS side. Since in the experiments presented in this thesis the temperature is low compared to the Fermi temperature the effects on the speed of sound in the BCS regime can be neglected. In the far BEC limit the mean field temperature becomes small which implies that thermal effects have in principle to be considered for weak interactions. However, the range of interactions we access in our experiments are such that the influence of temperature on the speed of first sound is small.

In contrast to the zero temperature situation, the mixing term $c_T^2 - c_S^2$ in Eq. 4.11 does not vanish at finite temperatures. Therefore, first and second sound feature both density and temperature oscillations. This coupling was utilized in the recent observation of second sound in a strongly interacting Fermi gas [83].

In this section we derive the speed of sound first for a non-interacting BEC and then include weak interactions. Thereafter, we treat the Fermi gas and the crossover region.

Non-interacting BEC

At finite temperature even a non-interacting BEC shows a non-trivial speed of sound which we derive in this section. According to [65] the energy and pressure in a non-interacting Bose gas below the critical temperature

$$T_c = \frac{2\pi\hbar^2}{m_D k_B}\left(\frac{n_D}{\zeta(3/2)}\right)^{2/3} \approx 0.218\frac{E_F}{k_B} \tag{4.41}$$

is given by

$$\begin{aligned} E &= N k_B \frac{9}{10}\sigma T \frac{\rho_N}{\rho} \\ p &= \zeta\left(5/2\right)\left(\frac{m_D}{2\pi\hbar^2}\right)^{3/2}\left(k_B T\right)^{5/2} \end{aligned} \tag{4.42}$$

which is independent of the density. Therefore, the isothermal speed of sound is $c_T^2 = \left(\frac{\partial p}{\partial \rho}\right)_T = 0$. The entropy per unit mass is given by

$$s = \frac{S}{N_D m_D} = \frac{3\sigma k_B}{2m_D}\frac{\rho_N}{\rho} = \frac{3\sigma k_B}{2m_D}\left(\frac{T}{T_c}\right)^{3/2} \tag{4.43}$$

with $\sigma = \frac{5\zeta(5/2)}{3\zeta(3/2)} \approx 0.856$. We see that the entropy is only carried by the normal component of the gas as one can expect. For the heat capacity c_V and the quantities c_2 and $c_S^2 - c_T^2$ we obtain:

$$\begin{aligned} c_V &= T\left(\frac{\partial s}{\partial T}\right)_\rho = \frac{3}{2}s = \frac{9\sigma k_B}{4m_D}\frac{\rho_N}{\rho} \\ c_2^2 &= \frac{\rho_{SF} s^2 T}{\rho_N c_V} = \sigma\frac{k_B T}{m_D}\frac{\rho_{SF}}{\rho} \\ c_S^2 - c_T^2 &= \left(\frac{\partial s}{\partial \rho}\right)_T^2 \frac{\rho^2 T}{c_V} = \sigma\frac{k_B T}{m_D}\frac{\rho_N}{\rho} \end{aligned} \tag{4.44}$$

where $\left(\frac{\partial s}{\partial \rho}\right)_T = -\frac{s}{\rho}$. By using $\rho = \rho_{SF} + \rho_N$ we see that

$$c_S^2 + c_2^2 = \left(c_S^2 - c_T^2\right) + c_2^2 + c_T^2 = \sigma\frac{k_B T}{m_D}. \tag{4.45}$$

With Eq. 4.13 we conclude:

$$\begin{aligned} u_1 &= \sqrt{\sigma\frac{k_B T}{m_D}} = v_F\sqrt{\frac{\sigma}{4}\frac{T}{T_F}} \\ u_2 &= 0 \end{aligned} \tag{4.46}$$

with the Fermi temperature $k_B T_F = E_F$. We see that in the non-interacting limit the second sound vanishes. This can be understood by keeping in mind that without interactions there is no restoring force for a local excess in superfluid density. Therefore, the additional degree of freedom introduced to the system by having a superfluid density cannot participate in the propagation of sound modes. Note, that the speed of sound given in Eq. 4.46 cannot be written in units of the Fermi velocity v_F and only as a function of $1/k_F a_A$. This is a substantial difference to the zero temperature limit in section 4.3.2.

Weakly interacting BEC

To judge the influence of a finite temperature in the case of a weakly interacting BEC I follow the arguments given by Heiselberg in Ref. [64]. The dispersion relation of an interacting BEC is first linear for low momenta k and becomes parabolic for larger k. The

linear part is caused by the interaction nU_0 and is important for energies (and temperatures) lower than the mean field energy $k_BT \lesssim k_BT^* = nU_0$. For higher temperatures the parabolic part has to be considered. The critical temperature of the BEC is given by Eq. 4.41 which does not change much under the influence of weak interactions [84]. Thus, we can write

$$\frac{T^*}{T_c} = 2\left(\zeta\left(3/2\right)\right)^{2/3} \frac{1}{\left(6\pi^2\right)^{1/3}} k_F a_D \approx k_F a_D. \tag{4.47}$$

Typical temperatures which are achieved in the experiment are on the order of half the critical temperature $T \approx T_c/2$. The phononic excitations are therefore dominant as soon as the interactions are strong enough, $1/k_F a_A \lesssim 1$ (with $a_D = 0.6 a_A$). However, this is a regime where the theory of a weakly interacting BEC is inaccurate as can be seen for example in Fig. 4.5. In the regime where the theory of a weakly interacting BEC is valid, $1/k_F a \gg 1$, we thus have to consider the quadratic part of the dispersion relation. Hence the entropy in Eq. 4.43 remains valid as well as the results given by the equations 4.44. We conclude:

$$c_S^2 + c_2^2 = \sigma \frac{k_B T}{m_D} + c_T^2. \tag{4.48}$$

We saw from Eq. 4.42 that the thermal contribution to the pressure p_T is independent from the density and thus does not contribute to the isothermal speed of sound $c_T^2 = (\partial p/\partial \rho)_T$. However, the pressure also has a contribution which has its origin in the interaction energy:

$$E_{int} = \frac{N_D^2 U_0}{2V}\left(1 + \frac{\rho_N}{\rho}\right). \tag{4.49}$$

The part ρ_N/ρ reflects that thermal atoms interact twice as strong compared to atoms in the ground state. This additional term is proportional to the entropy and thus does not contribute to the pressure of the gas:

$$p = -\left(\frac{\partial E}{\partial V}\right)_S = \frac{\rho^2 U_0}{2m_D^2} + p_T. \tag{4.50}$$

The isothermal speed of sound is then the same as in the zero temperature situation (Eq. 4.17)

$$c_T^2 = \left(\frac{\partial p}{\partial \rho}\right)_T = \frac{\rho U_0}{m_D^2} \tag{4.51}$$

and the speed of sound follows from Eq. 4.13:

$$u_{1/2}^2 = \frac{1}{2}\left(\frac{\sigma k_B T}{m_D} + c_T^2\right) \pm \sqrt{\left(\frac{1}{2}\left(\frac{\sigma k_B T}{m_D} + c_T^2\right)\right)^2 - \frac{\sigma k_B T}{m_D}\frac{\rho_{SF}}{\rho} c_T^2} \tag{4.52}$$

with c_T given by Eq. 4.23. Equation 4.52 shows that the relevant scale for temperature effects is the mean field temperature $k_BT^* = nU_0$. In a typical molecular BEC realized

in our experiments we have $T/T_c \approx 0.5$. Under such conditions, we can approximate the speed of first sound:

$$u_1 \approx \sqrt{\sigma \frac{k_B T}{m_D} + c_T^2}. \tag{4.53}$$

The error to the complete expression 4.52 at $T/T_c \approx 0.5$ is approximately 10 % for $1/k_F a_A \approx 2.2$ and less for other interaction strengths. In the BEC limit, $1/k_F a_A \gg 1$, expression 4.53 is exact as the superfluid fraction becomes negligible.

Interestingly, Eq. 4.51 shows that the isothermal speed of sound is a function of the total density ρ instead of just the superfluid density ρ_S. In the zero temperature situation (Eq. 4.17) we identified c_T with Bogoliubov phonons which are a result of the Gross-Pitaevskii equation and are thus strongly connected to the density of the superfluid fraction of the gas. This discrepancy can be explained by noting that the Gross-Pitaevskii equation does not account for finite temperature effects.

Degenerate non-interacting Fermi gas

The speed of sound in the non-interacting Fermi gas at finite temperature is more complicated as in the case of a non-interacting Bose gas. In the Fermi gas the combination of Pauli blocking and temperature implies that the pressure as well as the entropy contribute to the speed of sound. The non-interacting Fermi gas has no superfluid density and hence $c_2 = 0$. Thus, Eq. 4.13 simplifies to $u_1 = c_S$ and $u_2 = 0$. The energy and entropy of the gas are [68]:

$$E = \frac{3}{5} N E_F \left(1 + \frac{5\pi^2}{12}\left(\frac{T}{T_F}\right)^2 + \dots\right) \tag{4.54}$$

and

$$S = k_B N \frac{\pi^2}{2} \frac{T}{T_F}. \tag{4.55}$$

The pressure which follows from Eq. 4.54 is

$$p = -\left(\frac{\partial E}{\partial V}\right)_S = \frac{2}{5} n E_F \left(1 + \frac{5\pi^2}{12}\left(\frac{T}{T_F}\right)^2\right) \tag{4.56}$$

which leads to the isothermal speed of sound:

$$c_T^2 = \left(\frac{\partial p}{\partial \rho}\right)_T = \frac{1}{3} v_F^2 \left(1 + \frac{\pi^2}{12}\left(\frac{T}{T_F}\right)^2\right). \tag{4.57}$$

As the entropy given by Eq. 4.55 is linear in temperature we see $c_V = s = \frac{k_B}{m}\frac{\pi^2}{2}\frac{T}{T_F}$ which can be used to calculate c_S with the help of Eq. 4.9:

$$\begin{aligned} c_S^2 &= c_S^2 - c_T^2 + c_T^2 = \left(\frac{\partial s}{\partial \rho}\right)_T^2 \frac{\rho^2 T}{c_V} + c_T^2 = \frac{4}{9} sT + c_T^2 \\ &= \frac{1}{3} v_F^2 \left(1 + \frac{5\pi^2}{12}\left(\frac{T}{T_F}\right)^2\right). \end{aligned} \tag{4.58}$$

The same result can be obtained by directly calculating $c_S^2 = \left(\frac{\partial p}{\partial \rho}\right)_s$. Finally, the expression for the speed of first sound is

$$u_1 = c_S = v_F \frac{1}{\sqrt{3}} \left(1 + \frac{5\pi^2}{12}\left(\frac{T}{T_F}\right)^2\right)^{1/2}. \tag{4.59}$$

The modification to the zero temperature case, given by Eq. 4.29, is small for $\frac{T}{T_F} \ll \sqrt{\frac{12}{5\pi^2}} \approx 0.493$.

Weakly interacting BCS superfluid

In the case of a BCS superfluid we require $T < T_C$. The critical temperature is a function of the gap Δ which itself is an exponential function of the interaction parameter $1/k_F a_A$ [1]:

$$T_C \approx 0.57 \frac{\Delta}{k_B} \approx 0.61 \frac{E_F}{k_B} e^{\frac{\pi}{2 k_F a_A}}. \tag{4.60}$$

Hence, for weak interactions we demand $T \ll T_F$. Equation 4.59 shows that the relevant scale for temperature effects on the speed of first sound is the Fermi temperature and thus can be neglected. Therefore, Eq. 4.33 remains valid and $u_2 \approx c_2 \ll u_1$. The speed of second sound was calculated in Ref. [64]. It is zero for $T = 0$ and $T = T_c$ and shows a broad maximum around $T = 0.7 T_c$. The value of the maximum is approximately

$$\max(u_2) \approx 0.57 \frac{k_B T}{E_F} v_F \tag{4.61}$$

which contains the small parameter $k_B T / E_F < k_B T_C / E_F \ll 1$.

Crossover

The determination of the speed of sound in a gas with strong interactions $|1/k_F a| < 1$ and finite temperature is difficult since the type of the excitation and thus also the entropy is unknown. However, directly on resonance $1/k_F a = 0$ there is a measurement of the entropy by the Zwierlein group [58]. At high temperatures ($T/T_F \gtrsim 0.17$) the entropy is that of a non-interacting Fermi gas whereas for lower temperatures the entropy rapidly

drops which the authors of the paper interpret as a change in the nature of the excitations from free particles to phonons. We can therefore assume that the modification of the speed of sound due to temperature is a combination of the effects in a BEC (Eq. 4.52) and those of a Fermi gas (Eq. 4.59). In our experimental realisation the temperature effects are small in the two limits hence we expect them to be small in the BEC-BCS crossover as well. Reference [64] shows an approximation of the speed of sound at finite temperature which is only slightly different from the zero temperature result for $T/T_C \leq 0.75$

4.3.4 Influence of the trap

To calculate the speed of sound in a trapped system, the local density approximation can be applied. For the experiments we performed on the speed of sound this approximation is well justified as the changes in density (i.e. the wavelength of the sound wave) are long compared to the healing length of the gas. For each position in the cloud, the (local) speed of sound can then be calculated by using the local density and the formulas given in Tab. 4.2 on page 122. However, there are two additional points which have to be considered when comparing our measured data to the theoretical predictions:

- In the experiment it is only possible to measure integrated column densities. Hence, there is no direct access to k_F. A convenient strategy is to work with the Fermi number k_N of a non-interacting Fermi gas which is easily related to the total particle number via $\frac{\hbar^2 k_N^2}{2m} = \hbar\bar{\omega}\,(6N)^{1/3}$. The relation between $k_F a_A$ and $k_N a_A$ can be derived via the equation of state.

- In a very oblate cloud the circular sound wave moves outwards in an effective density which is the average density along the strongly confined direction as long as the system is hydrodynamic.

Fermi wavenumber of a non-interacting Fermi gas

Our measurements of the speed of sound in a strongly interacting Fermi gas are performed in a trapped and very oblate, but three-dimensional, gas. The images we record of the samples show a density which is integrated along the line-of-sight of the imaging optics. Therefore, there is no direct access to the local density of atoms which would be necessary to make a theoretical prediction for the speed of sound. To deal with this problem we measure the total particle number and define the Fermi wave number of a non-interacting gas via

$$\frac{\hbar^2 k_N^2}{2m} = \hbar\bar{\omega}\,(6N)^{1/3}\,. \tag{4.62}$$

The quantity k_N, defined by this equation, equals the real Fermi wave number (which is a function of the density $k_F^3/\left(6\pi^2\right) = n$) only far in the BCS limit. On resonance and in the BEC regime $k_F \neq k_N$. As k_N can be easily extracted from the experiment we need to derive the relation connecting k_F and k_N. To avoid confusion about the definition of

the two Fermi wave numbers I will write $k_n := k_F$ in the following to indicate that the quantity is derived from the density n.

The chemical potential in the centre of the trap at a certain interaction strength $x = 1/k_n a_A$ can be written as

$$\mu_0 = c n_0^\gamma \tag{4.63}$$

with the density in the trap centre n_0, the constant c and the polytropic index $\gamma > 0$. In the following I will show how to relate k_n and k_N using Eq. 4.63. In a harmonic trap $V(\vec{x}) = \frac{1}{2}m\left(\omega_x^2 x^2 + \omega_y^2 y^2 + \omega_z^2 z^2\right)$ the local chemical potential is $\mu\left(\vec{r}\right) = \mu_0 - V(\vec{x})$ which leads to the following density distribution:

$$n(\vec{x}) = n_0 \max\left(1 - \frac{x^2}{R_x^2} - \frac{y^2}{R_y^2} - \frac{z^2}{R_z^2}, 0\right)^{1/\gamma}. \tag{4.64}$$

Here R_i is the Thomas Fermi radius in the direction $i \in \{x, y, z\}$:

$$R_i = \sqrt{\frac{2\mu_0}{m\omega_i^2}}. \tag{4.65}$$

The central chemical potential μ_0 is fixed by the total particle number:

$$N = \int n(\vec{x})\,\mathrm{d}V. \tag{4.66}$$

Equation 4.66 evaluated with the density distribution given by Eq. 4.64 yields

$$N = n_0 \pi R_x R_y R_z \frac{\Gamma(1 + 1/\gamma)}{\Gamma(5/2 + 1/\gamma)}. \tag{4.67}$$

with the gamma function $\Gamma(x) = \int_0^\infty t^{x-1}\mathrm{e}^{-t}\,\mathrm{d}t$. The condition $\mu(\vec{x}) = 0$ for $\vec{x} \in \left\{(x, y, z)|\frac{x^2}{R_x^2} + \frac{y^2}{R_y^2} + \frac{z^2}{R_z^2} = 1\right\}$ fixes the radii R_i. Equation 4.67 connects the total particle number N with peak density in the cloud centre n_0. Therefore, we can relate the Fermi wave number of a non-interacting Fermi gas k_N to the Fermi wavenumber $k_n^3 = 6\pi^2 n_0$:

$$\begin{aligned}\frac{\hbar^2 k_N^2}{2m} = \hbar\bar{\omega}(6N)^{1/3} &= \hbar k_n \sqrt{\frac{2\mu_0}{m}} \left(\frac{\Gamma\left(1 + 1/\gamma\right)}{\sqrt{\pi}\Gamma\left(5/2 + 1/\gamma\right)}\right)^{1/3} \\ &= \frac{\hbar^2 k_n^2}{m} \sqrt{\frac{\mu_0}{E_n}} \left(\frac{\Gamma\left(1 + 1/\gamma\right)}{\sqrt{\pi}\Gamma\left(5/2 + 1/\gamma\right)}\right)^{1/3}\end{aligned} \tag{4.68}$$

with the mean trap frequency $\bar{\omega}^3 = \omega_x\omega_y\omega_z$ and the local Fermi energy in the trap centre $E_n = \frac{\hbar^2 k_n^2}{2m}$.

The two unknown parameters in Eq. 4.68, μ_0 and γ, need to be determined with the equation of state. If we write the energy per particle in the trap centre in the general form given by Eq. 4.34, $\frac{E_0}{N} = \frac{3}{5}E_n\epsilon(x)$, the chemical potential is

$$\mu_0 = \frac{\partial E_0}{\partial N} = E_n\left(\epsilon(x) - \frac{1}{5}x\epsilon'(x)\right), \tag{4.69}$$

where $\frac{\partial}{\partial N} = -\frac{x}{3N}\frac{\partial}{\partial x}$. The comparison of equations 4.63 and 4.69 yields an expression for the exponent γ as a function of the interaction strength x:

$$\gamma = \frac{\partial \ln \mu_0(x)}{\partial \ln n_0} = -\frac{1}{3}x\frac{\partial}{\partial x}\ln \mu_0(x) = \frac{2}{3} - \frac{1}{3}x\frac{\frac{4}{5}\epsilon'(x) - \frac{1}{5}x\epsilon''(x)}{\epsilon(x) - \frac{1}{5}x\epsilon'(x)}. \tag{4.70}$$

A plot of γ as a function of the interaction parameter is shown in Fig 4.7 based on $\epsilon(x)$ given by Eq. 4.37. The relation between k_n and k_N is obtained by combining equations 4.68 and 4.69:

$$k_N = k_n\sqrt{2}\left(\epsilon(x) - \frac{1}{5}x\epsilon'(x)\right)^{1/4}\left(\frac{\Gamma\left(1+1/\gamma\right)}{\sqrt{\pi}\Gamma\left(5/2+1/\gamma\right)}\right)^{1/6}. \tag{4.71}$$

In Fig. 4.8 a plot of $1/k_N a_A$ as a function of $x = 1/k_n a_A$ is shown by assuming that $\epsilon(x)$ is given by Eq. 4.37. Figure 4.9 shows the ratio k_N/k_n as a function of the interaction strength. Note, that the ratio of the corresponding Fermi velocities, $v_N = \frac{\hbar k_N}{m}$ and $v_n = \frac{\hbar k_n}{m}$, equals the ratio of the Fermi wavenumbers $\frac{v_N}{v_n} = \frac{k_N}{k_n}$.

As the energy per particle is known for a BEC and for a free Fermi gas we can give the expressions in those limits as well as for a gas directly on resonance:

- **Weakly interacting BEC:** For $x \gg 1$ the chemical potential is given by $\mu_0 = n_0 U_0$ and therefore $\gamma = 1$[6]. To first order in $1/x$ the quantity $\epsilon(x)$ is given by (see also Eq. 4.35)

  $$\epsilon(x) = \frac{5}{18\pi}\frac{1}{x}. \tag{4.72}$$

  According to Eq. 4.71 the relation between k_n and k_N is then:

  $$\begin{aligned} k_N &= k_n\sqrt{2}\left(\frac{1}{3\pi x}\frac{a_D}{a_A}\right)^{1/4}\left(\frac{8}{15\pi}\right)^{1/6} \\ &\approx 0.5286 \cdot k_n \frac{1}{x^{1/4}} \end{aligned} \tag{4.73}$$

  and therefore

  $$\frac{1}{k_N a_A} \approx 1.8918 \cdot \left(\frac{1}{k_n a_A}\right)^{5/4} \tag{4.74}$$

- **Non-interacting Fermi gas** In the limit $x \to -\infty$ the energy per particle is $\frac{E}{N} = \frac{3}{5}E_n$ and therefore $\epsilon(x) = 1$. It follows from Eq. 4.70 that $\gamma = 2/3$ and therefore

  $$k_N = k_n \tag{4.75}$$

  as expected.

[6] The same result is obtained by using the first order in $1/x$ of Eq. 4.35 in Eq. 4.70

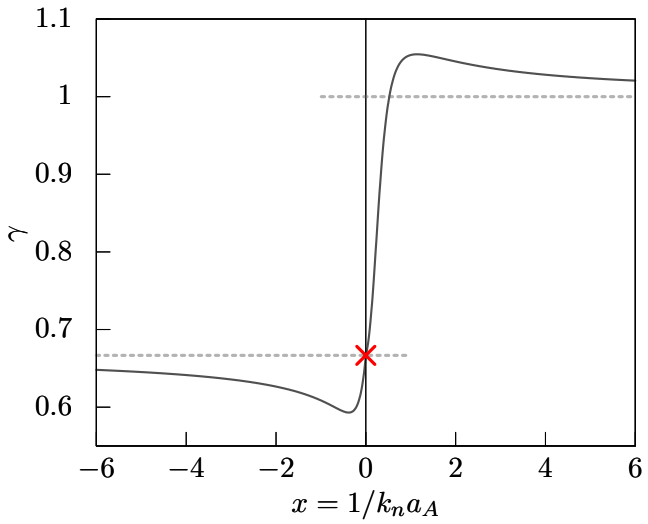

Figure 4.7: The exponent γ as given by Eq. 4.70 which determines the chemical potential in Eq. 4.63 as a function of the interaction parameter $x = 1/k_n a_A$. The solid line follows from the equation of state given by Eq. 4.37. The dashed lines are the limits in the BEC ($\gamma = 1$) and BCS $\gamma = 2/3$ regimes. The mark at $x = 0$ is the value on resonance where the chemical potential behaves similar to that of a non-interacting Fermi gas.

- **Resonant Fermi gas:** For $x = 0$ equations 4.70 and 4.71 greatly simplify and yield $\gamma = 2/3$ and

$$k_N = k_n \epsilon(0)^{1/4} \approx 0.805 \cdot k_n \tag{4.76}$$

with the Bertsch parameter $\epsilon(0) \approx 0.42$. The fact that the parameter γ is the same as in the limit of a free Fermi gas strengthens the intuition that a resonant Fermi gas behaves similar to a non-interacting Fermi gas in many aspects.

Effective density in the strongly confined direction

To understand the propagation of sound modes in very oblate trapped clouds we have to consider another effect that modifies the speed of sound. In our experiments the wavelength of the sound mode is larger than the spatial extend of the cloud in the strongly confined direction, $\lambda > R_z$. As long as the gas is hydrodynamic in the z-direction the propagation of the density wave is two-dimensional. There is no propagation in the z-direction and the propagation speed in radial direction can be expected to be a function of the average density $\bar{n}(x, y)$ along the z-direction. The same effect was encountered in the speed of sound measurements in Ref. [60] which were performed in a cigar shaped cloud. There the radially averaged density is determining the one-dimensional propagation of the sound wave. More profound theoretical studies of this effect have been published in references [62] and [63].

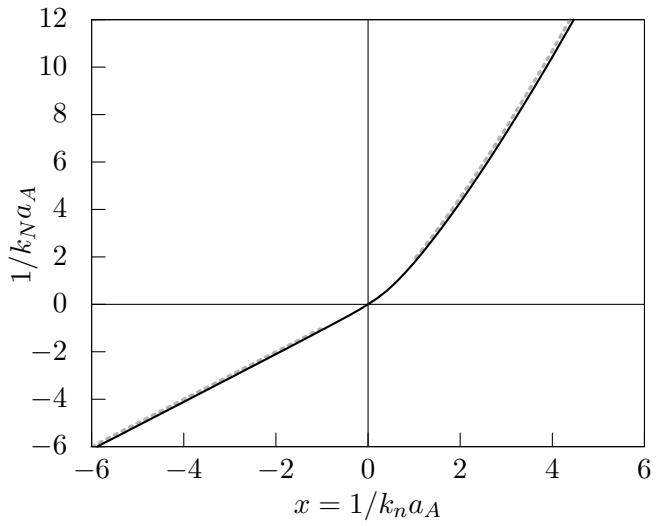

Figure 4.8: The interaction strength $1/k_N a_A$ in terms of the Fermi wavenumber of a non-interacting Fermi gas k_N as function of $1/k_n a$. The Fermi wavenumber k_n is a function of the central density whereas k_N is deduced from the total particle number in the trap. The relation between the two is required to compare the theoretical predictions of the speed of sound (which is a function of $1/k_n a$) to the experimentally measured values. In the experiment only k_N is directly accessible. The solid line assumes the equation of state 4.37. The dashed lines are the BEC and BCS limits given by equations 4.74 and 4.75.

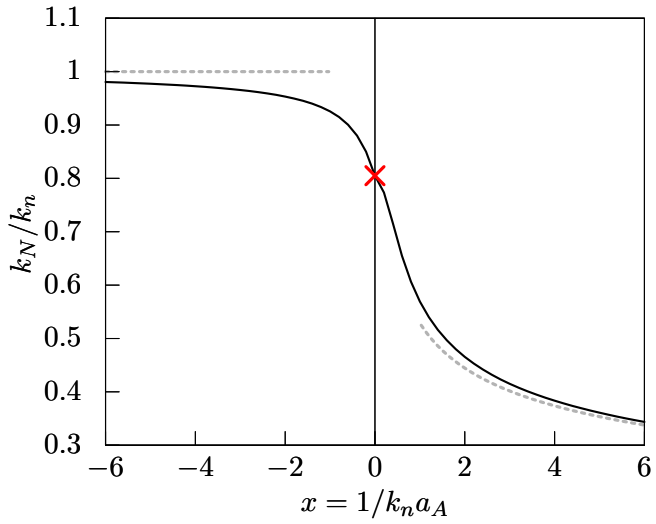

Figure 4.9: The ratio of the Fermi wavenumber of a non-interacting Fermi gas and the Fermi wavenumber k_N/k_n as a function of the interaction parameter $x = 1/k_n a_A$. The solid line assumes the equation of state 4.37. The dashed lines are the BEC and BCS limits given by equations 4.74 and 4.75.

For the case of a two-dimensional sound propagation in a cloud with a density distribution given by Eq. 4.64 the averaged density in the cloud centre $(x, y) = (0, 0)$ is given by

$$\bar{n}_0 = \frac{1}{2R_z} \int_{-R_z}^{R_z} n(0, 0, z)\, \mathrm{d}z = n_0 \frac{\sqrt{\pi}}{2} \frac{\Gamma\left(1 + 1/\gamma\right)}{\Gamma\left(3/2 + 1/\gamma\right)}. \tag{4.77}$$

Equation 4.77 simplifies to $\bar{n}_0 = \frac{2}{3} n_0$ in the BEC limit ($\gamma = 1$) and to $\bar{n}_0 = \frac{3\pi}{16} n_0$ in the BCS limit ($\gamma = \frac{2}{3}$). With $n_0 = \frac{k_n^3}{6\pi^2}$ Eq. 4.77 translates to

$$\bar{k}_n = k_n \left(\frac{\sqrt{\pi}}{2} \frac{\Gamma\left(1 + 1/\gamma\right)}{\Gamma\left(3/2 + 1/\gamma\right)} \right)^{1/3}, \tag{4.78}$$

where we defined the Fermi wavenumber $\bar{k}_n$ which corresponds to the averaged central density $\bar{n}_0$. A plot of the speed of sound including the averaging effect as a function of the Fermi wavenumber of a non-interacting Fermi gas k_N is shown in Figure 4.10. The kink of the curves directly on resonance is an artefact of the equation of state 4.37.

The averaging effect described above can only play a role as long as the interaction is large enough such that the gas is hydrodynamic in the strongly confined direction. According to Ref. [85] this is the case as long as the spatial extend of the system $2R_z$ is larger than the collisional mean free path $l \approx \frac{1}{\bar{n}A}$ with the s-wave scattering cross section[7] $A = 8\pi a^2$.

For most of our measurements of the speed of sound the mean free path l and the system size R_z were comparable to each other. It is therefore not clear if the averaged or the peak density should be used to describe the speed of sound and the measured data points should be in between the two predictions. However, for the measurements closer to the Feshbach resonance the gas was further in the hydrodynamic regime as for those measurements with weaker interactions. This argument is in good agreement with the experimental results shown in Fig. 4.3.

[7] The scattering length a is given by a_D for a BEC and by a_A in the BCS regime.

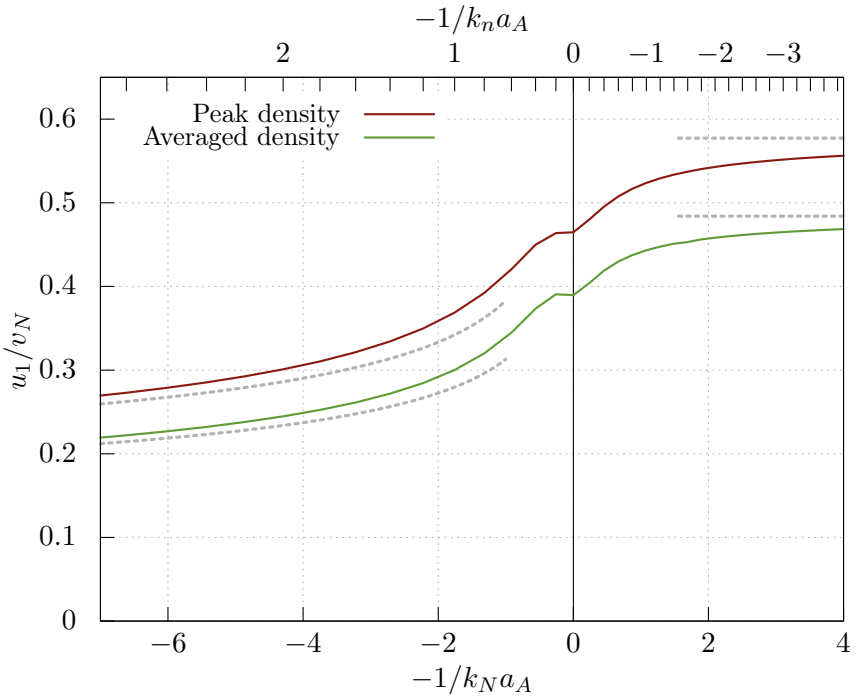

Figure 4.10: The speed of first sound at zero temperature in the trap centre in units of the Fermi velocity of a non-interacting Fermi gas v_N as a function of $-1/k_N a_A$. The upper x axis shows the corresponding value of $-1/k_n a_A$, see also Fig. 4.8. The negative sign is chosen to make the plot more intuitive for experiments with ^{6}Li where the BEC is realized at low magnetic fields. The green curve includes the averaging effect along the strongly confining direction whereas the red curve assumes that the peak density is relevant for the speed of sound. Note, that both curves are plotted in units of the local Fermi velocity v_N in the trap centre which does not include any averaging. The dashed lines are the analytic curves in the BEC and BCS limits with and without averaging.

4.4 Summary

We measured the speed of sound in the BEC-BCS crossover in a oblate ultracold fermionic gas. The results are in good agreement with theory. The most important aspects of the behaviour of the speed of sound in the crossover can be summarized as follows:

- In the BEC regime at zero temperature first and second sound are finite and are a result of the mean field interaction energy nU_0. The non-interacting BEC at $T = 0$ does not support first sound.
- In the BEC regime temperature effects become relevant for temperatures larger than the mean field temperature $T > T^* = nU_0/k_B$.
- Speed of sound in a Fermi gas at zero temperature is an effect due to Pauli blocking and interaction energy. Therefore, even the non-interacting Fermi gas supports the first sound mode.
- The relevant scale for temperature effects on the speed of first sound in a Fermi gas is the Fermi temperature.
- The calculation of the sound modes in the strongly interacting regime is difficult. Monte Carlo simulations can give insights to the zero temperature situation. The resulting speed of sound as a function of the interaction interpolates between the two known limits on the BEC and the BCS side.

For the conditions which are realized in our experiment ($T/T_C \approx 0.5$ on the BEC side and $|1/k_N a_A| < 7$), the temperature influence is small and can be neglected. The expressions for the speed of first sound in the different interaction regimes are shown again in Tab. 4.2. If the speed of sound is measured in a very oblate atom cloud which is thin compared to the wavelength of the sound wave and hydrodynamic in all directions it is the average density along the strongly confined direction which determines the speed of sound. Our data suggests that the measurements are performed in an interesting partially hydrodynamic regime. Finally, due to experimental reasons, we plot the speed of sound in units of the Fermi velocity of a non-interacting Fermi gas v_N which is a function of the total particle number. Similarly, the s-wave scattering length is compared to the Fermi wavenumber of a non-interacting Fermi gas k_N to quantify the interaction strength.

Interaction Regime	$u_1(T=0)$	$u_1(T>0)$
Non-interacting BEC $x \to +\infty$	0	$\sqrt{\sigma \frac{k_B T}{m_D}}$
Weakly interacting BEC $x \gg 1$	$\sqrt{\frac{n_D U_0}{m_D}} \approx 0.178 v_F \sqrt{k_F a_A}$	$\sqrt{\frac{n_D U_0}{m_D} + \sigma \frac{k_B T}{m_D}}$
Weakly interacting BEC $x > 1$	$\sqrt{\frac{n_D U_0}{m_D}\left(1 + \frac{32}{\sqrt{6\pi^3}}\left(\frac{a_D}{a_A}\right)^3 (k_F a_A)^3\right)}$	
Strongly interacting gas $\lvert x\rvert < 1$	$v_F \sqrt{\frac{1}{3}\epsilon(x) - \frac{1}{5}x\epsilon'(x) + \frac{1}{30}x^2\epsilon''(x)}$	
Resonant gas $x = 0$	$v_F \sqrt{\frac{\epsilon(0)}{3}}$	
Weakly interacting Fermi gas $x < -1$	$\frac{v_F}{\sqrt{3}}\sqrt{1 + \frac{2}{\pi}k_F a_A + \frac{8(11-2\ln 2)}{15\pi^2}(k_F a_A)^2}$	
Non-interacting Fermi gas $x \to -\infty$	$v_F \frac{1}{\sqrt{3}}$	$v_F \frac{1}{\sqrt{3}}\sqrt{1 + \frac{5\pi^2}{12}\left(\frac{T}{T_F}\right)^2}$

Table 4.2: Summary of the speed of first sound across the BEC-BCS crossover for zero and finite temperature. The interaction parameter is defined as $x = 1/k_F a_A$, with $k_F^3/(6\pi^2) = n$. On the BEC side the dimer mass and scattering length are $m_D = 2m$ and $a_D = 0.6 a_A$ where m is the mass of a single atom, a_A is the atom-atom scattering length and $\sigma \approx 0.856$ In the strongly correlated regime the parameter $\epsilon(x)$ describes the energy per particle of the gas and is given by Eq. 4.37.

5 The critical velocity across the BEC-BCS crossover

5.1 Introduction to superfluidity

Superconductivity is amongst those physical phenomena which have the highest potential impact on future technology. Superfluidity and superconductivity describe the astonishing property of sustained particle currents on a macroscopic scale without friction and their appearance is remarkably widespread, ranging from superfluid helium over the cores of neutron stars to metallic and non-metallic superconductors [1, 86]. The flowing particles are all condensed in the same quantum wave function which allows them to flow dissipationless over long times. Despite the tremendous efforts which have been put into the development of theories to describe this astonishing behaviour the underlying mechanisms are still not fully understood. On the one hand, there are several successful theories specialised on the description of particular superfluid systems. Examples are the Bogoliubov theory which describes the BEC state or the BCS theory which explains conventional superconductors. On the other hand, the microscopic effects in superfluid ^{4}He are not entirely understood and the situation is even more controversial for unconventional superconductors such as those in the cuprate family. One particular issue that arises in the description of those systems is that they feature strong interactions which make it difficult to describe their excitations as quasi-particles. Here experiments on ultracold fermions are a unique and powerful tool to gain deeper understanding. They are capable to probe the strongly interacting regime as well as the almost fully understood BEC and BCS regimes. Therefore the experiments can be verified and calibrated in the known limits and then used to investigate strongly correlated phenomena. Furthermore, modern cold fermion experiments offer control over other properties like dimensionality or lattice geometries which are likely to have significant importance in the creation of superfluid states.

In this chapter, I present our measurements of the superfluid critical velocity across the BEC-BCS crossover. Those measurements are the main result of this chapter and shown in Fig. 5.4. The corresponding theory is presented and the experimental data for the critical velocity is compared to the speed of sound which was discussed in chapter 4. We find that the critical velocity in the BEC regime does not behave as predicted by simple mean field theory. Simulations which were performed by Vijay Singh and Ludwig

Mathey were able to explain this discrepancy and are presented in the end of the chapter.

Part of this chapter will be published, the preprint reference is [87].

5.1.1 Theory and Landau's criterion

The Landau criterion for superfluidity makes the connection between the excitation spectrum of a superfluid and the critical velocity. To derive it I will follow the arguments given in Ref. [1]. Let us consider a rigid obstacle of large mass M moving at a velocity $\vec{v}$ trough a superfluid. The superfluid shall be at rest. For small $\vec{v}$ the flow around the obstacle will be frictionless and the obstacle will not experience any drag force. Above the critical velocity v_c, a non-zero drag force will appear and reduce the kinetic energy of the obstacle. This energy is dissipated into the surrounding fluid by creating excitations. The process has to conserve the total momentum and the energy of the system. If one such excitation has a momentum $\vec{p}$ and an energy $\epsilon(p)$ it will reduce the velocity of the obstacle by $\vec{\delta v}$. Therefore we conclude

$$\frac{1}{2}M\vec{v}^2 = \frac{1}{2}M\left(\vec{v}-\vec{\delta v}\right)^2 + \epsilon(p) \tag{5.1}$$

and

$$M\vec{v} = M\left(\vec{v}-\vec{\delta v}\right) + \vec{p}. \tag{5.2}$$

After elimination of $\vec{\delta v}$ and assuming that the mass M is large these two equation simplify to

$$\vec{p}\cdot\vec{v} = \epsilon(p). \tag{5.3}$$

Since $|\vec{p}\cdot\vec{v}| \leq pv$ the Landau velocity v_L, which is the minimal velocity for creating excitations, is given by

$$v_L = \min_{p\geq 0}\frac{\epsilon(p)}{p}. \tag{5.4}$$

The excitation spectrum for free particles is $\epsilon(p) \propto p^2$ and therefore $v_L = 0$. Hence, a system with an excitation spectrum which allows for free particle motion cannot be superfluid. Equation 5.4 could be experimentally confirmed by measuring the drag force experienced by a moving ion in superfluid ^{4}He [88]. The measured critical velocity of $v_c = 46\,\mathrm{m\,s^{-1}}$ (see Fig. 5.1) is in excellent agreement with the roton minimum [89] in the excitation spectrum shown in Fig. 5.2 if pressure effects are taken into account. The excitation spectrum itself could be obtained from neutron scattering experiments [90]. It is worth mentioning that the nature of the roton excitation is not entirely known. Here the study of superfluidity in ultracold gases might give the insights needed to develop a more complete understanding.

In the following sections I will describe superfluidity in quantum gases in the limiting cases of the BEC and the BCS theory. There, v_c is predicted to be limited by the creation of phonons (BEC) and the breaking of cooper pairs (BCS).

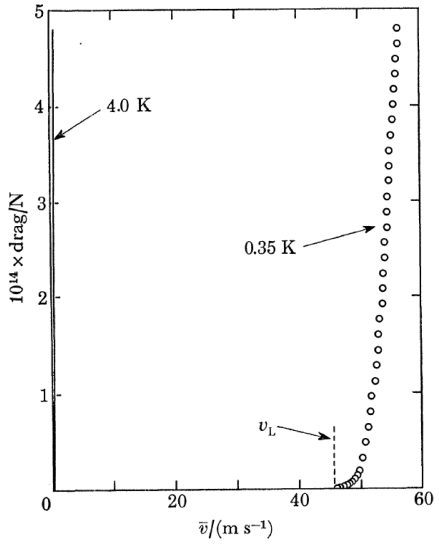

Figure 5.1: Measurement of the drag force experienced by an ion moving through superfluid ^{4}He as published in Ref. [88]. Drag sets in as soon as the Landau critical velocity v_L is reached (open circles). Here $v_L = 46\,\mathrm{m\,s^{-1}}$ was measured at a pressure of 25.3 bar close to the solidification pressure. For comparison the drag force of helium in the normal fluid phase is shown as well (solid line).

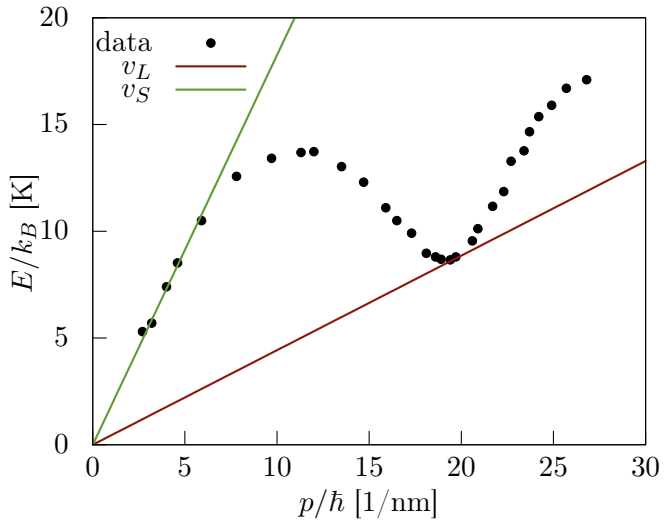

Figure 5.2: Excitation spectrum of superfluid ^{4}He obtained from neutron scattering experiments at standard pressure (black dots) [90]. The red line illustrates the Landau critical velocity v_L as given in Eq. 5.4. Its slope is $58\,\mathrm{m\,s^{-1}}$ and corresponds to the creation of rotons. The speed of sound $v_S = 239\,\mathrm{m\,s^{-1}}$ is significantly higher and can be extracted from the spectrum by a linear fit from the origin to the low momenta excitations (green line).

5.1.2 Superfluidity in a BEC

The ground state wave-function $\Psi(\vec{r})$ of an interacting BEC is well described by the mean field equation named after Eugene P. Gross and Lev P. Pitaevskii:

$$\left(-\frac{\hbar^2}{2m_D}\Delta + V(\vec{r}) + U_0\left|\Psi(\vec{r})\right|^2\right)\Psi(\vec{r}) = \mu\Psi(\vec{r}) \tag{5.5}$$

Here m_D is the mass of the constituent bosons, $V(\vec{r})$ is the confining potential and $U_0 = \frac{4\pi\hbar^2 a_D}{m_D}$ is the interaction parameter with the dimer-dimer s-wave scattering length a_D. The chemical potential μ has to be fixed such that the total particle number is $N = \int|\Psi|^2$. In order to obtain the superfluid critical velocity with Eq. 5.4 we have to calculate the excitation spectrum of the system described by Eq. 5.5. With the Bogoliubov approximation and in the case of a homogeneous system, i.e. for $V(\vec{r}) = 0$, one obtains the following excitation spectrum

$$\epsilon(k) = \sqrt{\frac{\hbar^2k^2}{2m_D}\left(\frac{\hbar^2k^2}{2m_D} + 2U_0n_0\right)} \tag{5.6}$$

with the particle density $n_D = |\Psi|^2$. This spectrum is quadratic for large momenta $\hbar k$ similar to free particles. For small momenta the spectrum becomes linear

$$\epsilon(k) = \sqrt{\frac{n_DU_0}{m_D}}\hbar k,\ k \ll \sqrt{4\pi a_DU_0} = \frac{\sqrt{4U_0n_Dm_D}}{\hbar}. \tag{5.7}$$

It is this linear part of the excitation spectrum which is defining the Landau critical velocity. Due to the linearity these low momenta excitations are usually refereed to as phonons and the corresponding velocity is the speed of sound u_1:

$$v_{L,BEC} = u_1 = \sqrt{\frac{n_DU_0}{m_D}}. \tag{5.8}$$

This mean field treatment naturally does not account for beyond mean field effects like vortex excitations. Under certain circumstances such beyond mean field excitations can be excited prior to phonons and thus lower the Landau velocity. Section 5.3.1 gives an overview on those excitations.

Temperature effects

The speed of sound gained from Bogoliubov theory (Eq. 5.8) coincides with the zero temperature result of the thermodynamic approach (Eq. 4.21). We saw in the previous chapter that finite temperature leads to an increase of the speed of sound whereas the superfluid fraction of the gas decreases. As the temperature reaches the critical temperature T_c, the critical velocity must vanish. Therefore we expect that finite temperatures reduce the critical velocity. Consequentially speed of sound and critical velocity do not

coincide for $T \neq 0$. A simple approximation which we can make is to use only the superfluid density n_S in Eq. 5.8 to calculate the critical velocity which then is

$$v_c = \sqrt{\frac{n_S U_0}{m_D}} \tag{5.9}$$

with

$$\frac{n_S}{n_D} = 1 - \left(\frac{T}{T_c}\right)^{\alpha} \tag{5.10}$$

where the exponent is $\alpha = 3/2$ in a homogeneous system and $\alpha = 3$ in a harmonically trapped system. If we assume a (local) condensate fraction of $\frac{n_S}{n_D} \approx 0.9$ in the cloud centre in our experiments the finite temperature would cause a reduction of the critical velocity of approximately 5 % which is less than our statistical measurement error.

Second sound

We showed in section 4.3.3 that at finite temperatures and finite interaction strength second sound is not just a temperature wave but also a density modulation propagating in the atom cloud[1]. Therefore we expect that the moving obstacle in our experiment can excite second sound at a velocity u_2 prior to first sound and the critical velocity should be given by $u_2 \approx \frac{1}{\sqrt{3}} u_1$ in the BEC regime. However, we assume that the density variation which is associated with a second sound wave is small and leads to small heating rates which cannot be resolved by our experiment. In Ref. [91] the coupling of the second sound mode to density variations is calculated for a unitary elongated Fermi gas, showing that it is small at low temperatures. We are not aware of any detailed studies concerning the superfluid critical velocity given by the speed of second sound.

5.1.3 BCS superfluidity

For $-1/k_N a_A > 1$ the superfluid is formed by loosely bound Cooper pairs according to BCS theory. A mean-field description [6] is generally considered to give fairly accurate results for weak interactions at $T = 0$. Then the lowest energy excitations is the breaking of Cooper pairs. Applying the Landau criterion results in a critical pair breaking velocity [92]

$$v_{pb}^2 = \frac{\sqrt{\Delta^2 + \mu^2} - \mu}{m}, \tag{5.11}$$

which simplifies to

$$v_{pb} \approx \frac{\Delta}{\hbar k_N} \tag{5.12}$$

in the deep BCS limit. Following the mean field approach, we calculate the gap Δ and the chemical potential μ at $T = 0$ by solving the gap and the number equation numerically

[1] The direct observation of second sound in Ref. [83] is an experimental proof of this coupling.

[93]. The resulting v_{pb} is plotted in black in Fig. 5.4. For more details on this approach I would like to refer the reader to Ref. [55]. The velocity which is obtained by this method can be considered as an upper bound of the pair breaking velocity as it only takes into account the density in the centre of the cloud. The stirring beam is also passing through lower density regions along its line-of-sight. Therefore, the observed critical velocity can be expected to be lower than the predicted value. We note that this approach does not correctly account for higher order corrections of μ and Δ in $k_N a$ [6].

Temperature effects

We do not take temperature effects into consideration when calculating the gap and the critical velocity. However, for measurements further in the BCS regime the temperature can easily approach the critical temperature and therefore reduce the energy gap. If we assume a temperature in our samples of $T/T_F = 0.07$ we conclude from Eq. 4.60 that there is no superfluid fraction for $-1/k_n a_A > 1.38$. However, for $T/T_c < 0.5$ the temperature dependence of the superfluid energy gap is negligible [94] and the critical velocity is close to the zero temperature situation. At a temperature of $T/T_F = 0.07$ this limits our theoretical approach to $-1/k_n a_A < 0.94$.

5.1.4 Superfluidity in the strongly correlated regime

For $|-1/k_n a_A| < 1$ mean field theories, like the Bogoliubov or the BCS theory, fail to describe the critical velocity accurately due to the lack of known quasi-particle excitations. However, mean-field BCS theory provides a closed form expression for the pair-breaking velocity and the speed of sound is known as described in chapter 4. Therefore, the speed of sound and the pair breaking mechanism mark upper limits to the critical velocity in the strongly interacting regime. Still, it is not clear which type of excitation governs the critical velocity in the $|-1/k_F a| < 1$ region.

5.2 Measurement procedure

To perform the actual stirring experiment, a red-detuned laser beam is focused on the gas which is prepared as described in chapter 3. The resulting attractive potential serves as an obstacle whose motion and speed v is controlled by reflecting the beam from a two-axis piezo controlled mirror[2]. It traces out a circular trajectory with a radius of 10 µm along lines of constant column density within the superfluid region of the gas. The beam has a wavelength of 780 nm and is focused to a $1/e^2$ waist of 2.4 µm × 1.9 µm. This size has to be compared to the relevant length scales for excitations of the atomic gas. In the BEC regime this is the healing length which is $\xi = 0.94\,\mu\text{m}$ for our measurement at $-1/k_F a \approx -3.5$. At unitary the interparticle distance $n^{-1/3} \approx 1.5\,\mu\text{m}$ is relevant. The power of the stirring beam is chosen such that the local column density is increased by approximately 85 %. Since the chemical potential μ for a constant column density depends on the value of $-1/k_F a_A$ where a_A is the s-wave scattering length, the actual beam power varies between 0.4 µW and 1.4 µW.

The stirring sequence proceeds as follows: First, a_A is set to the desired value by ramping the magnetic field to a value between 750 Gauss and 890 Gauss. After 50 ms thermalisation time the power of the already moving obstacle beam is linearly ramped up within 10 ms to avoid non-adiabatic effects. Next, the gas is stirred for 200 ms before the power of the obstacle beam is linearly ramped down in 5 ms with the beam still being kept in motion. After a thermalisation time of 100 ms the magnetic field is ramped to 680 Gauss in 100 ms and an in-situ absorption image of the atoms is taken. The previously mentioned condensate fractions were also measured at this field. For $v = 0\,\text{mm}\,\text{s}^{-1}$ we observe no heating of the cloud caused by the obstacle potential itself. For each stirring speed v we repeat this sequence typically ten times with identical settings and extract the radially averaged, line-of-sight integrated density distribution $\tilde{n}(r)$ from the mean of those datasets. Since the gas is well in the BEC regime during the image acquisition, we apply a bimodal fit and extract the central column densities $\tilde{n}(0)$.

Above (below) a certain critical velocity v_C we observe a (no) significant reduction in the central column density $\tilde{n}(0)$. As a function of stirring speed the behaviour of this quantity exhibits a distinct kink, as shown in Fig. 5.3. We identify this kink as the onset of heating at v_C where superfluidity breaks down. The exact value of v_C is extracted from a fit with a continuous bilinear function which has a constant value of $\tilde{n}_0$ below the critical velocity v_C and decreases linearly with slope A above:

$$\tilde{n} = \tilde{n}_0 \min\left(1, A\left(v - v_c\right)\right). \tag{5.13}$$

[2] Physik Instrumente (PI), S-334.2SD1 with controller E-616.SS0G. We use the controller well above the specified operation limits. The capacitance of the piezo mirror limits the bandwith to approximately 30 Hz for the required large tilt angles. The resulting low pass behaviour could be compensated by using larger set control voltages depending on the stirring frequency. Finally we were able to reach frequencies of up to 200 Hz for a 10 µm stirring radius of the reflected laser beam in the atom cloud. At larger stirring radii the achievable maximal frequency reduces.

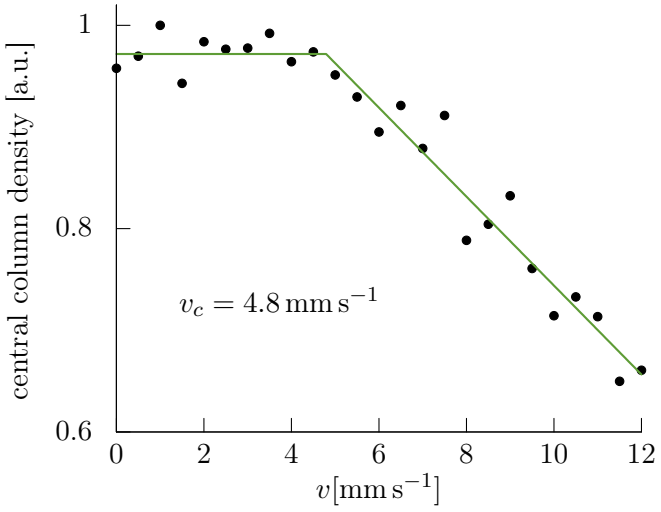

Figure 5.3: Data analysis for a measurement of the superfluid critical velocity. Below the critical velocity of $4.8\,\mathrm{mm\,s^{-1}}$ the central density is not affected by the stirring procedure. Avove the critical velocity we observe a reduction of the central density due to heating. The data shown was recorded for a magnetic field strength of 849 Gauss during the stirring time.

The free fit parameters are $\tilde{n}_0$, v_C and A. We were also able to confirm that stirring in a thermal (non-superfluid) cloud results in a vanishing critical velocity. We determine the critical velocities for different interaction strengths $-1/k_N a_A$ throughout the BEC-BCS crossover and plot them in units of the Fermi velocity v_N in Fig. 5.4. This is the main result of this chapter. The data shows a maximum of v_C close to $1/k_N a_A = 0$ and a decrease towards the BEC and the BCS side of the resonance. In physical units the values for the obtained critical velocities are between $1.7\,\mathrm{mm\,s^{-1}}$ and $6.3\,\mathrm{mm\,s^{-1}}$. The qualitative behaviour of the data points is as expected as the critical velocity on the BEC side should be given by the speed of sound which increases with the interaction strength. On the BCS side pair breaking is the responsible mechanism for the critical velocity. The pair binding energy is given by the gap Δ which is exponentially small with decreasing interaction. It is apparent that the measured critical velocity v_c is far less than the expectation. In the strongly correlated regime an explanation might be given by yet unknown types of excitations. But also in the BEC regime the speed of first sound u_1 is significantly larger than the measured values of v_c. There were several previous measurements of the critical velocity in other research groups which observed a similar behaviour.

5.2.1 Previous measurements

For weakly interacting BECs, the critical velocity should be given by the speed of first sound u_1. This has not been observed: Experiments found upper values for v_c/u_1 of

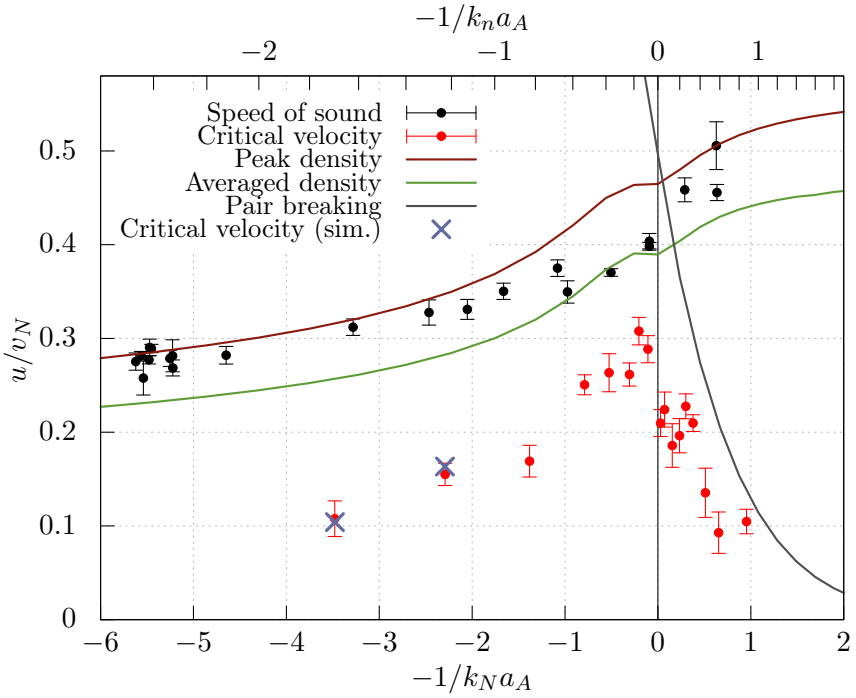

Figure 5.4: Measurement results of the superfluid critical velocity (red dots) and the speed of sound (black dots) as a function of the interaction strength $-1/k_N a_A$. The velocities are given in units of the Fermi velocity v_N. The upper x axis shows the corresponding value of $-1/k_n a_A$, see also Fig. 4.8. The red and green curves are the theoretical predictions for the speed of sound as derived in chapter 4. The grey curve is the critical velocity caused by the breaking of cooper pairs under the assumption that only the density in the centre of the cloud is relevant. The discrepancy between the critical velocity and the speed of sound in the BEC region ($-1/k_N a_A < -1$) is apparent. The error bars of the critical velocity are the fit errors of the bilinear fit function 5.13. The crosses mark the critical velocities obtained by the simulations presented in section 5.4.

approximately 10 % for three- and 60 % for two-dimensional dilute atomic BECs [95, 96, 97], respectively. For those experiments the spatial size of the perturbation was much larger than the healing length ξ. In this case vortex rings (3D) or pairs (2D) are expected to be excited rather than sound waves [98, 99].

In the strongly correlated regime the description in terms of weakly interacting quasiparticles breaks down and to our knowledge no theoretical prediction for v_C exists. Here, experiments with ultracold Fermi gases are ideally suited to study superfluidity in the BEC-BCS crossover, since the interaction strength can be tuned with Feshbach resonances. In an experiment by the Ketterle group [61], the critical velocity was probed in the strongly correlated regime with a moving optical lattice. At unitarity, they found $v_C/v_F = 0.25$ which is 30 % below the theory prediction for the speed of sound. Un-

fortunately, in the corresponding publication no data is given to compare their results with ours apart from the unitary point. Furthermore, their experiment did not allow for a precise determination of the Fermi wavenumber k_F, which would be necessary for a substantive comparison to theory [100].

After we completed our measurements we became aware of recent work which was performed in the group of Christoph Salomon where two superfluid clouds, one of ^{6}Li and one of ^{7}Li, are oscillating through each other [101]. The relative motion of the two clouds and the damping of the oscillation probe the critical velocity. They obtain a value of $v_c = 0.42 v_F$ which is close to the speed of sound at unitary $v_s \approx 0.45 v_F$, where v_F denotes the Fermi velocity in the ^{6}Li cloud. However, a theoretical shows that in their particular measurement scenario heating is predicted to occur for a relative velocity that equals the sum of the individual sound velocities of the two clouds [102]. The underlying reason is, that in contrast to the assumption made for the Landau criterion, the mass of the disturbing potential is comparable with the constituents of the gas and not infinite.

5.3 Discussion

To explain the discrepancy between the measured critical velocity v_c and the speed of first sound u_1 in the BEC regime multiple effects play a role which are discussed in this section. We found, that the finite temperature, the inhomogeneous density profile along the strongly confined direction, the circular instead of linear motion of the stirrer, and to a lesser degree the finite depth of the obstacle potential are relevant. To support the arguments given, I will later present simulation results obtained by Vijay Singh Ludwig Matthey in section 5.4.

5.3.1 Finite obstacle effects

The Landau criterion applied to the Bogoliubov theory or the BCS theory does not consider effects which are caused by a finite obstacle size. In our experiments the spotsize of the stirring beam is comparable to the healing length of the cold gas and thus finite size effects are in general possible.

- **Creation of a local density minimum:** The movement of the obstacle in the superfluid medium creates variations in the local density around the perturbation. This is intuitive for the case of a blue-detuned (repulsive) stirring beam which creates a density minimum thus reducing the local critical velocity. But even a red detuned (attractive) stirring beam is expected to create a density minimum in front of the obstacle which leads to a local reduction of the critical velocity as pointed out in Ref. [103]. The effect scales with the depth of the obstacle potential and should vanish in the limit of an infinitely shallow obstacle. We performed measurements of the critical velocity at different beam powers of the stirring beam and confirmed that this effect should have only minor influence on our results.

- **Local increase in flow speed:** When a disturbing potential is moving through the superfluid flow dynamics are created. For a repulsive obstacle, there will be flow around the obstacle thus creating a local density minimum. In the coordinate system of the obstacle that results in a local increase of flow velocity at the sides of the obstacle and thus the critical velocity is exceeded at a lower obstacle speed than what one would naively expect. An attractive obstacle shows a similar effect with the difference that the trajectories of the superfluid are attracted towards the obstacle creating a local density maximum.

- **Creation of vortices:** In the BEC regime we considered the Bogoliubov theory which concludes that the critical velocity is given by the speed of first sound. So far we did not consider beyond mean field effects. One prominent example is the excitation of vortices which can be created as vortex pairs, closed vortex rings or in other configurations. As pointed out in Ref. [99] and [103] it strongly depends on the size w of the disturbing potential if the speed of sound u_1 is larger or smaller

than the critical velocity for vortex excitation v_V. According to Ref. [99] u_1 should be lower than v_V for $w/\xi \lesssim 7$ ($\lesssim 1$ for [103]). In our experiment the ratio w/ξ is approximately 2.5 for the measurements at $-1/k_N a_A \approx -3.5$ and vortex excitations should not be solely responsible for the observed deviation between u_1 and v_c.

5.3.2 Trap effects

As pointed out in chapter 4 there are two different possibilities to define the Fermi wave number in a trap: either via the density $k_n^3 = \frac{n}{6\pi^2}$ or via the total particle number $\frac{\hbar^2 k_N^2}{2m} = \hbar\bar{\omega}\,(6N)^{1/3}$. Especially in the BEC regime the two definitions are not identical $k_N \neq k_n$, see section 4.3.4 for details.

For calculating the speed of sound in a strongly interacting, hydrodynamic gas we consider the average density along the z direction instead of the peak density of the cloud. The reason is that the waves in our measurements for the speed of sound have a large wavelength compared to the spatial extent $2R_z$ of the atom cloud in the strongly confined direction. Therefore, the waves effectively probe an average density. Concerning the measurement of the critical velocity this argument does no longer hold as the wavelength of the created Bogoliubov phonons can be as small as the healing length $\xi < 2R_z$ of the system. Such high momentum phonons are able to resolve the local density in the cloud which varies along the z direction. We can therefore argue that the critical velocity measured in the experiment should always vanish as in each measurement low density and non-superfluid regions in the outer region of the atom clouds are probed as well. Nevertheless, we observe clear signatures of a non-zero critical velocity which might be due to small heating rates associated with excitations in the low density regions.

Furthermore, we measure the critical velocity not in the cloud centre but at a stirring radius of 10 µm. The Thomas Fermi radii in the radial direction R_x, R_y were larger than 34 µm for all measurements. The resulting reduction of the expected critical velocity is then $< 5\,\%$ which is less than our measurement error.

5.3.3 Finite temperature

As discussed in sections 5.1.2 and 5.1.3 we expect temperature effects on v_c to be small for our experimental parameters. The simulations presented in section 5.4 suggest that temperature effects only have a minor effect on the reduction of the critical velocity in the experiments.

5.4 Simulation results

To gain a deeper understanding of our measurement results, the theory group of Ludwig Matthey and in particular his doctoral student Vijay Singh simulated our experiment with a classical field method which is the limiting case of the truncated Wigner method used in Ref. [104]. The time evolution of an ensemble of complex-valued fields is calculated using classical equations of motion. The initial states are generated from a grand canonical ensemble via a classical Metropolis algorithm. The simulations were performed in the BEC regime at a scattering length of $a_A = 3634\,a_{\mathrm{Bohr}} \approx 190\,\mathrm{nm}$ which corresponds to a magnetic field strength of $B \approx 755\,\mathrm{Gauss}$. To disentangle the multiple effects which potentially lead to a reduction of the observed critical velocity, I will first present the simulation of the simplest situation which is closest to the ideal case and can be properly described by Bogoliubov theory. Thereafter the parameters are successively changed such that the simulations finally are a close approximation of our experiment.

Most simple approximation: homogeneous and cold sample with a shallow stirrer and a linear stirring pattern

The most academic situation that was simulated is a homogeneous cold gas at a temperature of $T = 1\,\mathrm{nK}$ and a density of $n = 0.486\,\mu\mathrm{m}^{-3}$. The system is simulated on a grid with $60 \times 60 \times 3$ sites and periodic boundary conditions. The discretization length is $1\,\mu\mathrm{m}$. An attractive potential which is Gaussian shaped in the radial direction and cylindrical in the z direction with a depth of $U = k_B \cdot 1\,\mathrm{nK}$ simulates the stirring beam. The spatial extent of the simulated stirring potential is chosen similar to the size of the stirring beam in the experiment. The potential is linearly ramped on and off following the same protocol as the experiment and traces out a linear stirring pattern. During the simulated stirring, the heating rate of the gas is recorded as a function of the stirring speed, see Fig. 5.5. To determine v_c the fit function $A \cdot \left(v^2 - v_c^2\right)^2 / v + B$ is used for $v > v_c$ [105], with the free parameters A, B and v_c. In this case $v_c \approx 4.2\,\mathrm{mm\,s^{-1}}$ is obtained which is in good agreement with the Bogoliubov sound velocity of the sample $u_1 = 4.4\,\mathrm{mm\,s^{-1}}$.

Introduce a stronger stirrer

Next, the stirrer strength is increased to $U = k_B \cdot 30\,\mathrm{nK}$. In this situation the simulation results in a reduced critical velocity of $v_c = 3.2\,\mathrm{mm\,s^{-1}}$. A locally increased flow speed around the stirrer or the onset of vortex nucleation might be responsible for this reduction. As a comparison also a repulsive stirrer with $U = -k_B \cdot 30\,\mathrm{nK}$ was simulated with otherwise unchanged parameters. Here $v_c = 2.2\,\mathrm{mm\,s^{-1}}$ is obtained which indicates that a repulsive stirring potential reduces the critical velocity more than an attractive one.

Introduce higher sample temperature and change to a circular stirring pattern

To get to a closer approximation of our experimental measurements the simulated sample temperature is increased to $T = 10\,\mathrm{nK}$ and the stirring trajectory is changed such that it matches the one used in the experiment. The simulations show that both features reduce v_c by approximately 15 %. Having both present simultaneously causes a small further reduction of the critical velocity to $v_c = 2.7\,\mathrm{mm\,s^{-1}}$. The reduction at finite temperature might be due to vortex-antivortex excitations, or rotonic precursors of them. As the temperature is increased above the mean field energy, density fluctuations increase and vortices can nucleate at points of minimal density. That the circular motion can reduce v_c can be seen in perturbation theory performed in momentum space: here, the motion of the perturbation consists of a distribution of velocities rather than a single velocity.

Introduce inhomogeneities

To simulate our experiment as realistic as possible the spatial inhomogeneities are added to the simulations to account for trapping effects. The simulated cloud is trapped in a harmonic potential with trapping frequencies of $\omega_x = \omega_y = 2\pi \cdot 31\,\mathrm{Hz}$ and $\omega_z = 2\pi \cdot 446\,\mathrm{Hz}$. The resulting simulated Thomas Fermi radii are $R_x = R_y = 29\,\mu\mathrm{m}$ which is close to the experimentally observed value of 34 µm. The simulation grid was extended to $140 \times 140 \times 11$ sites. The simulated local density excess inside the stirrer is comparable to the excess observed in the experiment. The simulated critical velocity of $1.6\,\mathrm{mm\,s^{-1}}$ agrees excellently with the experimentally measured value of $1.7\,\mathrm{mm\,s^{-1}}$. We believe that the additional reduction of 39 % with respect to the homogeneous simulation result is mainly due to probing lower density regions along the stirrer axis For the trapped cloud the reduction in the central column density was simulated as well. The results are shown in the inset of Fig. 5.5 and are in good agreement with the experimental data.

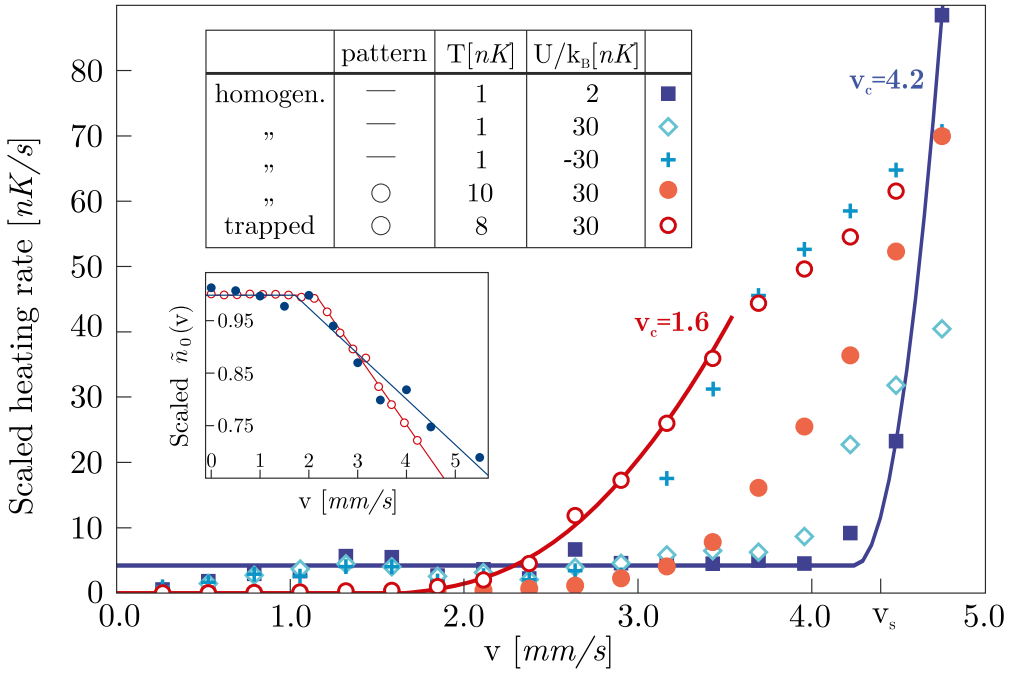

Figure 5.5: Simulated heating rates normalised by the stirrer depth U^2. The complexity is gradually increased: blue squares depict the idealized case of a very cold homogeneous sample stirred with linear pattern. The relative density excess in the weak stirrer potential $U = k_B \cdot 1\,\mathrm{nK}$ is only 3 %. In this case the extracted critical velocity $v_c = 4.2\,\mathrm{mm\,s^{-1}}$ is close to the Bogoliubov speed of sound which is $u_1 = 4.4\,\mathrm{mm\,s^{-1}}$ for all datasets. The red open circles depict a simulation of the experimental case: A trapped sample is stirred circularly with a stirrer of realistic depth. A reduced temperature is chosen for technical reasons. For this curve, the y-axis scaling factor is unity. In the inset, the results for the heating observed in the central column density are compared. The red open (blue filled) circles show the simulated (experimental) result. The bilinear fits to extract v_c are shown with solid lines. In the inset $U = k_B \cdot 35\,\mathrm{nK}$.

5.5 Conclusion

In conclusion, we have demonstrated the breakdown of superfluidity due to a moving obstacle across the BEC-BCS transition, for the first time in close analogy to Landau's Gedankenexperiment. We compare the results with theoretical predictions throughout and achieve quantitative understanding in the BEC regime by performing numerical simulations. Pointlike defects also play a role in strongly correlated high temperature superconductors. The experiment presented here provides the opportunity to isolate relevant effects in a very clean and controllable environment. Of particular interest for future studies are strongly correlated two-dimensional superfluids where the theoretical situation is far more unclear compared to three-dimensional systems even in the weakly interacting limits

6 Two-dimensional ultracold gases

The research on two-dimensional systems currently enjoys a high priority mainly due to its connection to high-temperature superconductivity. Modern experiments working with ultracold fermions provide the possibility to access and to simulate the physics in such systems in a very clean and controlled environment. However, in the past it was impossible to create single-layer two-dimensional clouds which restricted the studies on 2D systems to samples containing multiple layers with different densities and atom numbers. As a consequence, only averaged effects could be investigated. With the latest generation of experimental apparatuses, it becomes possible for the first time to create single-layer two-dimensional clouds and to locally image and manipulate the samples via microscope objectives. Such experiments are highly welcome from a theoretical point of view as well, since two-dimensional samples offer a rich variety of physics which cannot be accessed in other dimensionalities. Examples are the Berezinsky-Kosterlitz-Thouless (BKT) transition or polarized phases with deformed Fermi surfaces like the Fulde-Ferrell-Larkin-Ovchinnikov (FFLO) phase. Furthermore, single-layer two-dimensional samples form the basis for experiments which aim towards single-site and single-atom detection in combination with optical lattices. It can be anticipated that the experiment presented in this thesis will provide new insights, contributing to the development of theories describing 2D systems which are currently far less mature than comparable theories describing 1D or 3D systems.

In this chapter, I first give a brief and incomplete overview of the features of two-dimensional gases and point out several fundamental differences compared to three-dimensional systems. Next, I introduce the experimental approach to create 2D samples in our apparatus using an optical lattice and present a novel method to verify that only one layer of this lattice is occupied. In the last section, I show further advanced manipulation techniques which are integrated in the setup.

6.1 Theory of a two-dimensional cold gas

This section is intended to give a brief insight into 2D physics and to point out fundamental differences between 2D and 3D quantum gases. The section follows the lines of a review article by Bloch, Dalibard and Zwerger [5]. First, a pure two-dimensional system is discussed. Afterwards the more realistic case of 2D systems created in experiments is considered. In the latter the influence of the third dimension cannot be neglected completely.

6.1.1 Pure two-dimensional system

Non interacting Bose gas

To illustrate the impact of the dimensionality on the properties of an ultracold gas, consider the case of an ideal, homogeneous Bose gas in two (three) dimensions. The gas is described by its atom density n_{2D} (n_{3D}), the temperature T and the mass m of its constituents. Further, we can define the thermal de Broglie wavelength $\lambda_T = \frac{h}{\sqrt{2\pi m k_B T}}$. One can then find expressions for the degeneracy parameter $n_{2D}\lambda_T^2$ ($n_{3D}\lambda_T^3$) by using the Bose distribution and the density of states[1] for the atoms:

$$\begin{aligned} n_{2D}\lambda_T^2 &= -\ln\left(1 - e^{\frac{\mu}{k_B T}}\right) \\ n_{3D}\lambda_T^3 &= g_{3/2}\left(e^{\frac{\mu}{k_B T}}\right) \end{aligned} \tag{6.1}$$

where $g_{3/2}(z) = \sum_{n=1}^{\infty} \frac{z^n}{n^{3/2}}$. The chemical potential μ is given by the density and temperature such that Eq. 6.1 is fulfilled. In the three-dimensional case this is only possible for $n_{3D}\lambda_T^3 \leq g_{3/2}(0) = \zeta(3/2) \approx 2.612$. For higher values of $n_{3D}\lambda_T^3$, there is no solution for μ which indicates the formation of a BEC[2]. In contrast, the two-dimensional case in Eq. 6.1 admits a solution for arbitrary high values of $n_{2D}\lambda_T^2$ and therefore condensation does not occur at non-zero temperatures.

The result that there is no condensate in two dimensions changes if the gas is trapped in a harmonic potential $V(r) = \frac{1}{2}m\omega^2 r^2$, where ω is the trapping frequency. When applying the local density approximation, the expression for the degeneracy parameter becomes

$$n_{2D}(r)\lambda_T^2 = -\ln\left(1 - e^{\frac{\mu - V(r)}{k_B T}}\right). \tag{6.2}$$

Taking the limit $\mu \to 0$ and integrating over the two spatial dimensions yields an expression for the critical temperature T_c, below which a condensate emerges:

$$k_B T_c = \hbar\omega \frac{\sqrt{6N}}{\pi}. \tag{6.3}$$

[1] The density of states for a homogeneous gas in d dimensions is $g(\epsilon) \propto \epsilon^{(d/2)-1}$.

[2] Here condensation is defined as a macroscopic occupation of the ground state, rather than long-range phase coherence.

Although the presence of a trapping potential allows the formation of a condensate in two dimensions, the situation is still substantially different from a three-dimensional BEC. For non-zero temperatures, the density in the centre of the trapped cloud diverges in two dimensions $n_{2D}(0) \to \infty$, whereas it tends to a finite value in three dimensions $n_{3D}(0) = \frac{\zeta(3/2)}{\lambda_T^3}$.

Interacting gas

In three dimensions it is possible to apply a mean field theory to the problem of an interacting Bose gas as long as the interactions are not too strong. A mean field parameter U_0 is defined which yields a very simple expression for the chemical potential $\mu = n_{3D}U_0$. As this expression can be considered as an equation of state, all thermodynamic properties of the gas can be written as a function of U_0. In two dimensions such a convenient mean field treatment is impossible as the energy dependence of the scattering processes cannot be neglected. To show this, consider the scattering of a plane wave $e^{i\vec{k}\vec{x}}$ in the low energy limit. The wave function after the scattering event can be written as[3]

$$\Psi(\vec{x}) = e^{i\vec{k}\vec{x}} - \sqrt{\frac{\mathrm{i}}{8\pi}} f(k) \frac{e^{ikr}}{\sqrt{kr}} \tag{6.4}$$

where $f(k)$ is the dimensionless scattering amplitude. Since we restrict ourselves to low energy s-wave scattering, $f(k)$ is isotropic and can be written as

$$f(k) = \frac{4\pi}{2\ln\left(\frac{1}{ka_{2D}}\right) + \mathrm{i}\pi}. \tag{6.5}$$

Equation 6.5 defines the 2D scattering length a_{2D}. The dimensionless scattering amplitude vanishes in the low energy limit, i.e.

$$\lim_{k\to 0} f(k) = 0. \tag{6.6}$$

Further, the total scattering cross-section, which is defined as the integral of the differential cross-section $\left|f(k)/\sqrt{8\pi k}\right|^2$ over all solid angles, diverges in two dimensions, $\sigma_{2D} \to \infty$. In three dimensions it is finite and given by $\sigma_{3D} = 4\pi a_{3D}^2$. In the three-dimensional mean field theory the parameter $U_0 = \frac{4\pi\hbar^2 a_{3D}}{m}$ is intrinsically connected to the scattering amplitude at low energies. As the scattering amplitude vanishes in the two-dimensional situation (Eq. 6.6) a similar treatment is not possible.

Equation 6.1 shows that an ideal, homogeneous 2D Bose gas cannot condense at any non-zero temperature. This statement continues to hold under the presence of interaction. It was generally shown by Mermin, Wagner and Hohenberg [8, 9] that a continuous

[3] The normalization prefactors are omitted for clarity.

symmetry cannot be broken in two dimensions at any non-zero temperature. In particular, it forbids the presence of long range phase coherence and therefore Bose Einstein condensation. However, the formation of a so-called quasi-condensate is possible, which is described by a wave function $\Psi(\vec{x}) = \sqrt{n_{2D}(\vec{x})}e^{\mathrm{i}\phi(\vec{x})}$ with a fluctuating phase $\phi(\vec{x})$ but suppressed density fluctuations. The phase fluctuation themselves can appear either in the form of long-wavelength phonons or as quantized vortices around which the phase turns by 2π or multiples thereof. The formation of the quasi-condensate out of a thermal gas with decreasing temperature is described by the BKT transition [106, 107] which I will briefly sketch in the following. At very low temperatures, the phase fluctuations are dominated by phonons whereas density fluctuations are suppressed. Vortices exist only in the form of pairs and the first order correlation function shows an algebraic decay $ng^{(1)}(r) = \langle\Psi(r)\Psi(0)\rangle \propto r^{-\eta}$ in contrast to a BEC where the correlation function does not decay to zero. The exponent is $\eta = 1/(n_S\lambda_T^2)$, which relates the superfluid density n_S directly to the phase ordering (coherence) in the system[4]. The superfluid density decreases with increasing temperature until a critical temperature T_{BKT} is reached at which n_S suddenly jumps from a finite value $n_s\lambda_T^2 = 4$ to zero and the decay of $g^{(1)}$ becomes exponential. Microscopically, the transition is accompanied by the proliferation of the previously bound vortex pairs. The free vortices then distort the phase such that the superfluidity (which can be regarded as phase-stiffness) in the system disappears. For even higher temperatures, density fluctuations enter the system and the notion of vortices becomes inapplicable. The correlation function $g^{(1)}$ becomes Gaussian and the behaviour of the gas approaches that of an ideal gas [5].

There is an intuitive way to calculate the BKT transition temperature T_{BKT} by considering the contribution of a single vortex to the free energy of the system which shall have a spatial extent R. Around the singly charged vortex the (superfluid) flow field is given by $v(r) = \frac{\hbar}{mr}$. Hence, the corresponding kinetic energy is

$$E = \pi m n_S \int_\xi^R v^2(r) r \,\mathrm{d}r = \frac{\pi n_S \hbar^2}{m} \ln\left(\frac{R}{\xi}\right). \tag{6.7}$$

The lower bound of the integral is the healing length ξ which takes into account that the density in the vortex core drops to zero on approximately that length scale. The entropy S of the vortex is given by all possible positions of the vortex inside the systems of size R^2. The approximate size of the vortex itself is ξ^2 and therefore

$$S = k_B \ln\left(\frac{R^2}{\xi^2}\right). \tag{6.8}$$

Hence, the free energy is

$$F = E - TS = \frac{1}{2}k_B T\left(n_S\lambda_T^2 - 4\right)\ln\left(\frac{R}{\xi}\right). \tag{6.9}$$

[4]The densities here and in the following part of this chapter are 2D areal densities.

In the case of a large system $R \gg \xi$ and cold temperatures, the free energy is large and positive. Therefore, free vortices do not appear in the system[5]. With increasing temperature, the thermal de Broglie wavelength shrinks and above the critical temperature T_{BKT} the system favours the existence of free vortices to lower the free energy. The critical temperature is given by

$$\begin{aligned} n_S \lambda_T^2 &= 4 \\ \Leftrightarrow T_{BKT} &= \frac{\pi \hbar^2 n_S}{2 m k_B}. \end{aligned} \tag{6.10}$$

Although Eq. 6.10 is clean and simple, it is only of limited value to calculate T_{BKT} in an experiment, since the relation of the superfluid density to the total density n_S/n remains unknown.

6.1.2 Realistic two-dimensional system

The previous section considered a pure two-dimensional system and did not account for any contributions of a third dimension. However, in the experiments which can be performed on two-dimensional quantum gases, the third dimension cannot be neglected completely. In cold gas experiments the kinematics in the third direction are frozen out in the sense that a confining potential is applied in this direction which is strong enough that the first excited state of this potential cannot be reached by any other intrinsic energy scale of the system. For a harmonic potential with a trap frequency ω_z, this implies in particular $k_B T, \mu \ll \hbar \omega_z$. Under such conditions the two-dimensional scattering amplitude was calculated in Ref. [108, 109]. The scattering length is

$$a_{2D} = l_z \sqrt{\frac{\pi}{B}} e^{-\sqrt{\frac{\pi}{2}} \frac{l_z}{a_{3D}}} \tag{6.11}$$

with $B = 0.905$ and the harmonic oscillator length $l_z = \sqrt{\frac{\hbar}{m\omega_z}}$. A positive s-wave scattering length is connected to the presence of a bound state. Therefore, Eq. 6.11 implies that a two-component Fermi gas confined in two dimensions supports a molecular bound state for all 3D scattering lengths a_{3D}. The binding energy is given by $E_B = -\frac{4\hbar^2}{m a_{2D}^2}$. This is a further property of two-dimensional gases, which is substantially different from the three-dimensional situation where a bound state exists only on the BEC side of the Feshbach resonance. The scattering amplitude can be obtained with Eq. 6.5 and 6.11 and is given by

$$f(k) = \frac{4\pi}{\sqrt{2\pi} \frac{l_z}{a_{3D}} + \ln\left(\frac{B}{\pi k^2 l_z^2}\right) + \mathrm{i}\pi}. \tag{6.12}$$

[5] Note that bound vortex pairs with opposite charge are still possible, as the energy of such a pair is given by an expression similar to Eq. 6.7 with the upper bound of the integral given by the vortex separation $d \ll R$.

For $a_{3D} \ll l_z$, the logarithmic part in Eq. 6.12 can be neglected [108]

$$f(k) \approx \sqrt{8\pi}\frac{a_{3D}}{l_z} =: \tilde{g}_2 \ll 1 \tag{6.13}$$

defining a small dimensionless coupling parameter $\tilde{g}_2$. As a consequence, the scattering becomes energy independent and a mean field treatment is possible. The corresponding mean field parameter is $g_2 = \frac{\hbar^2\tilde{g}_2}{m}$ and the chemical potential becomes $\mu = g_2 n$ similar to the 3D situation. The fact that the scattering events are described by the scattering length a_{3D} distinguishes the regime $a_{3D} \ll l_z$ from a pure two-dimensional system and it is therefore referred to as quasi-2D regime. For such a quasi-2D gas there is a Monte Carlo calculation [110] for the *total* density at the critical point of the BKT transition: $n\lambda_T^2 = \ln\left(\frac{C}{\tilde{g}_2}\right)$ with $C = 380 \pm 3$. The same publication points out that the superfluid density in such a quasi-2D gas is smaller than the quasi-condensate density which is another remarkable difference compared to a 3D gas where the two densities are identical.

For the experimental apparatus presented in this thesis, the scattering length a_{3D} can be enhanced by making use of a Feshbach resonance and it is possible to access the regime where a_{3D} is comparable to or exceeds l_z. Then the full expression 6.12, including the energy dependence, becomes relevant and the situation is a close approximation of a pure 2D gas.

Quantification of the interaction strength

Similar to the three-dimensional gas, where the interaction strength is usually quantified as $x = \frac{1}{k_F a_{3D}}$, a dimensionless parameter needs to be defined for the same purpose in the two-dimensional case. The Fermi wavenumber in two dimensions is $k_F = \sqrt{4\pi n_{2D}}$, which is easily accessible in the experiment for all interaction strengths as there is no line-of-sight integration like in a 3D gas. The scattering length a_{2D} defined by Eq. 6.11 is always positive and the interaction strength can therefore be quantified via $\eta = \ln(k_F a_{2D})$. For ^{6}Li η is positive at high magnetic fields (BCS side) and negative at low magnetic fields (BEC side). However, $\eta = 0$ does not coincide with the 3D Feshbach resonance and the position of the zero crossing depends on the confinement length l_z in the vertical direction. Sometimes $n_{2D}a_{2D}^2$ is used as an equivalent to η. The presence of a molecular bound state for all interaction strengths offers another possibility to quantify the interaction strength via the molecular binding energy. The binding energy is $E_B = -\frac{4\hbar^2}{m a_{2D}^2}$ and depends solely on the scattering length a_{2D}. The interaction is then typically given as the ratio $-E_B/E_F$, where $E_F = \frac{\hbar^2 k_F^2}{2m}$. For ^{6}Li $-E_B/E_F$ is small at high magnetic fields and large at low magnetic fields. The point $-E_B/E_F = 1$ coincides neither with $\eta = 0$ nor with $x = 0$ in general.

6.1.3 Speed of sound in two dimensions

The microscopic properties of a 2D or quasi-2D quantum gas affect the macroscopic behaviour of the system. As it is questionable whether a mean field theory is appropriate

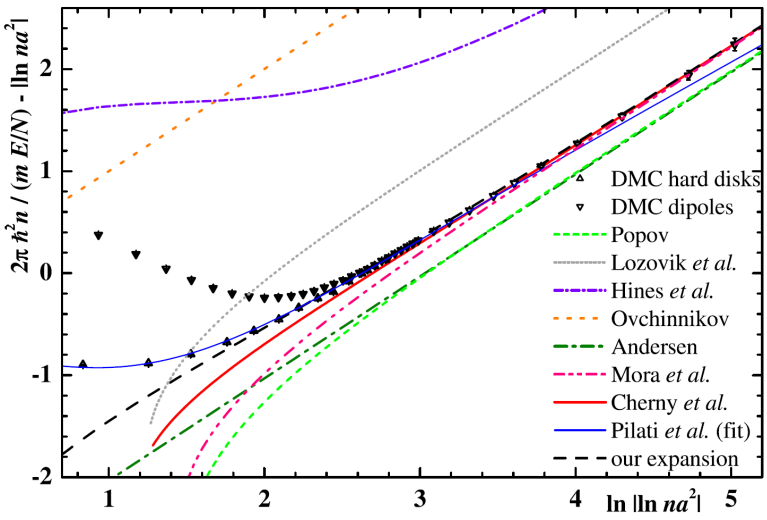

Figure 6.1: Different predictions for the equation of state of a two-dimensional Fermi gas as published in Ref. [113]. Plotted is the beyond mean field correction to the energy per particle of the gas as a function of the interaction strength.

to capture the scattering physics in a 2D system correctly, the description of macroscopic effects is non-trivial as well. As an illustrative example, I would like to consider the speed of sound. In chapter 4 we were able to calculate the speed of sound for a weakly interacting molecular three-dimensional BEC at $T = 0$ by considering the mean field energy of the gas and then applying basic thermodynamic relations. If the same procedure is applied to a quasi-2D situation, the speed of sound in units of the Fermi velocity is

$$\frac{u_1}{v_F} = \frac{1}{\sqrt{2}}, \tag{6.14}$$

which is independent of the interaction strength. According to Ref. [111] the result given in Eq. 6.14 holds even when additionally considering phase and amplitude fluctuations.

In contrast to the mean field result, the Monte Carlo calculation presented in Ref. [112] concludes that the equation of state, and therefore the speed of sound, depends significantly on the interaction strength. Reference [113] compares multiple suggested expressions for the equation of state and concludes that even first-order corrected mean field theories do not provide an accurate description for a weakly interacting 2D gas, not even for ultra weak interactions on the order of $na_{2D}^2 \approx 10^{-100} \Leftrightarrow \ln(k_F a_{2D}) \approx -114$.

Figure 6.1 shows several predictions for the equation of state at $T = 0$ as published in Ref. [113] and illustrates how valuable an experimental measurement of the equation of state would be to improve the understanding of such systems.

6.2 Setup III: From the squeeze trap to the lattice

In this section I present our approach to trap ultracold atoms in a potential such that the physics is governed by two-dimensional effects. First, I will introduce the concept which is based on the trapping of atoms in a blue-detuned optical lattice. Next, technical details will be discussed and finally I show a procedure to verify that only one single layer of the lattice is occupied. The latter is a crucial condition to work with in-situ imaging and to observe local effects in the cloud. The design and the integration of the lattice which we use to create the two-dimensional confinement was part of the master's project of Klaus Hueck and details can be found in his thesis [55].

6.2.1 Concept

The concept of our approach to create two-dimensional samples is that of an optical lattice. Two intersecting laser beams with identical frequency form an interference pattern which has a lattice spacing on the order of the wavelength. The resulting trapping frequencies are high enough to create a two-dimensional confinement even for larger atom numbers. We use blue-detuned laser beams with a wavelength of 532 nm which create a repulsive potential for the atoms as shown in Fig. 6.2. The two beams intersect each other at an angle of 5.2° which results in a lattice constant of 2.9 µm. An ultracold cloud of atoms is prepared in the squeeze trap as described in chapter 3 and afterwards the blue-detuned lattice is ramped up to load the atoms in between two of the interference maxima. During the loading sequence, the squeeze trap operates at high power and the magnetic field is ramped to the BEC side of the Feshbach resonance to ensure a small spatial extent of the cloud in the z direction. The laser beam of the squeeze trap is aligned such that the atoms are loaded into one single potential minimum of the lattice. If the position of the squeeze trap with respect to the lattice is changed by half a lattice spacing it is possible to create two identical atom clouds on top of each other. After the loading is completed the squeeze trap can be switched off and radial confinement is provided by magnetic trapping which is available due to the geometry of the coils generating the magnetic offset field. The main advantage of a blue-detuned lattice compared to a red-detuned one is that with increasing beam power the vertical trap frequency ω_z becomes larger whereas the radial trapping frequency ω_r is almost not affected. Therefore, high ratios of $\frac{\omega_z}{\omega_r}$ can be achieved which allows two-dimensional trapping of large atom numbers. Further parameters of the lattice trap are listed in Tab. 6.1.

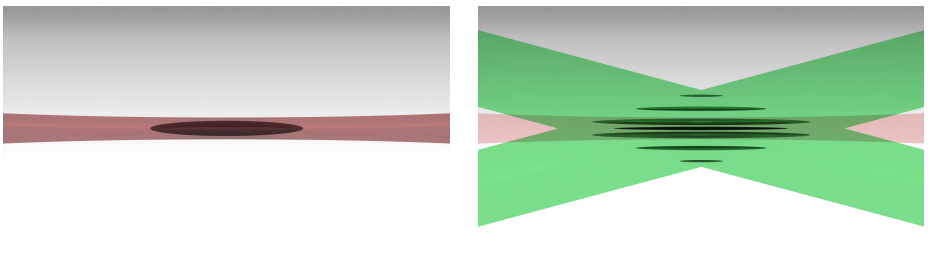

(a) Oblate cloud in the squeeze trap (b) Blue-detuned lattice for 2D confinement

Figure 6.2: The concept for the creation of single-layer two-dimensionally trapped atom clouds. (a) First, a cold oblate sample is prepared in the squeeze trap as described in chapter 3. (b) Two intersecting blue-detuned laser beams with a wavelength of 512 nm create an interference pattern. The additional confinement in the z-direction which is created by that lattice is sufficiently strong to achieve two-dimensional trapping. The lattice spacing is 2.9 µm and the squeeze trap is positioned such that the cloud is located in between two interference maxima.

6.2.2 Green lattice

The light for the green lattice is created by frequency doubling[6] of 1064 nm light created by a Nd:YAG laser[7] which is amplified with a fibre amplifier[8] prior to the second harmonic generation. The main design criterion of the 532 nm lattice is stability. For a reproducible transfer of atoms from the squeeze trap into one single layer of the lattice, it is necessary to reach a stability of the two traps with respect to each other of less than a lattice spacing. As there is no automatic feedback loop installed to stabilize beam pointing, a high level of mechanical stability is essential. Therefore, all the optics for the lattice and the squeeze trap are designed as rigid and compact as possible. In addition, the two fibre couplers for the 532 nm and the 1064 nm light are mounted in a symmetric arrangement on the two sides of a single, vertically installed optical breadboard. The beam splitting assembly to create the two laser beams for the lattice, is a customized design which was optimized for long term stability and low drifts of the beam pointing. A sketch of the assembly is shown in Fig. 6.3. After the two beams have been separated, they pass through a number of lenses for beam shaping. Afterwards, they are combined with the 1064 nm beam, which forms the squeeze trap, with a dichroic mirror. The lattice beams are shaped to reach an elliptical beam waist of 350 µm × 35 µm[9]. The achieved intersection area is almost circular in the radial plane. The spatial restrictions around the science cell make it difficult to perform manual readjustments to the optics of the lattice. Therefore, one of the lenses is mounted on a piezo actuated linear stage which can be remote controlled. The movement of the lens shifts the intersection position of

[6] Evans & Sutherland, doubling cavity
[7] Innolight, Mephisto MOPA
[8] Nufern, Sub-1174-22 Fibre Laser
[9] $1/e^2$ radius, intensity

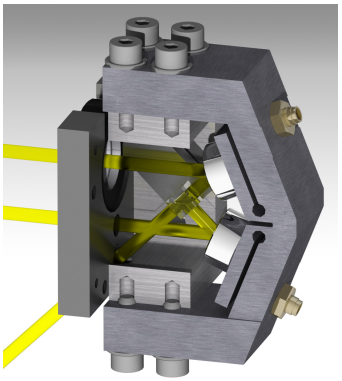

Figure 6.3: Assembly to split the 532 nm laser beam into two parallel beams in order to create the lattice for the two-dimensional confinement. The design minimizes drifts in the beam pointing while still providing a certain adjustment range by utilizing flexure bearings. The graphic is adopted from Ref. [55].

Description	Value
Lattice laser, wavelength	532 nm
Lattice laser, beam intersect angle	5.2°
Lattice laser, beam waist dimensions	35 µm × 350 µm
Lattice, spacing	2.9 µm
Lattice, vertical trap frequency at 600 mW	$\omega_z = 2\pi \cdot 24.8\,\mathrm{kHz}$
Trap frequency ratio at 600 mW and $B = 835$ Gauss	$\frac{\omega_z}{\omega_r} \approx 850$

Table 6.1: Properties of the confinement to create a two-dimensional gas.

the two 532 nm laser beams. A direct monitoring of the interference pattern is possible with the BEC-X camera. An exemplary picture can be seen in Fig. 6.4. The camera can also be used to align the lattice with respect to the squeeze trap[10].

6.2.3 Procedure and verification of single-layer two-dimensional confinement

This section presents detailed information on the loading sequence of the lattice trap and the verification scheme that only one single layer of this lattice is occupied. The achieved performance is discussed, including a measurement of the long term stability of the setup.

Sequence

The following procedure is used to create a two-dimensional single-layer sample: first, an ultracold cloud is prepared in the squeeze trap as described in chapter 3. The final evaporation power in the squeeze trap is typically chosen to be 20 mW. After the evaporation

[10] Note the focal shift of the imaging optics when comparing the 532 nm and 1064 nm light.

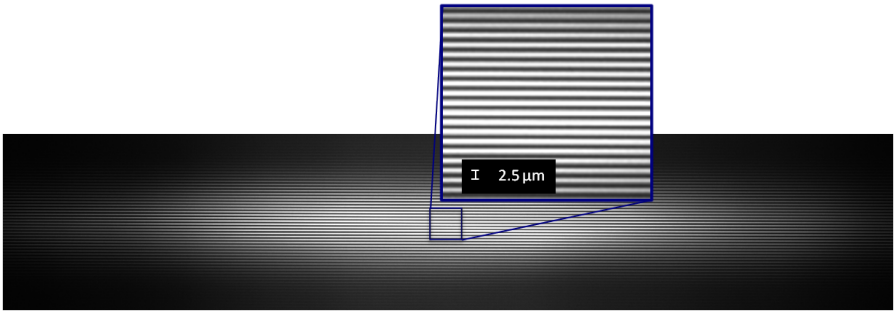

Figure 6.4: Image of the interference pattern used to create the two-dimensional gas acquired by the BEC-X camera. The spacing between two interference maxima is 2.9 µm. The imaging optics can resolve the lattice pattern even though it is below its resolution limit. The reason is that only a very small region in the optical Fourier space is necessary to describe the highly periodic pattern. As a result, only a very small fraction of the lens' aperture is actually used. The aberrations introduced by imperfections in this area are small enough to allow good imaging of the lattice. In contrast, the spatial extent of an atom cloud trapped in one of the interference minima cannot be resolved. As the lattice constant is known with a high precision, such images provide an easy and reliable method to calibrate the magnification of the camera.

is completed the cloud is re-compressed by exponentially increasing the beam power of the squeeze trap to 500 mW in 200 ms and subsequently ramping the magnetic field from 835 Gauss to 795 Gauss (coil current 105 A to 100 A) in 100 ms. Both the magnetic field ramp and the re-compression reduce the spatial extent of the cloud in the vertical direction and therefore simplify the loading of a single layer of the 2D lattice afterwards. After the magnetic ramp, the power of the lattice beams is exponentially increased to typically 600 mW[11] in 100 ms. After the lattice is switched on, the squeeze trap is switched off by exponentially lowering its power within 300 ms. Radial confinement is then provided by the magnetic field curvature ($\omega_R \approx 2\pi \cdot 29$ Hz at 835 Gauss). The atom cloud is now ready to be used for an experiment. Imaging can either be performed while the atoms are in the lattice or after the cloud is transferred back into the squeeze trap. When transferring the atoms back into the squeeze trap an exponential lowering of the lattice beam power over a time of 1 s is necessary to avoid heating. With the correct experimental parameters we observe no heating after transferring the atoms from the squeeze trap to the lattice and back, which indicates that the loading procedure outlined above is adiabatic.

Tunnelling

The lattice beam power can be changed to achieve varying trap frequencies in the vertical directions as shown in Figure 6.5. However, if the beam power is lowered too far, the tunnelling rate between different interference minima increases. As a result, multiple layers are occupied even if the loading sequence successfully loads atoms only into the

[11] Powers for the lattice beams are always given as the sum of both beams.

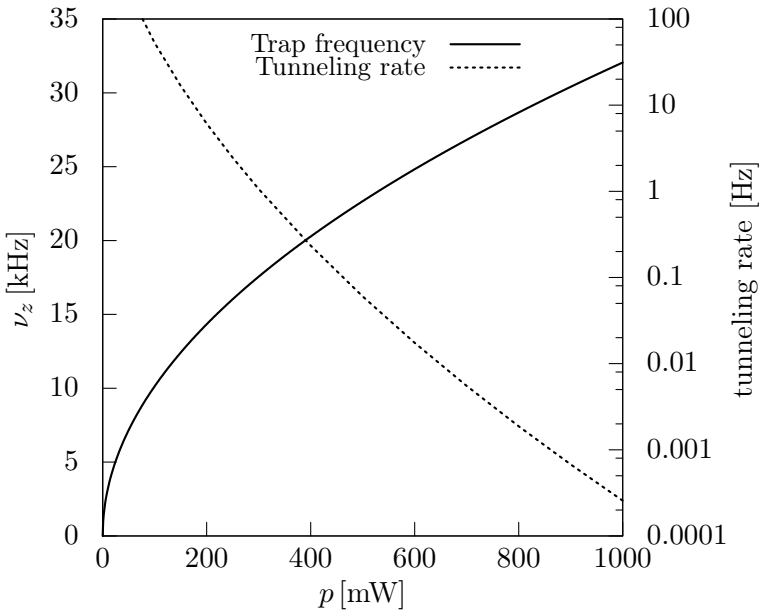

Figure 6.5: Vertical trap frequencies achieved in the squeeze trap as a function of the beam power p (solid line). The tunnelling rate between different layers of the lattice (dashed line) assumes that the lattice beam intensity is half of the peak intensity at the edge of the cloud.

central layer. The tunnelling rate is plotted in Fig. 6.5 under the assumption that there is no further confinement and that the cloud size is such that the laser beam power is reduced to one half at the clouds edge. If the beam power for the lattice exceeds 400 mW, the tunnelling rate becomes insignificant for typical experimental time scales and can be neglected. Tunnelling at low lattice beam powers can be strongly suppressed with the squeeze trap which imposes a strong relative potential offset to the different layers of the lattice. We observe no tunnelling on experimental time scales with the lattice operating at 50 mW and the squeeze trap at 30 mW.

Verification of single-layer loading

When using the loading scheme outlined above, it is crucial to verify that only one single layer of the lattice is populated with atoms. A lateral shift of the trap centre of the squeeze trap relative to the lattice by half a lattice spacing (1.5 µm) is sufficient to change the single-layer loading into a symmetric double layer loading. To monitor the loading performance we utilize a small misalignment between the lattice and the squeeze trap to our advantage as shown in Fig. 6.6. The plane which is defined by the squeeze trap is slightly tilted with respect to the plane defined by the interference pattern of the lattice. The tilting angle is approximately 1.5°. To verify that only one single layer of the lattice is occupied we image the cloud with the squeeze trap and the lattice

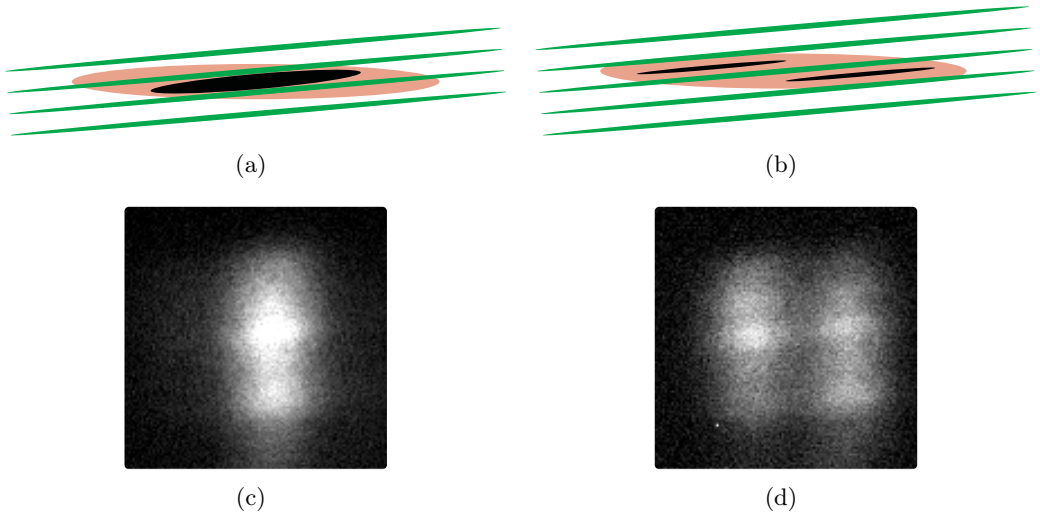

Figure 6.6: The scheme to verify single-layer loading into the 2D lattice. Figures (a) and (b) illustrate how the tilted lattice (green) with respect to the squeeze trapping region (red) separates the atoms (black) into multiple clouds if more than one layer of the lattice is populated. Figures (c) and (d) show the corresponding in situ absorption images. The images are acquired with the squeeze trap operating at 500 mW and the lattice at 600 mW. The magnetic field is 715 Gauss.

operating at high beam powers. As a result, the atoms which populate different layers of the lattice are laterally separated as illustrated in the figure. Therefore the acquired in situ absorption pictures verify weather the loading sequence performs as intended. By changing the pointing of the squeeze trap, the loading can be adjusted to achieve single-layer, symmetric double-layer or asymmetric double-layer loading.

By counting the atom numbers in the separated clouds it is possible to define a parameter s which describes the efficiency of the single-layer loading sequence:

$$s = \frac{N_{central}}{N}, \tag{6.15}$$

where $N_{central}$ is the atom number in the central layer. Typically a value of $s \approx 0.8$ can be achieved for a atom number of $N_{central} \approx 20000$. Loading of three or more layers is possible as well by changing the loading sequence such that the cloud is fairly large in the vertical direction when ramping up the lattice .

Performance

Typical atom numbers which can be trapped in a single layer of the 2D lattice are $N_{central} \approx 30000$ (per spin state). In momentum space we observe a bimodal distribution which we identify with a certain condensate fraction, which typically is around 50 % for 30000 atoms at a magnetic field of $B = 716$ Gauss. For higher magnetic fields closer to

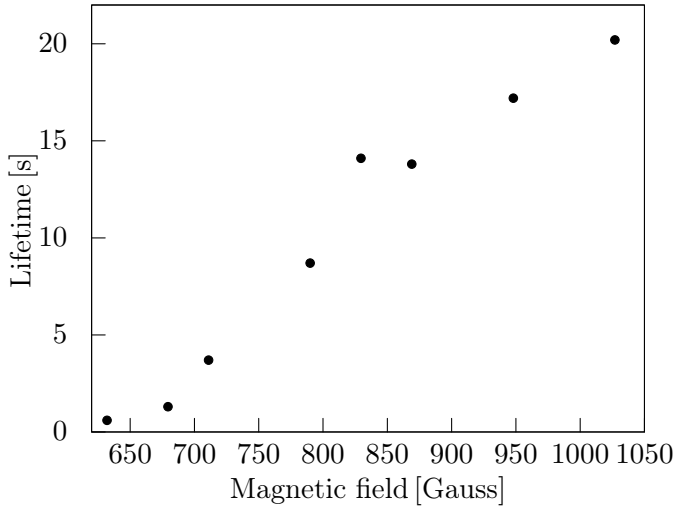

Figure 6.7: Lifetime of atom clouds trapped by the 2D lattice as a function of the magnetic field. The radial confinement is only due to the magnetic trapping and the squeeze trap is completely switched off. At low magnetic fields the dimers start to decay into lower molecular states which reduces the lifetime of the sample significantly.

the Feshbach resonance, the characterisation becomes more difficult due to the lack of a known equation of state which describes the system in the strongly interacting regime.

The lifetimes of the trapped (quasi-)2D gas are shown in Fig. 6.7. Towards the BEC limit the lifetimes are reduced as the dimers become more deeply bound and start to decay into lower vibrational and rotational states. The de-excited molecules are no longer resonant with the imaging light and the released energy is transferred to a third scattering partner which escapes the trap. The lifetimes in the lattice are considerably longer than those achieved by trapping in the squeeze trap (Figure 3.21 on page 88). It is assumed that imperfections of the squeeze trap are responsible for the reduction.

6.2.4 Advanced manipulation methods

The single-layer, two-dimensional ultracold gases serve as excellent starting point for experiments. With the highly resolving imaging optics and the possibility of tuning the interactions, many interesting aspects of 2D systems can be studied. However, the potential of the machine extends even further. A couple of additional manipulation methods have already been implemented. They either act on the sample and the response can be investigated or they allow us to control further properties of the atom cloud. Those techniques are briefly presented in the following. It should be mentioned that many of them have not been used yet for actual measurements.

RF manipulation of hyperfine states

So far, we considered balanced gases where two different hyperfine states are populated equally. The presence of two distinguishable states is a requirement to evaporatively cool the fermionic cloud. However, after the sample has been cooled down it might be interesting to create imbalanced gases or to transfer a fraction of the atoms into a third hyperfine state. For this purpose, radio frequency antennas have been installed in close proximity to the science cell. Details about the setup can be found in the master's thesis of Klaus Hueck [55]. One application of strongly imbalanced gases is to investigate the non-interacting Fermi gas. An interacting imbalanced Fermi gas features pairing of minority and majority atoms in the centre of the trap, whereas the majority atoms will form a purely polarized ring in the outer regions of the atom cloud. The polarized phase is non-interacting and can for example be used to calibrate the temperature in the experiment as the properties of the ideal gas are known, see for example supplemental material of Ref. [58].

Optical lattices

Currently, two different options are available to create optical lattices in the plane of the 2D ultracold gas. One is designed to imprint a small periodic structure onto the inner region of the gas cloud and uses light shone onto the atoms via the upper microscope objective. The other is a conventional retro-reflected lattice which can be either used to simulate the lattice of a condensed matter crystal or to pin the atoms on the lattice sites for imaging purposes.

1. The first lattice uses four far detuned laser beams with a wavelength of 1064 nm, shone onto the atom cloud via the upper microscope objective as shown in Fig. 6.8. Details can be found in the Bachelor's thesis of Niclas Luick [114]. The detuning with respect to the transition frequency of ^{6}Li is large enough to eliminate off-resonant scattering. The beams intersect with an angle of 59° and create a squared optical lattice with a lattice constant of 1080 nm. The individual beams have an adjustable spot size ranging from 15 µm to 30 µm[12] which is smaller than a typical atom cloud in our experiment. Therefore, the lattice can be used to realize cooling schemes which aim for a low entropy area in the centre of the cloud surrounded by a high entropy bath. Another possible application is the simulation of the Hubbard model surrounded by a bath of ultracold atoms.

   The large lattice constant in combination with the high resolution optical system allows to image single sites of the lattice using fluorescence imaging. During the imaging pulse, it is necessary to fix the atoms at their positions which can be achieved by ramping up the lattice beam power. However, due to the large detuning of the lattice beams, high powers are necessary and extreme care has to be taken that the beams do not reach the EMCCD sensor of the camera.

[12] $1/e^2$ radius, intensity

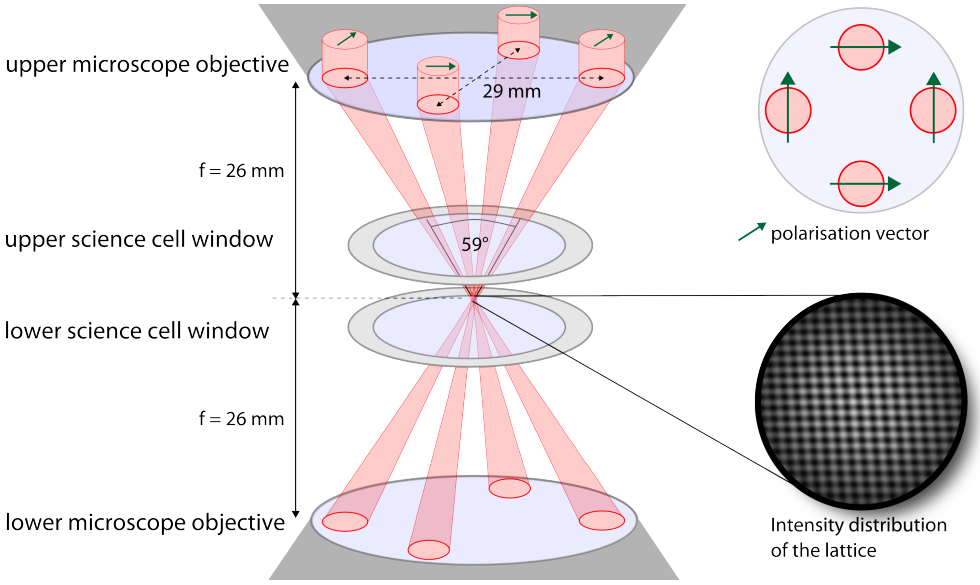

Figure 6.8: Concept of the far detuned optical lattice shone onto the atoms via the upper microscope objective. The four beams with a wavelength of 1064 nm interfere such that a square lattice with a lattice constant 1080 nm is created inside a circular area with an adjustable radius ranging from 15 µm to 30 µm. The polarisation of the beams is chosen such that only diametrically opposite beams interfere. Graphic adopted from Ref. [114].

2. The second lattice uses light at the wavelength of 672 nm and is created by two retro-reflected beams propagating in the same plane where the 2D gas is created in. The beams are perpendicular with respect to each other such that the created squared lattice has a lattice constant of 336 nm. The interference between two non counter-propagating beams is suppressed via different polarisation settings. The beam optics are mounted on the same breadboard around the science cell as the optics for the squeeze trap and the 532 nm lattice which creates the two-dimensional confinement. Details of the setup and the alignment procedures can be found in Ref. [55]. The beam waists of the two lattice beams measure 14 µm × 180 µm[13] which is larger than the typical atom clouds. Hence, the lattice can be used to pin the whole cloud for imaging purposes. With only 15 mW of beam power (per beam) at a wavelength of 672 nm, the lattice created has a depth of 4000 recoil energies. Therefore, the lattice is optimally suited for fluorescence imaging of clouds which have previously been manipulated with the far detuned lattice described above. The differing lattice constants ensure that atoms which were previously trapped in separate sites of the lattice shone through the microscope objective are still separated far enough from each other in the 672 nm lattice to allow single site imaging.

   The same setup can also create a retro-reflected lattice with a larger lattice constant by using light with the wavelength of 1064 nm. With such a lattice the Hubbard model can be simulated. The spacing between two lattice sites of 532 nm is slightly less than the resolution of the microscopes. However, with an optimized analysis of the acquired images single-site resolution is still within reach.

Creation of micro-potentials

A laser beam with a wavelength of 780 nm is focussed with the upper microscope objective to a waist of 0.9 µm which is comparable to several intrinsic length scales in the atom clouds. These are for example the de Broglie wavelength, the healing length and the interparticle distance. In combination with a piezo actuated mirror, this beam was used in the measurements of the speed of sound and the critical velocity presented in chapters 4 and 5. Details about the optical setup of this beam can be found in the Bachelor's thesis of Martin Schlederer [51]. With an additional 2D acousto-optic deflector, it is possible to create multiple small dipole traps in close proximity to each other. The relative positioning of those traps is controllable and simple geometries like square 2×2 plaquettes can be created. By rapidly sweeping the driving frequencies of the deflector, time-averaged potentials like e.g. a ring are possible. Time dependent potentials can be realized as well. The high level of controllability of the micro-potentials facilitates the study of small mesoscopic systems which are embedded in a bath of ultracold atoms.

[13] $1/e^2$ radius, intensity

7 Conclusion & outlook

Superfluidity is a remarkable phenomenon with high technological relevance. In its entirety it is still not completely understood, especially in strongly correlated systems. Our experiments contribute to the understanding of the superfluid state and how it behaves in the transition between the BEC and BCS states.

A thermodynamic equation of state is a powerful tool to describe many properties of a physical system. Our measurements of the speed of sound across the BEC-BCS crossover provide a benchmark to the theoretically predicted equation of state. Similar measurements in two-dimensional systems will offer valuable input to the development of a comprehensive theory describing the BEC-BCS transition in lower dimensions.

The machine that we have set up is able to create single-layer ultracold fermionic gases deep in the two-dimensional regime for the first time. The interaction strength between the constituents can be freely adjusted via a Feshbach resonance and the samples can be manipulated and probed with a resolution of around 700 nm. The capabilities of the setup are rounded off by various options to manipulate the gas. The apparatus has just recently been completed and the measurements of the sound velocity and the critical velocity are only the first experiments which have been performed with it. The potential of the machine has not yet been fully utilized and the future promises many interesting discoveries.

In the following I would like to list a few research directions which can be addressed in the near future and which do not require any major upgrades to the setup. The options listed below are incomplete and the rapid development of the field might open entirely new possibilities.

The speed of sound across the BEC-BCS crossover in two dimensions

As presented in chapter 4, the speed of sound is directly connected to the equation of state which describes the thermodynamic properties of the gas. Many properties of a two dimensional ultracold gas are still unknown including the equation of state. The speed of sound is therefore unknown as well which makes experimental studies desirable. We performed such measurements of the speed of sound in two-dimensional clouds and a preliminary analysis indicates that the equation of state obtained by quantum Monte Carlo simulations [112] is in reasonable agreement with the experimental results. In contrast, the mean-field prediction $v_s = \frac{1}{\sqrt{2}} v_F$ seems to be inadequate. A detailed presentation of those measurements will be made available soon in the doctoral thesis of Kai Morgener

[18] and in a research article which is currently in preparation.

Imbalanced gas and FFLO phase

The behaviour of imbalanced ultracold gases in two dimensions is not fully understood. One example is the Fulde-Ferrell-Larkin-Ovchinnikov (FFLO) phase [115] which features Cooper pairing at finite momentum and thus deformed Fermi surfaces. The FFLO phase was first detected in a superconducting bulk material in 2003 [116] but so far it could not be observed in a cold gas experiment. It is predicted to be rather unstable in 3D ultracold gases but to occupy a much larger area in the phase diagram of 2D Fermi gases [117, 118]. In our apparatus it is possible to create imbalanced gases and confine them in a two-dimensional trap. Under the assumption of the local density approximation, each absorption image which is taken of the atom cloud probes a certain range of the chemical potential and thus can be considered as a cross-section of the phase diagram. If the FFLO phase occupies a sufficiently large area in the phase diagram, a ring-like region in the 2D gas will be in the FFLO state. This region is predicted to show density modulations caused by the non vanishing momentum of the Cooper pairs. Those oscillations can than be detected by analysing high resolution in-situ absorption images.

Friedel oscillations

If a small perturbation is introduced into a Fermi gas, an isotropic spatial oscillation of the density around the position of the perturbation is predicted [119, 120]. These so called Friedel oscillations have already been observed in solids [121] but not yet in quantum gases. The oscillations can be easily understood by considering the following scattering argument. A fermion with a certain initial momentum state can only scatter if the final momentum state is available. In a gas which is cold compared to the Fermi temperature, only atoms with a momentum close to the Fermi momentum k_F are able to scatter. The wave function therefore oscillates with a spatial frequency k_F in the vicinity of an externally imprinted density disturbance. As a result the density oscillates with a spatial frequency of $2k_F$. A more detailed analysis shows that the amplitude of the oscillations decays as $1/r^3$ in three dimensions and as $1/r^2$ in two dimensions [122]. To observe these oscillations in our experiment, it is necessary to create a clear Fermi edge in the momentum distribution of the atoms which could be realized either far on the BCS side of the Feshbach resonance or by using a fully polarized sample. Further it is necessary to probe a region with constant density (and therefore constant k_F) to avoid averaging effects. Our two dimensional ultracold gases in combination with the high resolution imaging system is ideally suited to perform such an experiment.

Optical lattice experiments

The suggested experiments mentioned above do not utilize the possibility to impose an optical lattice onto the atom cloud. With such a lattice it is possible to use the machine

as a simulator for models which are proposed to describe solid state phenomena. The probably most prominent example is the Hubbard model which describes the behaviour of particles in a lattice at low temperatures by taking into account only the on-site interaction energy and the nearest neighbour tunnelling. The model attracts a lot of attention as it might explain high temperature superconductivity. Although the structure of the model is rather simple, its exact solutions away from half filling are still unknown. Cold atom experiments with optical lattices simulate the Hubbard model and thus can help to understand its properties.

Our experiment is particularly well suited for this type of research since it offers in-situ high resolution imaging. If the lattice constant is chosen sufficiently large, the microscope objectives are able to resolve the individual sites of the lattice. In addition, the single-layer two-dimensional confinement of the atoms avoids any averaging along the imaging axis. The possibility to study the spatial distribution of particles inside the optical lattice is unique to cold gas experiments and turns them into a valuable tool to improve the understanding of solid state phenomena.

Experiments with two layers

Our apparatus is able to produce two layers of two-dimensional clouds on top of each other, a configuration potentially useful for experiments as well. A symmetric loading of the two layers can be used to apply heterodyning techniques to gain access to the phase of the system similar to Ref. [123, 124]. Another experimental possibility would be to connect the two layers with a narrow channel created by a red-detuned laser beam from above. An asymmetric loading of the two layer creates a difference of the chemical potential along the channel which allows the study of conductance phenomena.

The controlled coupling of two-dimensional superconducting planes in high-temperature superconductors is a highly promising research topic which may lead to novel crystal structures and superconductors with even higher critical temperatures. Corresponding research is currently performed in Hamburg in the group of Andrea Cavalleri [125]. The realisation of an analogue to the situation in the layered superconductors in our cold atom experiment might be helpful to isolate and to understand the relevant effects in a very clean and controllable environment.

List of Figures

List of Tables

Bibliography

[1] D. R. Tilley and J. Tilley, *Superfluidity and Superconductivity*, Institute of Physics Publishing, London, 3 edn. (1990). 1, 113, 123, 124

[2] C. Chin, R. Grimm, P. Julienne, and E. Tiesinga, *Feshbach resonances in ultracold gases*, Rev. Mod. Phys. **82**, 1225 (2010). 1

[3] W. Ketterle and M. W. Zwierlein, *Making, probing and understanding ultracold Fermi gases*, in *Proceeding-International School of Physics Enrico Fermi*, vol. 164, 95, IOS Press; Ohmsha; 1999 (2007). 2

[4] W. Zwerger (ed.), *The BCS-BEC Crossover and the Unitary Fermi Gas*, vol. 836 of *Lecture Notes in Physics*, Springer Berlin Heidelberg (2012). 2

[5] I. Bloch, J. Dalibard, and W. Zwerger, *Many-body physics with ultracold gases*, Rev. Mod. Phys. **80**, 885 (2008). 2, 140, 142

[6] S. Giorgini, L. P. Pitaevskii, and S. Stringari, *Theory of ultracold atomic Fermi gases*, Rev. Mod. Phys. **80**, 1215 (2008). 2, 127, 128

[7] D. S. Petrov, C. Salomon, and G. V. Shlyapnikov, *Weakly Bound Dimers of Fermionic Atoms*, Phys. Rev. Lett. **93**, 090404 (2004). 2, 101, 103

[8] N. D. Mermin and H. Wagner, *Absence of Ferromagnetism or Antiferromagnetism in One- or Two-Dimensional Isotropic Heisenberg Models*, Phys. Rev. Lett. **17**, 1133 (1966). 3, 141

[9] P. C. Hohenberg, *Existence of Long-Range Order in One and Two Dimensions*, Phys. Rev. **158**, 383 (1967). 3, 141

[10] J. H. Drewes, *Aufbau eines hochauflösenden optischen Systems zur Untersuchung ultrakalter Quantengase*, Master's thesis, Universität Hamburg (2012). 4, 53, 60, 69

[11] E. L. Raab, M. Prentiss, A. Cable, S. Chu, and D. E. Pritchard, *Trapping of Neutral Sodium Atoms with Radiation Pressure*, Phys. Rev. Lett. **59**, 2631 (1987). 7

[12] K. B. Davis, M. O. Mewes, M. R. Andrews, N. J. van Druten, D. S. Durfee, D. M. Kurn, and W. Ketterle, *Bose-Einstein Condensation in a Gas of Sodium Atoms*, Phys. Rev. Lett. **75**, 3969 (1995). 7

[13] M. H. Anderson, J. R. Ensher, M. R. Matthews, C. E. Wieman, and E. A. Cornell, *Observation of Bose-Einstein Condensation in a Dilute Atomic Vapor*, Science **269**, 198 (1995). 7

[14] J. S. Krauser, U. Ebling, N. Fläschner, J. Heinze, K. Sengstock, M. Lewenstein, A. Eckardt, and C. Becker, *Giant Spin Oscillations in an Ultracold Fermi Sea*, Science **343**, 157 (2014). 8

[15] B. Zimmermann, *Microscopy of Ultra-Cold Fermionic Lithium*, Ph.D. thesis, ETH Zürich (2010). 8, 13, 49, 63

[16] T. Müller, *Microscopic Probing and Manipulation of Ultracold Fermions*, Ph.D. thesis, ETH Zürich (2011). 8

[17] B. Zimmermann, T. Müller, J. Meineke, T. Esslinger, and H. Moritz, *High-resolution imaging of ultracold fermions in microscopically tailored optical potentials*, New Journal of Physics **13**, 043007 (2011). 8

[18] K. Morgener, Ph.D. thesis, Universität Hamburg, in preparation. 10, 11, 17, 39, 46, 158

[19] M. E. Gehm, *Properties of 6Li* (2003). 12, 13, 41, 81

[20] D. Breuer and B. Heinrich, *Alkali- und Erdalkalihydroxide (Lithiumhydroxid, Natriumhydroxid, Kaliumhydroxid, Calciumhydroxid) [Air Monitoring Methods in German language, 2003]*, in *The MAK-Collection for Occupational Health and Safety*, –, Wiley-VCH Verlag GmbH & Co. KGaA (2002). 15

[21] A. Rabenau, *Lithium nitride and related materials case study of the use of modern solid state research techniques*, Solid State Ionics **6**, 277 (1982). 15

[22] M. S. Ortman and E. M. Larsen, *Preparation, Characterization, and Melting Point of High-Purity Lithium Oxide*, Journal of the American Ceramic Society **66**, 645 (1983). 15

[23] J. F. O'Hanlon, *A User's Guide to Vacuum Technology*, vol. 3, Wiley-Interscience (2003). 16

[24] F. Wittkötter, *Realisierung einer Resonator-Dipolfalle zur Erzeugung ultrakalter Fermigase*, Diploma thesis, Universität Hamburg (2011). 17, 26, 27, 38

[25] R. Mottl, *A bowtie resonator trap to load, transport and cool fermionic atoms*, Master's thesis, ETH Zürich (2009). 25

[26] W. Weimer, *Stabilizing a Diode Laser on a Narrow Linewidth Ring Cavity*, Master's thesis, ETH Zürich (2010). 25, 34

[27] E. D. Black, *An introduction to Pound-Drever-Hall laser frequency stabilization*, American Journal of Physics **69**, 79 (2001). 31

[28] H. J. Metcalf and P. van der Straten, *Laser Cooling and Trapping*, Springer-Verlag New York (1999). 35

[29] T. A. Savard, K. M. O'Hara, and J. E. Thomas, *Laser-noise-induced heating in far-off resonance optical traps*, Phys. Rev. A **56**, R1095 (1997). 36, 89

[30] U. Schünemann, H. Engler, R. Grimm, M. Weidemüller, and M. Zielonkowski, *Simple scheme for tunable frequency offset locking of two lasers*, Review of Scientific Instruments **70**, 242 (1999). 40

[31] C. Zipkes, *Lasersystem zum Kühlen, Fangen und Abbilden von fermionischem Lithium*, Diploma thesis, ETH zürich (2007). 42

[32] M. R. Andrews, C. G. Townsend, H.-J. Miesner, D. S. Durfee, D. M. Kurn, and W. Ketterle, *Observation of Interference Between Two Bose Condensates*, Science **275**, 637 (1997). 51

[33] J. R. Abo-Shaeer, C. Raman, J. M. Vogels, and W. Ketterle, *Observation of Vortex Lattices in Bose-Einstein Condensates*, Science **292**, 476 (2001). 51

[34] M. Greiner, I. Bloch, O. Mandel, T. W. Hänsch, and T. Esslinger, *Exploring Phase Coherence in a 2D Lattice of Bose-Einstein Condensates*, Phys. Rev. Lett. **87**, 160405 (2001). 51

[35] Y. Castin and R. Dum, *Bose-Einstein Condensates in Time Dependent Traps*, Phys. Rev. Lett. **77**, 5315 (1996). 52

[36] M. W. Zwierlein, J. R. Abo-Shaeer, A. Schirotzek, C. H. Schunck, and W. Ketterle, *Vortices and superfluidity in a strongly interacting Fermi gas*, Nature **435**, 1047 (2005). 52

[37] F. Dalfovo and M. Modugno, *Free expansion of Bose-Einstein condensates with quantized vortices*, Phys. Rev. A **61**, 023605 (2000). 52

[38] N. Gemelke, X. Zhang, C.-L. Hung, and C. Chin, *In situ observation of incompressible Mott-insulating domains in ultracold atomic gases*, Nature **460**, 995 (2009). 52

[39] T. Müller, B. Zimmermann, J. Meineke, J.-P. Brantut, T. Esslinger, and H. Moritz, *Local Observation of Antibunching in a Trapped Fermi Gas*, Phys. Rev. Lett. **105**, 040401 (2010). 52

[40] J. F. Sherson, C. Weitenberg, M. Endres, M. Cheneau, I. Bloch, and S. Kuhr, *Single-atom-resolved fluorescence imaging of an atomic Mott insulator*, Nature **467**, 68 (2010). 52

[41] W. S. Bakr, J. I. Gillen, A. Peng, S. Folling, and M. Greiner, *A quantum gas microscope for detecting single atoms in a Hubbard-regime optical lattice*, Nature **462**, 74 (2009). 52, 82

[42] S. P. Rath, T. Yefsah, K. J. Günter, M. Cheneau, R. Desbuquois, M. Holzmann, W. Krauth, and J. Dalibard, *Equilibrium state of a trapped two-dimensional Bose gas*, Phys. Rev. A **82**, 013609 (2010). 52

[43] *Poster presented by the group of Selim Jochim at the DPG spring meeting in Berlin* (2014). 52

[44] J. W. Goodman, *Fourier Optics*, Robert & Company Publishers (2005). 54

[45] Rayleigh, *XXXI. Investigations in optics, with special reference to the spectroscope*, Philosophical Magazine Series 5 **8**, 261 (1879). 55

[46] C. Weitenberg, *Single-Atom Resolved Imaging and Manipulation in an Atomic Mott Insulator*, Ph.D. thesis, Ludwig-Maximilians-Universität München (2011). 57

[47] V. N. Mahajan, *Strehl ratio for primary aberrations: some analytical results for circular and annular pupils*, J. Opt. Soc. Am. **72**, 1258 (1982). 58

[48] V. N. Mahajan, *Strehl ratio for primary aberrations in terms of their aberration variance*, J. Opt. Soc. Am. **73**, 860 (1983). 58

[49] J. Meineke, *Fluctuations and Correlations in Ultracold Fermi Gases*, Ph.D. thesis, ETH Zürich (2012). 63, 81

[50] E. Hecht, *Optik*, Oldenbourg Wissenschaftsverlag GmbH (2009). 68

[51] M. Schlederer, *Erzeugung von Mikropotentialen zur Manipulation von ultrakalten Fermigasen*, Bachelor's thesis, Universität Hamburg (2013). 76, 77, 80, 155

[52] C.-L. Hung and C. Chin, *In situ imaging of atomic quantum gases*, eprint arXiv:1312.0498v2 (2013). 78

[53] G. Reinaudi, T. Lahaye, Z. Wang, and D. Guéry-Odelin, *Strong saturation absorption imaging of dense clouds of ultracold atoms.*, Optics letters **32**, 3143 (2007). 80

[54] W. Ketterle, D. S. Durfee, and S.-K. D. M., *Making, probing and understanding Bose-Einstein condensates*, eprint arXiv:cond-mat/9904034 (1999). 81

[55] K. Hueck, *Erzeugung und Untersuchung von ultrakalten, zweidimensionalen Fermi-Gasen*, Master's thesis, Universität Hamburg (2013). 83, 84, 86, 107, 128, 146, 148, 153, 155

[56] L. D. Carr, G. V. Shlyapnikov, and Y. Castin, *Achieving a BCS Transition in an Atomic Fermi Gas*, Phys. Rev. Lett. **92**, 150404 (2004). 87

[57] H. Heiselberg, *Collective Modes of Trapped Gases at the BEC-BCS Crossover*, Phys. Rev. Lett. **93**, 040402 (2004). 89

[58] M. J. H. Ku, A. T. Sommer, L. W. Cheuk, and M. W. Zwierlein, *Revealing the Superfluid Lambda Transition in the Universal Thermodynamics of a Unitary Fermi Gas*, Science **335**, 563 (2012). 93, 109, 113, 153

[59] M. R. Andrews, D. M. Kurn, H.-J. Miesner, D. S. Durfee, C. G. Townsend, S. Inouye, and W. Ketterle, *Propagation of Sound in a Bose-Einstein Condensate*, Phys. Rev. Lett. **79**, 553 (1997). 93, 94

[60] J. Joseph, B. Clancy, L. Luo, J. Kinast, A. Turlapov, and J. E. Thomas, *Measurement of Sound Velocity in a Fermi Gas near a Feshbach Resonance*, Phys. Rev. Lett. **98**, 170401 (2007). 93, 94, 95, 117

[61] D. E. Miller, J. K. Chin, C. A. Stan, Y. Liu, W. Setiawan, C. Sanner, and W. Ketterle, *Critical Velocity for Superfluid Flow across the BEC-BCS Crossover*, Phys. Rev. Lett. **99**, 070402 (2007). 93, 131

[62] T. K. Ghosh and K. Machida, *Sound velocity and multibranch Bogoliubov spectrum of an elongated Fermi superfluid in the BEC-BCS crossover*, Phys. Rev. A **73**, 013613 (2006). 96, 117

[63] P. Capuzzi, P. Vignolo, F. Federici, and M. P. Tosi, *Sound propagation in elongated superfluid fermionic clouds*, Phys. Rev. A **73**, 021603 (2006). 96, 117

[64] H. Heiselberg, *Sound modes at the BCS-BEC crossover*, Phys. Rev. A **73**, 013607 (2006). 98, 101, 110, 113, 114

[65] C. J. Pethick and H. Smith, *Bose-Einstein Condensation in Dilute Gases*, Cambridge University Press, 2 edn. (2008). 98, 99, 101, 102, 109

[66] G. E. Astrakharchik, J. Boronat, J. Casulleras, Giorgini, and S., *Equation of State of a Fermi Gas in the BEC-BCS Crossover: A Quantum Monte Carlo Study*, Phys. Rev. Lett. **93**, 200404 (2004). 101, 105, 106

[67] T. D. Lee, K. Huang, and C. N. Yang, *Eigenvalues and Eigenfunctions of a Bose System of Hard Spheres and Its Low-Temperature Properties*, Phys. Rev. **106**, 1135 (1957). 103

[68] F. Schwabl, *Statistische Mechanik*, Springer-Verlag Berlin Heidelberg (2000). 104, 112

[69] T. D. Lee and C. N. Yang, *Many-Body Problem in Quantum Mechanics and Quantum Statistical Mechanics*, Phys. Rev. **105**, 1119 (1957). 104

[70] J. Carlson, S.-Y. Chang, V. R. Pandharipande, and K. E. Schmidt, *Superfluid Fermi Gases with Large Scattering Length*, Phys. Rev. Lett. **91**, 050401 (2003). 105, 109

[71] S. Y. Chang, V. R. Pandharipande, J. Carlson, and K. E. Schmidt, *Quantum Monte Carlo studies of superfluid Fermi gases*, Phys. Rev. A **70**, 043602 (2004). 105, 109

[72] N. Manini and L. Salasnich, *Bulk and collective properties of a dilute Fermi gas in the BCS-BEC crossover*, Phys. Rev. A **71**, 033625 (2005). 106

[73] D. M. Eagles, *Possible Pairing without Superconductivity at Low Carrier Concentrations in Bulk and Thin-Film Superconducting Semiconductors*, Phys. Rev. **186**, 456 (1969). 107

[74] A. Leggett, *Diatomic molecules and cooper pairs*, in A. Pekalski and R. Przystawa (eds.), *Lecture Notes in Physics*, vol. 115, 13–27–, Springer Berlin Heidelberg (1980). 107

[75] P. Arnold, J. E. Drut, and D. T. Son, *Next-to-next-to-leading-order e expansion for a Fermi gas at infinite scattering length*, Phys. Rev. A **75**, 043605 (2007). 109

[76] Y. Nishida and D. T. Son, *e Expansion for a Fermi Gas at Infinite Scattering Length*, Phys. Rev. Lett. **97**, 050403 (2006). 109

[77] H. Hu, X.-J. Liu, and P. D. Drummond, *Equation of state of a superfluid Fermi gas in the BCS-BEC crossover*, EPL (Europhysics Letters) **74**, 574 (2006). 109

[78] R. B. Diener, R. Sensarma, and M. Randeria, *Quantum fluctuations in the superfluid state of the BCS-BEC crossover*, Phys. Rev. A **77**, 023626 (2008). 109

[79] R. Haussmann and W. Zwerger, *Thermodynamics of a trapped unitary Fermi gas*, Phys. Rev. A **78**, 063602 (2008). 109

[80] M. Bartenstein, A. Altmeyer, S. Riedl, S. Jochim, C. Chin, J. H. Denschlag, and R. Grimm, *Crossover from a Molecular Bose-Einstein Condensate to a Degenerate Fermi Gas*, Phys. Rev. Lett. **92**, 120401 (2004). 109

[81] J. Kinast, A. Turlapov, J. E. Thomas, Q. Chen, J. Stajic, and K. Levin, *Heat Capacity of a Strongly Interacting Fermi Gas*, Science **307**, 1296 (2005). 109

[82] M. E. Gehm, S. L. Hemmer, S. R. Granade, K. M. O'Hara, and J. E. Thomas, *Mechanical stability of a strongly interacting Fermi gas of atoms*, Phys. Rev. A **68**, 011401 (2003). 109

[83] L. A. Sidorenkov, M. K. Tey, R. Grimm, Y.-H. Hou, L. Pitaevskii, and S. Stringari, *Second sound and the superfluid fraction in a Fermi gas with resonant interactions*, Nature **498**, 78 (2013). 109, 127

[84] S. Giorgini, L. P. Pitaevskii, and S. Stringari, *Condensate fraction and critical temperature of a trapped interacting Bose gas*, Phys. Rev. A **54**, R4633 (1996). 111

[85] A. Griffin, W.-C. Wu, and S. Stringari, *Hydrodynamic Modes in a Trapped Bose Gas above the Bose-Einstein Transition*, Phys. Rev. Lett. **78**, 1838 (1997). 119

[86] P. S. Shternin, D. G. Yakovlev, C. O. Heinke, W. C. G. Ho, and D. J. Patnaude, *Cooling neutron star in the Cassiopeia A supernova remnant: evidence for superfluidity in the core*, Monthly Notices of the Royal Astronomical Society: Letters **412**, L108 (2011). 123

[87] W. Weimer, K. Morgener, V. P. Singh, J. Siegl, K. Hueck, N. Luick, L. Mathey, and H. Moritz, *The critical velocity in the BEC-BCS crossover*, eprint arXiv:cond-mat/1408.5239v1 (2014). 124

[88] D. R. Allum, P. V. E. McClintock, and A. Phillips, *The Breakdown of Superfluidity in Liquid ^{4}He: An Experimental Test of Landau's Theory*, Philosophical Transactions of the Royal Society of London. Series A, Mathematical and Physical Sciences **284**, 179 (1977). 124, 125

[89] L. Landau, *Theory of the Superfluidity of Helium II*, Phys. Rev. **60**, 356 (1941). 124

[90] D. G. Henshaw and A. D. B. Woods, *Modes of Atomic Motions in Liquid Helium by Inelastic Scattering of Neutrons*, Phys. Rev. **121**, 1266 (1961). 124, 125

[91] G. Bertaina, L. Pitaevskii, and S. Stringari, *First and Second Sound in Cylindrically Trapped Gases*, Phys. Rev. Lett. **105**, 150402 (2010). 127

[92] R. Combescot, M. Y. Kagan, and S. Stringari, *Collective mode of homogeneous superfluid Fermi gases in the BEC-BCS crossover*, Phys. Rev. A **74**, 042717 (2006). 127

[93] M. Marini, F. Pistolesi, and G. Strinati, *Evolution from BCS superconductivity to Bose condensation: analytic results for the crossover in three dimensions*, The European Physical Journal B **1**, 151 (1998). 128

[94] B. Mühlschlegel, *Die thermodynamischen Funktionen des Supraleiters*, Zeitschrift für Physik **155**, 313 (1959). 128

[95] C. Raman, M. Köhl, R. Onofrio, D. S. Durfee, C. E. Kuklewicz, Z. Hadzibabic, and W. Ketterle, *Evidence for a Critical Velocity in a Bose-Einstein Condensed Gas*, Phys. Rev. Lett. **83**, 2502 (1999). 131

[96] R. Onofrio, C. Raman, J. M. Vogels, J. R. Abo-Shaeer, A. P. Chikkatur, and W. Ketterle, *Observation of Superfluid Flow in a Bose-Einstein Condensed Gas*, Phys. Rev. Lett. **85**, 2228 (2000). 131

[97] R. Desbuquois, L. Chomaz, T. Yefsah, J. Leonard, J. Beugnon, C. Weitenberg, and J. Dalibard, *Superfluid behaviour of a two-dimensional Bose gas*, Nat Phys **8**, 645 (2012). 131

[98] R. Feynman, *Chapter II Application of Quantum Mechanics to Liquid Helium*, in C. Gorter (ed.), *Progress in Low Temperature Physics*, vol. 1, 17–53, Elsevier (1955). 131

[99] J. S. Stießberger and W. Zwerger, *Critcal velocity of superfluid flow past large obstacles in Bose-Einstein condensates*, Phys. Rev. A **62**, 061601 (2000). 131, 133, 134

[100] G. Watanabe, F. Dalfovo, F. Piazza, L. P. Pitaevskii, and S. Stringari, *Critical velocity of superfluid flow through single-barrier and periodic potentials*, Phys. Rev. A **80**, 053602 (2009). 132

[101] I. Ferrier-Barbut, M. Delehaye, S. Laurent, A. T. Grier, M. Pierce, B. S. Rem, F. Chevy, and S. C., *A mixture of Bose and Fermi superfluids*, eprint arXiv:cond-mat/1404.2548v1 (2014). 132

[102] Y. Castin, I. Ferrier-Barbut, and C. Salomon, *The Landau critical velocity for a particle in a Fermi superfluid*, eprint arXiv:cond-mat/1408.1326v1 (2014). 132

[103] T. Aioi, T. Kadokura, T. Kishimoto, and H. Saito, *Controlled Generation and Manipulation of Vortex Dipoles in a Bose-Einstein Condensate*, Phys. Rev. X **1**, 021003 (2011). 133, 134

[104] A. C. Mathey, C. W. Clark, and L. Mathey, *Decay of a superfluid current of ultracold atoms in a toroidal trap*, Phys. Rev. A **90**, 023604 (2014). 135

[105] G. E. Astrakharchik and L. P. Pitaevskii, *Motion of a heavy impurity through a Bose-Einstein condensate*, Phys. Rev. A **70**, 013608 (2004). 135

[106] V. L. Berezinskii, *Destruction of long-range order in one-dimensional and two-dimensional systems possesing a continues symmetry group. II. quantum systems*, Sov. Phys. JETP **34**, 610 (1972). 142

[107] J. M. Kosterlitz and D. J. Thouless, *Ordering, metastability and phase transitions in two-dimensional systems*, Journal of Physics C: Solid State Physics **6**, 1181 (1973). 142

[108] D. S. Petrov, M. Holzmann, and G. V. Shlyapnikov, *Bose-Einstein Condensation in Quasi-2D Trapped Gases*, Phys. Rev. Lett. **84**, 2551 (2000). 143, 144

[109] D. S. Petrov and G. V. Shlyapnikov, *Interatomic collisions in a tightly confined Bose gas*, Phys. Rev. A **64**, 012706 (2001). 143

[110] N. Prokof'ev, O. Ruebenacker, and B. Svistunov, *Critical Point of a Weakly Interacting Two-Dimensional Bose Gas*, Phys. Rev. Lett. **87**, 270402 (2001). 144

[111] L. Salasnich, P. A. Marchetti, and F. Toigo, *Superfluidity, sound velocity, and quasicondensation in the two-dimensional BCS-BEC crossover*, Phys. Rev. A **88**, 053612 (2013). 145

[112] G. Bertaina and S. Giorgini, *BCS-BEC Crossover in a Two-Dimensional Fermi Gas*, Phys. Rev. Lett. **106**, 110403 (2011). 145, 157

[113] G. E. Astrakharchik, J. Boronat, J. Casulleras, I. L. Kurbakov, and Y. E. Lozovik, *Equation of state of a weakly interacting two-dimensional Bose gas studied at zero temperature by means of quantum Monte Carlo methods*, Phys. Rev. A **79**, 051602 (2009). 145

[114] N. Luick, *Optische Gitter für die räumlich aufgelöste Untersuchung von ultrakalten Quantengasen*, Bachelor's thesis, Universität Hamburg (2013). 153, 154

[115] P. Fulde and R. A. Ferrell, *Superconductivity in a Strong Spin-Exchange Field*, Phys. Rev. **135**, A550 (1964). 158

[116] A. Bianchi, R. Movshovich, C. Capan, P. G. Pagliuso, and J. L. Sarrao, *Possible Fulde-Ferrell-Larkin-Ovchinnikov Superconducting State in* $CeCoIn_5$, Phys. Rev. Lett. **91**, 187004 (2003). 158

[117] G. J. Conduit, P. H. Conlon, and B. D. Simons, *Superfluidity at the BEC-BCS crossover in two-dimensional Fermi gases with population and mass imbalance*, Phys. Rev. A **77**, 053617 (2008). 158

[118] M. J. Wolak, B. Grémaud, R. T. Scalettar, and G. G. Batrouni, *Pairing in a two-dimensional Fermi gas with population imbalance*, Phys. Rev. A **86**, 023630 (2012). 158

[119] J. Friedel, *XIV. The distribution of electrons round impurities in monovalent metals*, Philosophical Magazine Series 7 **43**, 153 (1952). 158

[120] W. A. Harrison, *Solid State Theory*, International Series in Pure and Applied Physics, McGraw-Hill, Inc. (1970). 158

[121] H. A. Mizes and J. S. Foster, *Long-Range Electronic Perturbations Caused by Defects Using Scanning Tunneling Microscopy*, Science **244**, 559 (1989). 158

[122] G. Y. Hu and R. F. O'Connell, *Polarisability of a two-dimensional electron gas including fluctuation effects*, Journal of Physics C: Solid State Physics **21**, 4325 (1988). 158

[123] A. Polkovnikov, E. Altman, and E. Demler, *Interference between independent fluctuating condensates*, Proceedings of the National Academy of Sciences **103**, 6125 (2006). 159

[124] Z. Hadzibabic, P. Kruger, M. Cheneau, B. Battelier, and J. Dalibard, *Berezinskii-Kosterlitz-Thouless crossover in a trapped atomic gas*, Nature **441**, 1118 (2006). 159

[125] W. Hu, S. Kaiser, D. Nicoletti, C. R. Hunt, I. Gierz, M. C. Hoffmann, M. Le Tacon, T. Loew, B. Keimer, and A. Cavalleri, *Optically enhanced coherent transport in YBa2Cu3O6.5 by ultrafast redistribution of interlayer coupling*, Nat Mater **13**, 705 (2014). 159

Acknowledgements - Danksagung

Diese Arbeit ist durch die tatkräftige und engagierte Unterstützung einiger Menschen entstanden, bei denen ich mich hier bedanken möchte.

Insbesondere ist dies mein Mitstreiter Kai Morgener. Von Beginn an haben wir unzählige Stunden im Labor verbracht, um das Lithium Experiment voran zu treiben. Zu Beginn sind wir unter den Tischen herumgekrochen, haben meterweise Bleche entgratet und hunderte Schrauben angezogen. Später sind dann unzählige Mess- und Optimierungsstunden dazu gekommen. Nicht zuletzt ist es deiner humorvollen und intelligenten Art zu verdanken, dass dies jede Menge Spaß machte und auch stets wunderbar funktionierte.

Auch bei den neueren Mitgliedern des Lithiumteams Jonas, Klaus und Niclas möchte ich mich ganz herzlich bedanken. Es ist eine besondere Freude mit euch zusammen zu arbeiten und auch immer wieder interessante Dinge abseits der Arbeit zu unternehmen. Ich kann mir kein besseres Team vorstellen, um das Lithium Experiment weiter zu betreiben und zu verbessern.

Ein ganz besonderer Dank gebührt Henning Moritz. Du bist es, der mich zum ersten mal mit kalten Gasen in einer Vorlesung an der ETH Zürich in Kontakt gebracht hat und anschließend auf allen Schritten, von der ersten Studienarbeit über den Master bis zum Doktorat, als Lehrer und Mentor begleitet hast. Seit du die Gruppe in Hamburg leitest hast du vieles vollbracht, was an dieser Stelle erwähnenswert wäre. Hier möchte ich hervorheben, dass es letztendlich deine vorausschauende Art ist, welche unsere Gruppe in Hamburg zu dem macht, was sie ist. Du findet kontinuierlich die richtigen Menschen, um ein Team aufzubauen, in dem sich alle wohl fühlen und erstaunliches leisten können.

Ich möchte mich ebenso bei den Ehemaligen unserer Gruppe bedanken. Dies sind Florian, Niels und Jan-Henning. Die tolle Atmosphäre, welche ihr in die Gruppe gebracht habt, lebt bis heute.

Mittlerweile ist unsere Forschungsgruppe deutlich gewachsen und weitere Experimente sind im Aufbau. Insbesondere bei den Ytterbianern und Kalium-Fängern Johannes, Jascha und Phillip möchte ich mich bedanken, für euren Einsatz und die vielen Impulse, die von euch ausgehen.

Was die Arbeit am Institut für Laserphysik ganz besonders bereichert, ist die großartige Zusammenarbeit mit den anderen Forschungsgruppen. Insbesondere der Gruppe Sengstock haben wir, als Gruppe Moritz, viel zu verdanken. Ihr habt uns wunderbar aufgenommen als wir als neue Gruppe am Institut begonnen haben und wenn wir Rat oder Ausrüstung benötigen, ist immer jemand zur Stelle der uns hilft. Ich möchte insbesondere Christoph Becker dafür danken, dass er als mein Zweitbetreuer im GRK immer verfügbar war und Klaus Sengstock für das freundliche Erstellen des Gutachtens für diese Arbeit.

Vijay Singh und Ludwig Mathey möchte ich für die gute Zusammenarbeit und die vielen Inputs danken, insbesondere bei der Arbeit an der kritischen Geschwindigkeit.

Beim Aufbau des Experiments konnte unsere Gruppe immer auf eine gute technische Unterstützung zurück greifen. Ein Dankeschön dafür an Reinhard Mielck, Stephan Garbers und Ralf Lühr. Ebenso möchte ich dem gesamten Team unserer Werkstatt um Herrn Fleig danken. Ihr habt mit der sauberen und zeitnahen Fertigstellung unserer Aufträge maßgeblich zum erfolgreichen Aufbau des Experiments beigetragen.

Ein ganz besonders herzliches Dankeschön auch an meine Familie und besonders an meine Eltern Martina und Peter. Ihr habt mich immer voll unterstützt und letzten Endes diese Arbeit erst ermöglicht.

Besonders herzlich möchte ich mich bei Ling bedanken.
感谢伶在过去的一年中对我无私的帮助。你总是在我身边耐心地鼓励我，陪伴我，给我无微不至的关怀。谢谢你。